



PACIFIC EARTHQUAKE ENGINEERING RESEARCH CENTER

Analytical Modeling of Reinforced Concrete Walls for Predicting Flexural and Coupled– Shear-Flexural Responses

Kutay Orakcal

Leonardo M. Massone

and

John W. Wallace

University of California, Los Angeles

Analytical Modeling of Reinforced Concrete Walls for Predicting Flexural and Coupled- Shear-Flexural Responses

Kutay Orakcal

Leonardo M. Massone

John W. Wallace

Department of Civil and Environmental Engineering
University of California, Los Angeles

PEER Report 2006/07
Pacific Earthquake Engineering Research Center
College of Engineering
University of California, Berkeley

October 2006

ABSTRACT

This study investigates an effective modeling approach that integrates important material characteristics and behavioral response features (e.g., neutral axis migration, tension stiffening, gap closure, and nonlinear shear behavior) for a reliable prediction of reinforced concrete (RC) wall response. A wall macro-model was improved by implementing refined constitutive relations for materials and by incorporating a methodology that couples shear and flexural response components. Detailed calibration of the model and comprehensive correlation studies were conducted to compare the model results with test results for slender walls with rectangular and T-shaped cross sections, as well as for short walls with varying shear-span ratios.

Flexural response predictions of the analytical model for slender walls compare favorably with experimental responses for flexural capacity, stiffness, and deformability, although some significant variation is noted for local compressive strains. For T-shaped walls, model predictions are reasonably good, although the model can not capture the longitudinal strains along the flange. The coupled shear-flexure model captures reasonably well the measured responses of short walls with relatively large shear-span ratios (e.g., 1.0 and 0.69). Better response predictions can be obtained for walls with lower shear-span ratios upon improving the model assumptions related to the distribution of stresses and strains in short walls.

ACKNOWLEDGMENTS

This work was supported in part by the Earthquake Engineering Research Centers Program of the National Science Foundation under award number EEC-9701568 through the Pacific Earthquake Engineering Research (PEER) Center.

Any opinions, findings, and conclusions or recommendations expressed in this material are those of the author(s) and do not necessarily reflect those of the National Science Foundation.

CONTENTS

ABSTRACT	iii
ACKNOWLEDGMENTS	iv
TABLE OF CONTENTS	v
LIST OF FIGURES	ix
LIST OF TABLES	xv
1 INTRODUCTION	1
1.1 General.....	1
1.2 Objectives and Scope.....	3
1.3 Organization.....	5
2 RELATED RESEARCH	7
3 FLEXURAL MODELING — ANALYTICAL MODEL DESCRIPTION	21
4 FLEXURAL MODELING — MATERIAL CONSTITUTIVE MODELS	29
4.1 Constitutive Model for Reinforcement.....	29
4.2 Constitutive Models for Concrete.....	36
4.2.1 Hysteretic Constitutive Model by Yassin (1994).....	36
4.2.2 Hysteretic Constitutive Model by Chang and Mander (1994).....	43
4.2.2.1 Compression Envelope Curve.....	44
4.2.2.2 Tension Envelope Curve.....	49
4.2.2.3 Hysteretic Properties of the Model.....	51
4.3 Modeling of Tension Stiffening.....	60
4.4 Summary.....	68
5 NONLINEAR ANALYSIS STRATEGY	73
5.1 Nonlinear Quasi-Static Problem.....	74
5.2 Incremental Iterative Approach — Newton-Raphson Scheme.....	75
5.3 Applied Nonlinear Analysis Solution Strategy.....	78
5.3.1 First Iteration Cycle, $j = 1$	79
5.3.2 Equilibrium Iteration Cycles, $j \geq 2$	80
5.3.3 Incrementation Strategy: Incrementation of Selected Displacement Component.....	82
5.3.4 Iterative Strategy: Iteration at Constant Displacement.....	83
5.3.5 Convergence Criteria and Re-Solution Strategy.....	83
5.4 Summary.....	84
6 FLEXURAL MODELING — ANALYTICAL MODEL RESULTS AND PARAMETRIC SENSITIVITY STUDIES	85
6.1 Review of Analytical Model.....	85

6.2	Analytical Model Response	89
6.3	Parametric Sensitivity Studies	95
6.3.1	Material Constitutive Parameters.....	95
6.3.2	Model Parameters	107
6.4	Summary	111
7	FLEXURAL MODELING — EXPERIMENTAL CALIBRATION AND VERIFICATION	113
7.1	Overview of Experimental Studies	113
7.1.1	Test Specimen Information.....	113
7.1.2	Materials.....	115
7.1.3	Testing Apparatus	117
7.1.4	Instrumentation and Data Acquisition	121
7.1.5	Testing Procedure.....	125
7.2	Calibration of the Analytical Model	126
7.2.1	Calibration for Model Geometry.....	127
7.2.2	Calibration for Constitutive Material Parameters	129
7.2.2.1	Steel Stress-Strain Relations.....	129
7.2.2.2	Concrete Stress-Strain Relations	131
7.2.2.3	Shear Force–Deformation Relation.....	135
7.3	Model Results and Comparison with Experimental Results.....	135
7.3.1	Rectangular Wall, RW2	141
7.3.2	T-Shaped Wall, TW2	147
7.4	Summary	153
8	MODELING OF COUPLED SHEAR AND FLEXURAL RESPONSES: ANALYTICAL MODEL DESCRIPTION	155
8.1	Experimental Evidence of Flexure-Shear Interaction.....	155
8.1.1	Overview of Tests	156
8.1.2	Instrumentation for Measuring Flexural and Shear Deformations	158
8.1.3	Measurement of Flexural Deformations	158
8.1.4	Measurement of Shear Deformations: Corrected “X” Configuration.....	159
8.1.5	Experimental Force versus Displacement Relations for Shear and Flexure ...	159
8.2	Base Model: Multiple-Vertical-Line-Element Model (MVLEM).....	161
8.3	Incorporating Displacement Interpolation Functions.....	162
8.4	Nonlinear Analysis Solution Strategy: Finite Element Formulation	166
8.5	Modeling of Shear-Flexure Interaction.....	168
8.6	Numerical Methodology for Proposed Model	169
8.7	Material Constitutive Models.....	173

8.7.1	Constitutive Model for Reinforcing Steel	174
8.7.2	Constitutive Model for Concrete.....	175
9	MODELING OF COUPLED SHEAR AND FLEXURAL RESPONSES — EXPERIMENTAL VERIFICATION	181
9.1	Panel Behavior	181
9.2	Slender Wall Response	183
9.2.1	Test Overview	183
9.2.2	Model Calibration	183
9.2.3	Model Correlation with Test Results	184
9.3	Short Wall Response	186
9.3.1	Overview of Tests	187
9.3.2	Model Calibration	188
9.3.3	Model Correlation with Test Results	188
9.4	Sensitivity of Short Wall Analytical Results to Model Discretization	191
9.5	Experimental Shear Strain and Horizontal Normal Strain Distributions in Short Walls.....	193
9.5.1	Shear Strain Distributions	194
9.5.2	Horizontal Normal Strain Distributions.....	195
9.6	Sensitivity of Short Wall Analytical Results to the Zero-Resultant-Horizontal- Stress Assumption.....	197
10	SUMMARY AND CONCLUSIONS.....	201
10.1	Flexural Modeling.....	201
10.2	Shear-Flexure Interaction Model	204
10.3	Suggested Improvements to Analytical Models	205
	REFERENCES.....	207

LIST OF FIGURES

Fig. 2.1	Beam-column element model	8
Fig. 2.2	Wall rocking and effect of neutral axis shift on vertical displacements.....	8
Fig. 2.3	Three-vertical-line-element model (TVLEM).....	9
Fig. 2.4	Axial-stiffness hysteresis model (ASHM) (Kabeyasawa et al., 1983)	9
Fig. 2.5	Origin-oriented-hysteresis model (OOHM) (Kabeyasawa et al., 1983).....	10
Fig. 2.6	Axial-element-in-series model (AESM) (Vulcano and Bertero, 1986).....	11
Fig. 2.7	Axial force–deformation relation of the AESM	11
Fig. 2.8	Multiple-vertical-line-element-model (Vulcano et al., 1988).....	13
Fig. 2.9	Modified axial-element-in-series model (Vulcano et. al., 1988).....	13
Fig. 2.10	Constitutive law adopted in original MVLEM for reinforcing steel	14
Fig. 2.11	Constitutive laws adopted in original MVLEM for concrete	15
Fig. 2.12	Force-deformation relations adopted in modified MVLEM	16
Fig. 2.13	Modification of the TVLEM (Kabeyasawa et al., 1997).....	17
Fig. 3.1	MVLEM element.....	21
Fig. 3.2	Modeling of wall with MVLEM.....	22
Fig. 3.3	Tributary area assignment.....	22
Fig. 3.4	Rotations and displacements of MVLEM element.....	22
Fig. 3.5	Origin-oriented-hysteresis model for horizontal shear spring.....	24
Fig. 3.6	Uncoupling of modes of deformation of MVLEM element.....	24
Fig. 3.7	Element deformations of MVLEM element (Vulcano et al., 1988)	27
Fig. 4.1	Constitutive model for steel (Menegotto and Pinto, 1973).....	31
Fig. 4.2	Degradation of cyclic curvature.....	32
Fig. 4.3	Stress-strain relation generated by Menegotto and Pinto (1973) model.....	33
Fig. 4.4	Sensitivity of stress-strain relation to cyclic curvature parameters	33
Fig. 4.5	Stress shift due to isotropic strain hardening (Filippou et al., 1983).....	34
Fig. 4.6	Effect of isotropic strain hardening on stress-strain relation	35
Fig. 4.7	Modified Kent and Park model (1982) for concrete in compression	37
Fig. 4.8	Hysteretic unloading and reloading rules (Yassin, 1994).....	39
Fig. 4.9	Hysteretic parameters of model by Yassin (1994)	40
Fig. 4.10	Hysteresis loops in tension (Yassin, 1994).....	41

Fig. 4.11	Compression and tension envelopes of Chang and Mander (1994) model	46
Fig. 4.12	Confinement mechanism for circular and rectangular cross sections (Chang and Mander, 1994).....	49
Fig. 4.13	Hysteretic parameters of Chang and Mander (1994) model.....	52
Fig. 4.14	Unloading from compression envelope curve (Chang and Mander, 1994).....	55
Fig. 4.15	Continuous hysteresis in compression and tension (Chang and Mander, 1994)	56
Fig. 4.16	Transition curves before cracking (Chang and Mander, 1994)	57
Fig. 4.17	Transition curves after cracking (Chang and Mander, 1994)	57
Fig. 4.18	Numerical instabilities in hysteretic rules.....	59
Fig. 4.19	Axial-element-in-series model.....	61
Fig. 4.20	Two-parallel-component-model	62
Fig. 4.21	Average stress-strain relation by Belarbi and Hsu for concrete in tension.....	63
Fig. 4.22	Effect of tension stiffening on reinforcing bars	64
Fig. 4.23	Average stress-strain relation by Belarbi and Hsu (1994) for reinforcing bars embedded in concrete	66
Fig. 4.24	Stress-strain relations for concrete in tension.....	67
Fig. 4.25	Stress-strain relations for reinforcing bars.....	68
Fig. 4.26	Compression envelopes for concrete — model vs. test results	69
Fig. 4.27	Tension envelopes for concrete — model comparisons	70
Fig. 5.1	Sample model assembly with degrees of freedom	73
Fig. 5.2	Newton-Raphson iteration scheme	76
Fig. 5.3	Nodal-displacement and internal resisting-force increments	76
Fig. 5.4	Load limit points within sample quasi-static load-displacement path.....	77
Fig. 5.5	Representation of adapted nonlinear analysis solution scheme for single-degree-of-freedom system	81
Fig. 5.6	Iterative strategy and residual displacements	82
Fig. 6.1	Multiple-vertical-line-element model.....	86
Fig. 6.2	Tributary area assignment.....	86
Fig. 6.3	Constitutive model parameters for reinforcing steel (Menegotto and Pinto, 1973) ..	87
Fig. 6.4	Hysteretic constitutive model for concrete (Chang and Mander, 1994).....	88
Fig. 6.5	Hysteretic constitutive model for concrete (Yassin, 1994)	88
Fig. 6.6	Load-displacement response predicted by analytical model	90
Fig. 6.7	Predicted variation in position of neutral axis	91

Fig. 6.8	Predicted longitudinal strain histories	91
Fig. 6.9	Effect of axial load on analytical response	92
Fig. 6.10	Monotonic and quasi-static responses	93
Fig. 6.11	Analytical load-displacement response predictions obtained using different constitutive relations for concrete.....	95
Fig. 6.12	Sensitivity of analytical response to steel yield stress	97
Fig. 6.13	Sensitivity of analytical response to steel strain-hardening ratio	98
Fig. 6.14	Sensitivity of analytical response to hysteretic parameters for steel	99
Fig. 6.15	Effect of concrete tensile strength on analytical response.....	101
Fig. 6.16	Effect of concrete tensile plastic stiffness on analytical response.....	103
Fig. 6.17	Sensitivity of analytical response to concrete compressive strength and associated parameters	106
Fig. 6.18	Strength degradation in analytical response	107
Fig. 6.19	Sensitivity of response to number of MVLEM and uniaxial elements	109
Fig. 6.20	Sensitivity of response to center of rotation parameter c	110
Fig. 7.1	RC wall specimens tested by Thomsen and Wallace (1995).....	114
Fig. 7.2	Profile view of specimen RW2 showing placement of reinforcement.....	114
Fig. 7.3	Wall cross-sectional views	116
Fig. 7.4	Measured concrete stress-strain relations	117
Fig. 7.5	Measured steel stress-strain relations	118
Fig. 7.6	Schematic of test setup (Thomsen and Wallace, 1995).....	119
Fig. 7.7	Photograph of test setup (Thomsen and Wallace, 1995).....	119
Fig. 7.8	Load transfer assembly	120
Fig. 7.9	Hydraulic actuator	120
Fig. 7.10	Instrumentation on wall specimens	121
Fig. 7.11	Instrumentation used to measure pedestal movement	123
Fig. 7.12	Wire potentiometers used to measure shear deformations	124
Fig. 7.13	Instrumentation located within first story.....	124
Fig. 7.14	Embedded concrete strain gage in boundary element	125
Fig. 7.15	Lateral drift routines for specimens RW2 and TW2	126
Fig. 7.16	Model discretization and tributary area assignment	128
Fig. 7.17	Constitutive model for reinforcing steel and associated parameters	129
Fig. 7.18	Calibration of constitutive model for reinforcing steel.....	130

Fig. 7.19	Constitutive model for concrete and associated parameters.....	132
Fig. 7.20	Calibration of constitutive model for unconfined concrete in compression.....	133
Fig. 7.21	Calibration of constitutive model for concrete in tension	133
Fig. 7.22	Calibration of constitutive model for confined concrete	134
Fig. 7.23	Measured first-story shear deformations	137
Fig. 7.24	Measured second-story shear deformations.....	138
Fig. 7.25	Top lateral displacement history of wall specimens.....	139
Fig. 7.26	Axial load history of wall specimens.....	140
Fig. 7.27	Wall RW2, measured vs. predicted load-displacement responses	141
Fig. 7.28	Wall RW2, lateral displacement profiles.....	143
Fig. 7.29	Wall RW2, first-story flexural deformations.....	144
Fig. 7.30	Wall RW2, concrete strain measurements by LVDTs vs. predictions	145
Fig. 7.31	Wall RW2, steel strain gage measurements vs. predictions	145
Fig. 7.32	Wall RW2, concrete strain gage measurements vs. predictions.....	146
Fig. 7.33	Wall TW2, measured vs. predicted load-displacement responses.....	148
Fig. 7.34	Wall TW2, lateral displacement profiles.....	148
Fig. 7.35	Wall TW2, first-story flexural deformations	149
Fig. 7.36	Wall TW2, measured concrete strains along wall flange vs. predictions.....	150
Fig. 7.37	Wall TW2, measured steel strains along wall flange vs. predictions	150
Fig. 7.38	Wall TW2, concrete strain measurements by LVDTs vs. predictions	151
Fig. 7.39	Wall TW2, steel strain gage measurements at wall base level vs. predictions.....	152
Fig. 7.40	Wall TW2, concrete strain gage measurements vs. predictions	153
Fig. 8.1	General instrument configuration: RW2 and SRCW	157
Fig. 8.2	Uncorrected shear deformation measured at wall base	158
Fig. 8.3	First- and second-story deformations: RW2.....	160
Fig. 8.4	Story deformations: SRCW1	161
Fig. 8.5	MVLEM element and incorporated displacement field components	162
Fig. 8.6	Definition of center of rotation	163
Fig. 8.7	Center of rotation for specimen SRCW3.....	164
Fig. 8.8	Element section rotation	166
Fig. 8.9	Trial displacement state at section (j) of coupled model element	170
Fig. 8.10	Trial strain state at section (j) of coupled model element.....	171

Fig. 8.11	Trial stress state at strip (i) in section (j) in principal directions	171
Fig. 8.12	Trial stress state for concrete at strip (i) in section (j) in x-y direction.	172
Fig. 8.13	Trial stress state for concrete and steel (combined) in x-y direction.....	172
Fig. 8.14	Flowchart for biaxial behavior.....	173
Fig. 8.15	Constitutive model for reinforcing steel.....	176
Fig. 8.16	Constitutive model for concrete in tension.....	178
Fig. 8.17	Constitutive model for concrete in compression.....	179
Fig. 9.1	Test results vs. model element predictions for panel responses	182
Fig. 9.2	Lateral load–top displacement response of specimen RW2	185
Fig. 9.3	Lateral load–displacement responses at first-story level (RW2).....	186
Fig. 9.4	Lateral load–displacement responses for short wall specimens	190
Fig. 9.5	Sensitivity of model results to number of strips and model elements	192
Fig. 9.6	Shear strain measurements for specimen S2	194
Fig. 9.7	Horizontal strain (ϵ_x) measurements for specimen S2.....	196
Fig. 9.8	Average horizontal strain (ϵ_x) measurements for specimen S2	196
Fig. 9.9	Lateral load-displacement responses for short wall specimens 152 and 16 — zero horizontal stress and zero horizontal strain cases	198

LIST OF TABLES

Table 7.1	Calibrated parameters for concrete in tension and steel in compression.....	131
Table 7.2	Calibrated parameters for concrete in compression and steel in tension.....	131
Table 7.3	Peak lateral top displacements at applied drift levels.....	139
Table 9.1	Properties of selected short wall specimens	180

1 Introduction

1.1 GENERAL

Reinforced concrete (RC) structural walls are effective for resisting lateral loads imposed by wind or earthquakes on building structures. They provide substantial strength and stiffness as well as the deformation capacity needed to meet the demands of strong earthquake ground motions. Extensive research, both analytical and experimental, has been carried out to study the behavior of RC walls and of RC frame-wall systems. In order to analytically predict the inelastic response of such structural systems under seismic loads, the hysteretic behavior of the walls and the interaction of the walls with other structural members should be accurately described by reliable analytical tools. Prediction of the inelastic wall response requires accurate, effective, and robust analytical models that incorporate important material characteristics and behavioral response features such as neutral axis migration, concrete tension-stiffening, progressive crack closure, nonlinear shear behavior, and the effect of fluctuating axial force and transverse reinforcement on strength, stiffness, and deformation capacity.

Analytical modeling of the inelastic response of RC wall systems can be accomplished either by using either microscopic finite element models based on a detailed interpretation of the local behavior, or by using phenomenological macroscopic or meso-scale models based on capturing overall behavior with reasonable accuracy. An effective analytical model for analysis and design of most systems should be relatively simple to implement and reasonably accurate in predicting the hysteretic response of RC walls and wall systems. Although microscopic finite element models can provide a refined and detailed definition of the local response, their efficiency, practicality, and reliability are questionable due to complexities involved in developing the model and interpreting the results. Macroscopic models, on the other hand, are

practical and efficient, although their application is restricted based on the simplifying assumptions upon which the model is based.

As discussed by Vulcano and Bertero (1987), the nonlinear analysis of RC wall systems can be efficiently carried out by using analytical models based on a macroscopic approach rather than by using detailed microscopic models. However, a reliable model for practical nonlinear analysis of RC walls is not available in commonly used structural analysis platforms, such as DRAIN-2DX and SAP2000. Use of a single beam-column element at the wall centroidal axis is a common modeling approach (e.g., FEMA 356, *Prestandard and Commentary for the Seismic Rehabilitation of Buildings*, 2000). In this case, an equivalent column is used to model the properties of the wall, and girders with rigid end zones are connected to the column at each floor level. The rotations of a beam-column element occur about the centroidal axis of the wall; therefore, migration of the neutral axis along the wall cross section during loading and unloading is not captured. Consequently, rocking of the wall and interaction with any connecting elements (e.g., girders), both in the plane of the wall and perpendicular to the wall, may not be properly considered. According to FEMA 356 (*Prestandard*, 2000) interaction of the wall with other structural and nonstructural elements should be considered, which implies that more detailed models be used.

Various phenomenological macroscopic models have been proposed to capture important behavioral features for predicting the inelastic response of RC structural walls. As a result of extensive studies, the multi-component-in-parallel model (MCPM), later referred to as multiple-vertical-line-element model (MVLEM) proposed by Vulcano et al. (1988) has been shown to successfully balance the simplicity of a macroscopic model and the refinements of a microscopic model. The MVLEM captures essential response characteristics (e.g., shifting of the neutral axis, and the effect of a fluctuating axial force on strength and stiffness), which are commonly ignored in simple models, and offers the flexibility to incorporate refined material constitutive models and important response features (e.g., confinement, progressive gap closure and nonlinear shear behavior) in the analysis. Prior work identified that wall flexural responses can be accurately predicted by the MVLEM if refined hysteretic constitutive laws are adopted in the model (Vulcano et al., 1988). However, such models usually consider uncoupled shear and flexural responses, which is inconsistent with experimental observations, even for relatively slender walls (Massone and Wallace, 2004).

1.2 OBJECTIVES AND SCOPE

Although relatively extensive research has been conducted to develop a MVLEM for structural walls, the MVLEM has not been implemented into widely available computer programs and limited information is available on the influence of material behavior on predicted responses. As well, the model has not been sufficiently calibrated with and validated against extensive experimental data for both global (e.g., wall displacement and rotation) and local (i.e., section curvature and strain at a point) responses. The reliability of the model in predicting the shear behavior of walls is questionable and an improved methodology that relates flexural and shear responses is needed. As well, the model has not been assessed and calibrated for walls with flanged (e.g., T-shaped) cross sections. According to FEMA 356 (*Prestandard*, 2000), either a modified beam-column analogy (Yan and Wallace, 1993) or a multiple-spring approach (as in the MVLEM) should be used for modeling rectangular walls and wall segments with aspect (height-to-length) ratios smaller than 2.5, as well as for flanged wall sections with aspect ratios smaller than 3.5. However, either the MVLEM or a similar multiple-spring model is not available in most codes. The leading and most recently released structural analysis software used in the industry for reinforced concrete design applications, “RAM Perform” (RAM International, 2003), uses a fiber-cross-section element for modeling of slender walls; however, the nonlinear response is represented by simplified ad hoc force-deformation relations (trilinear force-deformation envelopes and simple hysteresis rules) as opposed to incorporating well-calibrated material behavior in the model response.

Given the shortcomings noted above, a research project was undertaken at the University of California, Los Angeles, to investigate and improve the MVLEM for both slender and squat RC walls, as well as to calibrate and validate it against extensive experimental data. More recent modifications of the MVLEM (Fischinger et al., 1990; Fajfar and Fischinger, 1990; Fischinger et al., 1991, 1992) have included implementing simplified force-deformation rules for the model sub-elements to capture the behavior observed in experimental results; however, the resulting models are tied to somewhat arbitrary force-deformation parameters, the selection of which was based on engineering judgment. An alternative approach is adopted here, where up-to-date and state-of-the-art cyclic constitutive relations for concrete and reinforcing steel are adopted to track the nonlinear response at both the global and local levels, versus the use of simplified (ad hoc) force-deformation rules as done in prior studies. Therefore, the MVLEM implemented in this

study relates the predicted response directly to material behavior without incorporating any additional empirical relations. This allows the designer to relate analytical responses directly to physical material behavior and provides a more robust modeling approach, where model improvements result from improvement in constitutive models, and refinement in the spatial resolution of the discrete model. The analytical model, as adopted here, is based on a fiber modeling approach, which is the current state-of-the-art tool for modeling slender reinforced concrete members.

Upon implementation of updated and refined cyclic constitutive relations in the analytical model, the effectiveness of the MVLEM for modeling and simulating the inelastic response of reinforced concrete structural walls was demonstrated. Variation of model and material parameters was investigated to identify the sensitivity of analytically predicted global and local wall responses to changes in these parameters as well as to identify which parameters require the greatest care with respect to calibration.

Once the model was developed, the accuracy and limitations of the model were assessed by comparing responses predicted with the model to responses obtained from experimental studies of slender walls for rectangular and T-shaped cross sections. Appropriate nonlinear analysis strategies were adopted in order to compare model results with results of the drift-controlled cyclic tests subjected to prescribed lateral displacement histories. The analytical model was subjected to the same conditions experienced during testing (e.g., loading protocol, fluctuations in applied axial load). Wall test results were processed and filtered to allow for a direct and refined comparison of the experimental results with the response prediction of the analytical model. The correlation of the experimental and analytical results was investigated in detail, at various response levels and locations (e.g., forces, displacements, rotations, and strains in steel and concrete).

Furthermore, improved nonlinear shear behavior was incorporated in the analytical modeling approach. The formulation of the original fiber-based model was extended to simulate the observed coupling behavior between nonlinear flexural and shear responses in RC walls, via implementing constitutive RC panel elements into the formulation. Results obtained with the improved model were compared with test results for both slender wall and short wall specimens. The formulation of the analytical model proposed and the constitutive material models used in this study were implemented in the open-source computational platform OpenSees (“OpenSees”), being developed by the Pacific Earthquake Engineering Research Center.

In summary, the objectives of this study are:

1. to develop an improved fiber-based modeling approach for simulating flexural responses of RC structural walls, by implementing updated and refined constitutive relations for materials,
2. to adopt nonlinear analysis solution strategies for the analytical model,
3. to investigate the influence of material behavior on the analytical model response, and to conduct studies to assess the sensitivity of the analytically predicted global and local wall responses to changes in material and model parameters,
4. to carry out detailed calibration studies of the analytical model and to conduct comprehensive correlation studies between analytical model results and extensive experimental results at various response levels and locations,
5. to further improve the modeling methodology, in order to improve the shear response prediction of the analytical model, considering the coupling of flexural and shear responses in RC structural walls,
6. to assess effectiveness and accuracy of the analytical model in predicting the nonlinear responses of both slender and squat reinforced concrete walls, and to arrive at recommendations upon applications and further improvements of the model,
7. to implement the formulation of the analytical models proposed and the constitutive material models used in this study into a commonly used structural analysis platform.

1.3 ORGANIZATION

This report is divided into ten chapters. Chapter 2 provides a review of previous research conducted on the development of the analytical model. Chapter 3 gives a description of the improved analytical model, as implemented in this study. Chapter 4 describes the hysteretic constitutive relations for materials incorporated in the analytical model for predicting flexural responses. Numerical solution strategies adopted to conduct nonlinear analyses using the analytical model are described in Chapter 5. Chapter 6 provides an examination of analytical model results and attributes, and also investigates the sensitivity of the model results to material and model parameters. Chapter 7 provides information on correlation of the analytical model results with experimental results for wall flexural responses. A description of the experimental program, detailed information on calibration of the model, and comparisons of model results

with extensive experimental data at global and local response levels are presented. Chapter 8 describes the methodology implemented in the fiber-based analytical model to simulate the observed coupling between flexural and shear wall responses. A detailed description of the improved analytical model is presented, and analytical model results are compared with test results for slender and short wall specimens to evaluate the modeling approach. A summary and conclusions are presented in Chapter 10. Recommendations for model improvements and extensions are also provided. Chapters 3, 5, 6, and 7 provide information mostly on the flexural response modeling aspects of this analytical study, whereas coupled shear and flexural response modeling aspects are presented in Chapters 8 and 9.

2 Related Research

Various analytical models have been proposed for predicting the inelastic response of RC structural walls. A common modeling approach for wall hysteretic behavior uses a beam-column element at the wall centroidal axis with rigid links on beam girders. Commonly a one-component beam-column element model is adopted. This model consists of an elastic flexural element with a nonlinear rotational spring at each end to account for the inelastic behavior of critical regions (Fig. 2.1); the fixed-end rotation at any connection interface can be taken into account by a further nonlinear rotational spring. To more realistically model walls, improvements, such as multiple spring representation (Takayanagi and Schnobrich, 1976), varying inelastic zones (Keshavarzian and Schnobrich, 1984), and specific inelastic shear behavior (Aristizabal, 1983) have been introduced into simple beam-column elements. However, inelastic response of structural walls subjected to horizontal loads is dominated by large tensile strains and fixed end rotation due to bond slip effects, associated with shifting of the neutral axis. This feature cannot be directly modeled by a beam-column element model, which assumes that rotations occur around points on the centroidal axis of the wall. Therefore, the beam-column element disregards important features of the experimentally observed behavior (Fig. 2.2), including variation of the neutral axis of the wall cross section, rocking of the wall, and interaction with the frame members connected to the wall (Kabeyasawa et al., 1983).

Following a full-scale test on a seven-story RC frame-wall building in Tsubaka, Japan, Kabeyasawa et al. (1983) proposed a new macroscopic three-vertical-line-element model (TVLEM), to account for experimentally observed behavior that could not be captured using an equivalent beam-column model. The wall member was idealized as three vertical line elements with infinitely rigid beams at the top and bottom (floor) levels (Fig. 2.3); two outside truss elements represented the axial stiffness of the boundary columns, while the central element was a one-component model with vertical, horizontal, and rotational springs concentrated at the base.

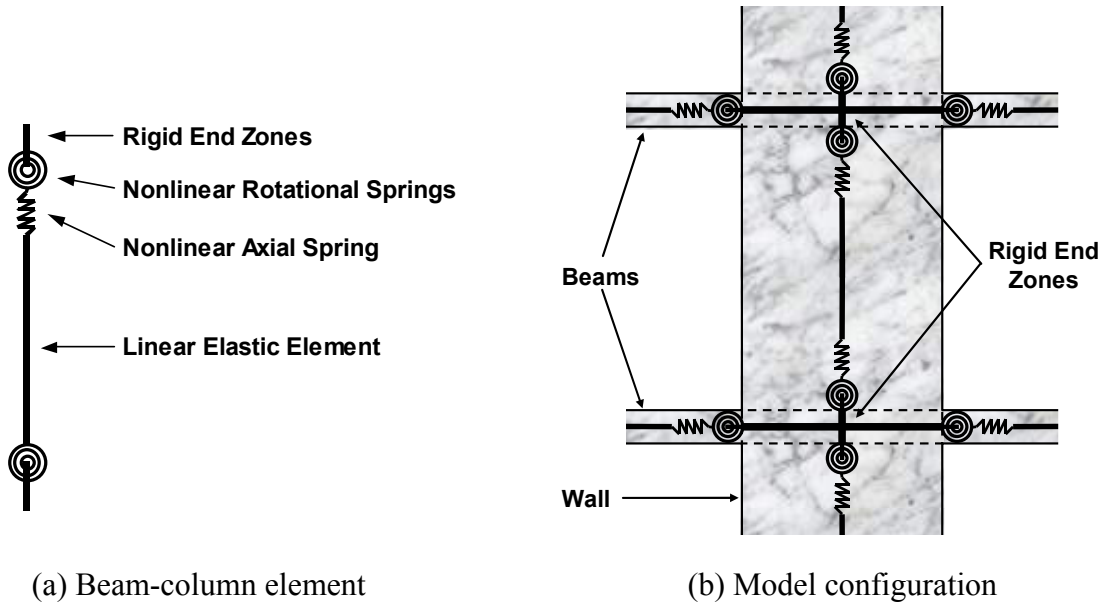


Fig. 2.1 Beam-column element model

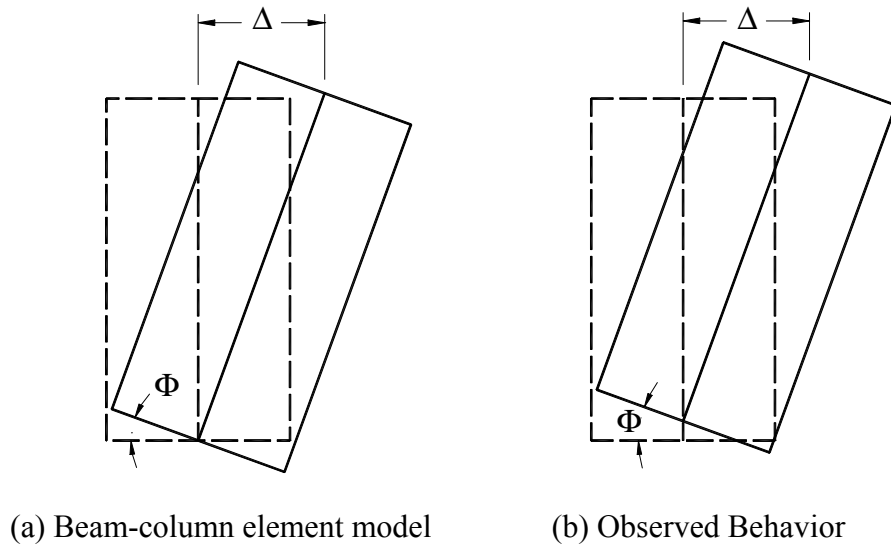


Fig. 2.2 Wall rocking and effect of neutral axis shift on vertical displacements

The axial-stiffness hysteresis model (ASHM), defined by the rules shown in Figure 2.4, was used to describe the axial force–deformation relation of the three vertical line elements of the wall model. An origin-oriented-hysteresis model (OOHM) was used for both the rotational and horizontal springs at the base of the central vertical element (Fig. 2.5). The stiffness properties of the rotational spring were defined by referring to the wall area bounded by the inner

faces of the two boundary columns (central panel only); therefore, displacement compatibility with the boundary columns was not enforced. Shear stiffness degradation was incorporated, but was assumed to be independent of the axial force and bending moment.

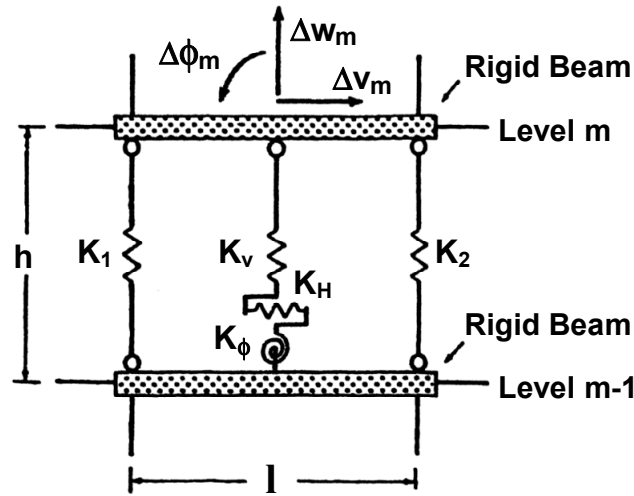


Fig. 2.3 Three-vertical-line-element model (TVLEM)

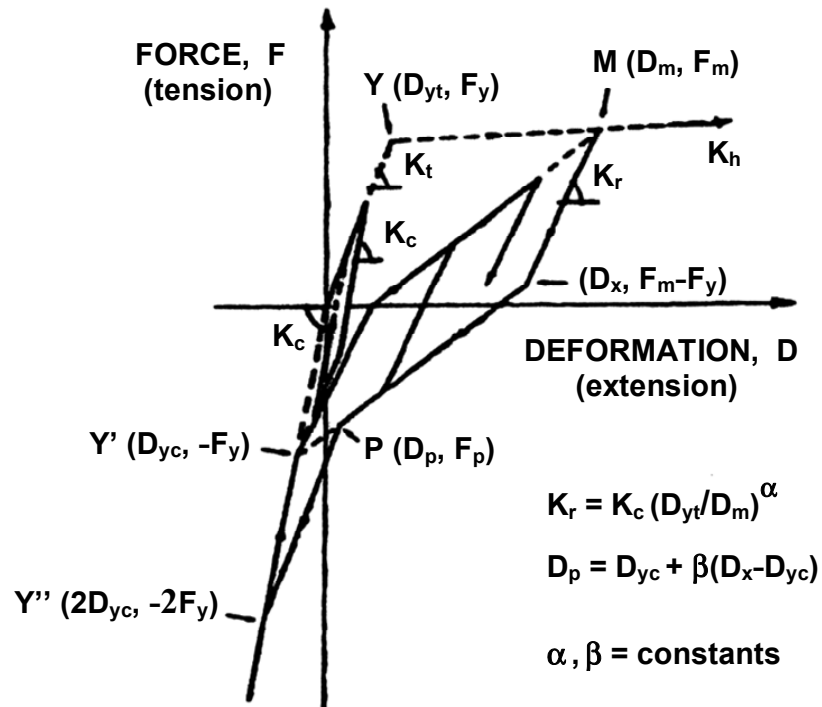


Fig. 2.4 Axial-stiffness hysteresis model (ASHM) (Kabeyasawa et al., 1983)

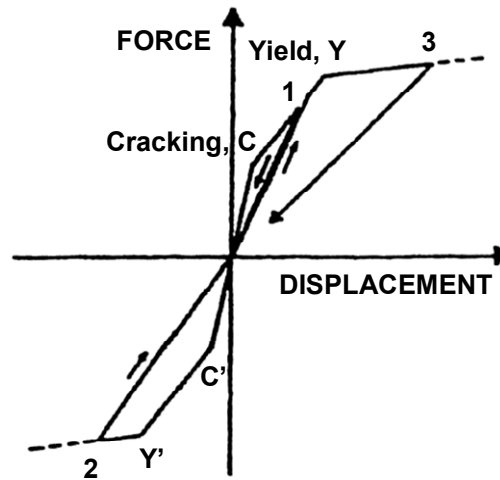


Fig. 2.5 Origin-oriented hysteresis model (OOHM) (Kabeyasawa et al., 1983)

Although the model accounted for fluctuation of the neutral axis of the wall and the interaction of the wall with surrounding frame elements (i.e., often referred to as “outrigger”), and predicted global responses (top displacement, base shear, axial deformation at wall boundaries, rotation at beam ends) compared favorably with experimental responses, general application of this model was limited by difficulties in defining the properties and physical representation of the springs representing the panel, and the incompatibility that exists between the panel and the boundary columns.

Vulcano and Bertero (1986) modified the TVLEM by replacing the axial-stiffness hysteresis model (ASHM) with the two-axial-element-in-series model (AESM) shown in Figure 2.6. Element 1 in Figure 2.6 was a one-component model to represent the overall axial stiffness of the column segments in which the bond is still active, while element 2 in Figure 2.6 is a two-component model to represent the axial stiffness of the remaining segments of steel (S) and cracked concrete (C) for which the bond has almost completely deteriorated. The AESM was intended to idealize the main features of the actual hysteretic behavior of the materials and their interaction (yielding and hardening of the steel, concrete cracking, contact stresses, bond degradation, etc.). Even though refined constitutive laws could have been assumed for describing the hysteretic behavior of the materials and their interaction, very simple assumptions (i.e., linearly elastic behavior for element 1, and bilinear behavior with strain hardening and linearly elastic behavior in compression neglecting tensile strength, respectively, for steel and concrete components of the element 2) were made in order to assess the effectiveness and the reliability of

the proposed model. The axial force–deformation relation generated by AESM is shown in Figure 2.7. The origin-oriented hysteresis model (OOHM) was again used for the rotational and the shear spring at the wall centerline.

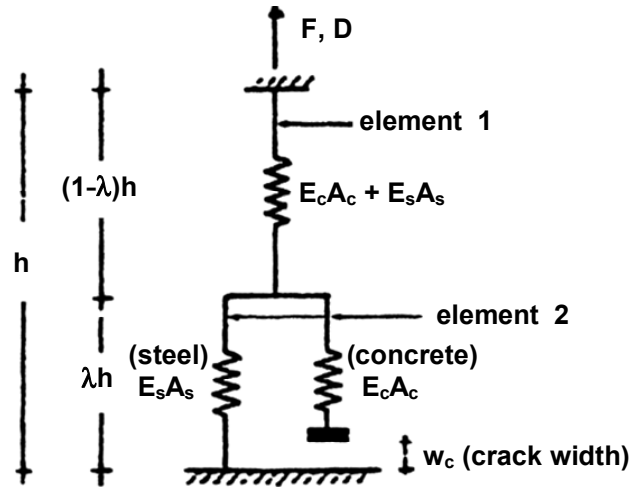


Fig. 2.6 Axial-element-in-series model (AESM) (Vulcano and Bertero, 1986)

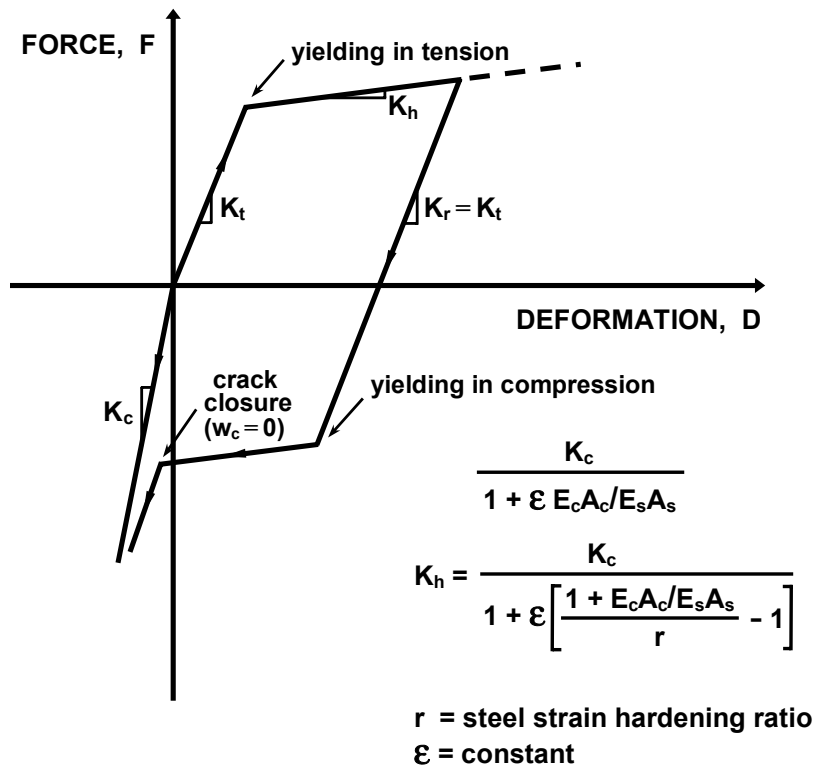


Fig. 2.7 Axial force–deformation relation of AESM

Although discrepancies were observed between predicted and measured shear behavior for the wall specimens used to evaluate the accuracy of the model, global response (base shear versus top displacement) correlated very well with experimental results given that inelastic wall response was dominated by flexural deformations (i.e., essentially elastic shear response was anticipated). The authors concluded that the proposed AESM reasonably captured measured flexural behavior, whereas the OOHM was unsuitable for predicting inelastic shear deformations. Overall, it was concluded that the modified TVLEM was an effective means to model inelastic flexural response of walls in multistory structures. However, the modified TVLEM did not address the lack of displacement compatibility between the rotational spring and the boundary columns, or the potential dependence of the shear stiffness on cracks produced due to combined bending and axial load (i.e., flexural cracking). It was also emphasized that displacement components for the model were very sensitive to the ad hoc selection of modeling parameters, such as the bond degradation parameter, the strain-hardening ratio, and the yield strength of the horizontal spring.

Vulcano, Bertero, and Colotti (1988) proposed the multi-component-in-parallel model (MCPM, also referred to as multiple-vertical-line element model MVLEM) to obtain a more refined description of the flexural behavior of the wall by (a) modifying the geometry of the wall model to gradually account for the progressive yielding of reinforcement and (b) using more refined hysteretic rules based on the actual behavior of the materials and their interactions to describe the response of the two elements in series constituting the AESM described above. The flexural response of a wall member was simulated by a multi-uniaxial-element-in-parallel model with infinitely rigid beams at the top and bottom floor levels. In this approach, the two external elements represented the axial stiffnesses (K_1 and K_2) of the boundary columns, while two or more interior elements, with axial stiffnesses K_3 to K_n , represented the axial and flexural behavior of the central panel (Fig. 2.8). A horizontal spring, with stiffness K_h and hysteretic behavior described by the OOHM (Fig. 2.5) simulated the nonlinear shear response of the wall element. The relative rotation of the wall element occurred around the point placed on the central axis of the wall member at height ch . Selection of the parameter c was based on the expected curvature distribution along the interstory height h and varied between 0 and 1 for single curvature over height of an element.

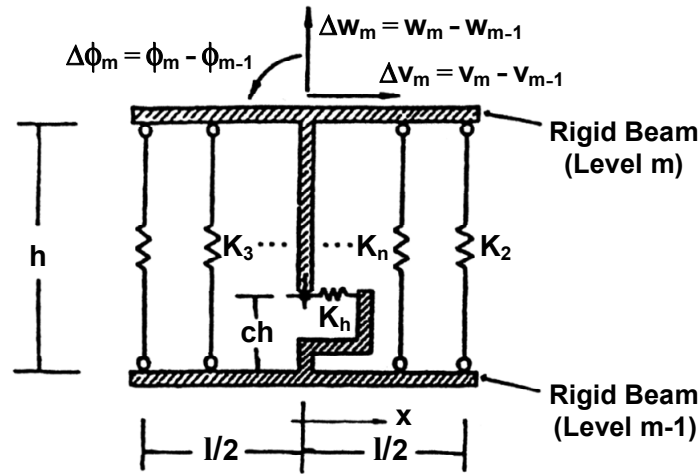


Fig. 2.8 Multiple-vertical-line-element-model (Vulcano et al., 1988)

A modified version of the AESM was proposed by the authors to describe the response of the uniaxial vertical elements (Fig. 2.9). Analogous to the original AESM, the two elements in series represented the axial stiffness of the column segments in which the bond remained active (element 1) and those segments for which the bond stresses were negligible (element 2). Unlike the original AESM, element 1 consisted of two parallel components to account for the mechanical behavior of the uncracked and cracked concrete (C) and the reinforcement (S). A dimensionless parameter λ was introduced to define the relative length of the two elements (representing cracked and uncracked concrete) to account for tension stiffening.

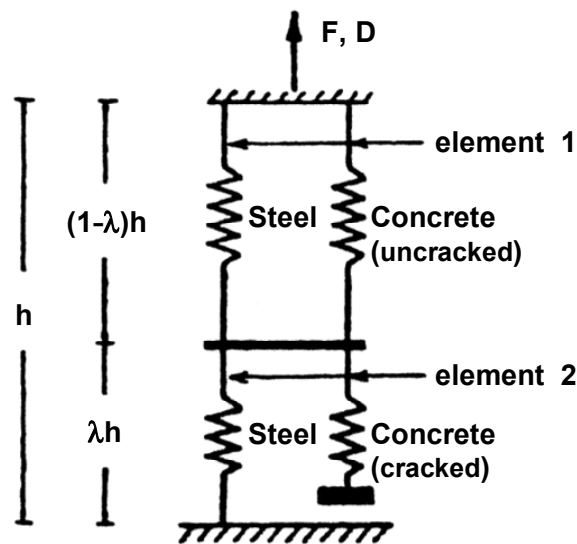


Fig. 2.9 Modified axial-element-in-series model (Vulcano et al., 1988)

Relatively refined constitutive laws were adopted to idealize the hysteretic behavior of the materials. The stress-strain relation proposed by Menegotto and Pinto (1973) was adopted by the authors to describe the hysteretic response of reinforcing steel (Fig. 2.10). The stress-strain relation proposed by Colotti and Vulcano (1987) was adopted for uncracked concrete (Fig. 2.11(a)). The stress-strain relation proposed by Bolong et al. (1980), which accounts for the contact stresses due to the progressive opening and closing of cracks, was used to model cracked concrete (Fig. 2.11(b)). Under monotonic tensile loading, the tension-stiffening effect was incorporated by manipulating the value of the dimensionless parameter λ such that the tensile stiffness of the uniaxial model in Figure 2.9 would be equal to the actual tensile stiffness of the uniaxial RC member as:

$$\left\{ \frac{(1-\lambda)h}{E_{ct}A_c + E_sA_s} + \frac{\lambda h}{E_sA_s} \right\}^{-1} = \frac{E_sA_s}{h} \frac{\varepsilon_s}{\varepsilon_m} \quad (1.1)$$

where $E_{ct}A_c$ and E_sA_s are the axial stiffnesses in tension of the concrete and of the reinforcement, respectively, and $\varepsilon_s/\varepsilon_m$ is the ratio of the steel strain in a cracked section to the current average strain for the overall member, evaluated by the empirical law proposed by Rizkalla and Hwang (1984). Under cyclic loading, the value of λ was based on the peak tensile strain obtained in prior cycles, and remained constant during loading and unloading unless the peak tensile strain obtained in prior cycles was exceeded.

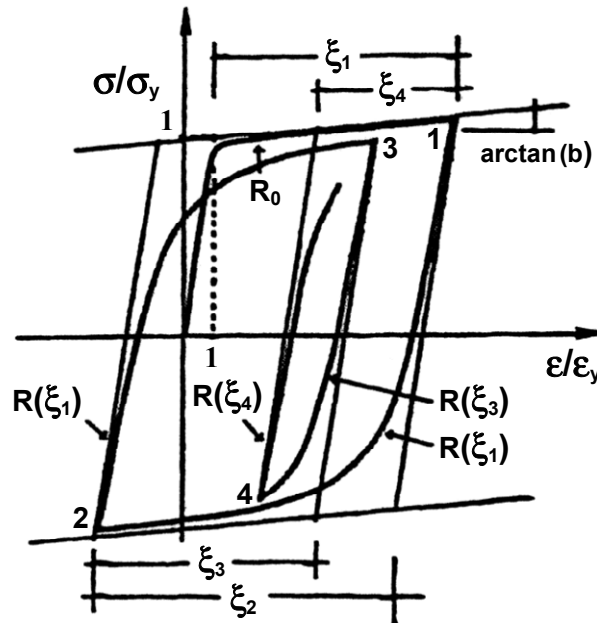
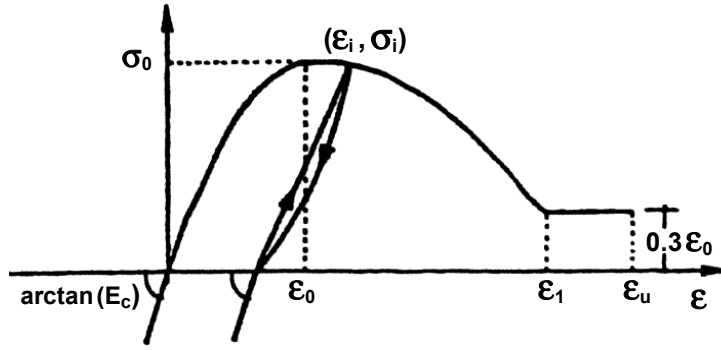
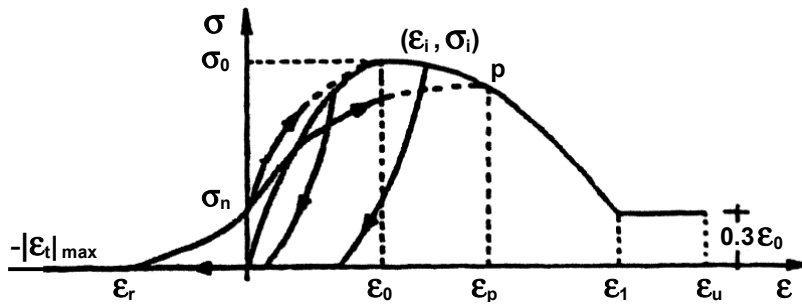


Fig. 2.10 Constitutive law adopted in original MVLEM for reinforcing steel



(a) Uncracked concrete (Colotti and Vulcano, 1987)



(b) Cracked concrete (Bolong et al., 1980)

Fig. 2.11 Constitutive laws adopted in original MVLEM for concrete

Comparison with experimental results indicated that, with the refined constitutive laws adopted, a reliable prediction of inelastic flexural response (base shear versus top displacement) was obtained, even with relatively few uniaxial elements ($n = 4$). In addition, greater accuracy was obtained by calibrating the parameter c defining the relative rotation center of the generic wall member, versus using more uniaxial elements. Therefore the authors concluded that the use of relatively simple constitutive laws for the materials and including tension stiffening provided a reliable model well suited for practical nonlinear analysis of multistory RC frame-wall structural systems. The OOHM used to model nonlinear shear behavior still had shortcomings, and the relative contribution of shear and flexural displacement components was difficult to predict and varied significantly with the selection of model parameters.

As mentioned above, the accuracy in predicting the flexural response of the wall by the multiple-vertical-line-element model (MVLEM) was very good when the constitutive laws in Figures 2.10–2.11 were adopted for the modified AESM components in Figure 2.9, even where relatively few uniaxial elements are used. However, because the constitutive laws incorporated

into the model are relatively sophisticated, to improve the effectiveness of the MVLEM without compromising accuracy, the use of simplified constitutive laws was investigated.

Fischinger et al. (1990) introduced simplified hysteretic rules to describe the response of both the vertical and horizontal springs (Fig. 2.12). The so-called modified MVLEM also proved to be very efficient in prediction of the cyclic response of a RC structural wall; however, the model included numerous parameters, some of which could be easily be defined, while others were difficult to define (in particular, the parameters of inelastic shear behavior and the parameter β in Figure 2.12(a) defining the fatness of the hysteresis loops). Therefore, the analytical results obtained using the modified MVLEM were based on somewhat arbitrary force-deformation parameters, the selection of which depended on engineering judgment.

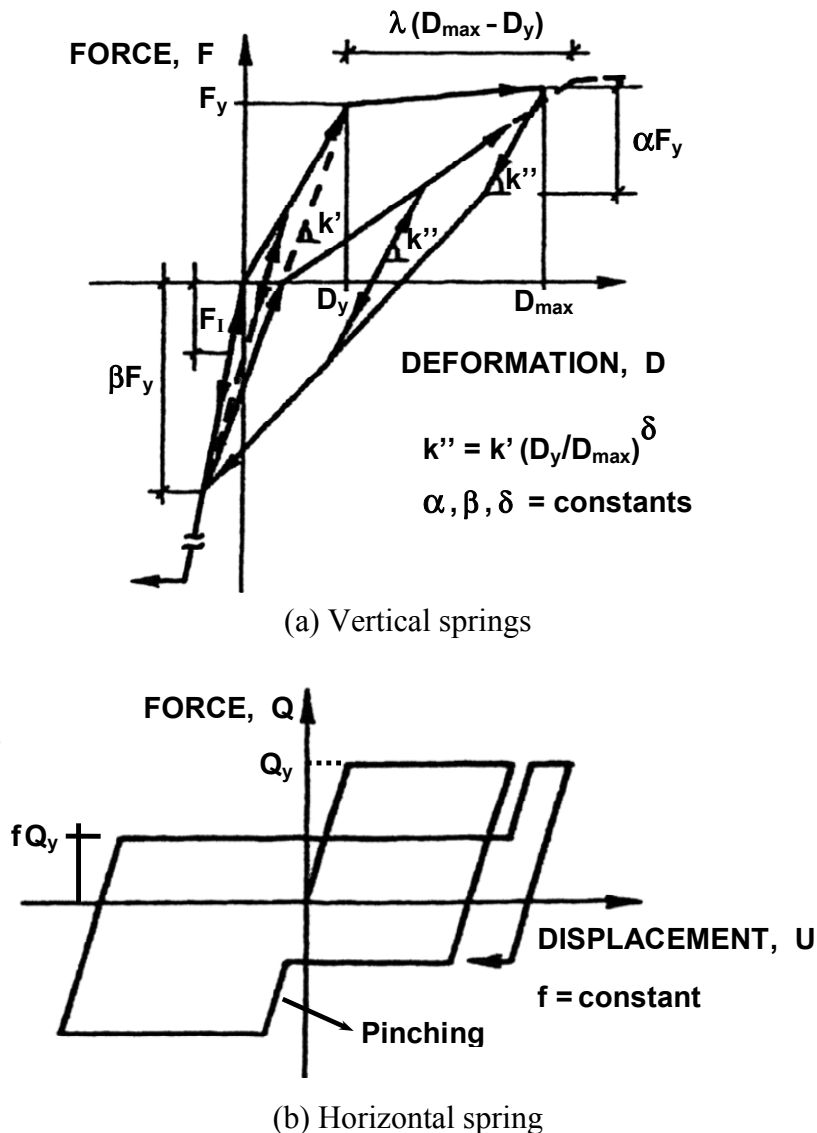


Fig. 2.12 Force-deformation relations adopted in modified MVLEM

A further variant of the modified MVLEM was applied in a study by Fajfar and Fischinger (1990), who, in order to reduce the uncertainty in the assumption of a suitable value for the parameter c , used a stack of a larger number of model elements placed one upon the other. A later study conducted by Fischinger, Vidic, and Fajfar (1992), showed that the modified MVLEM was well suited for modeling coupled wall response. It was also emphasized that better models are needed to account for cases with significant inelastic shear deformations as well as for cases with high levels of axial force, where the influence of transverse reinforcement (confinement on the nonlinear behavior of the vertical springs (in compression)) was found to be an important consideration.

A more recent study by Kabeyasawa (1997) proposed a modification to the original three-vertical-line-element model (TVLEM) in order to improve the prediction of the overall (shear and flexural) behavior of RC structural walls for both monotonic and reversed cyclic loading. The primary modification of the TVLEM involved substituting a two-dimensional nonlinear panel element for the vertical, horizontal, and rotational springs at the wall centerline (Fig. 2.13). Comparisons with experimental results indicated that both the TVLEM and the new panel-wall macro element (PWME) could be used to accurately model coupled walls under monotonic and reversed cyclic lateral loading and axial load. However, both models were found to be unstable for cases with high axial load and significant cyclic nonlinear shear deformations. Simulation of the concrete shear response as a function of axial load appeared to be a weak point for the PWME model.

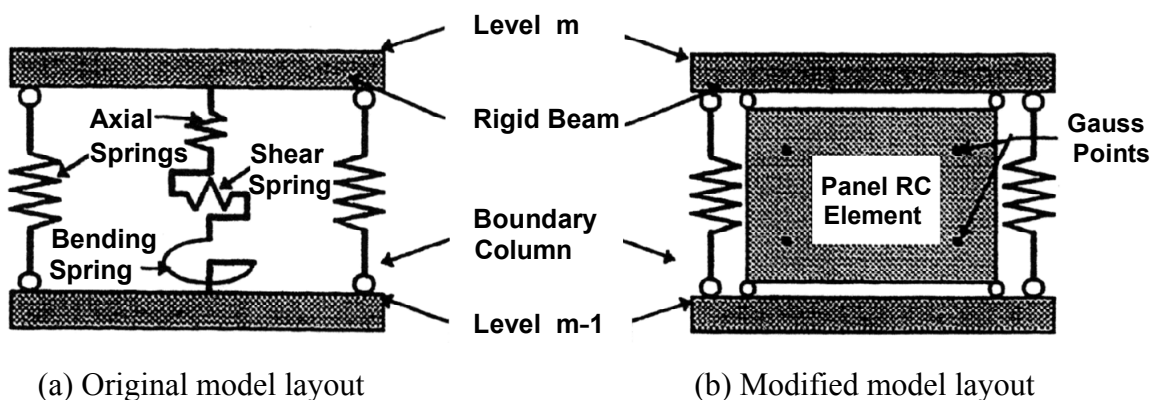


Fig. 2.13 Modification of TVLEM (Kabeyasawa et al., 1997)

The MVLEM was also modified using a similar approach to incorporate coupling between axial and shear components of RC wall response. Colotti (1993) modified the MVLEM

model by substituting the horizontal spring of each MVLE with a single two-dimensional nonlinear panel element in the MVLEM. In general, the results obtained using this model were more accurate compared with prior macro-models that use ad hoc shear force–deformation relations, although the relative contributions of shear and flexural deformations on wall displacements computed using this model showed discrepancies with experimental data. Shear deformations predicted by the model were, in some cases, approximately 20% greater than measured values. The model retained the inability to incorporate interaction between shear and flexure, as it considered coupling between shear and axial responses only, which was shown experimentally by Massone and Wallace (2004) to be unrealistic.

However, various approaches to consider the coupling between flexural and shear response components have been reported in the literature. One approach, by Takayanagi et al. (1979), involves using a shear force–displacement relation having a yield point (force at shear yield yielding) based on the lateral load to reach flexural yielding, so that flexural and yielding behavior are initiated simultaneously during loading. Another common approach involves using the finite element formulation together with constitutive reinforced concrete panel elements (e.g., modified compression field theory (MCFT, Vecchio and Collins, 1986); rotating-angle softened-truss model (RA-STM, Belarbi and Hsu, 1994; Pang and Hsu, 1995); disturbed stress field model (DSFM, Vecchio, 2000)). Even so, the direct application of the finite element method may provide relatively accurate results,

A simplification of a fully implemented finite element formulation with constitutive reinforced concrete panel elements is a one-story macro-element based on relatively simple uniaxial constitutive material relations for modeling flexural response components, together with a shear force versus displacement relation coupled with the axial load on the element, as proposed by Colotti (1993). However, as mentioned in the previous paragraph, this methodology incorporates coupling of shear and axial response components only, whereas axial-shear-flexure interaction is not considered. One way to address this limitation is to adopt a sectional analysis approach, by dividing the one-story macro-element into vertical segments (e.g., uniaxial elements in the MVLEM), with axial-shear coupling incorporated in each segment, so as to attain shear-flexure coupling, since the axial responses of the vertical segments constitute the flexural response of the element (Bonacci, 1994). An approach based on adopting this idea for a standard displacement-based element with a cross-sectional multilayer or fiber discretization was

proposed by Petrangeli et al. (1999a), and provided reasonably good response predictions for slender elements (Petrangeli, 1999b).

In this study, the multiple-vertical-line-element model (MVLEM) was improved by adopting refined constitutive relations for materials, and detailed calibration correlation studies were conducted to investigate the effectiveness of the model in predicting flexural responses of walls under cyclic loading. A description of the flexural model, as adopted in this study, is presented in the following chapter. The MVLEM was further modified in this study, using an approach similar to that of Petrangeli et al. (1999a), to incorporate interaction between flexure and shear components of wall response. A description of the shear-flexure interaction modeling methodology adopted is presented in the Chapter 8.

3 Flexural Modeling — Analytical Model Description

The analytical model, as adopted here, resembles a macroscopic fiber model, which is the current state-of-the-art tool for modeling slender reinforced concrete structural elements. The model in Figure 3.1 is an implementation of the generic two-dimensional MVLEM wall element. A structural wall is modeled as a stack of m MVLEM elements, which are placed upon one another (Fig. 3.2).

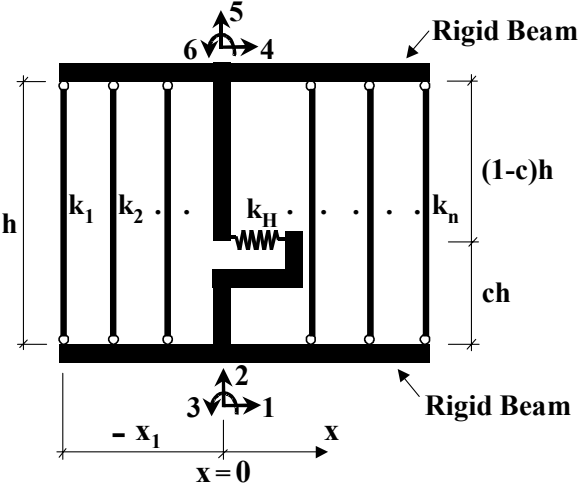


Fig. 3.1 MVLEM element

The flexural response is simulated by a series of uniaxial elements (or macro-fibers) connected to rigid beams at the top and bottom (e.g., floor) levels: the two external truss elements (at least two, with axial stiffnesses k_1 and k_n) represent the axial stiffnesses of the boundary columns, while the interior elements (at least two, with axial stiffnesses k_2, \dots, k_{n-1}) represent the axial and flexural stiffness of the central panel. The stiffness properties and force-displacement relations of the uniaxial elements are defined according to cyclic constitutive models and the tributary area assigned to each uniaxial element (Fig. 3.3). The number of the

uniaxial elements (n) can be increased to obtain a more refined description of the wall cross section.

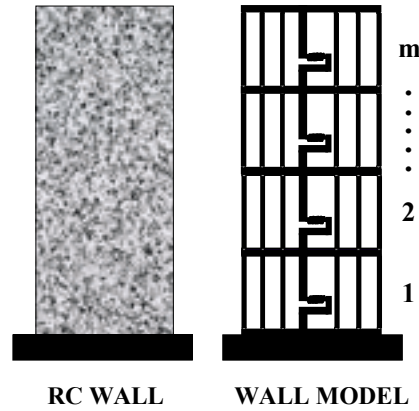


Fig. 3.2 Modeling of a wall with MVLEM

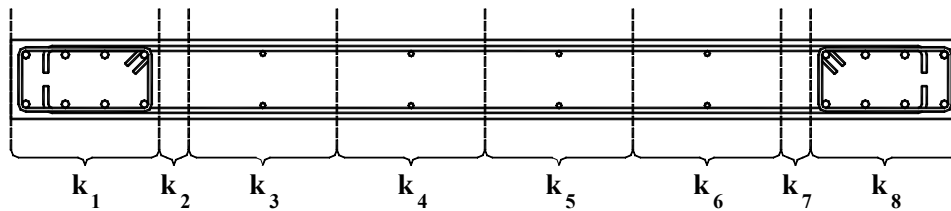


Fig. 3.3 Tributary area assignment

The relative rotation between the top and bottom faces of the wall element occurs around the point placed on the central axis of the element at height ch (Fig. 3.4). Rotations and resulting transverse displacements are calculated based on the wall curvature, derived from section and material properties, corresponding to the bending moment at height ch of each element (Fig. 3.4).

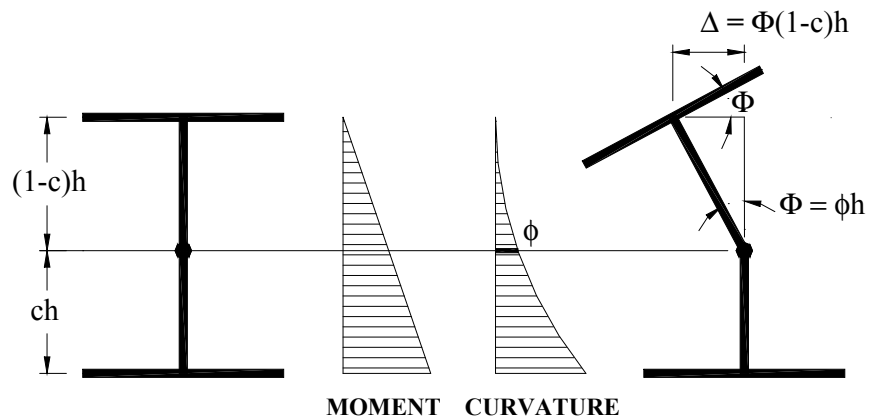


Fig. 3.4 Rotations and displacements of MVLEM element

A suitable value of the parameter c is based on the expected curvature distribution along the element height h . For example, if moment (curvature) distribution along the height of the element is constant, using a value of $c = 0.5$ yields “exact” rotations and transverse displacements for elastic and inelastic behavior. For a triangular distribution of bending moment over the element height, using $c = 0.5$ yields exact results for rotations in the elastic range but underestimates displacements. Selection of c becomes important in the inelastic range, where small changes in moment can yield highly nonlinear distributions of curvature. Consequently, lower values of c should be used to take into account the nonlinear distribution of curvature along the height of the wall. A value of $c = 0.4$ was recommended by Vulcano et al. (1988) based on comparison of the model response with experimental results. Stacking more elements along the wall height, especially in the regions where inelastic deformations are expected, will result in smaller variations in the moment and curvature along the height of each element, thus improving analytical accuracy (Fischinger et al., 1992).

A horizontal spring placed at the height ch , with a nonlinear hysteretic force-deformation behavior following an origin-oriented hysteresis model (OOHM) (Kabeyasawa et al., 1983) was originally suggested by Vulcano et al. (1988) to simulate the shear response of the wall element. A trilinear force-displacement backbone curve with pre-cracked, post-cracked and post-yield shear stiffness values of the wall cross section was adopted to define the stiffness and force-deformation properties of the horizontal spring in each wall element. Unloading and reloading occurred along straight lines passing through the origin (Fig. 3.5). The OOHM was proven to be unsuitable by Vulcano and Bertero (1987) for an accurate idealization of the shear hysteretic behavior especially when high shear stresses are expected. Improved predictions of wall shear response likely require consideration of the interaction between shear and flexure responses.

The first part of this study focuses on modeling and simulation of the flexural responses of slender RC walls, thus a linear elastic force-deformation behavior was adopted for the horizontal “shear” spring. For the present model, flexural and shear modes of deformation of the wall member are uncoupled (i.e., flexural deformations do not affect shear strength or deformation), and the horizontal shear displacement at the top of the element does not depend on c (Fig. 3.6). However, the second part of this study involves extending the formulation of present model was extended to simulate coupled shear and flexural wall responses, as described in Chapters 8 and 9.

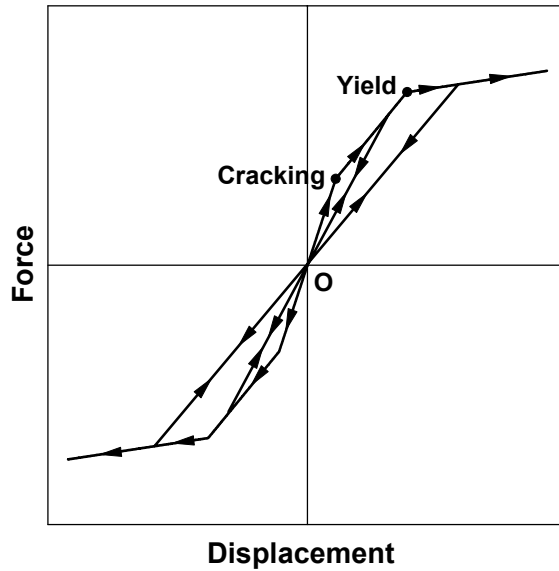


Fig. 3.5 Origin-oriented hysteresis model for horizontal shear spring

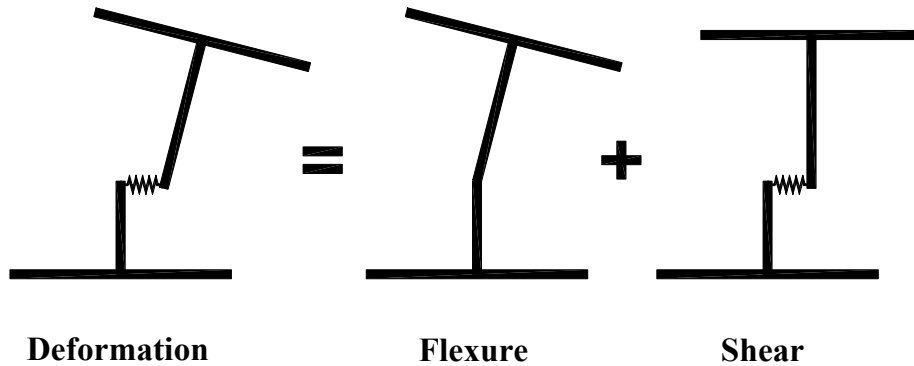


Fig. 3.6 Uncoupling of modes of deformation of MVLEM element

A single two-dimensional MVLE has six global degrees of freedom, three of each located at the center of the rigid top and bottom beams (Fig. 3.1). The strain level in each uniaxial element is obtained from the element displacement components (translations and rotations) at the six nodal degrees of freedom using the plane-sections-remain-plane kinematic assumption. Accordingly, if $[\delta]$ is a vector that represents the displacement components at the six nodal degrees of freedom of each MVLE (Fig. 3.1):

$$[\delta] = \begin{bmatrix} \delta_1 \\ \delta_2 \\ \delta_3 \\ \delta_4 \\ \delta_5 \\ \delta_6 \end{bmatrix} \quad (3.1)$$

then, the resulting deformations of the uniaxial elements are obtained as:

$$[u] = [a] \cdot [\delta] \quad (3.2)$$

where $[u]$ denotes the axial deformations of the uniaxial elements:

$$[u] = \begin{bmatrix} u_1 \\ u_2 \\ \cdot \\ \cdot \\ u_i \\ \cdot \\ \cdot \\ u_n \end{bmatrix} \quad (3.3)$$

and $[a]$ is the geometric transformation matrix that converts the displacement components at the nodal degrees of freedom to uniaxial element deformations:

$$[a] = \begin{bmatrix} 0 & -1 & -x_1 & 0 & 1 & x_1 \\ 0 & -1 & -x_2 & 0 & 1 & x_2 \\ \cdot & \cdot & \cdot & \cdot & \cdot & \cdot \\ \cdot & \cdot & \cdot & \cdot & \cdot & \cdot \\ 0 & -1 & -x_i & 0 & 1 & x_i \\ \cdot & \cdot & \cdot & \cdot & \cdot & \cdot \\ \cdot & \cdot & \cdot & \cdot & \cdot & \cdot \\ 0 & 0 & -x_n & 0 & 0 & x_n \end{bmatrix} \quad (3.4)$$

The average axial strain in each uniaxial element (ε_i) can then be calculated by simply dividing the axial deformation by the element height, h :

$$\varepsilon_i = \frac{u_i}{h} \quad (3.5)$$

The average strains in concrete and steel are typically assumed equal (perfect bond) within each uniaxial element.

The deformation in the horizontal shear spring (u_H) of each MVLE can be similarly related to the deformation components $[\delta]$ at the six nodal degrees of freedom as:

$$u_H = [b]^T [\delta] \quad (3.6)$$

where the geometric transformation vector $[b]$ is defined as:

$$[b] = \begin{bmatrix} 1 \\ 0 \\ -ch \\ -1 \\ 0 \\ -(1-c)h \end{bmatrix} \quad (3.7)$$

The stiffness properties and force-deformation relations of the uniaxial elements are defined according to the uniaxial constitutive relations adopted for the wall materials, (i.e., concrete and steel), as well as the tributary area assigned to each uniaxial element. For a prescribed strain level (ε_i) at the i -th uniaxial element, the axial stiffness of the i -th uniaxial element (k_i) is defined as:

$$k_i = \frac{(E_c)_i (A_c)_i}{h} + \frac{(E_s)_i (A_s)_i}{h} \quad (3.8)$$

where $(E_c)_i$ and $(E_s)_i$ are the material tangent moduli (strain derivatives of the adopted constitutive stress-strain relations), respectively for concrete and steel, at the prescribed strain level (ε_i); $(A_c)_i$ and $(A_s)_i$ are the tributary concrete and steel areas assigned to the uniaxial element, and h is the element height. The axial force in the i -th uniaxial element (f_i) is defined similarly as:

$$f_i = (\sigma_c)_i (A_c)_i + (\sigma_s)_i (A_s)_i \quad (3.9)$$

where $(\sigma_c)_i$ and $(\sigma_s)_i$ are the uniaxial stresses, respectively, for concrete and steel, obtained from the implemented constitutive relations at the prescribed strain (ε_i). The stiffness of the horizontal shear spring (k_H) and the force in the horizontal spring (f_H) for a prescribed spring deformation (u_H) are derived from the force-deformation relation adopted in the model for shear (e.g., origin-oriented-hysteresis relation or linear elastic relation).

Consequently, for a specified set of displacement components at the six nodal degrees of freedom of a generic wall element, if k_H is the stiffness of the horizontal spring, k_i is the

stiffness of the i -th uniaxial element, and x_i is the distance of the i -th uniaxial element to the central axis of the element, the stiffness matrix of the element relative to the six degrees of freedom is obtained as:

$$[K_e] = [\beta]^T \cdot [K] \cdot [\beta] \quad (3.10)$$

where $[\beta]$ denotes the geometric transformation matrix converting the element degrees of freedom to the element deformations of extension, relative rotation at the bottom and relative rotation at the top of each wall element (Fig. 3.7):

$$[\beta] = \begin{bmatrix} 0 & -1 & 0 & 0 & 1 & 0 \\ -1/h & 0 & 1 & 1/h & 0 & 0 \\ -1/h & 0 & 0 & 1/h & 0 & 1 \end{bmatrix} \quad (3.11)$$

and

$$[K] = \begin{bmatrix} \sum_{i=1}^n k_i & -\sum_{i=1}^n k_i x_i & \sum_{i=1}^n k_i x_i \\ k_H c^2 h^2 + \sum_{i=1}^n k_i x_i^2 & k_H c(1-c)h^2 - \sum_{i=1}^n k_i x_i^2 \\ \text{symm.} & k_H (1-c)^2 h^2 + \sum_{i=1}^n k_i x_i^2 \end{bmatrix} \quad (3.12)$$

is the element stiffness matrix relative to the three pure deformation degrees of freedom shown in Figure 3.7.

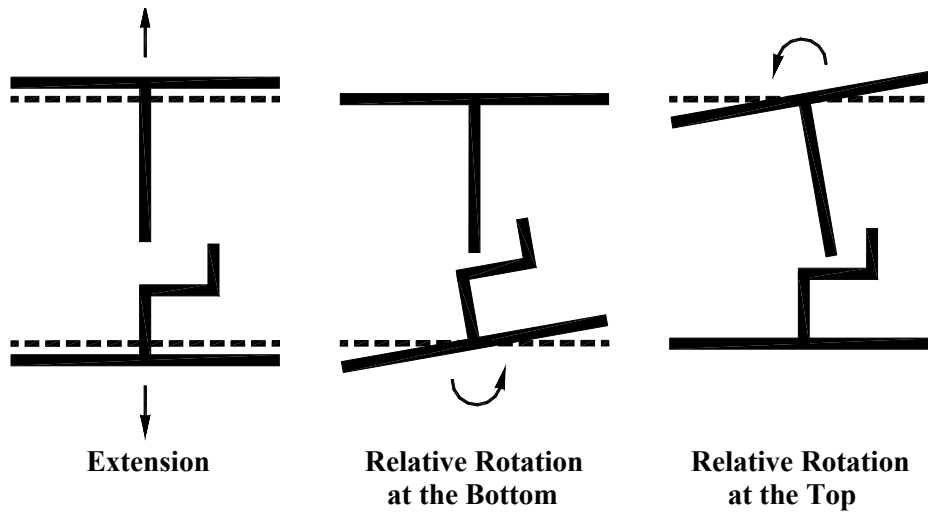


Fig. 3.7 Element deformations of MVLEM element (Vulcano et al., 1988)

Similarly, if f_H is the force in the horizontal spring, and f_i is the force in the i -th uniaxial element, the internal (resisting) force vector of the wall element relative to the six degrees of freedom is obtained from equilibrium as:

$$[F_{\text{int}}] = \begin{bmatrix} f_H \\ -\sum_{i=1}^n f_i \\ -f_H c h - \sum_{i=1}^n f_i x_i \\ -f_H \\ \sum_{i=1}^n f_i \\ -f_H (1-c)h + \sum_{i=1}^n f_i x_i \end{bmatrix} \quad (3.13)$$

Overall, the MVLEM implemented in this study is an efficient approach to relate the predicted wall flexural response directly to uniaxial material behavior without incorporating any additional empirical relations. Its physical concept is clear, and the required computational effort is reasonable. The primary simplification of the model involves applying the plane-sections-remain-plane kinematic assumption to calculate the average strain level within each of the uniaxial sub-elements. The only parameters associated with the wall model are the number of uniaxial elements used along the length of the wall cross section (n), the number of MVLEM elements stacked on top of each other along the height of the wall (m), and the parameter defining the location of the center of rotation along the height of each MVLEM element (c). The number of the uniaxial elements (n) and the MVLEM elements (m) can be increased to obtain a more refined description of the wall cross geometry and a more accurate representation of the flexural response. In addition to the model parameters, parameters associated with the material constitutive relations govern the analytical response predictions. Details of the constitutive models adopted in this study for steel and concrete are described in the following chapter.

4 Flexural Modeling — Material Constitutive Models

The MVLEM implemented in this study relates the predicted flexural response directly to uniaxial material behavior without incorporating any additional empirical relations. The approach adopted here involves implementing state-of-the-art cyclic constitutive relations for concrete and reinforcing steel to track the nonlinear response of the model sub-elements, versus the use of simplified (ad hoc) force-deformation rules as done in prior studies (Fischinger et al., 1990; Fajfar and Fischinger, 1990; Fischinger et al., 1991, 1992). The stiffness and force-deformation properties of the model sub-elements are derived from uniaxial stress-strain behavior of materials; therefore, responses obtained using the present wall model are governed by the properties and parameters of the adopted material constitutive relations. Details of the uniaxial hysteretic constitutive models used in this study for steel and concrete are described in the following sections.

4.1 CONSTITUTIVE MODEL FOR REINFORCEMENT

The uniaxial constitutive stress-strain relation implemented in the wall model for reinforcing steel is the well-known nonlinear hysteretic model of Menegotto and Pinto (1973), as extended by Filippou et al. (1983) to include isotropic strain-hardening effects. The model is computationally efficient and capable of reproducing experimental results with accuracy. The relation is in the form of curved transitions (Fig. 4.1), each from a straight-line asymptote with slope E_0 (modulus of elasticity) to another straight-line asymptote with slope $E_1 = bE_0$ (yield modulus) where the parameter b is the strain-hardening ratio. The curvature of the transition curve between the two asymptotes is governed by a cyclic curvature parameter R , which permits the Bauschinger effect to be represented.

The uniaxial hysteretic stress-strain ($\sigma - \varepsilon$) relation of Menegotto and Pinto (1973) takes the form:

$$\sigma^* = b\varepsilon^* + \frac{(1-b)\varepsilon^*}{(1+\varepsilon^{*R})^{1/R}} \quad (4.1)$$

where

$$\xi^* = \frac{\varepsilon - \varepsilon_r}{\varepsilon_0 - \varepsilon_r} \quad (4.2)$$

and

$$\sigma^* = \frac{\sigma - \sigma_r}{\sigma_0 - \sigma_r} \quad (4.3)$$

Equation (4.1) represents the curved transition from the elastic asymptote with slope E_0 to the yield asymptote with slope $E_1 = bE_0$ (Fig. 4.1). Parameters σ_r and ε_r are the stress and strain at the point of strain reversal, which also forms the origin of the asymptote with slope E_0 . Parameters σ_0 and ε_0 are the stress and strain at the point of intersection of the two asymptotes. Parameter b is the strain-hardening ratio, that is the ratio between the slopes E_1 and E_0 , and R is the parameter that influences the curvature of the transition curve between the two asymptotes (and thus permits the Bauschinger effect to be represented). As indicated in Figure 4.1, the strain and stress pairs $(\varepsilon_r, \sigma_r)$ and $(\varepsilon_0, \sigma_0)$ are updated after each strain reversal.

The tangent modulus (E_t) of the stress-strain relation is obtained by differentiating the equations above, and is given by the following expression:

$$E_t = \frac{d\sigma}{d\varepsilon} = \left(\frac{\sigma_0 - \sigma_r}{\varepsilon_0 - \varepsilon_r} \right) \frac{d\sigma^*}{d\varepsilon^*} \quad (4.4)$$

where

$$\frac{d\sigma^*}{d\varepsilon^*} = b + \left[\frac{1-b}{(1+\varepsilon^{*R})^{1/R}} \right] \left[1 - \frac{\varepsilon^{*R}}{1+\varepsilon^{*R}} \right] \quad (4.5)$$

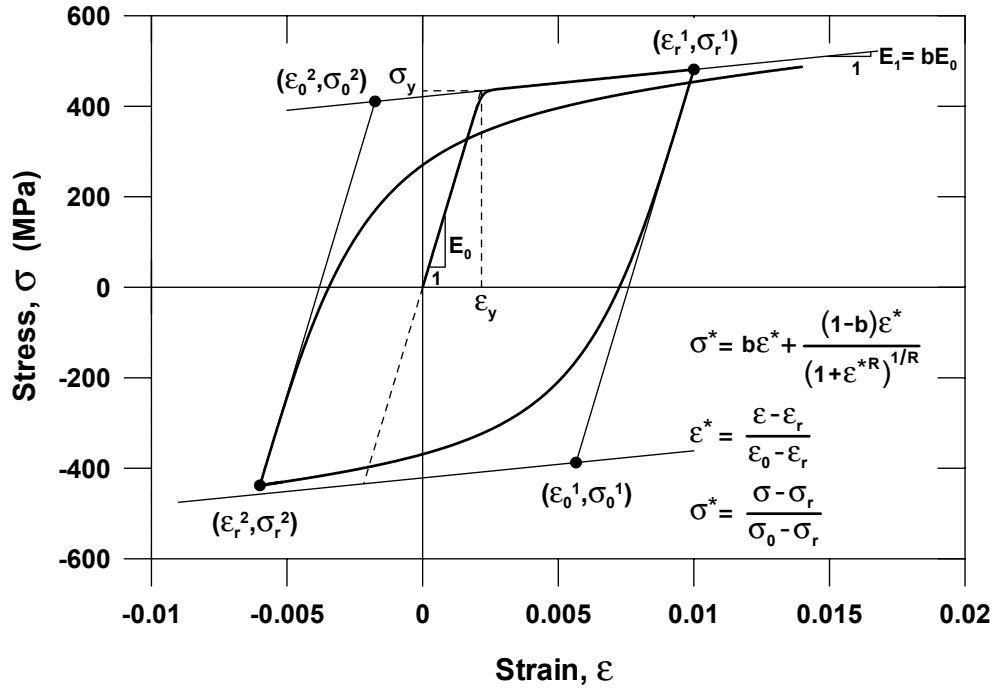


Fig. 4.1 Constitutive model for steel (Menegotto and Pinto, 1973)

The curvature parameter R is dependent on the absolute strain difference between the current asymptote intersection point and the previous maximum or minimum strain reversal point (Fig. 4.2) depending on whether the current strain is increasing or decreasing, respectively. The expression for R takes the form suggested by Menegotto and Pinto:

$$R = R_0 - \frac{a_1 \xi}{a_2 + \xi} \quad (4.6)$$

where R_0 is the value assigned to the parameter R for initial (or monotonic) loading, and a_1 and a_2 are experimentally determined parameters that represent the degradation of the curvature within subsequent cycles. The absolute strain difference between the current asymptote intersection point and the previous maximum or minimum strain reversal point is represented by the parameter ξ (Fig. 4.2), which can be expressed as:

$$\xi = \left| \frac{(\varepsilon_m - \varepsilon_0)}{\varepsilon_y} \right| \quad (4.7)$$

where ε_m is the maximum or minimum strain, at the previous point of strain reversal, depending on whether the current strain is increasing or decreasing, respectively. Parameter ε_0

is the strain at the current intersection point of the two asymptotes, and parameter ε_y is the strain at monotonic yield point (Fig. 4.1). As shown in Figure 4.2, both ε_m and ε_0 lie on the same asymptote, and ξ is updated following a strain reversal.

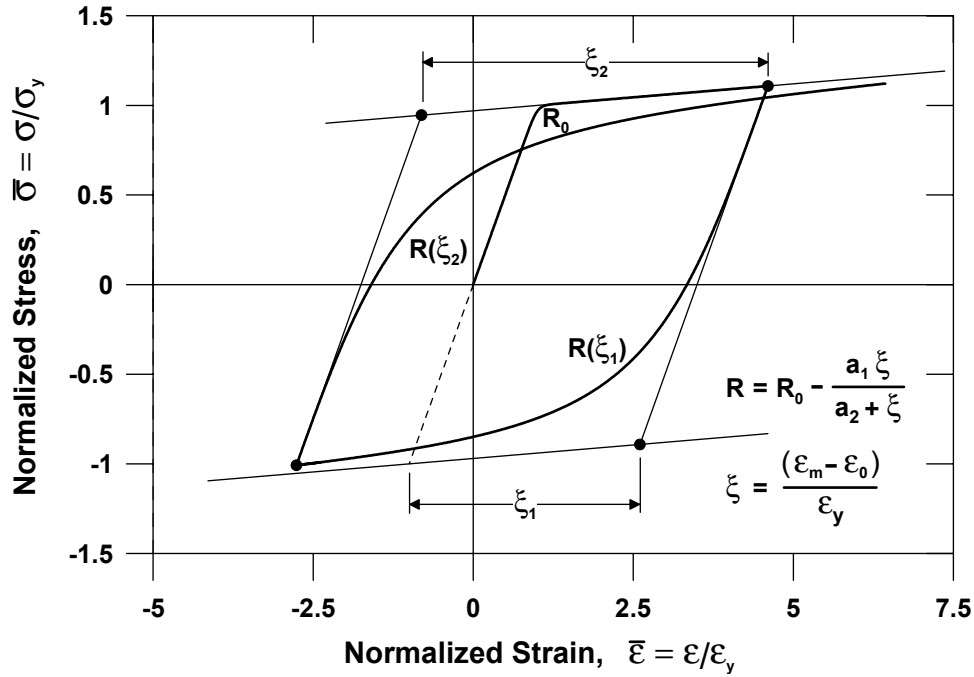


Fig. 4.2 Degradation of cyclic curvature

Accordingly, Figure 4.3 shows an illustrative hysteretic stress-strain relation, generated by the Menegotto and Pinto model, for a representative strain history typically experienced by reinforcing bars located within the inelastic deformation region of a RC wall subjected to cyclic loading. Figure 4.4 compares the stress-strain histories generated by the constitutive model for two different sets of values for parameters R_0 , a_1 , and a_2 (accounting for the cyclic degradation of the curvature coefficient R), experimentally calibrated by prior researchers ($R_0, a_1, a_2 = 20, 18.5, 0.15$ by Menegotto and Pinto, 1973; $R_0, a_1, a_2 = 20, 18.5, 0.0015$ by Elmsorsi et al., 1998) based on results of cyclic tests on reinforcing bars. The figure reveals how the constitutive model simulates different levels of cyclic degradation of the curvature of the stress-strain relation, accounting for the Bauschinger effect.

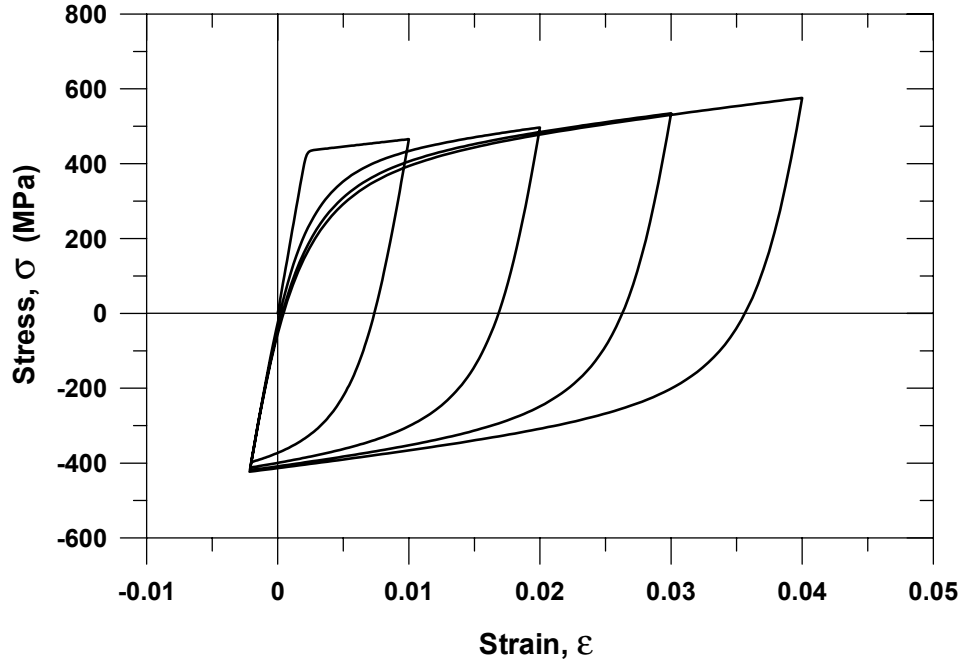


Fig. 4.3 Stress-strain relation generated by Menegotto and Pinto (1973) model

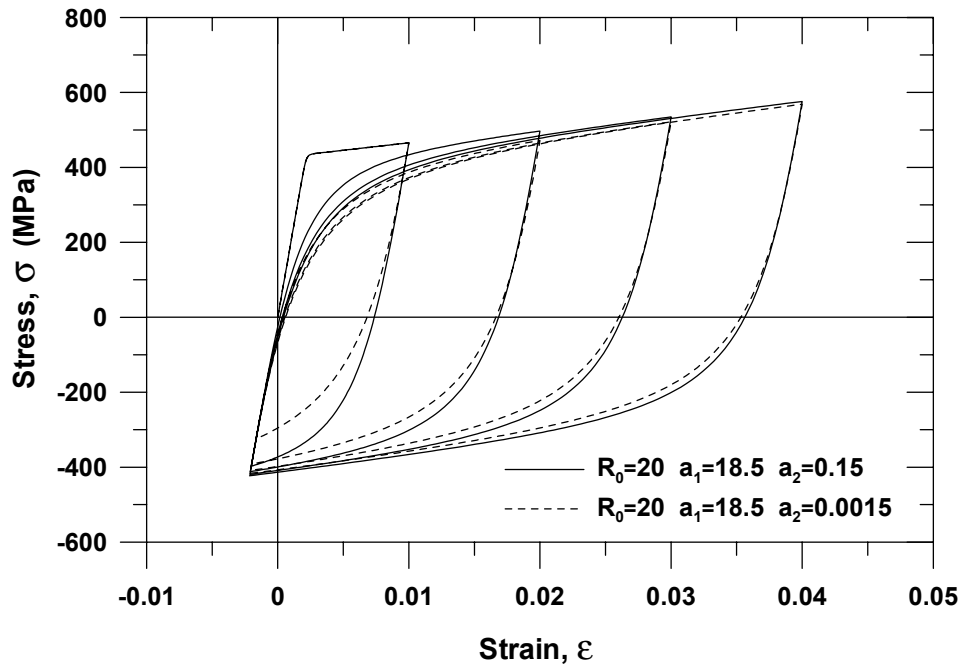


Fig. 4.4 Sensitivity of stress-strain relation to cyclic curvature parameters

As discussed by Filippou et al. (1983), the effect of isotropic hardening can be important when modeling the cyclic behavior of reinforcing bars in RC members. The presence of isotropic strain hardening can have a pronounced effect on the strain developed in the reinforcing bars

during crack closure, as illustrated in Figure 4.5. At a stress σ_1 , which satisfies equilibrium, the corresponding strains of the two models in Figure 4.5 (strains ε_1' and ε_1'') are significantly different.

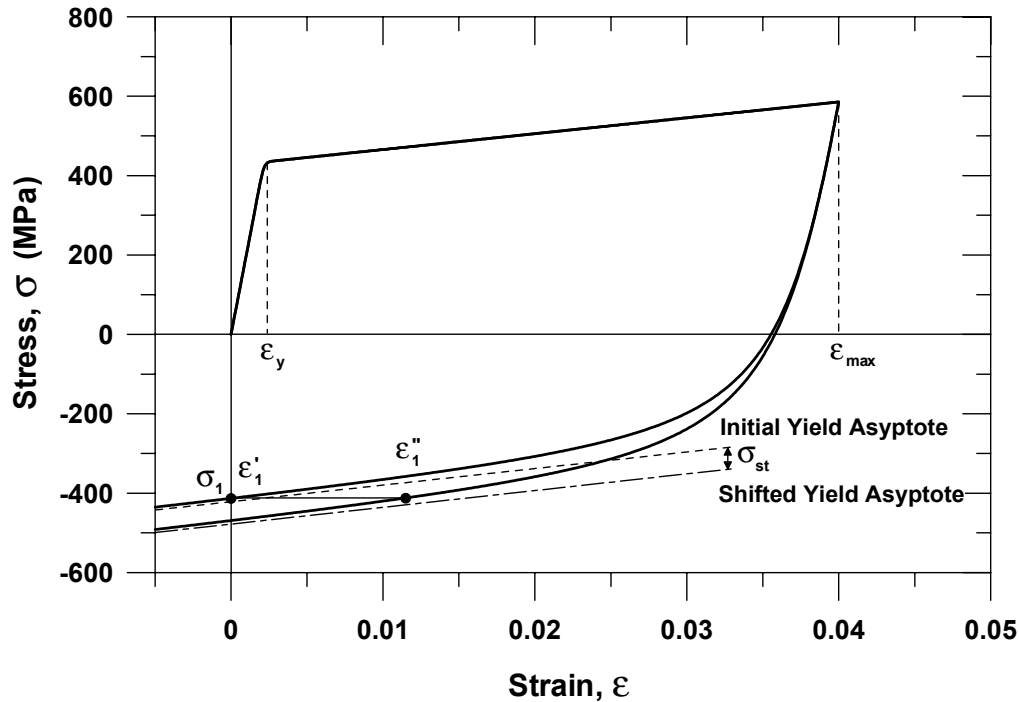


Fig. 4.5 Stress shift due to isotropic strain hardening (Filippou et al., 1983)

In order to account for isotropic strain hardening to improve the prediction of the strains in reinforcing bars in RC members during crack closure, Filippou et al. (1983) proposed a modification to the original model by Menegotto and Pinto (1973) by introducing a stress shift to the yield asymptote. The shift is accomplished by moving the initial (or monotonic) yield asymptote by a stress magnitude, σ_{st} , parallel to its direction (Fig. 4.5). This idea was introduced by Stanton and McNiven (1979), who imposed both a stress and a strain shift on the monotonic envelope curve to arrive at a very accurate representation of hysteretic steel behavior under generalized strain histories. The simplification introduced by Filippou et al., compared to the model by Stanton and McNiven, involves the assumption that the monotonic envelope can be approximated by a bilinear curve, which simplifies the yield asymptotes to straight lines. Thus, the form and simplicity of the original model (Menegotto and Pinto, 1973) was retained, while a substantial improvement in results was achieved (Filippou et al., 1983).

The imposed stress shift of the yield asymptotes (σ_{st}) depends on several parameters of strain history. The main parameter suggested in by Stanton and McNiven (1979) was the sum of the absolute values of plastic strains up to the most recent strain reversal. Because of differences in the formulation the model used by Filippou et al. (1983), the authors decided to choose the maximum plastic strain as the main parameter on which the yield asymptote shift depends. The relation proposed by Filippou et al. takes the form:

$$\frac{\sigma_{st}}{\sigma_y} = a_3 \left(\frac{\varepsilon_{\max}}{\varepsilon_y} - a_4 \right) \quad (4.8)$$

where ε_{\max} is the absolute maximum strain at the instant of strain reversal, ε_y , σ_y are, respectively, the strain and stress at yield, and a_3 and a_4 are experimentally determined parameters. Based on test results, Filippou et al. calibrated the parameter values as: $R_0 = 20$, $a_1 = 18.5$, $a_2 = 0.15$, $a_3 = 0.01$, and $a_4 = 7$, with the values for the first three parameters previously suggested by Menegotto and Pinto (1973).

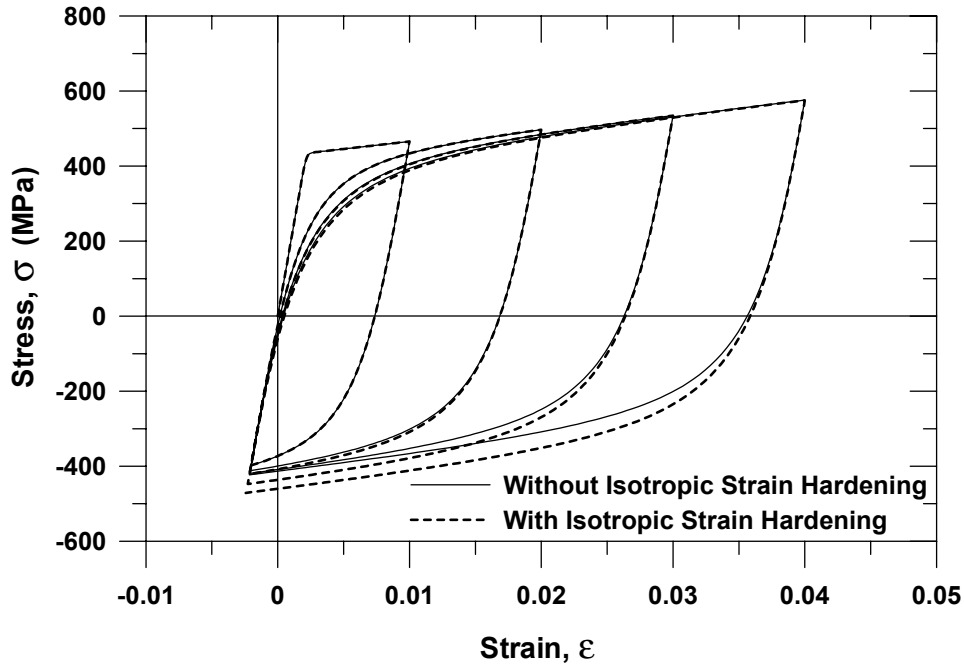


Fig. 4.6 Effect of isotropic strain hardening on stress-strain relation

To illustrate the effect of the imposed stress shift on a typical stress-strain history for reinforcing bars, Figure 4.6 compares the analytical results of the model with and without

isotropic strain-hardening effects included. Upon implementation of the above relation proposed by Filippou et al. (1983), the accuracy of the original Menegotto and Pinto (1973) model in representing experimental results from cyclic tests on reinforcing bars was substantially improved, particularly within the strain region where gap closure would be expected. At the same time, the model is almost as simple and computationally efficient as the original model. The modification proposed by Filippou et al. to the hysteretic model of Menegotto and Pinto, was therefore implemented in the present wall model to account for the isotropic strain-hardening effects on reinforcing bars.

4.2 CONSTITUTIVE MODELS FOR CONCRETE

For an accurate and reliable prediction of wall flexural response using a MVLEM as proposed, an effective and robust hysteretic constitutive model for concrete is needed. The model addresses important issues such as the hysteretic behavior in both cyclic compression and tension; the progressive degradation of stiffness of the unloading and reloading curves for increasing values of strain; and the effects of confinement, tension stiffening, and gradual crack closure. Two different constitutive models with such capabilities were adopted in this study, the first being relatively simple and commonly used, and the latter more refined and generalized.

4.2.1 Hysteretic Constitutive Model by Yassin (1994)

Studies on the stress-strain relations of concrete under cyclic loading have been much fewer than those under monotonic loading. Sinha et al. (1964) and Karsan and Jirsa (1969) have studied the behavior of plain concrete subjected to repetitions of compressive stress. It was found in these studies that the envelope for cyclic loading coincided with the stress-strain curve for monotonic loading. A uniaxial hysteretic model proposed by Yassin (1994), based on the experimental results from Sinha et al. (1964) and Karsan and Jirsa (1969), is the first of the two constitutive models for concrete used in this study. The model takes into account concrete damage and hysteresis, while retaining computational efficiency.

The monotonic envelope curve of the hysteretic model for concrete in compression follows the monotonic stress-strain relation model of Kent and Park (1971) as extended by Scott, Park, and Priestley (1982). Even though more accurate and complete monotonic stress-strain

models have been published since, the so-called modified Kent and Park model offers a good balance between simplicity and accuracy, and is widely used.

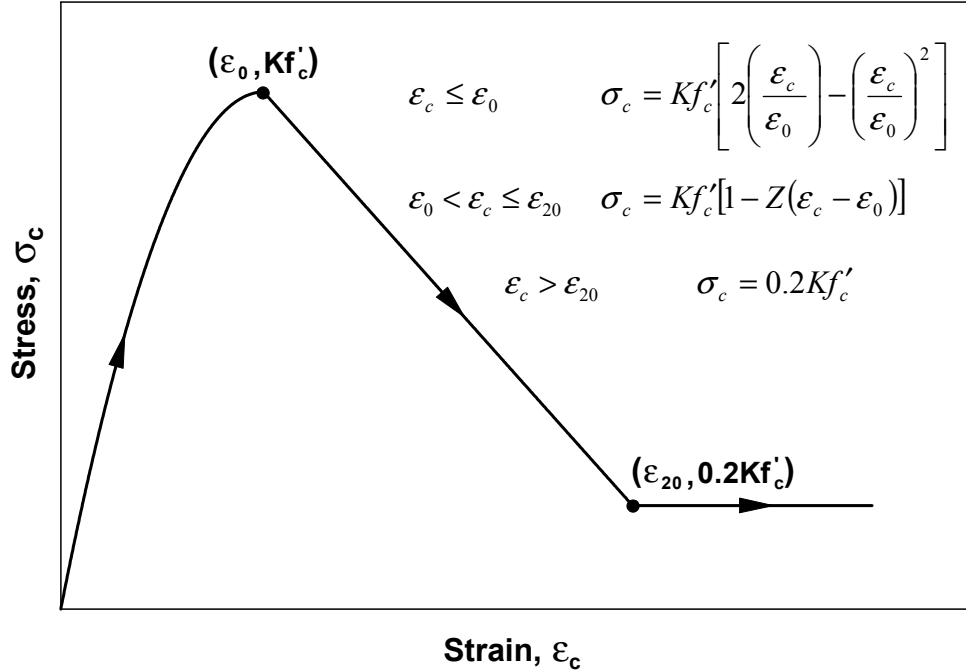


Fig. 4.7 Modified Kent and Park model (1982) for concrete in compression

In the modified Kent and Park model (Fig. 4.7), the monotonic concrete stress-strain ($\sigma_c - \varepsilon_c$) relation in compression is described by three regions. Adopting the convention that compression is positive, the three regions are:

$$\text{Region OA: } \varepsilon_c \leq \varepsilon_0 \quad \sigma_c = Kf'_c \left[2 \left(\frac{\varepsilon_c}{\varepsilon_0} \right) - \left(\frac{\varepsilon_c}{\varepsilon_0} \right)^2 \right] \quad (4.9)$$

$$\text{Region AB: } \varepsilon_0 < \varepsilon_c \leq \varepsilon_{20} \quad \sigma_c = Kf'_c [1 - Z(\varepsilon_c - \varepsilon_0)] \quad (4.10)$$

$$\text{Region BC: } \varepsilon_c > \varepsilon_{20} \quad \sigma_c = 0.2Kf'_c \quad (4.11)$$

The corresponding tangent moduli (E_t) are given by the following expressions:

$$\varepsilon_c \leq \varepsilon_0 \quad E_t = \frac{2Kf'_c}{\varepsilon_0} \left(1 - \frac{\varepsilon_c}{\varepsilon_0} \right) \quad (4.12)$$

$$\varepsilon_0 < \varepsilon_c \leq \varepsilon_{20} \quad E_t = -ZKf'_c \quad (4.13)$$

$$\varepsilon_c > \varepsilon_{20} \quad E_t = 0 \quad (4.14)$$

where

$$\varepsilon_0 = 0.002K \quad (4.15)$$

$$K = 1 + \frac{\rho_s f_{yh}}{f'_c} \quad (4.16)$$

$$Z = \frac{0.5}{\frac{3 + 0.29f'_c}{145f'_c - 1000} + 0.75\rho_s \sqrt{\frac{h'}{s_h}} - 0.002K} \quad (4.17)$$

In the equations above, ε_0 is the concrete strain at maximum compressive stress, ε_{20} is the concrete strain at 20% of maximum compressive stress, K is a factor that accounts for the strength increase due to confinement, Z is the strain softening slope, f'_c is the concrete compressive cylinder strength (unconfined peak compressive stress) in MPa, f_{yh} is the yield strength of transverse reinforcement in MPa, ρ_s is the ratio of the volume of transverse reinforcement to the volume of concrete core measured to the outside of stirrups, h' is the width of concrete core measured to the outside of stirrups, and s_h is the center to center spacing of stirrups or hoop sets.

The hysteretic unloading and reloading rules proposed by Yassin (1994) are a set of linear stress-strain relations, as shown in Figure 4.8. The figure illustrates that hysteretic behavior occurs in both compression and tension. Although the compressive and tensile hysteresis loops are continuous, they are discussed separately for the sake of clarity.

For compression, successive stiffness degradation for both unloading and reloading, for increasing values of maximum strain, are shown in Figure 4.9. The stiffness degradation is such that the projections of all reloading lines intersect at a common point R . Point R is determined by the intersection of the tangent to the monotonic envelope curve at the origin and the projection of the unloading line from point B, which corresponds to a concrete strength $0.2f'_c$ (Fig. 4.9). The strain and stress at the intersection point are given by the following expressions:

$$\varepsilon_r = \frac{0.2Kf'_c - E_{20}\varepsilon_{20}}{E_c - E_{20}} \quad (4.18)$$

$$\sigma_r = E_c \varepsilon_r \quad (4.19)$$

where E_c is the tangent modulus of the monotonic envelope curve at the origin, and E_{20} is the unloading modulus at point B of the monotonic envelope curve with a compressive stress of

$0.2f'_c$. The magnitude of E_{20} has to be determined experimentally; a value of 10% of E_c was used by Yassin (1994).

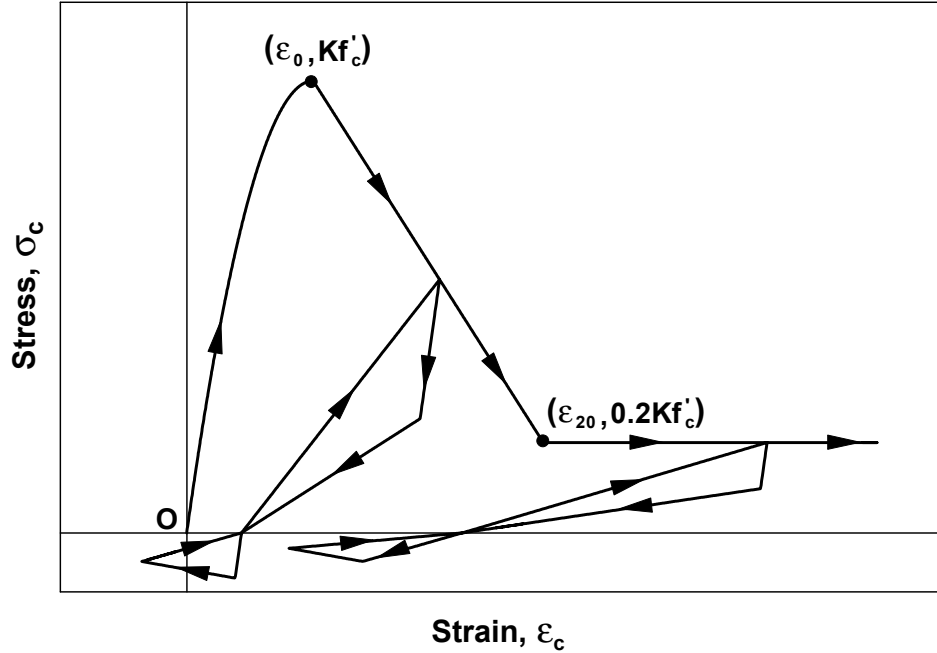


Fig. 4.8 Hysteretic unloading and reloading rules (Yassin, 1994)

Upon unloading from and reloading to a point on the compressive monotonic envelope (point D in Fig. 4.9), and above the zero stress axis (point H in Fig. 4.9), the model response follows two hysteretic branches that are defined by the following equations:

$$\text{Maximum branch (line HD): } \sigma_{\max} = \sigma_m + E_r(\varepsilon_c - \varepsilon_m) \quad (4.20)$$

$$\text{Minimum branch (line HE): } \sigma_{\min} = 0.5E_r(\varepsilon_c - \varepsilon_t) \quad (4.21)$$

where

$$E_r = \frac{\sigma_m - \sigma_r}{\varepsilon_m - \varepsilon_r} \quad (4.22)$$

$$\varepsilon_t = \varepsilon_m - \frac{\sigma_m}{E_r} \quad (4.23)$$

Parameters σ_m and ε_m are the stress and strain at the unloading point on the compressive monotonic envelope, respectively. Therefore, the position of the unloading and reloading loop depends on the position of the unloading point. For partial loading and unloading cycles within

the loops, the model follows a straight line with slope E_c . In the numerical implementation, a trial stress and tangent modulus are assumed based on the linear elastic behavior with slope E_c :

$$\sigma_c^T = \sigma_c' + E_c \Delta \varepsilon_c \quad (4.24)$$

where σ_c^T is the new trial stress, σ_c' is the previous stress state, and $\Delta \varepsilon_c$ is the strain increment. The following rules are then used to determine actual stress and tangent modulus of the model:

$$\text{if } \sigma_{\min} \leq \sigma_c^T \leq \sigma_{\max} \quad \text{then } \sigma_c = \sigma_c^T \quad \text{and} \quad E_t = E_c \quad (4.25)$$

$$\text{if } \sigma_c^T < \sigma_{\min} \quad \text{then } \sigma_c = \sigma_{\min} \quad \text{and} \quad E_t = 0.5E_r \quad (4.26)$$

$$\text{if } \sigma_c^T > \sigma_{\max} \quad \text{then } \sigma_c = \sigma_{\max} \quad \text{and} \quad E_t = E_r \quad (4.27)$$

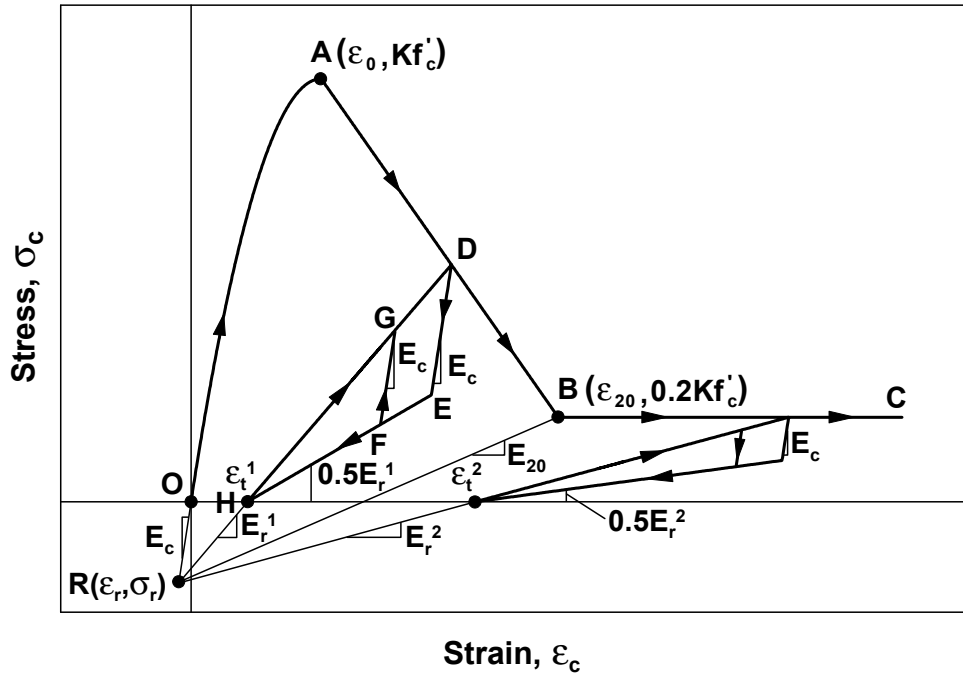


Fig. 4.9 Hysteretic parameters of model by Yassin (1994)

The tensile behavior of the model (Fig. 4.8) takes into account tension stiffening and the degradation of the unloading and reloading stiffness for increasing values of maximum tensile strain after initial cracking. The maximum tensile strength of concrete is assumed to be equal to:

$$f_t' = 0.623 \sqrt{f_c'} \quad (4.28)$$

where f'_t and f'_c are expressed in MPa. Figure 4.10 shows two consecutive tensile hysteresis loops, which are part of a sample cyclic history that also includes compressive stresses. The model assumes that tensile stress can occur anywhere along the strain axis, either as a result of initial tensile loading or as a result of unloading from a compressive state. In the latter case, a tensile stress occurs under a compressive strain. The tensile stress-strain relation is defined by three points with coordinates $(\varepsilon_t, 0)$, $(\varepsilon_n, 0)$ and $(\varepsilon_u, 0)$, as represented by points J, K, and M, respectively, in Figure 4.10.

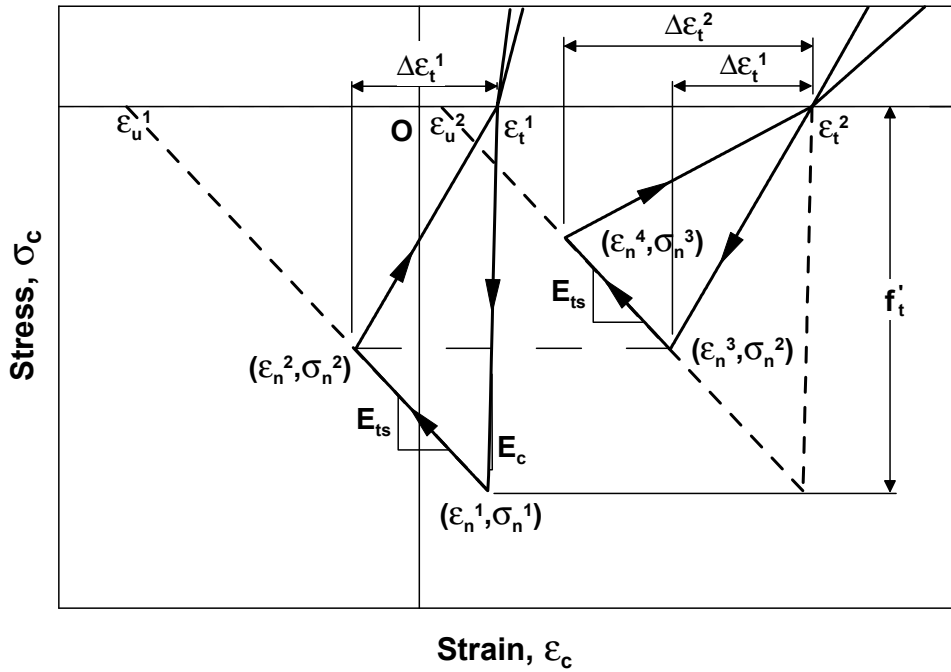


Fig. 4.10 Hysteresis loops in tension (Yassin, 1994)

Parameter ε_t is the strain at the point where the unloading line from the compressive stress region crosses the strain axis and changes with maximum compressive strain. Parameters ε_n and σ_n are the strain and stress at the peak of the tensile stress-strain relation and are given by the following expressions:

$$\varepsilon_n = \varepsilon_t + \Delta\varepsilon_t \quad (4.29)$$

$$\sigma_n = f'_t \left(1 + \frac{E_{ts}}{E_c} \right) - E_{ts} \Delta\varepsilon_t \quad (4.30)$$

where $\Delta\varepsilon_t$ is the previous maximum differential between tensile strain and ε_t as shown in Figure 4.10. Before initial cracking, $\Delta\varepsilon_t$ is equal to f'_t/E_c . Parameter E_{ts} is the tension-stiffening modulus, a value of 5% of E_c was used for E_{ts} by Yassin (1994). Parameter ε_u is the strain at the point where the tensile stress is reduced to zero and is given by the expression:

$$\varepsilon_u = \varepsilon_t + f'_t \left(\frac{1}{E_{ts}} + \frac{1}{E_c} \right) \quad (4.31)$$

Given these control points, the tensile stress-strain relation and the tangent moduli are defined by the following equations (assuming the convention that tension is positive):

$$\text{Region JK : } \varepsilon_t < \varepsilon_c \leq \varepsilon_n \quad \sigma_c = E_t(\varepsilon_c - \varepsilon_t) \quad E_t = \frac{\sigma_n}{\varepsilon_n - \varepsilon_t} \quad (4.32)$$

$$\text{Region KM: } \varepsilon_n < \varepsilon_c \leq \varepsilon_u \quad \sigma_c = \sigma_n + E_t(\varepsilon_c - \varepsilon_n) \quad E_t = -E_{ts} \quad (4.33)$$

$$\text{Region MN: } \varepsilon_c > \varepsilon_u \quad \sigma_c = 0 \quad E_t = 0 \quad (4.34)$$

If $\varepsilon_n \geq \varepsilon_u$, then σ_n , σ_c , and E_t are all assumed to be zero. The modulus E_{ts} controls the degree of tension stiffening (the contribution of tensile concrete resistance between cracks) by controlling the slope of the region KM. The steeper the slope, the smaller the contribution of tension stiffening. Tensile unloading and reloading are governed by the equation for the region JK, which also includes stiffness degradation for increasing values strain differential $\Delta\varepsilon_t$. The value of $\Delta\varepsilon_t$ changes whenever $\varepsilon_c > \varepsilon_n$.

The constitutive model described above, with the monotonic envelope of Kent and Park (1971) extended by Scott, Park, and Priestley (1982) and the hysteretic relations proposed by Yassin (1994), was adopted in the present wall model as a simple and practical alternative to simulate the hysteretic behavior of concrete. Due to its computational efficiency and reasonable level of accuracy, the constitutive model is commonly used by researchers, and is implemented in the state-of-the-art computational platform OpenSees (“OpenSees”) developed by the Pacific Earthquake Engineering Research Center at the University of California, Berkeley. The model successfully generates continuous stress-strain behavior in hysteretic compression and tension, and considers damage in the form of cyclic stiffness degradation.

The primary shortcoming of this concrete constitutive model is the inability of the model to simulate gradual gap closure due to progressive contact stresses within the cracks in concrete. This may significantly impair the accuracy in predicting the pinching properties (i.e.,

characteristic variation in section stiffness from unloading to reloading in the opposite direction) of RC elements subjected to cyclic loading. Another limitation of the constitutive model is that it lacks the flexibility of a generalized model. The model does not allow control on most of the parameters associated with the monotonic and hysteretic branches of the stress-strain relation, thus restraining the calibration of the model or re-assessment of the parameters as new data become available. Furthermore, the monotonic stress-strain envelope associated with the constitutive model may be considered out of date, more accurate monotonic stress-strain models for both unconfined and confined concrete have been proposed since.

Based on these shortcomings, a more robust, accurate, and generalized constitutive model for concrete was implemented in the MVLEM, as a second and superior alternative. Details of the model are presented in the following section.

4.2.2 Hysteretic Constitutive Model by Chang and Mander (1994)

The uniaxial hysteretic constitutive model developed by Chang and Mander (1994) was also adopted in the present wall model as the basis for the stress-strain relation for concrete. The constitutive model by Chang and Mander is an advanced, rule-based, generalized, and nondimensional model that simulates the hysteretic behavior of confined and unconfined, ordinary and high-strength concrete in both cyclic compression and tension. Upon development of the model, the authors focused particular emphasis on the transition of the stress-strain relation upon crack opening and closure, which had not been adequately addressed in previous models. Most existing models (including the model by Yassin (1994) previously described) assume sudden crack closure with rapid change in section modulus (i.e., sudden pinching behavior).

Similar to the model by Yassin (1994), in the model by Chang and Mander, the monotonic curve forms the envelope for the hysteretic stress-strain relation. This was shown to be a reasonable assumption based on experimental results presented by Sinha et al. (1964) and Karsan and Jirsa (1969), and modeled by Mander et al. (1988a) for unconfined concrete in cyclic compression. Mander et al. (1988b) also performed tests for confined concrete and validated their model. Experiments by Gopalaratnam and Shah (1985) and Yankelevsky and Reinhardt (1987) have shown that this is also the case for concrete in cyclic tension. Thus, in the model by Chang and Mander, concrete in tension is modeled with a cyclic behavior similar to that in

compression. The model envelopes for compression and tension have control on the slope of the stress-strain behavior at the origin, and the shape of both the ascending and descending (i.e., pre-peak and post-peak) branches of the stress-strain behavior. The shape of the envelopes can be feasibly altered while keeping the values of the peak stress and the strain at peak stress constant, allowing a refined calibration for modeling. In order to define the compression and tension envelopes, the model by Chang and Mander uses the Tsai's equation (Tsai, 1988), which is based on the equation by Popovics (1973), an equation that has proven to be very useful in describing the monotonic compressive stress-strain curve for concrete.

4.2.2.1 Compression Envelope Curve

The compression envelope curve of the model by Chang and Mander is defined by the initial slope E_c , the peak coordinate (ϵ'_c, f'_c) , a parameter r from Tsai's (1988) equation defining the shape of the envelope curve, and a parameter $x_{cr}^- > 1$ to define the spalling strain (Fig. 4.11).

Both the compression and tension envelope curves can be written in nondimensional form by the use of the following equations:

$$y(x) = \frac{nx}{D(x)} \quad (4.35)$$

$$z(x) = \frac{(1-x^r)}{[D(x)]^2} \quad (4.36)$$

where,

$$D(x) = 1 + \left(n - \frac{r}{r-1} \right) x + \frac{x^r}{r-1} \quad r \neq 1 \quad (4.37)$$

$$D(x) = 1 + (n-1 + \ln x)x \quad r = 1 \quad (4.38)$$

and n and x are defined for the compression envelope as:

$$x^- = \left| \frac{\epsilon_c}{\epsilon'_c} \right| \quad (4.39)$$

$$n^- = \left| \frac{E_c \epsilon'_c}{f'_c} \right| \quad (4.40)$$

The nondimensional spalling strain can be calculated by:

$$x_{sp} = x_{cr}^- - \frac{y(x_{cr}^-)}{n^- z(x_{cr}^-)} \quad (4.41)$$

In the equations above, ε_c is the concrete strain, ε'_c is the concrete strain at peak unconfined (or confined) stress, f'_c is the unconfined (or confined) concrete strength, E_c is the concrete initial Young's modulus, x^- is the nondimensional strain on the compression envelope, x_{cr}^- is the nondimensional critical strain on the compression envelope curve (used to define a tangent line up to the spalling strain), x_{sp} is the nondimensional spalling strain, $y(x)$ is the nondimensional stress function, $z(x)$ is the nondimensional tangent modulus function (Fig. 4.11)

The stress f_c and the tangent modulus E_t at any given strain on the compression envelope curve are defined by:

$$f_c = f_c^-(x^-) \quad (4.42)$$

$$E_t = E_t^-(x^-) \quad (4.43)$$

where $f_c^-(x^-)$ and $E_t^-(x^-)$ are defined as:

If $x^- < x_{cr}^-$ (Tsai's equation)

$$f_c^- = f'_c y(x^-) \quad (4.44)$$

$$E_t^- = E_c z(x^-) \quad (4.45)$$

If $x_{cr}^- \leq x^- \leq x_{sp}$ (Straight line)

$$f_c^- = f'_c [y(x_{cr}^-) + n^- z(x_{cr}^-)(x^- - x_{cr}^-)] \quad (4.46)$$

$$E_t^- = E_c z(x_{cr}^-) \quad (4.47)$$

If $x > x_{sp}$ (Spalled)

$$f_c^- = E_t^- = 0 \quad (4.48)$$

Once the concrete is considered to be spalled, the stresses are zero from that moment on. Confined concrete can be considered not to spall, in such a case a large value of x_{cr}^- should be defined. The minus superscript in the equations above refers to the stress-strain behavior in compression.

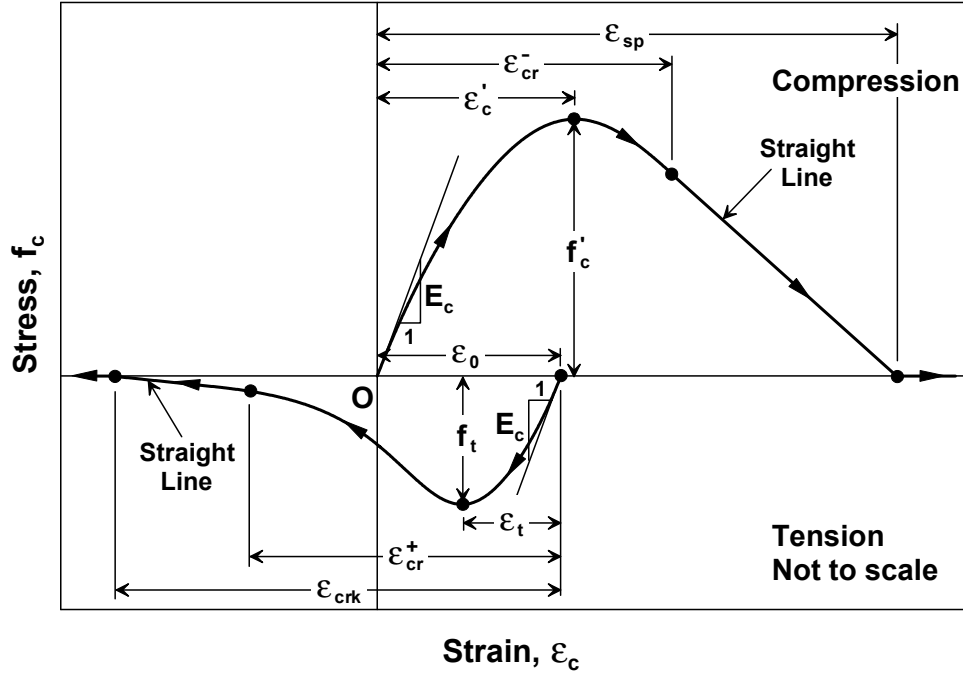


Fig. 4.11 Compression and tension envelopes of Chang and Mander (1994) model

The material parameters associated with the compression envelope curve of the model are the concrete strength f'_c , the concrete strain at peak stress ϵ'_c , the concrete initial Young's modulus (modulus of elasticity) E_c , the Tsai's parameter r defining the shape of the compression envelope, and the nondimensional critical strain x_{cr}^- where the envelope curve starts following a straight line. All of these parameters can be controlled and manipulated based on specific experimental results for a refined calibration of the compression envelope. Nevertheless, Chang and Mander (1994) have proposed empirical relations for the parameters E_c , ϵ'_c , and r defined based on a detailed review of previous research. Parameters E_c , ϵ'_c , and r associated with the unconfined compression envelope can be empirically related to the unconfined concrete strength f'_c (MPa) as:

$$\text{Initial modulus of elasticity: } E_c = 8200f'_c \text{ MPa} \quad (4.49)$$

$$\text{Strain at peak stress: } \epsilon'_c = \frac{(f'_c)^{1/4}}{28} \quad (4.50)$$

$$\text{Shape parameter: } r = \frac{f'_c}{5.2} - 1.9 \quad (4.51)$$

The compressive envelope of the model by Chang and Mander (1994) for confined concrete complies with the generalized confinement model developed by Mander et al. (1988a), which is applicable to RC members with either circular or rectangular cross sections and any general type and configuration of reinforcement (Fig. 4.12). For rectangular sections, the effectively confined concrete area is given by the expression:

$$A_e = \left(b_c d_c - \sum_{i=1}^n \frac{(w'_i)^2}{6} \right) \left(1 - 0.5 \frac{s'}{b_c} \right) \left(1 - 0.5 \frac{s'}{d_c} \right) \quad (4.52)$$

whereas the concrete core area is given by:

$$A_{cc} = b_c d_c - A_{st}$$

The lateral confinement pressure (imposed by the transverse steel) for each direction is calculated as:

$$f'_{lx} = k_e \rho_x f_{yh} \quad (4.53)$$

$$f'_{ly} = k_e \rho_y f_{yh} \quad (4.54)$$

in which,

$$k_e = \frac{A_e}{A_{cc}} \quad (\text{the confinement effectiveness coefficient}) \quad (4.55)$$

$$\rho_x = \frac{A_{sx}}{s d_c} \quad (4.56)$$

A_{sx} = total area of transverse reinforcement parallel to the x axis

$$\rho_y = \frac{A_{sy}}{s b_c} \quad (4.57)$$

A_{sy} = total area of transverse reinforcement parallel to the y axis

The equation proposed by Chang and Mander (1994) to represent the analytical confinement coefficient K takes the form (as an approximation of the ultimate strength surface proposed by Mander et al., 1988a):

$$K = \frac{f'_{cc}}{f'_c} = 1 + A\bar{x} \left(0.1 + \frac{0.9}{1 + B\bar{x}} \right) \quad (4.58)$$

with:

$$\bar{x} = \frac{f'_{l1} + f'_{l2}}{2f'_c} \quad (4.59)$$

$$r = \frac{f'_{l1}}{f'_{l2}} \quad f'_{l2} \geq f'_{l1} \quad (4.60)$$

$$A = 6.8886 - (0.6096 + 17.275r)e^{-4.989r} \quad (4.61)$$

$$B = \frac{4.5}{\frac{5}{A}(0.9849 - 0.6306e^{-3.8939r}) - 0.1} \quad (4.62)$$

where the analytical confinement coefficient K is the ratio of the confined concrete strength f'_{cc} to the unconfined concrete strength f'_c .

Equation 4.58 can be represented in the form of:

$$f'_{cc} = f'_c + k_1 f_l \quad (4.63)$$

By taking f_l as the average of f_{l1} and f_{l2} this can be rewritten as:

$$K = \frac{f'_{cc}}{f'_c} = 1 + k_1 \bar{x} \quad (4.64)$$

where,

$$k_1 = A \left(0.1 + \frac{0.9}{1 + B\bar{x}} \right) \quad (4.65)$$

The strain at peak stress for confined concrete (ε'_{cc}) as adopted by Chang and Mander takes the form:

$$\varepsilon'_{cc} = \varepsilon'_c (1 + k_2 \bar{x}) \quad (4.66)$$

with,

$$k_2 = 5k_1 \quad (4.67)$$

where ε'_c is the strain at peak unconfined stress.

The confinement parameters described above were validated by Mander et al. (1988b) and Chang and Mander (1994) against extensive experimental data from tests on RC column specimens under eccentric loading.

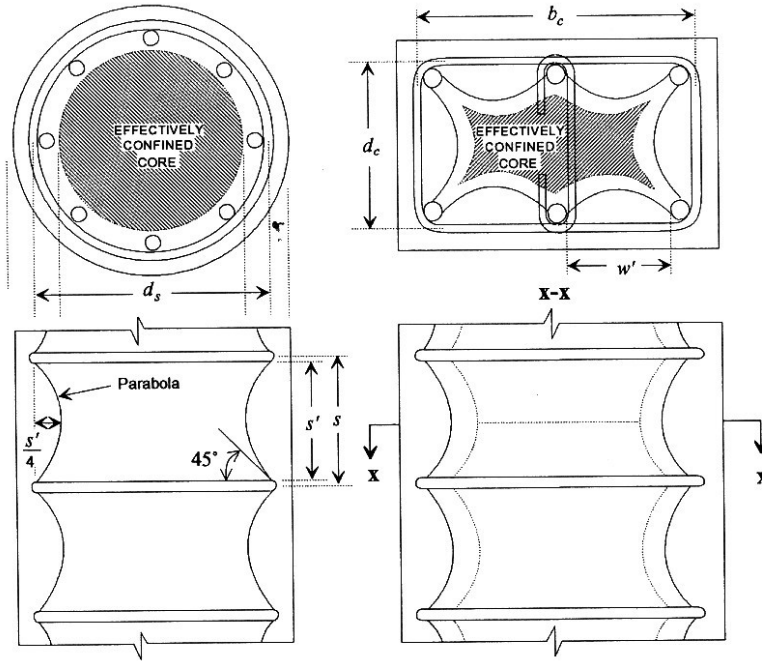


Fig. 4.12 Confinement mechanism for circular and rectangular cross sections (Chang and Mander, 1994)

4.2.2.2 Tension Envelope Curve

The shape of the tension envelope curve in the Chang and Mander model is the same as that of the compression envelope curve (Fig. 4.11). The curve is shifted to a new origin ϵ_0 , as explained in the following section. The nondimensional parameters for the tension envelope curve are given by:

$$x^+ = \left| \frac{\epsilon_c - \epsilon_0}{\epsilon_t} \right| \quad (4.68)$$

$$n^+ = \frac{E_c \epsilon_t}{f_t} \quad (4.69)$$

The nondimensional cracking strain is given by:

$$x_{crk} = x_{cr}^+ - \frac{y(x_{cr}^+)}{n^+ z(x_{cr}^+)} \quad (4.70)$$

where ε_c is the concrete strain, ε_t is the concrete strain at peak tension stress, f_t is the concrete tensile strength, E_c is the concrete initial Young's modulus, x^+ is the nondimensional strain on the tension envelope curve, x_{cr}^+ is the critical strain on the tension envelope curve (used to define a tangent line up to the cracking strain), and x_{crk} is the cracking strain (Fig. 4.11).

The stress f_c and the tangent modulus E_t for any given strain on the tension envelope curve are defined as:

$$f_c = f_c^+(x^+) \quad (4.71)$$

$$E_t = E_t^+(x^+) \quad (4.72)$$

where $f_c^+(x^+)$ and $E_t^+(x^+)$ are defined as:

If $x^+ < x_{cr}^+$ (Tsai's equation)

$$f_c^+ = f_t y(x^+) \quad (4.73)$$

$$E_t^+ = E_c z(x^+) \quad (4.74)$$

If $x_{cr}^+ \leq x^+ \leq x_{crk}$ (Straight line)

$$f_c^+ = f_t [y(x_{cr}^+) + n^+ z(x_{cr}^+) (x^+ - x_{cr}^+)] \quad (4.75)$$

$$E_t^+ = E_c z(x_{cr}^+) \quad (4.76)$$

If $x > x_{crk}$ (Cracked)

$$f_c^+ = E_t^+ = 0 \quad (4.77)$$

where the functions y and z are defined by Equations 4.35–4.36. When the concrete is cracked it is considered no longer to resist any tension stress, as a result of crack opening, but on the other hand a gradual crack closure is considered to take place. Concrete experiencing tension stiffening can be considered not to crack completely, that is, a large value of x_{cr}^+ can be defined. The plus superscript refers to the stress-strain behavior in tension.

The parameters associated with the tension envelope curve include the concrete tensile strength f_t , the strain at peak tensile stress ε_t , and the parameter r defining the shape of the tension envelope curve. The critical strain on the tension envelope curve x_{cr}^+ (where the envelope curve starts following a straight line) can be controlled and calibrated based on either

experimental results or empirical relations (e.g., Collins and Mitchell, 1991; Belarbi and Hsu, 1994) to model the behavior of concrete in tension and the tension-stiffening phenomenon.

4.2.2.3 Hysteretic Properties of the Model

In order to define the cyclic properties of concrete in compression, statistical regression analyses were performed by Chang and Mander (1994) on an extensive experimental database that included data from Sinha et al. (1964), Karsan and Jirsa (1969), Spooner and Dougill (1975), Okamoto et al. (1976) and Tanigawa and Uchida (1979). Based on the regression analyses, empirical relations were developed for key hysteretic parameters such as those for secant stiffness (E_{sec}) and plastic stiffness (E_{pl}) upon unloading from, and stress and strain offsets (Δf and $\Delta \varepsilon$) upon return to the compression envelope (Fig. 4.13). The hysteretic parameters for cyclic compression are given by:

$$E_{sec}^- = E_c \left(\frac{\left| \frac{f_{un}^-}{E_c \varepsilon_c'} + 0.57 \right|}{\left| \frac{\varepsilon_{un}^-}{\varepsilon_c'} + 0.57 \right|} \right) \quad (4.78)$$

$$E_{pl}^- = 0.1 E_c \exp \left(-2 \left| \frac{\varepsilon_{un}^-}{\varepsilon_c'} \right| \right) \quad (4.79)$$

$$\Delta f^- = 0.09 f_{un}^- \sqrt{\left| \frac{\varepsilon_{un}^-}{\varepsilon_c'} \right|} \quad (4.80)$$

$$\Delta \varepsilon^- = \frac{\varepsilon_{un}^-}{1.15 + 2.75 \left| \frac{\varepsilon_{un}^-}{\varepsilon_c'} \right|} \quad (4.81)$$

where ε_c' is the strain at peak compressive stress, E_c is the initial Young's modulus, and f_{un} and ε_{un} are the unloading stress and strain.

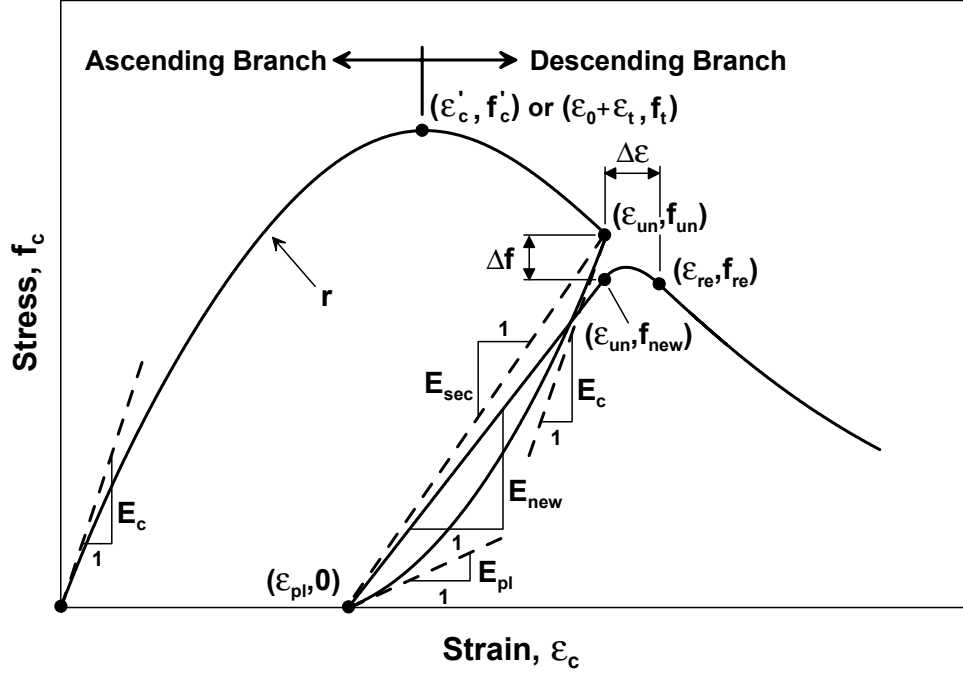


Fig. 4.13 Hysteretic parameters of Chang and Mander (1994) model

Parameters such as the plastic (residual) strain upon unloading (ε_{pl}), new stress (f_{new}) and tangent modulus (E_{new}) upon return to unloading strain from the envelope curve (ε_{un}), and the strain (ε_{re}), stress (f_{re}) and tangent modulus (E_{re}) at the point of return to the envelope curve are can be geometrically derived from these empirical relations (Fig. 4.13) as:

$$\varepsilon_{pl}^- = \varepsilon_{un}^- - \frac{f_{un}^-}{E_{sec}^-} \quad (4.82)$$

$$f_{new}^- = f_{un}^- - \Delta f^- \quad (4.83)$$

$$E_{new}^- = \frac{f_{new}^-}{\varepsilon_{un}^- - \varepsilon_{pl}^-} \quad (4.84)$$

$$\varepsilon_{re}^- = \varepsilon_{un}^- + \Delta \varepsilon^- \quad (4.85)$$

$$f_{re}^- = f^- \left(\left| \frac{\varepsilon_{re}^-}{\varepsilon'_c} \right| \right) \quad (4.86)$$

$$E_{re}^- = E^- \left(\left| \frac{\varepsilon_{re}^-}{\varepsilon'_c} \right| \right) \quad (4.87)$$

For cyclic behavior in tension, Chang and Mander modified the empirical relations defined in Equations 4.78–4.81, based on test results by Yankelevsky and Reinhardt (1987) as:

$$E_{sec}^+ = E_c \left(\frac{\left| \frac{f_{un}^+}{E_c \varepsilon_t} \right| + 0.67}{\left| \frac{\varepsilon_{un}^+ - \varepsilon_0}{\varepsilon_t} \right| + 0.67} \right) \quad (4.88)$$

$$E_{pl}^+ = \frac{E_c}{\left| \frac{\varepsilon_{un}^+ - \varepsilon_0}{\varepsilon_t} \right|^{1.1} + 1} \quad (4.89)$$

$$\Delta f^+ = 0.15 f_{un}^+ \quad (4.90)$$

$$\Delta \varepsilon^+ = 0.22 (\varepsilon_{un}^+ - \varepsilon_0) \quad (4.91)$$

where ε_t is the strain at peak tensile stress, E_c is the initial Young's modulus and ε_0 is the shifted origin of the tensile envelope curve. The derived parameters for tension are thus:

$$\varepsilon_{pl}^+ = \varepsilon_{un}^+ - \frac{f_{un}^+}{E_{sec}^+} \quad (4.92)$$

$$f_{new}^+ = f_{un}^+ - \Delta f^+ \quad (4.93)$$

$$E_{new}^+ = \frac{f_{new}^+}{\varepsilon_{un}^+ - \varepsilon_{pl}^+} \quad (4.94)$$

$$\varepsilon_{re}^+ = \varepsilon_{un}^+ + \Delta \varepsilon^+ \quad (4.95)$$

$$f_{re}^+ = f^+ \left(\frac{\varepsilon_{re}^+ - \varepsilon_0}{\varepsilon_t} \right) \quad (4.96)$$

$$E_{re}^+ = E^+ \left(\frac{\varepsilon_{re}^+ - \varepsilon_0}{\varepsilon_t} \right) \quad (4.97)$$

A reversal from the compression envelope curve is done as shown in Figure 4.14, by calculating the shifted origin (ε_0) of the tension envelope curve and evaluating the unloading strain (ε_{un}^+) from the tension envelope curve. The variables that define this reversal curve are calculated as follows:

Calculate the compression strain ductility as:

$$x_u^- = \left| \frac{\varepsilon_{un}^-}{\varepsilon_c'} \right| \quad (4.98)$$

Calculate the tension strain ductility:

$$x_u^+ = \left| \frac{\varepsilon_{un}^+ - \varepsilon_0}{\varepsilon_t} \right| \quad (4.99)$$

If $x_u^+ < x_u^-$, then:

$$x_u^+ = x_u^- \quad (4.100)$$

$$\varepsilon_0 = 0 \quad (4.101)$$

$$\varepsilon_{un}^+ = x_u^+ \varepsilon_t$$

$$f_{un}^+ = f_c^+(x_u^+) \quad \text{using Eq. 4.71} \quad (4.102)$$

Calculate:

$$\Delta\varepsilon_0 = \frac{2f_{un}^+}{E_{sec}^+ + E_{pl}^-} \quad (4.103)$$

Finally,

$$\varepsilon_0 = \varepsilon_{pl}^- + \Delta\varepsilon_0 - x_u^+ \varepsilon_t \quad (4.104)$$

$$\varepsilon_{un}^+ = x_u^+ \varepsilon_t + \varepsilon_0 \quad (4.105)$$

Accordingly, upon each unloading from the compression envelope, the origin of the tension envelope is shifted based on the unloading strain from the compression envelope (ε_{un}^-), and the unloading strain from the tension envelope (ε_{un}^+) is re-evaluated so that it corresponds to a tension strain ductility equal to the compression strain ductility experienced just before unloading from the compression envelope, or a previously experienced actual tension strain ductility, whichever is greater.

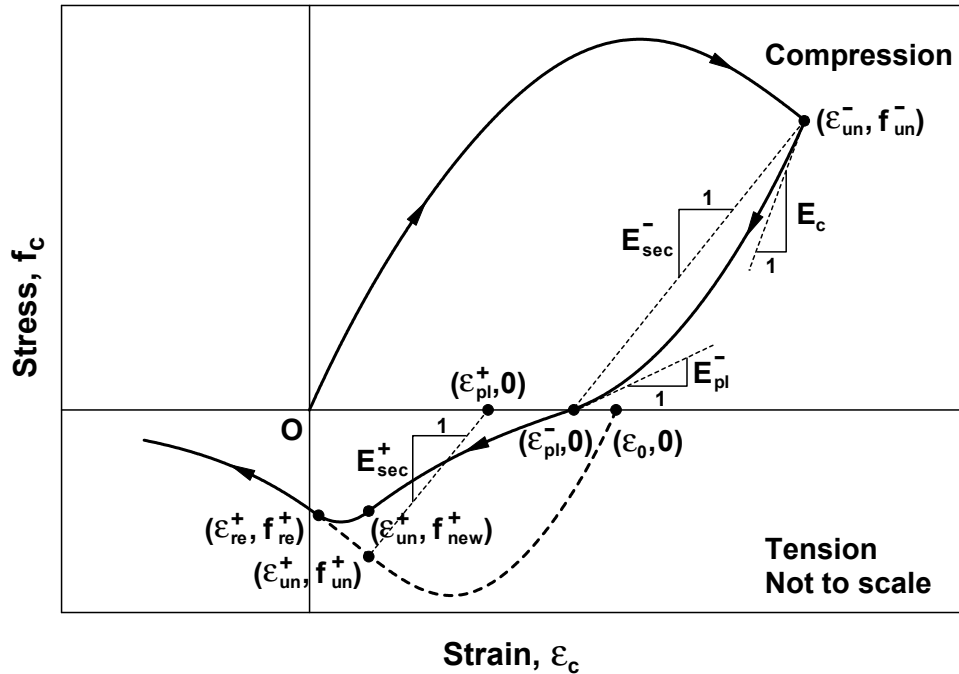


Fig. 4.14 Unloading from compression envelope curve (Chang and Mander, 1994)

In terms of modeling generalized hysteretic behavior, the constitutive model uses smooth “connecting” curves for unloading and reloading between the compression and tension envelope curves, and smooth “transition” curves for partial unloading and reloading between the connecting curves (Fig. 4.15). The connecting and transition curves are geometrically defined such that they commence at the prescribed starting point (e.g., $\epsilon_{un}^-, f_{un}^-$ in Fig. 4.13) with a prescribed initial slope (e.g., E_c), and end up at a prescribed final (target) point (e.g., $\epsilon_{pl}^-, 0$) with a prescribed final slope (e.g., E_{pl}^-). Both connecting and transition curves have slope continuity with uniform sign of curvature (second strain derivative of the curve equation) in between the starting and final points.

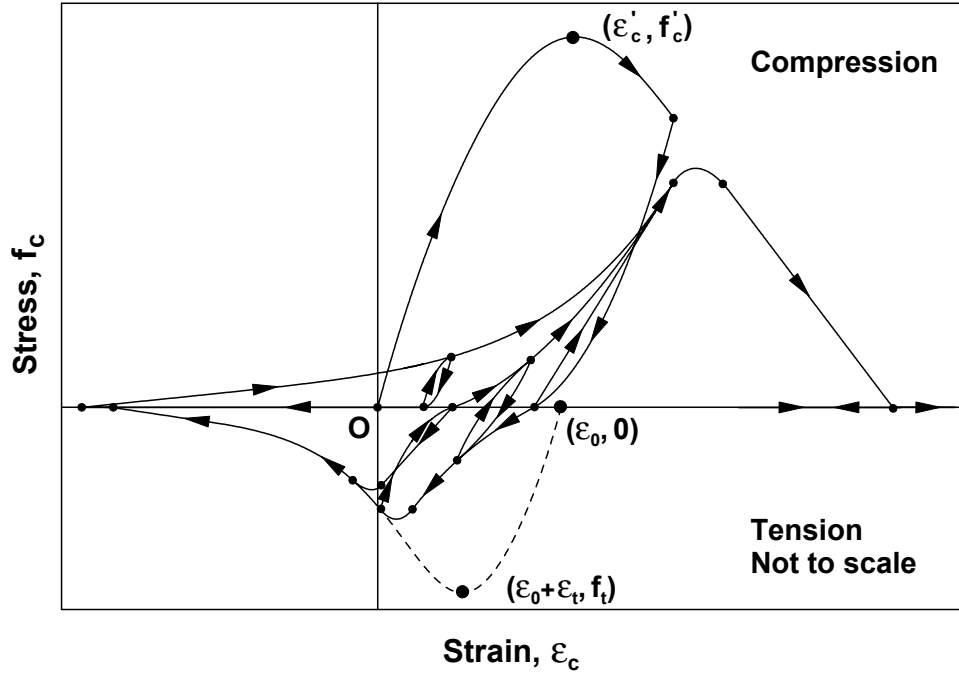


Fig. 4.15 Continuous hysteresis in compression and tension (Chang and Mander, 1994)

Chang and Mander (1994) proposed empirical expressions for determining the position of the target points for the transition curves. As shown in Figure 4.16, which illustrates the transition between two connecting curves before cracking, a reversal from the connecting curve at point A(ϵ_a, f_a) will target point B(ϵ_b, f_b) through a transition curve, and an incomplete loading on the same transition curve (i.e., unloading prior to the passing of point B) will target the point A(ϵ_a, f_a) again through a transition curve in the opposite direction. The relation between points A and B is computed through the relation:

$$\frac{\epsilon_a - \epsilon_{pl}^-}{\epsilon_{un}^+ - \epsilon_{pl}^-} = \frac{\epsilon_{un}^- - \epsilon_b}{\epsilon_{un}^- - \epsilon_{pl}^+} \quad (4.106)$$

After cracking, the tension envelope is zero, and the connecting curve upon unloading (i.e., strain reversal) represents gap closure (Fig. 4.17). A reversal from the gap closure – connecting curve at point A (ϵ_a, f_a) targets the horizontal axis at a strain ϵ_b through a transition curve. The target strain ϵ_b is calculated by the expression:

$$\epsilon_b = \epsilon_a - \frac{f_a}{E_{sec}^-} \quad (4.107)$$

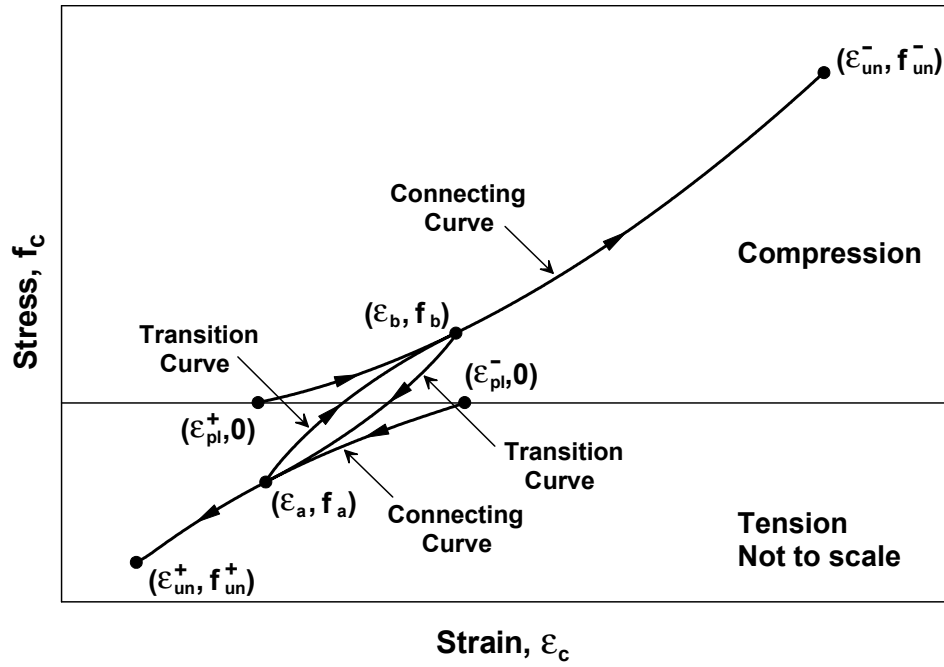


Fig. 4.16 Transition curves before cracking (Chang and Mander, 1994)

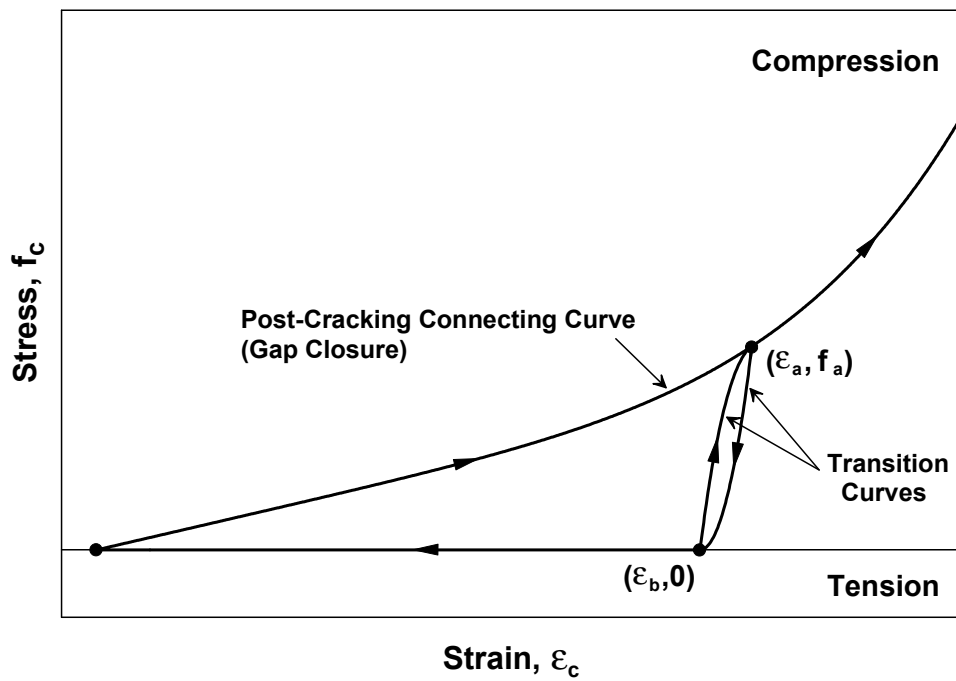


Fig. 4.17 Transition curves after cracking (Chang and Mander, 1994)

Reversal from the transition curve will target the point A again (Fig. 4.17). The initial slope of each transition curve (in Figs. 4.16–4.17) is equal to the concrete initial Young's modulus (E_c), whereas the final slope is equal to the slope of the connecting curve at the target (final) point of the transition curve.

The generalized equation used in the constitutive model to represent the connecting and transition curves takes the form:

$$f_c = f_I + (\varepsilon_c - \varepsilon_I) \left[E_I + A |\varepsilon_c - \varepsilon_I|^R \right] \quad (4.108)$$

$$E_t = \frac{\partial f_c}{\partial \varepsilon_c} = E_I + A(R+1) |\varepsilon_c - \varepsilon_I|^{R-1} \quad (4.109)$$

in which,

$$R = \frac{E_F - E_{SEC}}{E_{SEC} - E_I} \quad (4.110)$$

$$A = \frac{E_{SEC} - E_I}{|\varepsilon_F - \varepsilon_I|^R} \quad (4.111)$$

with,

$$E_{SEC} = \frac{f_F - f_I}{\varepsilon_F - \varepsilon_I} \quad (4.112)$$

where f_c is the concrete stress, ε_c is the concrete strain, E_t is the concrete tangent modulus, f_I is the stress at initial point, f_F is the stress at final (target) point, ε_I is the strain at initial point, ε_F is the strain at final point, E_I is the tangent modulus at initial point, E_F is the tangent modulus at final point, E_{SEC} is the secant modulus between the initial and final points, and R and A are equation parameters. The equations represent a stress-strain relation with single sign of curvature and slope continuity between the initial and target points.

It has been observed in this study that the hysteretic rules of the Chang and Mander model occasionally yield some minor numerical inconsistencies. For some strain histories, using connecting and transition curves with no change in the sign of the curvature is geometrically incompatible for commencing at a starting point with a prescribed initial slope and ending at a target point with a prescribed ending slope. For example, the stress-strain history shown in Figure 4.18 would require the connecting or transition curve that commences at the starting point (e.g., $\varepsilon_{un}^+, f_{un}^+$), with the initial slope (e.g., E_{new}^+); to have changes in the sign of curvature in order

to reach the target point (e.g., $\varepsilon_{re}^+, f_{re}^+$), with the ending slope (E_{re}^+). Similar conditions persist upon unloading from the tension envelope. For such cases, where curves with uniform sign of curvature are geometrically insufficient, a straight line with a secant slope was adopted here to represent the connecting or transition curve between the starting and target points (Fig. 4.18).

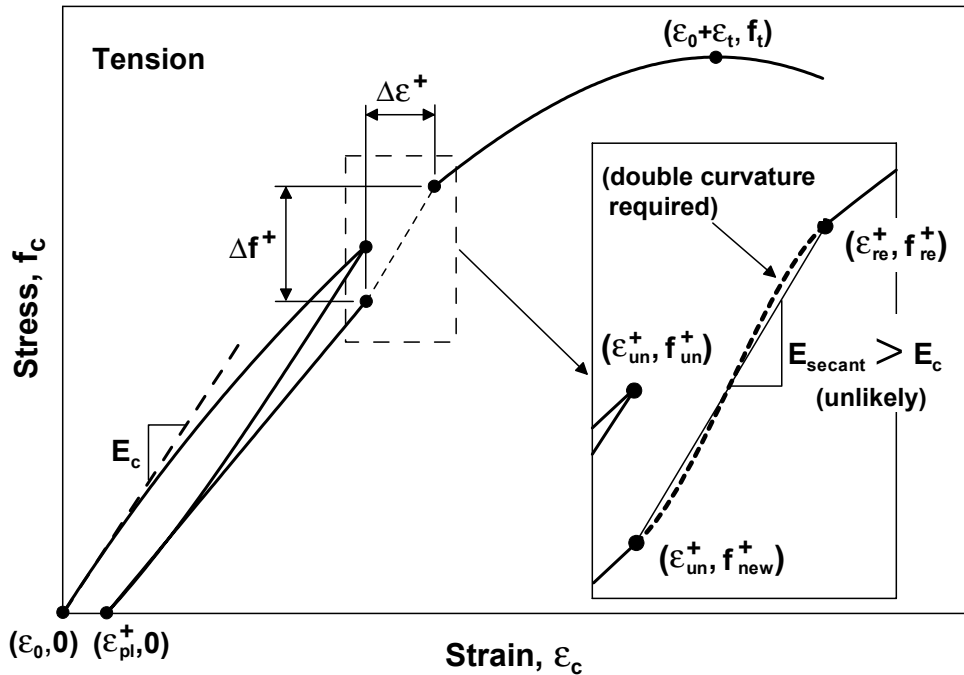


Fig. 4.18 Numerical instabilities in hysteretic rules

Another inconsistency in the model is associated with the value of this secant slope. For the same example strain history (Fig. 4.18), and for a range of values for unloading tensile strain (roughly for $\varepsilon_{un}^+ < \varepsilon_0 + 0.5\varepsilon_t$), using the stress and strain offsets (Δf^+ and $\Delta \varepsilon^+$) of Mander and Chang can result in a value of the secant modulus which is larger than the initial Young's modulus (E_c). This is physically unlikely and may also lead to convergence problems in the nonlinear solution algorithm. Under such exceptional conditions, for simplicity, the stress and strain offsets in tension (Δf^+ and $\Delta \varepsilon^+$) were eliminated from the model in this study. It is believed that the numerical inconsistencies in the model are primarily associated with the hysteretic parameters defined for cyclic tension (Eqs. 4.88–4.91). The accuracy of the model parameters for cyclic tension was validated with relatively limited experimental data from Yankelevsky and Reinhardt (1987). Chang and Mander remarked that better

calibration/validation of the model may be possible as more experimental data become available for cyclic tension. The minor adjustments implemented here do not induce a significant deviation from stress-strain relations generated by the original model but were necessary in order to implement the model into a nonlinear solution algorithm and ensure its stability and consistency under various arbitrary strain histories. Apart from these minor numerical inconsistencies, the model successfully generates continuous hysteretic stress-strain relations with slope continuity for confined and unconfined concrete in both compression and tension (Fig. 4.15).

Overall, the model by Chang and Mander (1994) is the current state-of-the-art uniaxial constitutive relation for modeling the cyclic stress-strain behavior of concrete. It simulates gradual crack opening and closure under cyclic loading and incorporates a refined and well-established definition of the hysteretic properties. The model is in the form of a generalized stress-strain relation, which can further be advanced by re-assessment of model parameters, or upon availability of further experimental results (e.g., for cyclic tension). It allows control of the parameters associated with the monotonic envelopes as well as the hysteretic parameters for a refined calibration of the stress-strain relation based on particular experimental results, or for conducting sensitivity studies on model parameters. The model was verified for cyclic compression using an extensive test database (Sinha et al., 1964; Karsan and Jirsa, 1969; Okamoto et al., 1976; Tanigawa and Uchida, 1979; Mander et al., 1984) and was shown to accurately simulate test results for both confined and unconfined concrete. Further details of the model can be found in the referenced report (Chang and Mander, 1994).

4.3 MODELING OF TENSION STIFFENING

The contribution of cracked concrete to the tensile resistance of RC members is known as the effect of tension stiffening. The concrete between the cracks, which is still bonded to the reinforcing steel bars, contributes to the tensile resistance of the member. The tension-stiffening phenomenon plays a significant role in reducing the post-cracking deformations of reinforced concrete structures, and has been proven by researchers (e.g., Vecchio and Collins, 1988; Collins and Mitchell, 1991; Belarbi and Hsu, 1994; Pang and Hsu, 1995; Hsu and Zhang, 1996; Mansour et al., 2001; Hsu and Zhu, 2002) to considerably influence the post-cracking stiffness, yield capacity, and shear behavior of reinforced concrete members.

Upon development of the original MVLEM by Vulcano et al. (1988), tension stiffening was modeled using an axial-element-in-series model (AESM) (Fig. 4.19) to describe the response of the uniaxial sub-elements of the model. The two elements in series represented the segment along the uniaxial elements in which the bond remained active (element 1) and the segment for which the bond stresses were negligible (element 2). The concrete within element 1 was considered to be uncracked and modeled with a linear elastic behavior. The cracked concrete within element 2 was considered to have no contribution (zero stresses) to the axial stiffness of the AESM under increasing tensile strains. A dimensionless parameter λ was introduced to define the relative length of the two elements (representing cracked and uncracked concrete) to account for tension stiffening. Under monotonic tensile loading, the tension-stiffening effect was incorporated by manipulating the value of the dimensionless parameter λ such that the tensile stiffness of the uniaxial model in Figure 4.19 would be equal to the actual (experimentally observed) tensile stiffness of a tension stiffened uniaxial element evaluated on the basis of an empirical law suggested by proposed by Rizkalla and Hwang (1984).

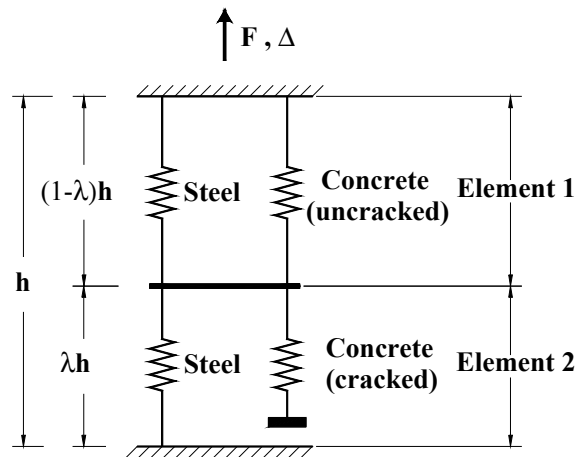


Fig. 4.19 Axial-element-in-series model

The law suggested by Rizkalla and Hwang (1984) relates the ratio of the steel strain within cracks to the average strain of a reinforced concrete member under monotonic axial tensile loading. Under cyclic loading, it was assumed that the value of λ was kept constant during unloading from the tensile stress state, equal to the value corresponding to the maximum

tensile strain previously attained; if this maximum strain was exceeded during a tensile reloading, the value of λ was updated as for the case of monotonic tensile loading.

In this study, instead of the AESM, a two-parallel-component model (Colotti, 1993) (Fig. 4.20) is adopted for the uniaxial elements of the present wall model, and concrete and steel within each uniaxial element are subjected to the same average (smeared) strains. The tension-stiffening effects are directly incorporated into the constitutive stress-strain relations implemented for concrete and steel, as described in the following paragraphs.

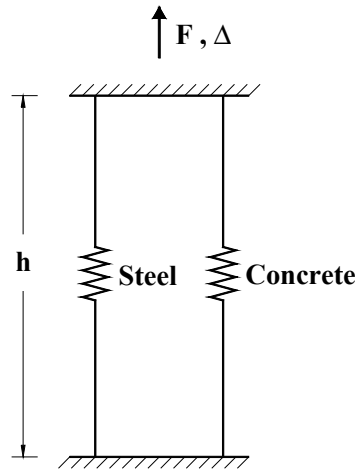


Fig. 4.20 Two-parallel-component-model

As investigated in detail by Belarbi and Hsu (1994), modeling of the tension-stiffening phenomenon must consider two effects simultaneously. First, an average (smeared) tensile stress-strain curve must be considered for cracked concrete; and second, the stress-strain curve of bare mild steel bars must be replaced by an average (smeared) stress-strain curve for steel bars stiffened by concrete between cracks. Accordingly, based on extensive tests of reinforced concrete panels subjected to normal stresses, Belarbi and Hsu (1994) developed two constitutive models: one for the average tensile stress-strain relation of concrete and one for the average tensile stress-strain relation of steel reinforcing bars stiffened by concrete. The tension-stiffening models proposed by Belarbi and Hsu have also been used and validated experimentally in more recent studies to model the shear behavior of RC membrane elements (e.g., Pang and Hsu, 1995; Hsu and Zhang, 1996; Mansour, Lee, and Hsu, 2001; Hsu and Zhu, 2002).

The average stress-strain relation proposed by Belarbi and Hsu for concrete in tension takes the form (Fig. 4.21):

$$\text{If } \varepsilon_c \leq \varepsilon_{cr} \quad \text{then } \sigma_c = E_c \varepsilon_c \quad (4.113)$$

$$\text{If } \varepsilon_c > \varepsilon_{cr} \quad \text{then } \sigma_c = f_{cr} \left(\frac{\varepsilon_{cr}}{\varepsilon_c} \right)^{0.4} \quad (4.114)$$

where:

$$E_c = 3875 \sqrt{f'_c} (\text{MPa}) \quad (4.115)$$

$$f_{cr} = 0.31 \sqrt{f'_c} (\text{MPa}) \quad (4.116)$$

$$\varepsilon_{cr} = 0.00008 \quad (4.117)$$

In the equation above, ε_c is the average concrete tensile strain, σ_c is the average concrete tensile stress, E_c is the initial Young's modulus of the average stress-strain relation, f_{cr} is concrete the tensile cracking stress, and ε_{cr} is the concrete strain at cracking.

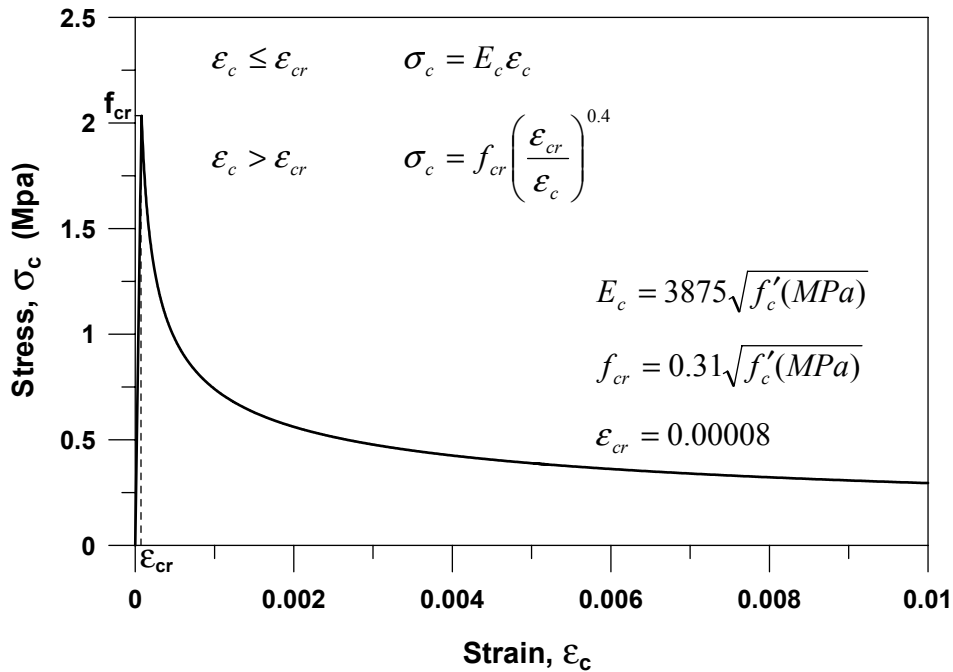


Fig. 4.21 Average stress-strain relation by Belarbi and Hsu for concrete in tension

The relation consists of an ascending straight line before cracking and a descending curve to the power of 0.4 after cracking (Fig. 4.21). The expressions for f_{cr} , ε_{cr} , E_c , and the power constant 0.4 in Equation (4.117) are obtained from the average and best fit of experimental

results from testing 17 RC panels with concrete cylinder compressive strengths ranging between 36.9 MPa and 47.7 MPa.

Belarbi and Hsu (1994) also identified how the average stress-strain relation of reinforcing steel bars surrounded by concrete is different than the stress-strain relation of bare steel bars (Fig. 4.22).

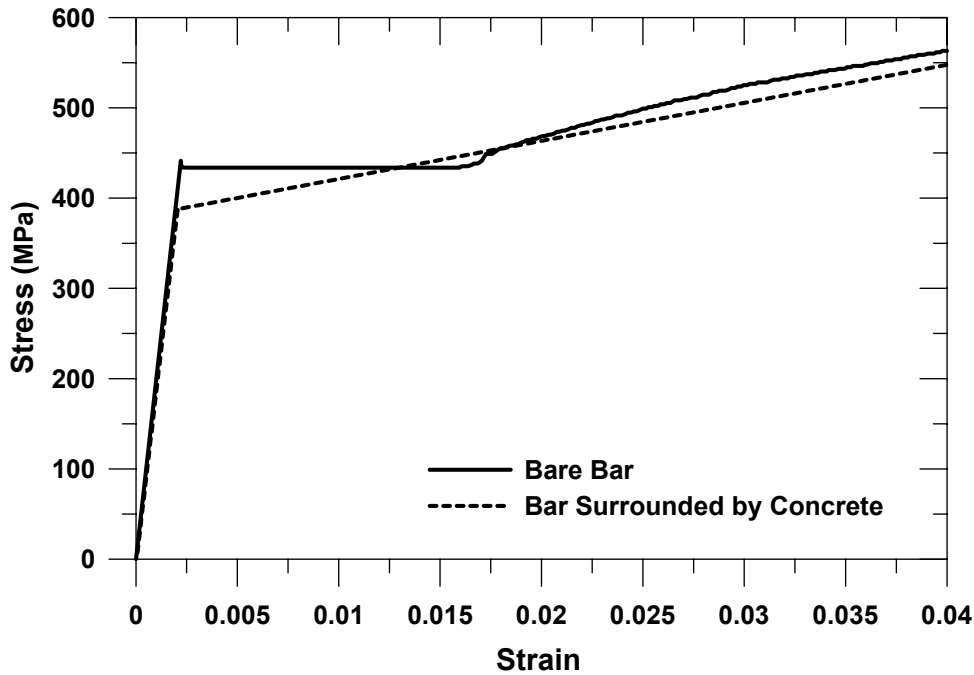


Fig. 4.22 Effect of tension stiffening on reinforcing bars

The most important difference was found to be the lowering of the yield stress, σ_y , as yielding of a reinforced concrete element occurs when the steel stress at the cracked section reaches the yield strength of the bare bar. At the same time, the average steel stress smeared along the length of the element reaches a level lower than that of the yield stress of the bare bar. Based on experimental data from the RC panels, the reduction of the yield stress of bars embedded in concrete were found to be empirically dependent on the cross-sectional area ratio of the longitudinal steel in the panel (ρ) and the ratio of concrete cracking stress (f_{cr}) to the steel yield stress (σ_y). The strain-hardening slope (plastic modulus) of the steel bars embedded in concrete was also observed to differ from the plastic modulus of bare bars with the variation also dependent on the above parameters.

Based on evaluation and characterization of experimental data from the RC panels, Belarbi and Hsu (1994) proposed a simple bilinear constitutive model for steel bars embedded in concrete (Fig. 4.23). The stress-strain relation is represented by two straight lines, the first straight line with a slope E_s (steel modulus of elasticity) covering the elastic range of strains, and the second straight line with a slope E_p^* representing the plastic range.

The stress at the intersection of the two lines (σ_n^*) and the plastic slope (E_p^*) are given by the following expressions:

$$\sigma_n^* = (0.93 - 2B)\sigma_y \quad (4.118)$$

$$E_p^* = (0.02 + 0.25B)E_s \quad (4.119)$$

where the parameter B is defined as:

$$B = \frac{1}{\rho} \left(\frac{f_{cr}}{\sigma_y} \right)^{1.5} \quad (4.120)$$

In the equations above, σ_y and E_s are the yield stress and modulus of elasticity of the bare steel bars, (ρ) is the cross-sectional area ratio of the longitudinal steel bars in the RC element (limited to a minimum of 0.25% in Mansour, Lee and Hsu, 2001), and (f_{cr}) is the concrete cracking stress, obtained according to the relation in Equation 4.116. Equation 4.119 was derived assuming that the plastic modulus of “bare” steel bars (E_p) is approximately equal to 2.5% of the modulus of elasticity ($E_p = 0.025E_s$). For a more general case, Equation 4.119 can be expanded as:

$$E_p^* = (0.8b + 0.25B)E_s \quad (4.121)$$

where b is the strain-hardening ratio (E_p/E_s) defined for the bare steel bars.

Accordingly, the bilinear model of Belarbi and Hsu (1994) for modeling the average (smeared) stress-strain behavior of steel reinforcing bars embedded in concrete takes the form (Fig. 4.23):

$$\text{If } \varepsilon_s \leq \varepsilon_n, \sigma_s = E_s \varepsilon_s \quad (4.122)$$

$$\text{If } \varepsilon_s > \varepsilon_n, \sigma_s = (0.93 - 2B)\sigma_y + (0.8b + 0.25B)E_s (\varepsilon_s - \varepsilon_n) \quad (4.123)$$

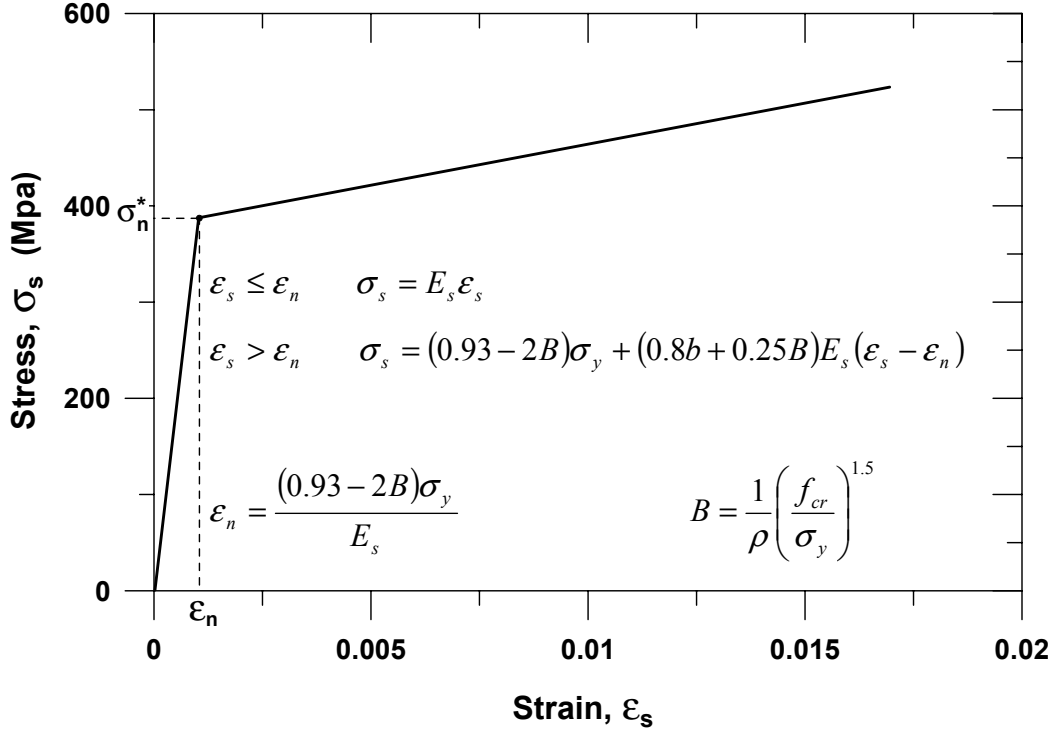


Fig. 4.23 Average stress-strain relation by Belarbi and Hsu (1994) for reinforcing bars embedded in concrete

where σ_s is the average stress, ε_s is the average strain, ε_n is the average strain defined at the intersection of the two lines:

$$\varepsilon_n = \frac{\sigma_n^*}{E_s} = \frac{(0.93 - 2B)\sigma_y}{E_s} \quad (4.124)$$

and E_s , σ_y , and b are the modulus of elasticity, yield stress, and strain-hardening ratio experimentally measured for bare steel bars.

The constitutive relations implemented in the present wall model for concrete and steel can be controlled and calibrated to follow accurately the relations developed by Belarbi and Hsu (1994) (or similar average stress-strain relations) to model tension stiffening for monotonic loading. For example, Figure 4.24 shows a comparison of a representative tension envelope curve (or monotonic tensile stress-strain curve) generated by the Chang and Mander model (1994) with the average stress-strain relation proposed by Belarbi and Hsu (1994) for concrete.

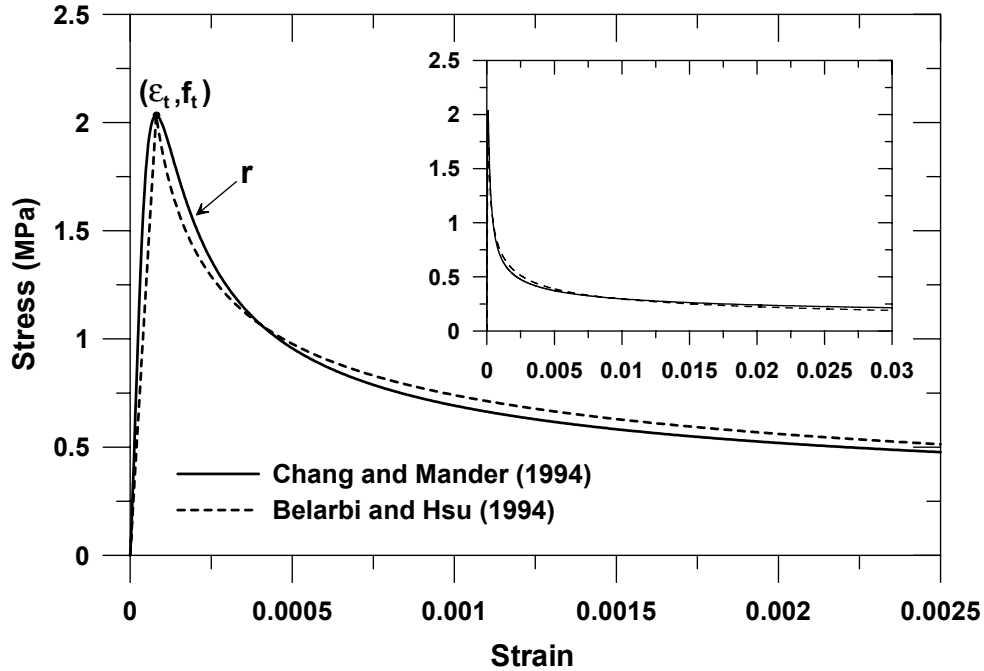


Fig. 4.24 Stress-strain relations for concrete in tension

The shape of the tension envelope curve in Chang and Mander’s model is conveniently controlled through the shape parameter r (in addition to the initial Young’s modulus E_c , the peak tensile stress f_t , and the strain at peak tensile stress ϵ_t) (Figs. 4.11 and 4.13). The primary difference in the two tension envelopes is that the envelope generated using the Chang and Mander model also accounts for the nonlinearity of the stress-strain relation prior to cracking (as observed experimentally by Yankelevsky and Reinhardt, 1987). Similarly, the tensile elastic and yield asymptotes in the steel stress-strain model by Menegotto and Pinto (1973) (which constitute the monotonic tensile stress-strain relation) can be calibrated through the parameters σ_y (yield stress) and b (strain-hardening ratio) to precisely follow the bilinear stress-strain relation of Belarbi and Hsu for steel bars embedded in concrete (Fig. 4.25).

To model the tension-stiffening effects under cyclic loading, the calibrated monotonic stress-strain relations will be used in this study as the tension envelope curve for concrete and the tensile elastic and yield asymptotes for steel, together with the unloading and reloading rules of the hysteretic constitutive models described in the previous sections. On the whole, the approach adopted here to model tension stiffening is a more refined and up-to-date methodology compared to the one that involves the use of the axial-element-in-series model (AESM) as implemented by

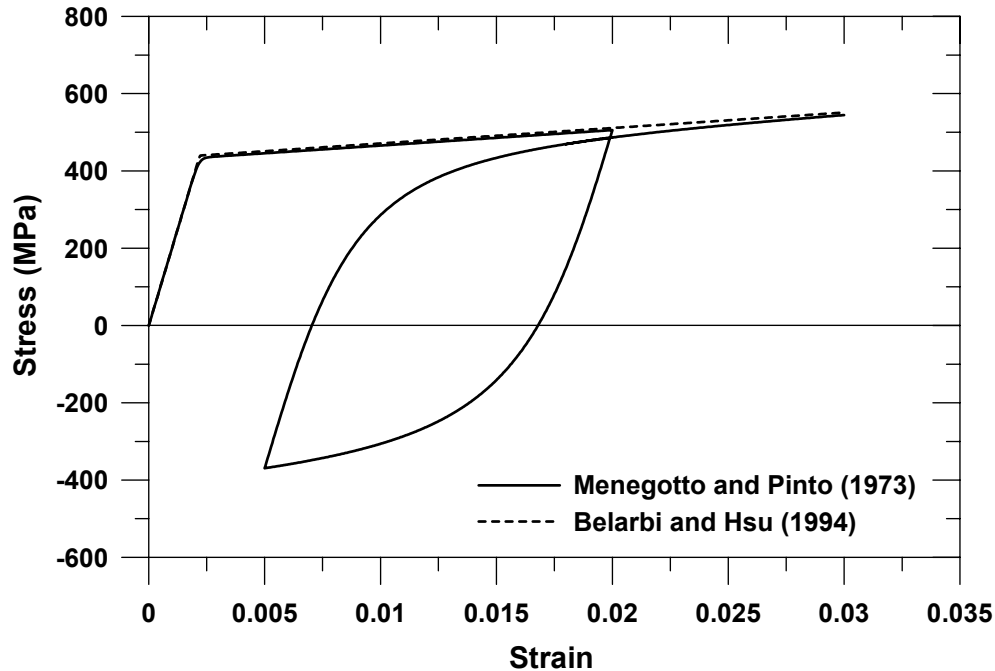


Fig. 4.25 Stress-strain relations for reinforcing bars

Vulcano et al. (1988) in the original MVLEM. The tension-stiffening phenomenon is incorporated at the material level, considering the effects on both steel and concrete, based on a more robust and manageable theory as well as extensive experimental studies.

4.4 SUMMARY

Since the MVLEM adopted in this study relates the analytical response directly to uniaxial material behavior, extensive consideration was given to the selection and refinement of the robust and state-of-the-art constitutive relations implemented in the analytical model. For an accurate and reliable prediction of wall flexural response, it was necessary that the relations selected had been validated with extensive experimental data.

The reinforcing steel stress-strain behavior implemented in the wall model is the widely used nonlinear hysteretic model of Menegotto and Pinto (1973), as extended by Filippou et al. (1983) to include isotropic strain-hardening effects. This model was shown to be capable of reproducing experimental results with accuracy; the model results agree very well with experimental results from cyclic tests on reinforcing bars (e.g., Menegotto and Pinto, 1973; Filippou et al., 1983; Elmorsi et al., 1998).

Two different constitutive models for concrete (Yassin, 1994; Chang and Mander, 1994) were adopted in the present wall model. Both models address important issues such as the hysteretic behavior in continuous cyclic compression and tension, the progressive degradation of stiffness of the unloading and reloading curves for increasing values of strain, and the effects of confinement and tension stiffening. However, the Chang and Mander model (1994), being the current state-of-the-art uniaxial constitutive relation for modeling the cyclic stress-strain behavior of concrete, is clearly superior to the hysteretic model by Yassin (1994). The Chang and Mander model is a generalized constitutive model that allows control of the parameters associated with the monotonic envelopes, as well as the hysteretic parameters, for a refined calibration of the stress-strain relation based on particular experimental results. For example, Figure 4.26 compares the results of the Chang and Mander model and the model by Yassin, with results of axial compressive stress-strain tests performed on standard cylinder specimens of concrete used in the construction of a reinforced concrete structural wall specimen (Thomsen and Wallace, 1995). By calibration of its parameters (parameters associated with the initial tangent modulus, the peak stress, the strain at peak stress and the shape of the stress-strain curve), the model by Chang and Mander can simulate the test results accurately; whereas the model by Yassin (with the only parameters for calibration being the peak stress and the strain at peak stress) fails to provide an accurate representation.

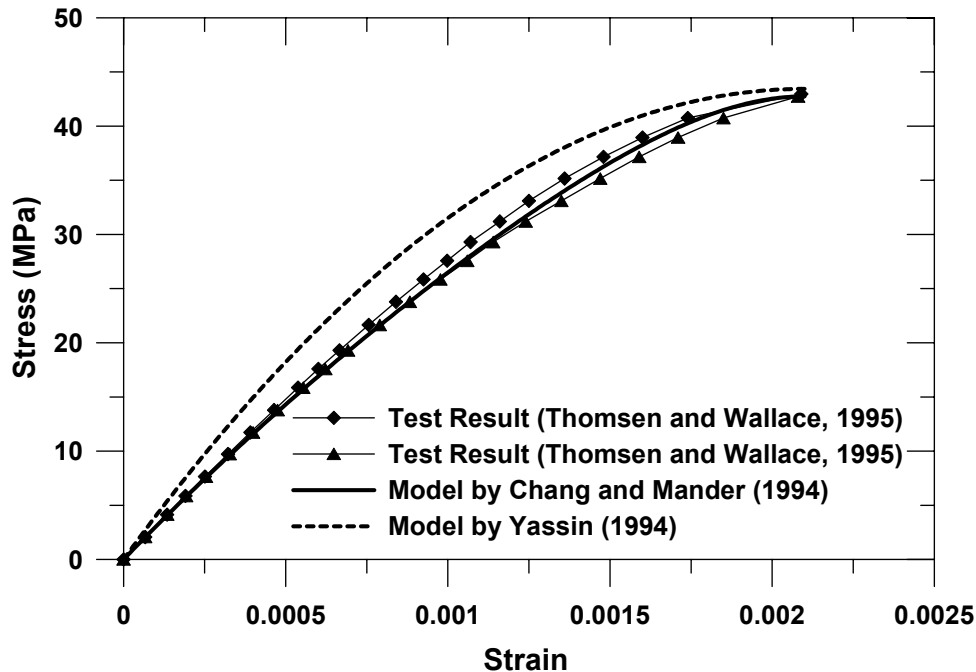


Fig. 4.26 Compression envelopes for concrete — model vs. test results

Similarly, Figure 4.27 shows a comparison of the results of the Chang and Mander model and the model by Yassin, with the relation developed by Belarbi and Hsu (1994) based on experimental data, for the average tensile stress-strain behavior of concrete experiencing tension stiffening. Again, the model by Yassin fails to represent the observed behavior accurately. Furthermore, the Chang and Mander model successfully simulates the gradual closure of cracks (Figs. 4.15, 4.17) under cyclic loading due to progressive contact stresses within the cracks. On the other hand, the model by Yassin assumes sudden crack closure (Fig. 4.8), which may significantly impair the accuracy in predicting the pinching properties of the RC wall modeled. Due to these limitations, the model by Yassin was very seldom used in this study. It was implemented in the wall model as a simple and widely used (e.g., OpenSees) alternative, and was included in this chapter to signify the refinements of the model by Chang and Mander.

Finally, the modeling of the tension-stiffening phenomenon, as described in the previous section, was performed at the material level, with effects on both concrete and steel considered, based on a comprehensive theory and extensive experimental validation (Belarbi and Hsu, 1994).

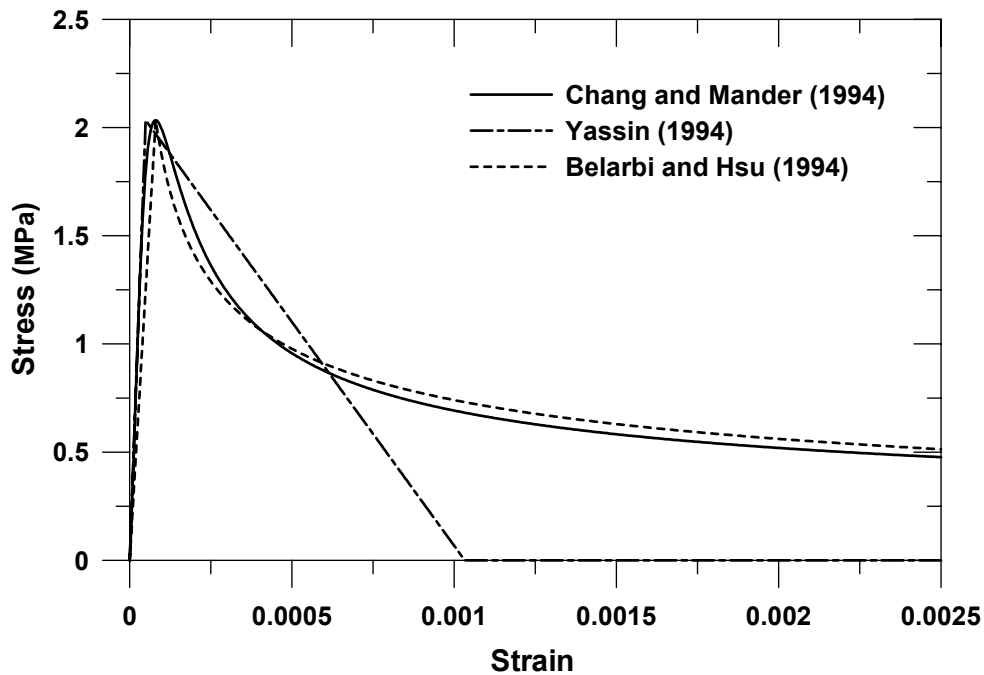


Fig. 4.27 Tension envelopes for concrete — model comparisons

The constitutive material models described in this chapter, and the formulation of the MVLEM elements described in Chapter 3, were implemented in Matlab (MathWorks, 2001), together with a direct stiffness assembly procedure to assemble the MVLEM elements into a complete wall model and an incremental-iterative numerical scheme to perform nonlinear quasi-static (monotonic or cyclic) analyses of the model. Details of the nonlinear analysis solution strategy adopted in this study are described in the following chapter.

5 Nonlinear Analysis Strategy

The macro-wall-model elements formulated in Chapter 3 and the material constitutive relations described in Chapter 4 were implemented in Matlab (MathWorks, 2001) together with a direct stiffness assembly procedure to assemble the MVLEM elements into a complete wall model (Fig. 5.1) and an incremental-iterative solution strategy to perform nonlinear quasi-static (monotonic or cyclic) analysis of the wall model. The nonlinear analysis solution strategy adapted is described in this chapter.

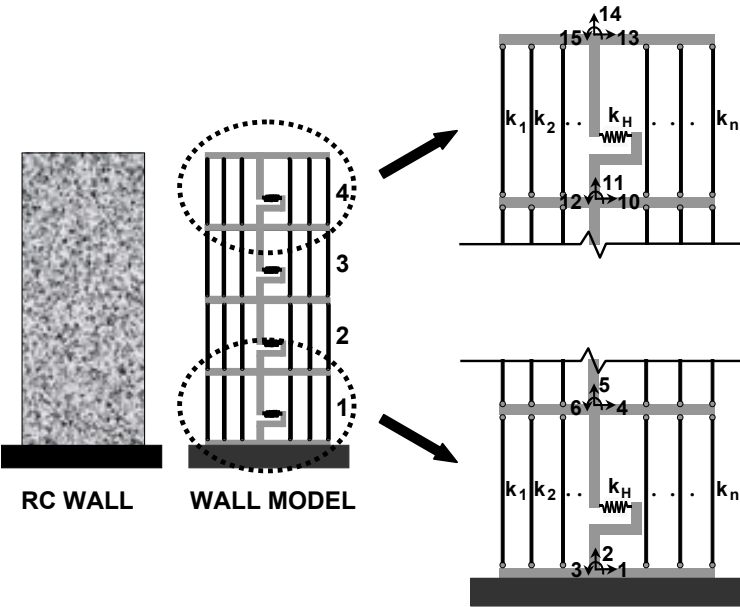


Fig. 5.1 Sample model assembly with degrees of freedom

Various incremental-iterative numerical schemes can be implemented for the nonlinear analysis of the wall model depending on the type of loading. For example, the conventional force-controlled Newton-Raphson solution scheme can be adopted for nonlinear dynamic analysis of the wall model. In this study in order to conduct a nonlinear quasi-static analysis of the wall model, a displacement-controlled iterative solution strategy, based on a specified

incrementation of a selected displacement component (at a selected degree of freedom), was adapted. In this strategy, iterations are performed on both displacement and load components to obtain static equilibrium within a specified tolerance, while keeping constant the value of the selected displacement component. This solution strategy was implemented in order to better correlate the model response with drift-controlled cyclic test results on RC wall specimens which are typically subjected to prescribed lateral displacement histories at the top of the wall (e.g., Thomsen and Wallace, 1995). Numerical solution strategies to conduct nonlinear analyses using the model are described in the following sections.

5.1 NONLINEAR QUASI-STATIC PROBLEM

Quasi-static response is generated when the externally applied cyclic loads or displacements are applied with a sufficiently slow loading rate that they do not induce dynamic effects. A nonlinear analysis strategy that is capable of reproducing the entire nonlinear quasi-static response of the multi-degree-of-freedom model, including load and displacement limits points within the static load path of the model, is desired.

The nonlinear equilibrium equation associated with the quasi-static response can be expressed as:

$$\{F_{\text{int}}(\delta)\} = \{F_{\text{ext}}\} \quad (5.1)$$

where $\{F_{\text{int}}(\delta)\}$ is the internal resisting force vector, being a nonlinear functional of system (nodal-degree-of-freedom) displacements, and $\{F_{\text{ext}}\}$ is the external force vector, representing the externally applied forces at the nodal degrees of freedom. It should be noted that in the case of a linear elastic system, the static problem would reduce to the linear equation:

$$[K]\{\delta\} = \{F_{\text{ext}}\} \quad (5.2)$$

where $[K]$ denotes the stiffness matrix and $\{\delta\}$ is the vector of nodal displacements. Equation (5.1) is a nonlinear algebraic equation in $\{\delta\}$ due to the nonlinear relation between the resisting force vector $\{F_{\text{int}}\}$ and the vector of nodal displacements $\{\delta\}$.

5.2 INCREMENTAL ITERATIVE APPROACH — NEWTON-RAPHSON SCHEME

An iterative-incremental nonlinear analysis strategy is required to solve the nonlinear algebraic equation for the quasi-static problem. The nonlinear equation can be linearized by the conventional Newton-Raphson method, which forms a basis for various iterative strategies, and solved for the vector of nodal displacements $\{\delta\}$, by iterating within a load step until convergence is achieved. Figure 5.2 illustrates a schematic of the Newton-Raphson solution algorithm, with the incremental equation of equilibrium expressed as:

$$\{\Delta F_{\text{int}}(\Delta\delta)\} = \{\Delta F_{\text{ext}}\} \quad (5.3)$$

where $\{\Delta F_{\text{int}}(\Delta\delta)\}$ is the incremental restoring force vector being a nonlinear functional of the incremental nodal-displacement vector $(\Delta\delta)$, and $\{\Delta F_{\text{ext}}\}$ is the incremental external load vector.

Equation (5.3) is linearized within an arbitrary load step i about $\{\delta\} = \{\delta\}_i$, yielding the equation for the first iteration of the load step:

$$[K]_i^1 \{\Delta\delta\}_i^1 = \{\Delta F_{\text{ext}}\}_i \quad (5.4)$$

where $[K]_i^1$ denotes the tangent stiffness matrix of the system at the beginning of the load step obtained by differentiating the nonlinear internal resisting force functional:

$$[K]_i^1 = \left. \frac{d(F_{\text{int}})}{d(\delta)} \right|_{\delta=\delta_i} \quad (5.5)$$

The linearized incremental equilibrium equation for the j 'th iteration of the Newton-Raphson scheme within the load step i can be written as:

$$[K]_i^j \{\Delta\delta\}_i^j = \{\Delta R\}_i^j \quad (5.6)$$

where

$$\{\Delta R\}_i^j = \{\Delta R\}_i^{j-1} - \{\Delta F_{\text{int}}\}_i^{j-1} \quad (5.7)$$

The term $\{\Delta R\}_i^j$ represents the vector of residual forces (Fig. 5.2) and the term $\{\Delta F_{\text{int}}\}_i^{j-1}$ is the increment of internal resisting forces for the iteration being equal to the difference between the two internal resisting force vectors: $\{F_{\text{int}}\}_i^{j-1} - \{F_{\text{int}}\}_i^{j-2}$ (Fig. 5.3).

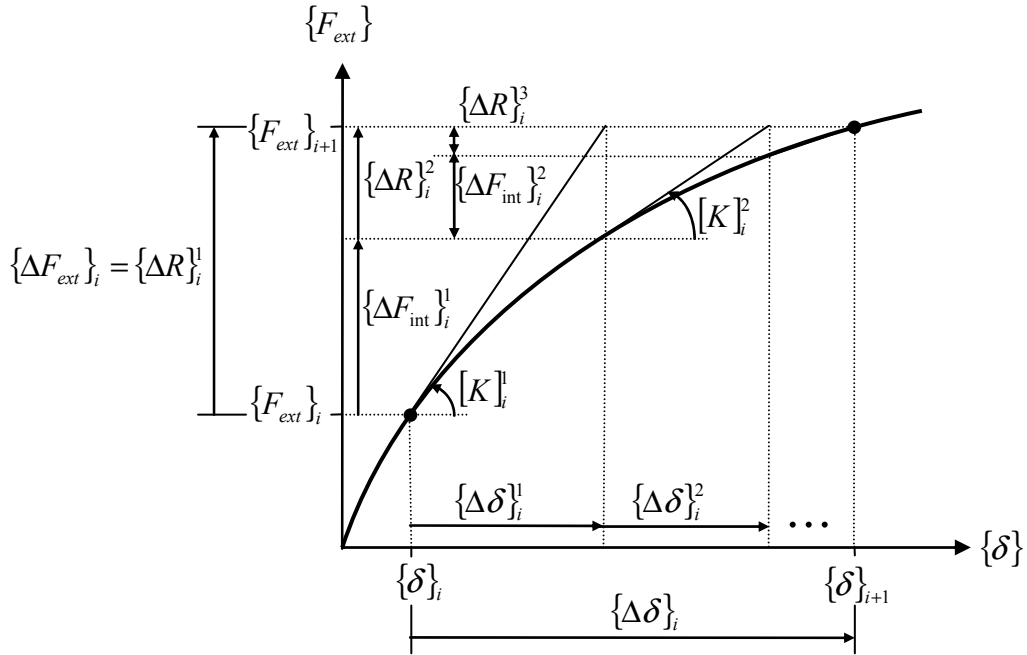


Fig. 5.2 Newton-Raphson iteration scheme

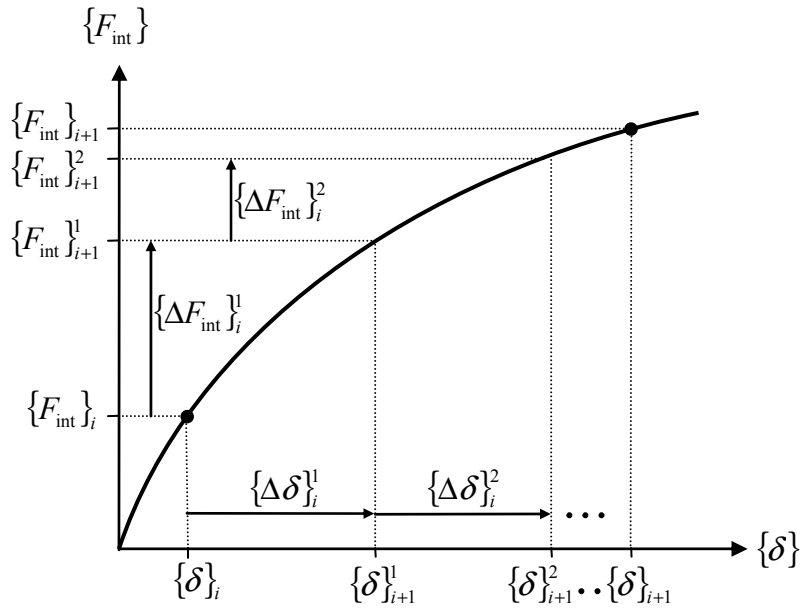


Fig. 5.3 Nodal-displacement and internal resisting-force increments

Solving for $\{\Delta\delta\}_i^j$ within successive iterations, convergence is achieved by minimizing the vector of residual forces to a specified value of tolerance. The resulting incremental nodal-displacement vector for the i th load step can be computed as the sum:

$$\{\Delta\delta\}_i = \{\Delta\delta\}_i^1 + \{\Delta\delta\}_i^2 + \dots + \{\Delta\delta\}_i^l \quad (5.8)$$

where l is the number of iterations performed in order to achieve convergence. The strategy follows the same scheme in subsequent load steps.

Although the well-known Newton-Raphson strategy successfully linearizes the equilibrium equation to obtain an iterative solution, it is incapable of passing load limit points (Fig. 5.4) within the quasi-static load-displacement path of the system because the load level is held constant while iterations are conducted to achieve convergence. It is included here to provide a solid basis for a more complex iterative strategy described in following subsection.

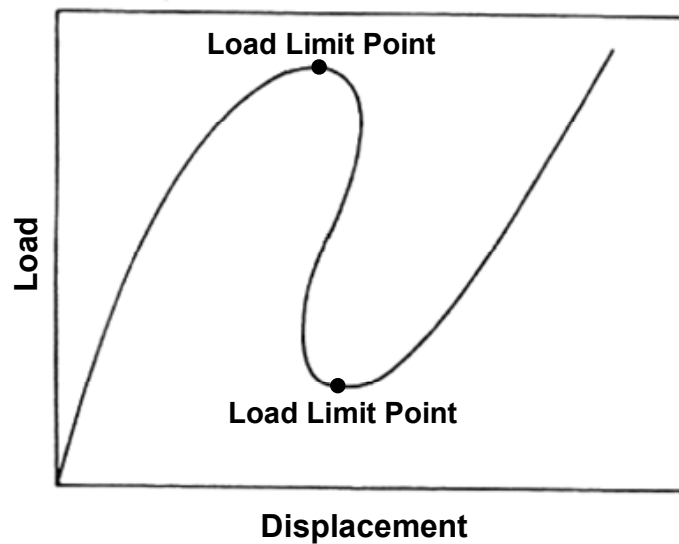


Fig. 5.4 Load limit points within sample quasi-static load-displacement path

For incremental nonlinear analysis approaches, passing load limit points is extremely difficult due to the near singular nature of the tangent stiffness matrix in the neighborhood of a load limit point. Iterations should be performed on externally applied loads as well as nodal displacements by introducing constraint equations within the solution strategy to proceed beyond a load limit point. Several different techniques have been proposed for this purpose, the most well known being “iteration at constant arc-length” introduced by Wempner (1971) and updated by Ricks (1979). The iterative solution technique that has been used in this study is an adaptation of the arc-length method, with a displacement-controlled iterative strategy, based on incrementation of selected displacement components of the model (see also Clarke and Hancock, 1990). Details of the iterative strategy are presented in following sections. The strategy was selected in order to correlate the model responses with results for drift-controlled cyclic test

results on RC wall specimens (described in Chapter 7). The selected displacement component to be incremented throughout the nonlinear analysis is thus along the horizontal degree of freedom at the top of the wall model.

5.3 APPLIED NONLINEAR ANALYSIS SOLUTION STRATEGY

An incremental-iterative displacement-controlled solution technique was implemented for nonlinear analysis using a MVLEM for RC walls. The hysteretic constitutive material relations were used to determine global nonlinear hysteretic structural response based on satisfying both equilibrium conditions and force-deformation relations at each load step. The solution method described is based on a modified Newton-Raphson approach, that is, the tangent stiffness matrix is computed at the beginning of each load step and held constant for each load step. An iterative strategy, based on constant displacements with incrementation of selected displacement components was used for the purpose of passing load limit points and to allow comparison with experimental results.

The incremental-iterative solution strategy described here is ideally suited for obtaining the complete static load–deflection response of a structural model. In the incremental-iterative method, each load step consists of the application of an increment of external load with subsequent iterations required to satisfy the total equilibrium equations within a specified tolerance. In this text, the notation adopted is to use the subscript i to denote load step number i , and the superscript j to denote the iteration cycle j (within load step i). Iteration cycles begin at $j = 1$, which is defined to correspond to an increment of external load. The equilibrium iterations commence at $j = 2$. The scalar λ denotes a load parameter to be used in combination with a reference external load vector (assuming external loading to be proportional), and $\{\delta\}$ is the vector of nodal displacements at the model degrees of freedom. There are two distinct strategies required for the successful completion of a single load step in an incremental-iterative scheme:

1. Selection of a suitable external load increment $\Delta\lambda_i^1$ for the first iteration cycle. The selected increment is referred to as the “initial load increment,” and the particular strategy used to determine it is referred to as the “load incrementation strategy.”
2. Selection of an appropriate “iterative strategy” for use in subsequent iterative cycles ($j \geq 2$) where the aim is to restore equilibrium as rapidly as possible. If iterations are

performed on the load parameter $\Delta\lambda_i^j$ as well as on the nodal displacements $\{\delta\}_i^j$, then an additional constraint equation involving $\Delta\lambda_i^j$ is required. It is the form of this constraint equation that distinguishes the various iteration strategies.

A description of the incremental-iterative technique for a single load step i is described in the following subsections. It is assumed that perfect convergence has been achieved at the conclusion of load step $(i-1)$ so that the solution $(\lambda_{i-1}, \{\delta\}_{i-1})$ is known to satisfy total equilibrium (Fig. 5.5).

5.3.1 First Iteration Cycle, $j = 1$

The new load step starts with the computation of the tangent stiffness matrix $[K_t]_i$ based on the known displacements (strains) and loads (stresses) at the conclusion of the previous load step. The “tangent” displacements $\{\delta_t\}_i$ for this load step are then computed as the solution of:

$$[K_t]_i \{\delta_t\}_i = \{F_t\}_i \quad (5.9)$$

in which $\{F_t\}_i$ is the reference external load vector, typically as specified in the input data for the problem. The magnitude of the tangent displacements is arbitrary, only their direction is important. Next, the value of the initial load increment $\Delta\lambda_i^1$ is determined according to a particular load incrementation strategy, referred to as the “incrementation of a selected displacement component” in this study. The incremental displacements are then evaluated by scaling the tangent displacements:

$$\{\Delta\delta\}_i^1 = \Delta\lambda_i^1 \{\delta_t\}_i \quad (5.10)$$

The total displacements and load level are updated from those existing at the conclusion of the previous load step (Fig. 5.5) as:

$$\{\delta\}_i^1 = \{\delta\}_{i-1} + \{\Delta\delta\}_i^1 \quad (5.11)$$

$$\lambda_i^1 = \lambda_{i-1} + \Delta\lambda_i^1 \quad (5.12)$$

At this stage the solution does not satisfy total equilibrium within the specified tolerance, so additional iterative cycles are required to restore equilibrium.

5.3.2 Equilibrium Iteration Cycles, $j \geq 2$

The well-known Newton-Raphson or modified Newton-Raphson iterative strategies are incapable of passing limit points because the load level is held constant while iterating to obtain convergence; therefore, the load parameter $\Delta\lambda_i^j$ must be allowed to vary if limit points are to be overcome. With a varying load parameter, a general solution technique evolves if it is assumed that for any iteration $j \geq 2$ within load step i , the change in the incremental displacements can be expressed as:

$$[K_I]_i \{\Delta\delta\}_i^j = \Delta\lambda_i^j \{F_I\}_i - \{\psi\}_i^{j-1} \quad (5.13)$$

where,

$$\{\psi\}_i^{j-1} = \{F_{int}\}_i^{j-1} - \{F_{ext}\}_i^{j-1} \quad (5.14)$$

Equation (5.14) represents the net internal out-of-balance (or “residual”) force acting on the structure at the conclusion of the previous iteration. The vector $\{F_{int}\}_i^{j-1}$ represents the internal nodal forces obtained at equilibrium from element contributions (forces in the uniaxial elements and horizontal springs in the present model). For proportional loading, the external forces $\{F_{ext}\}_i^{j-1}$ at the conclusion of the previous iteration may be expressed as:

$$\{F_{ext}\}_i^{j-1} = \lambda_i^{j-1} \{F_I\}_i \quad (5.15)$$

The right-hand side of the equation (5.13) is linear in $\Delta\lambda_i^j$; thus the final solution can be written as the linear combination of two vectors:

$$\{\Delta\delta\}_i^j = \Delta\lambda_i^j \{\delta_I\}_i + \{\Delta\delta_R\}_i^j \quad (5.16)$$

in which $\{\delta_I\}_i$ are the tangent displacements, already computed for $j=1$, and $\{\Delta\delta_R\}_i^j$ are the “residual” displacements (Fig. 5.6) obtained from Equation (5.17):

$$[K_I]_i \{\Delta\delta_R\}_i^j = -\{\psi\}_i^{j-1} \quad (5.17)$$

The variation of the load parameter $\Delta\lambda_i^j$ is obtained by solving an appropriate constraint equation, as described in the following subsection. The incremental change to the nodal displacements for this iteration is computed using Equation (5.16), and the total displacements and load level are updated from the previous iteration (Fig. 5.5) as:

$$\{\delta\}_i^j = \{\delta\}_i^{j-1} + \{\Delta\delta\}_i^j \quad (5.18)$$

$$\lambda_i^j = \lambda_i^{j-1} + \Delta\lambda_i^j \quad (5.19)$$

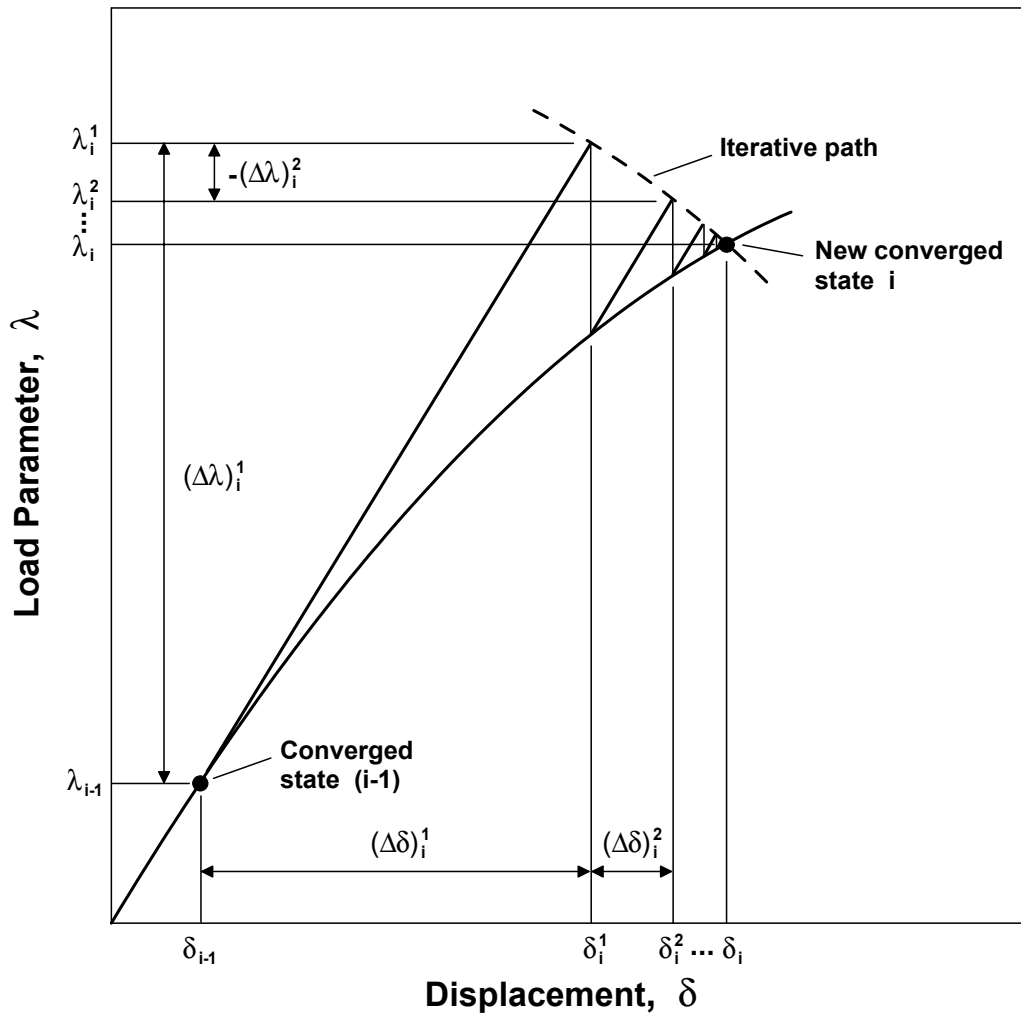


Fig. 5.5 Representation of adapted nonlinear analysis solution scheme for single-degree-of-freedom system

Iteration cycles are continued until a convergence criterion based on either the structure forces or displacements is satisfied. If convergence is not achieved within a specified number of cycles, or if divergence of the solution is detected, a re-solution strategy may be adopted. The convergence criterion and the re-solution scheme used in this study are described in a subsequent section.

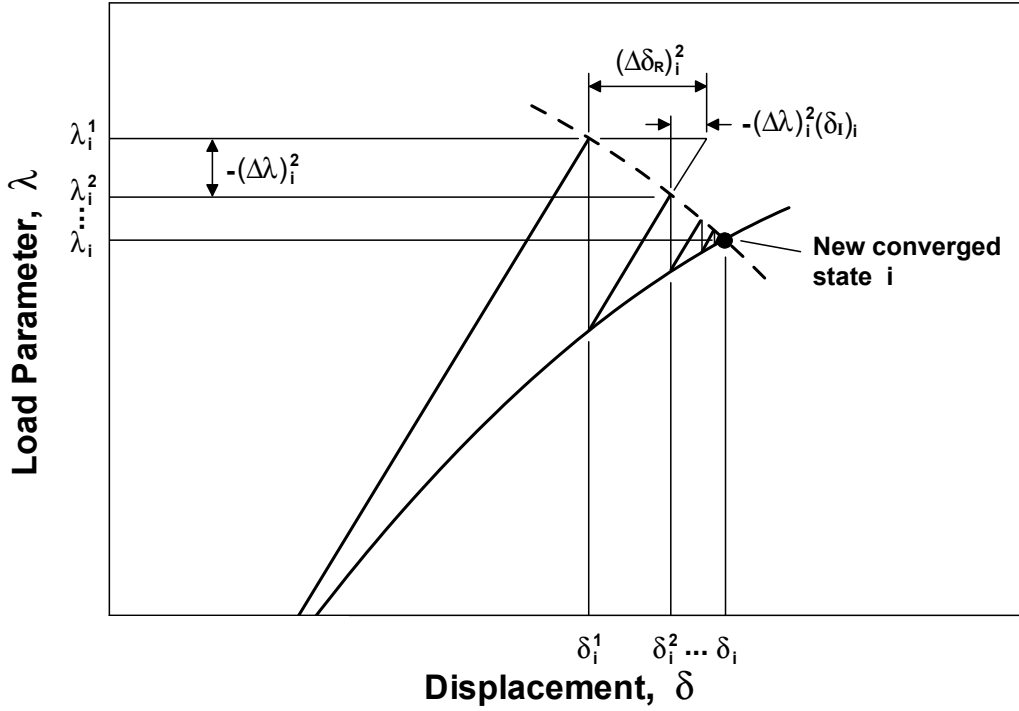


Fig. 5.6 Iterative strategy and residual displacements

5.3.3 Incrementation Strategy: Incrementation of Selected Displacement Component

The analysis results are to be calibrated and compared with lateral drift-controlled cyclic tests performed on RC wall specimens as described in Chapter 7. In order to simulate the test conditions, an incrementation strategy based on a selected displacement component is adopted in the nonlinear analysis strategy. The initial load increment of each load step is chosen to limit a specified “key” displacement δ_n (being the lateral top displacement of the wall in this study) in the structure. If it is assumed that perfect convergence is achieved at the conclusion of the previous load step, the displacement increment $(\Delta\delta_n)_i$ can be expressed as:

$$(\Delta\delta_n)_i = \Delta\lambda_i^1 \{b_n\}^T \{\delta_I\}_i \quad (5.20)$$

in which $\{b_n\}$ is a vector containing unity in the n th row and zero elsewhere. Hence,

$$\Delta\lambda_i^1 = \frac{(\Delta\delta_n)_i}{\{b_n\}^T \{\delta_I\}_i} \quad (5.21)$$

5.3.4 Iterative Strategy: Iteration at Constant Displacement

The constant displacement iteration strategy described here is an example of a more general technique presented by Powell and Simons (1981). It was adopted in this study in order to perform a displacement-controlled analysis that successfully proceeds beyond load limit points, defined as the points of load reduction within the static load path of a structure, where softening behavior is initiated (Fig. 5.4).

In the first iteration ($j = 1$), the key displacement component in the structure (δ_n in this case) is incremented by a prescribed amount as described in the preceding subsection. This displacement component is held constant during subsequent iterations ($j \geq 2$). Denoting the key displacement component as δ_n , the n th component in the vector of nodal degrees of freedom, the increment in δ_n can be expressed as:

$$\Delta\delta_n = \{b_n\}^T \{\Delta\delta_R\}_i^j \quad (5.22)$$

in which $\{b_n\}$ is a vector of zero entries except for unity in the n th row. From equation (5.16),

$$\Delta\delta_n = \Delta\lambda_i^j \{b_n\}^T \{\delta_I\}_i + \{b_n\}^T \{\Delta\delta_R\}_i^j \quad (5.23)$$

If the value of δ_n is to remain unchanged during the equilibrium equations (constant displacement) then $\Delta\delta_n = 0$, giving the iterative change in the load parameter:

$$\Delta\lambda_i^j = \frac{-\{b_n\}^T \{\Delta\delta_R\}_i^j}{\{b_n\}^T \{\delta_I\}_i} \quad (5.24)$$

5.3.5 Convergence Criteria and Re-Solution Strategy

Within the analysis, iteration cycles are continued until a convergence criterion based on structure displacements is satisfied at the end of each load step. If convergence is not achieved within a specified number of cycles, a re-solution strategy for that load step is selected in this study.

A convergence criterion based on the incremental displacements is used. The stringent maximum norm is adopted in the present study to test for convergence, that is:

$$\text{Maximum norm: } \|\mathcal{E}\|_{\infty} = \max_k \left| \frac{\Delta\delta_k}{\delta_k} \right| \quad (5.25)$$

where $\Delta\delta_k$ is the change in the displacement component k during the current iteration cycle and δ_k is the value of that displacement component updated at the end of the previous iteration. Convergence is attained when:

$$\|\mathcal{E}\|_{\infty} < \zeta_c \quad (5.26)$$

where the tolerance ζ_c is typically in the range of 10^{-2} to 10^{-5} depending on the desired accuracy.

In the solution technique described above, a re-resolution strategy was incorporated. A re-resolution is necessary if convergence is not attained at each load step within the maximum specified number of iterative cycles or if the solution appears to be diverging. An increase of stiffness within a single load step is the most frequently encountered reason for nonconvergence for the MVLEM. The re-resolution is facilitated by recovering the previous converged load step at displacement level $\{\delta\}_{i-1}$, and starting the current load step over using the initial stiffness matrix of the first load step (undeformed configuration). If convergence is still not attained within the number of specified iterations, the value of the prescribed displacement increment $\Delta\delta_n$ is changed (usually decreased), and the current step is repeated until an increment that satisfies convergence and complies with the applied displacement history, is found.

5.4 SUMMARY

The incremental-iterative solution strategy implemented in this study is ideal for obtaining the complete quasi-static load-deflection response of the analytical wall model. Iterations are performed on both displacement and load components to obtain static equilibrium within a specified tolerance, while keeping the value of a selected displacement component (e.g., lateral displacement at the top of the wall) constant. Calibration of the analytical model and comparison of model results with results of lateral drift-controlled cyclic tests performed on RC wall specimens is presented in Chapter 7. The following chapter (Chapter 6) describes attributes of the analytical model response and sensitivity of model results to model and material parameters.

6 Flexural Modeling — Analytical Model Results and Parametric Sensitivity Studies

The macro wall model formulated in Chapter 3 and the material constitutive relations described in Chapter 4 were implemented in Matlab (MathWorks, 2001) together with the incremental-iterative solution strategy described in Chapter 5 to perform nonlinear quasi-static analyses of the analytical wall model. Attributes of the analytical model response and sensitivity of the model results to both model and material parameters are presented in this chapter.

6.1 REVIEW OF ANALYTICAL MODEL

The multiple-vertical-line-element model (MVLEM), as implemented in this study, is an effective and robust modeling and analysis tool for predicting the inelastic response of RC walls and wall systems. The model incorporates important material characteristics and behavioral response features such as neutral axis migration, tension-stiffening, progressive gap closure, concrete confinement, nonlinear shear behavior, and the effect of fluctuating axial force on strength and stiffness. A detailed description of the model and implemented constitutive relations were presented in Chapters 3 and 4, respectively. A brief review of the model attributes and material constitutive features is provided in the following paragraphs.

A structural wall is modeled as a stack of m MVLEM elements, which are placed one upon the other (Fig. 6.1). The flexural response is simulated by a series of uniaxial elements (or macro-fibers) connected to infinitely rigid beams at the top and bottom (e.g., floor) levels. The primary simplification of the model involves applying the plane-sections-remain-plane assumption in calculating the strain level in each uniaxial element according to values of displacement or rotation at the degrees of freedom of each wall element. The stiffness properties and force-displacement relations of the uniaxial elements are defined according to detailed constitutive stress-strain relations implemented in the model for concrete and steel and the

tributary area assigned to each uniaxial element (Fig. 6.2). The strains in concrete and steel are typically assumed to be equal (perfect bond) within each uniaxial element. The relative rotation between the top and bottom faces of the wall element occurs around the point placed on the central axis of the element at height ch . A suitable value of the parameter c is based on the expected curvature distribution along the element height h . A horizontal spring placed at the height ch , possibly with a nonlinear hysteretic force-deformation relation, simulates the shear response of the wall element. However, this study focuses on modeling of the flexural response, thus a linear elastic force-deformation behavior was adopted for the horizontal “shear” spring. For the present model, flexural and shear modes of deformation of the wall member are uncoupled (i.e., flexural deformations do not affect shear strength or deformation), and the horizontal shear displacement at the top of the element does not depend on c .

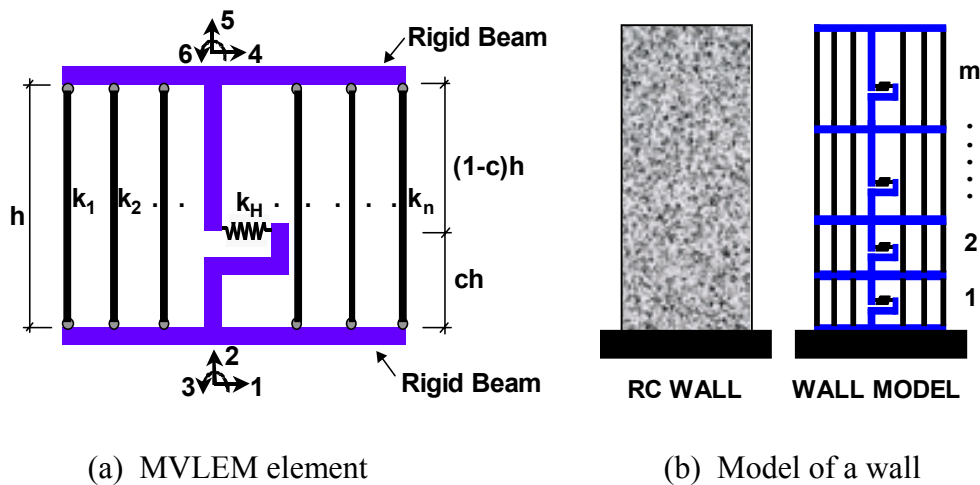


Fig. 6.1 Multiple-vertical-line-element model

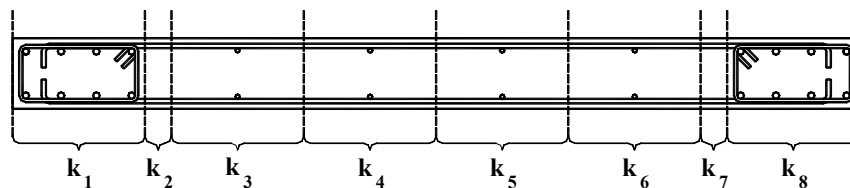


Fig. 6.2 Tributary area assignment

The reinforcing steel stress-strain behavior implemented in the wall model is the well-known nonlinear relation of Menegotto and Pinto (1973) (Fig. 6.3), as extended by Filippou et al. (1983) to include isotropic strain-hardening effects.

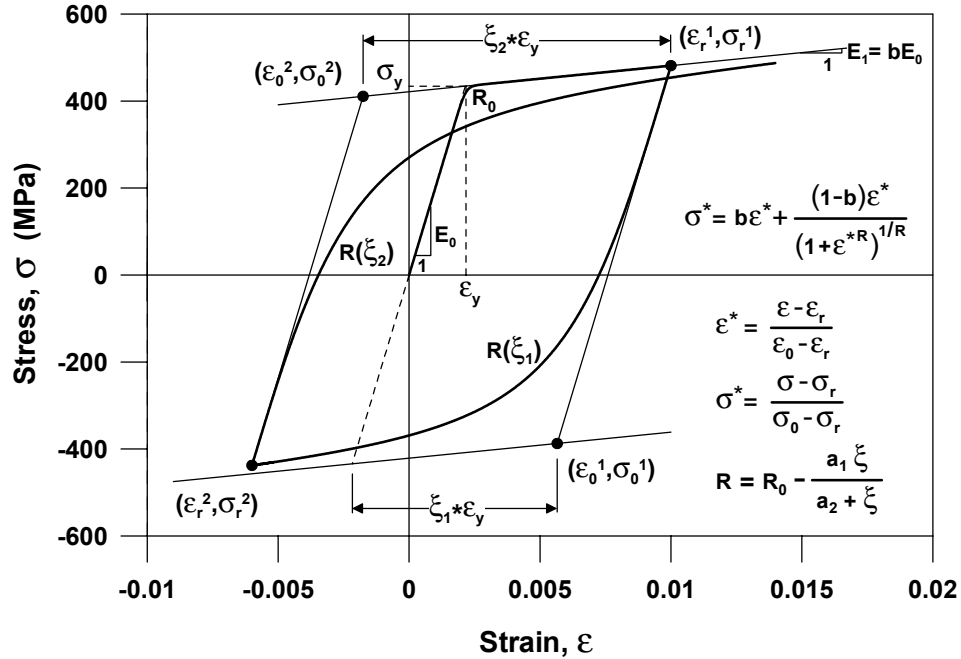


Fig. 6.3 Constitutive model parameters for reinforcing steel (Menegotto and Pinto, 1973)

Two different constitutive models for concrete (Yassin, 1994; Chang and Mander, 1994) were adopted in the wall model. Both models address important issues such as the hysteretic behavior in continuous cyclic compression and tension, the progressive degradation of stiffness of the unloading and reloading curves for increasing values of strain, and the effects of confinement and tension stiffening. However, the model by Chang and Mander (1994) is a more general and comprehensive model that allows control of the parameters associated with the monotonic envelopes, as well as the hysteretic parameters (Figs. 4.11, 4.13), for a refined definition of the stress-strain relation that can be calibrated with experimental results. Furthermore, the model by Chang and Mander successfully simulates the gradual closure of cracks due to progressive contact stresses (Fig. 6.4), whereas the model by Yassin assumes sudden crack closure (Fig. 6.5), which may impair significantly the accuracy in predicting the pinching properties of reinforced concrete elements. Due to these limitations, the model by Yassin was very seldom used in this study. It was implemented in the wall model as a simple and widely used (e.g., OpenSees) alternative, and is referred to in this chapter to highlight the refinements of the model by Chang and Mander. The constitutive material relations implemented in this study can be controlled and calibrated to follow the relations developed by Belarbi and

Hsu (1994) or similar empirical relations to model tension stiffening (tensile resistance of cracked concrete bonded to reinforcing bars between cracks).

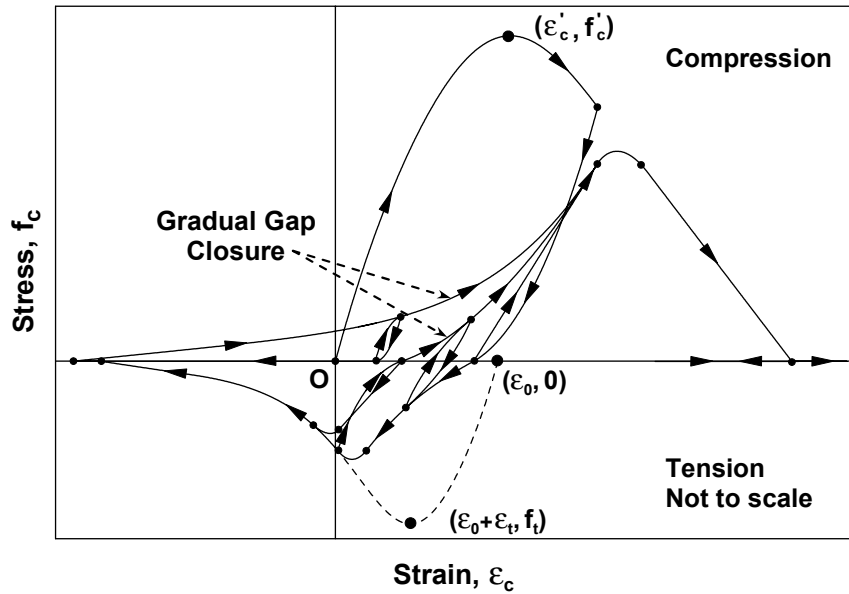


Fig. 6.4 Hysteretic constitutive model for concrete (Chang and Mander, 1994)

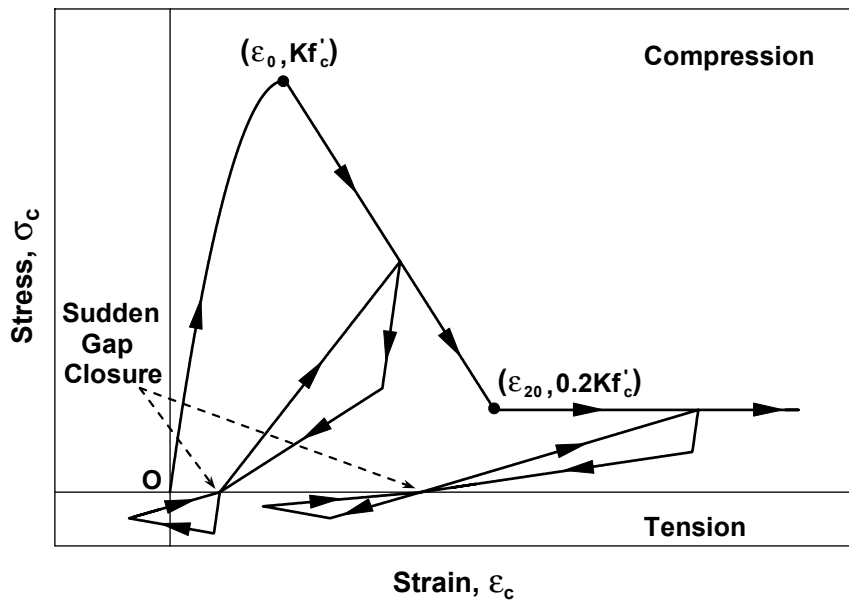


Fig. 6.5 Hysteretic constitutive model for concrete (Yassin, 1994)

6.2 ANALYTICAL MODEL RESPONSE

The macro wall model was implemented in Matlab (MathWorks, 2001) together with a direct stiffness assembly procedure to assemble the MVLEM elements into a complete wall model, and the incremental-iterative numerical scheme described in Chapter 5 to perform nonlinear quasi-static (monotonic or cyclic) analyses of wall models. As described in detail in Chapter 5, a displacement-controlled iterative solution strategy based on a specified incrementation of a selected displacement component was adopted. Iterations are performed on both displacement and load components to obtain static equilibrium within a specified tolerance, while keeping constant the value of the selected displacement component. This solution strategy was selected in order to better correlate the model response with drift-controlled cyclic test results on RC wall specimens (Thomsen and Wallace, 1995) subjected to prescribed lateral displacement histories at the tops of the walls.

The wall specimens tested by Thomsen and Wallace (1995) were used to assess and calibrate the analytical model. Design and reinforcement details for the wall specimens and the loading protocol, as well as details on model calibration and comparison of the analytical and experimental results are presented in detail in Chapter 7. This chapter focuses on characteristic attributes of the analytical model response, as well as the sensitivity of the model response to changes in model parameters and the parameters associated with constitutive material relations.

Figure 6.6 shows an illustrative lateral load – top displacement response prediction obtained using a wall model that incorporates the constitutive relations by Chang and Mander (1994) for concrete, and Menegotto and Pinto (1973) for reinforcing steel. The model response in the figure is for a rectangular wall specimen (specimen RW2 tested by Thomsen and Wallace, 1995) with height of 3.66 m, thickness of 102 mm, length of 1.22 m, and an applied axial load of approximately $0.07A_g f'_c$. The analytical results were obtained using a model configuration with 8 MVLEM elements along the height of the wall, 8 uniaxial elements (macro-fibers) along the length, and $c = 0.4$, and for an applied lateral displacement history at the top of the wall similar to the one used in the test program (i.e., cyclic drift levels of 0.1%, 0.25%, 0.5%, 0.75%, 1%, 1.5%, 2%, and 2.5%). The applied lateral displacement history for the model was corrected for the pedestal rotation of the wall specimen, as described in Chapter 7.

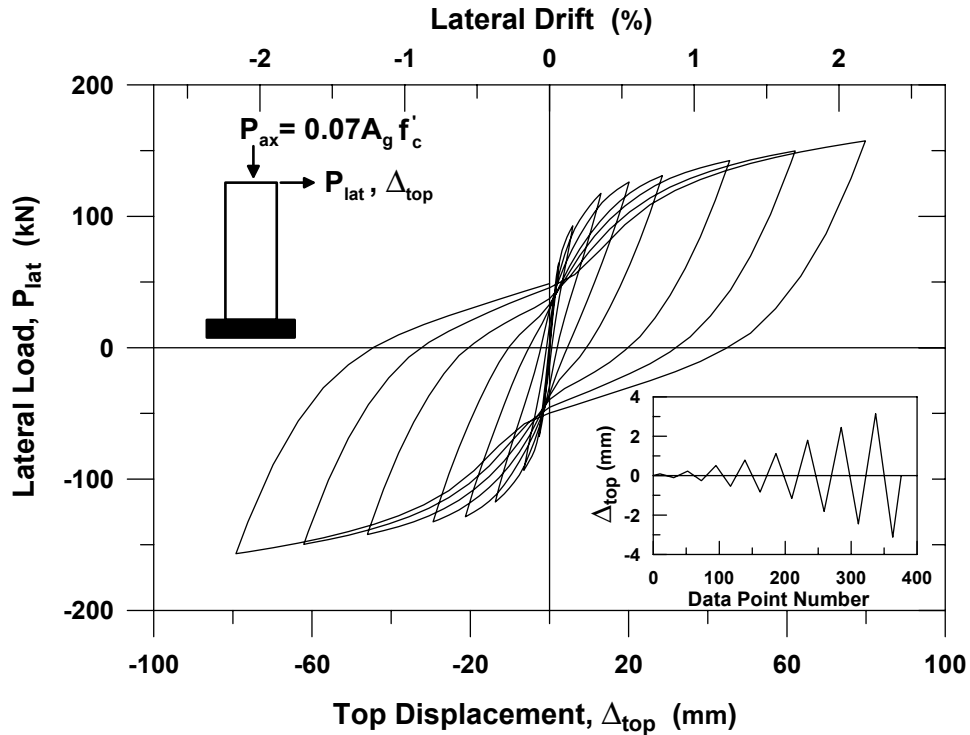


Fig. 6.6 Load-displacement response predicted by analytical model

The analysis results clearly reflect actual characteristics of cyclic wall response, including stiffness degradation, shape of the load-displacement hysteresis loops, plastic (residual) displacements at zero load, and pinching. The model successfully captures the variation of the neutral axis depth for a cyclic displacement history applied at the top of the wall, as shown in Figure 6.7, which displays the predicted position of the neutral axis in the MVLE at the base of the wall, normalized by the wall length. The distance from the centroid of the wall cross section to the neutral axis approaches infinity when the lateral displacement (and thus rotation) of the wall approaches zero, and reaches its local extrema or limit points (peaks and valleys) at peak displacement (displacement reversal) points.

Figure 6.8 compares the average longitudinal strain histories predicted at the extreme concrete fiber and at the centroid of the wall for the element at the base of the wall, demonstrating the effect of applied displacement history and neutral axis migration on the predicted strains. The longitudinal strains are not symmetric with respect to the zero strain axis; and the strains predicted at the center of the wall are tensile for almost the entire loading history, except for a range of small displacements (due to the presence of axial load).

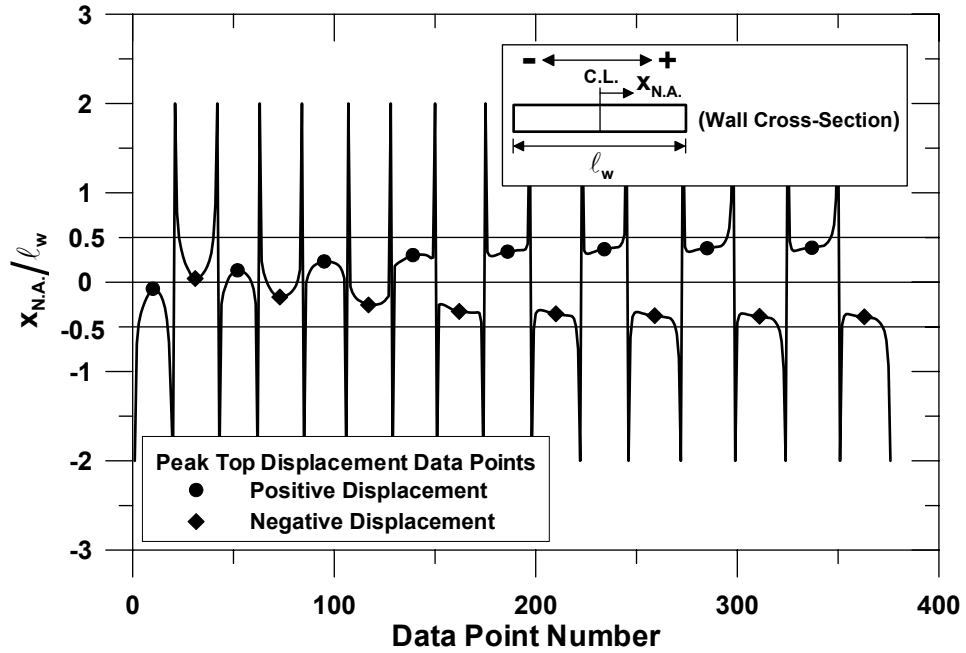


Fig. 6.7 Predicted variation in position of neutral axis

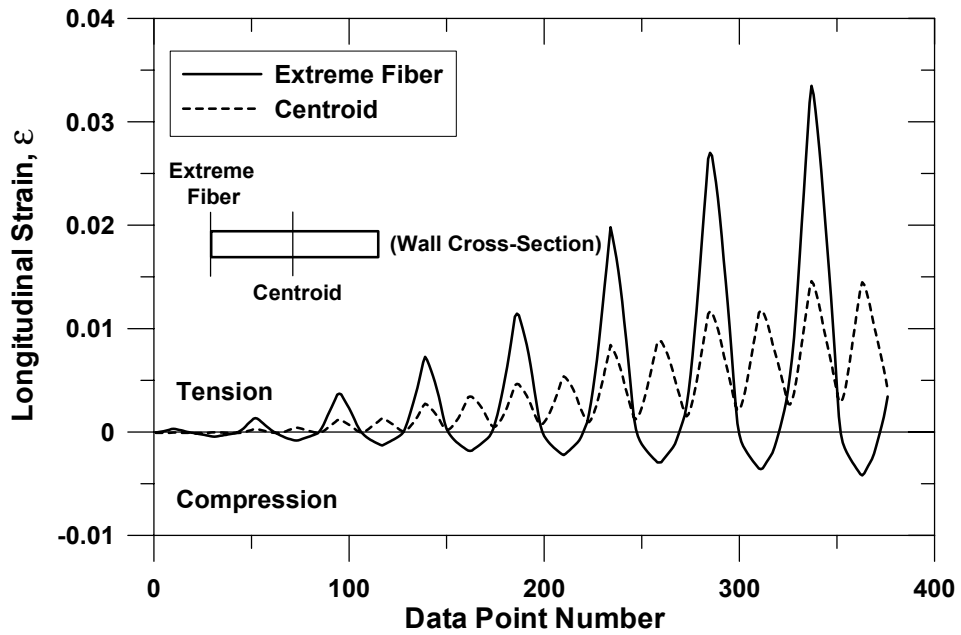


Fig. 6.8 Predicted longitudinal strain histories

The MVLEM directly considers the effect of varying axial load on the wall response, which although constant in this case, might vary in some cases (e.g., under dynamic loads such as earthquakes). Figure 6.9 shows a comparison of the analytically predicted lateral load versus

top displacement responses for an applied axial load of zero and $0.10A_g f'_c$, clearly displaying the significant impact of axial load on the wall response. Higher axial load results in larger lateral load capacity of the wall at all drift levels, and a more pronounced pinching behavior upon unloading to reloading in the opposite direction.

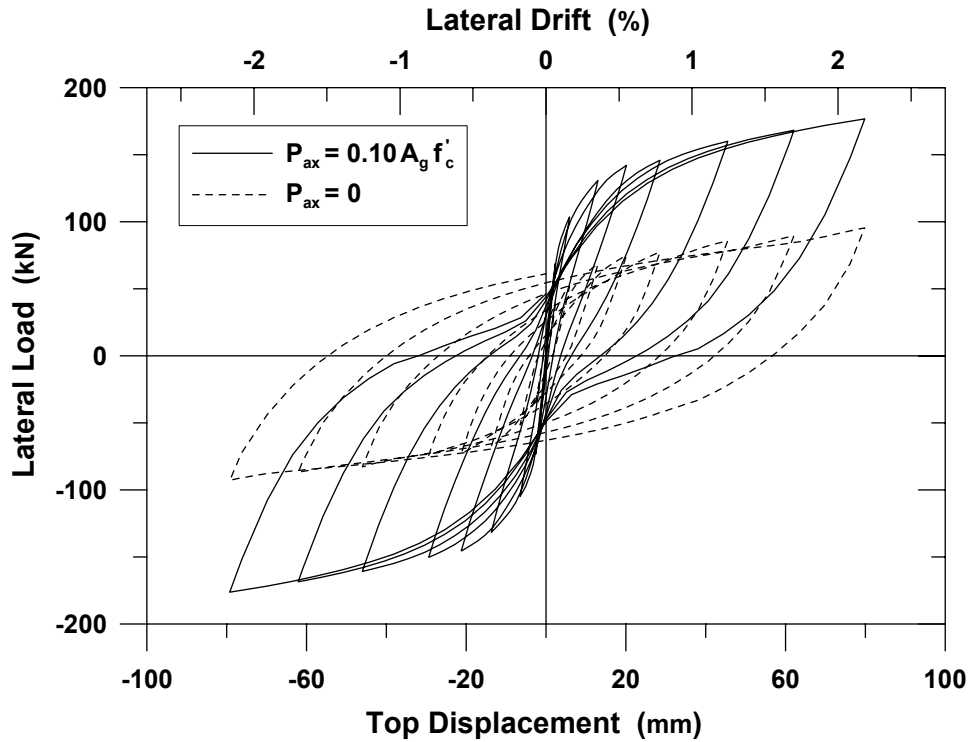
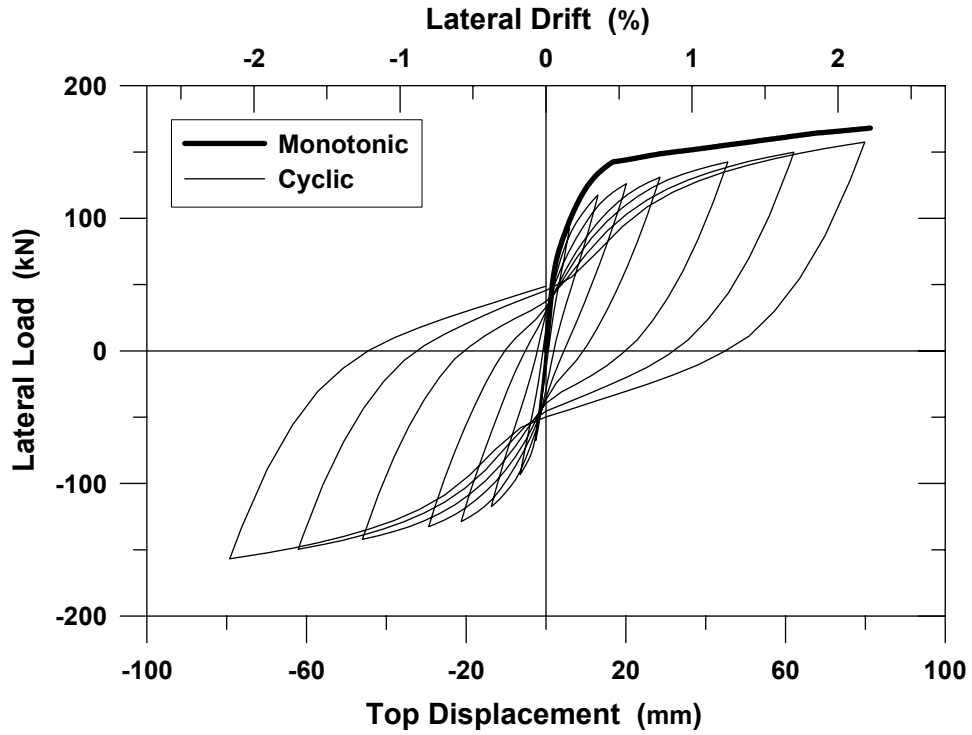
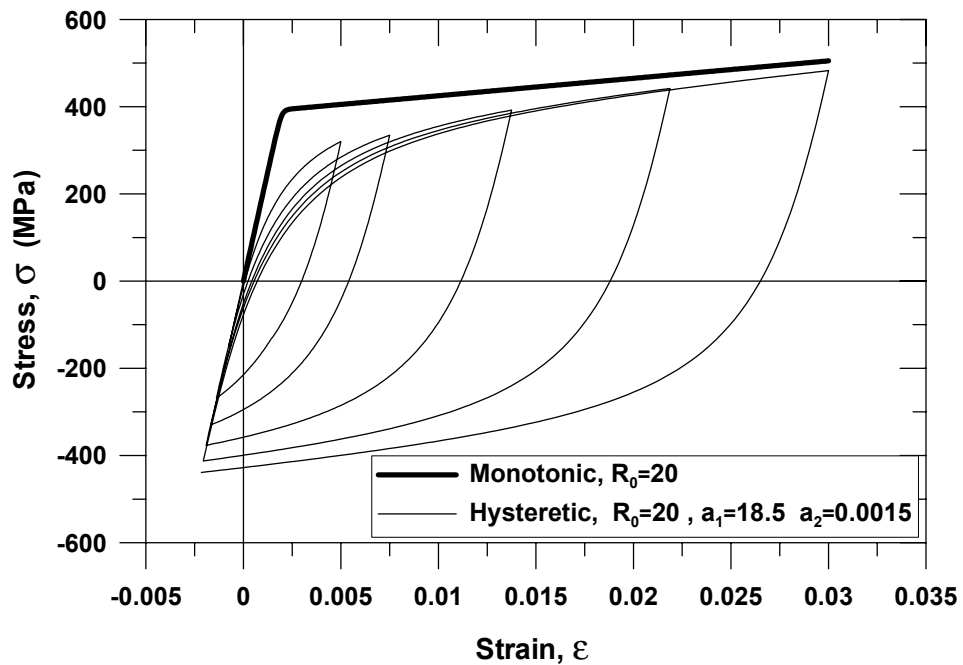


Fig. 6.9 Effect of axial load on analytical response

The monotonic and quasi-static lateral load – top displacement responses predicted by the wall model are compared in Figure 6.10(a). The model successfully simulates the cyclic strength degradation associated with the Bauschinger’s effect observed in reinforcing steel. Figure 6.10(b) shows a comparison of sample monotonic and cyclic stress-strain relations for reinforcing steel, generated by the constitutive model by Menegotto and Pinto (1973), in which Bauschinger’s effect is illustrated. The monotonic stress-strain relation is essentially bilinear, since the curvature parameter R is assigned a large value for monotonic loading ($R = R_0 = 20$); whereas the parameters a_1 and a_2 (see Fig. 6.3) account for cyclic degradation of the curvature parameter R , and thus allow modeling of the Bauschinger’s effect. This behavior is reflected in the analytical lateral load – top displacement response of the wall shown in Figure 6.10(a).



(a) Monotonic and quasi-static load-displacement responses predicted by the model



(b) Monotonic and hysteretic stress-strain response histories for reinforcing steel

Fig. 6.10 Monotonic and quasi-static responses

The monotonic load-displacement response of the wall produces lateral load capacities larger than that of the cyclic response at all drift levels. This is because the monotonic stress-strain relation of reinforcing steel generates higher stresses compared to the hysteretic stress-strain relation, due to Bauschinger's effect (Fig. 6.10(b)). The shape of the monotonic lateral load – top displacement response predicted by the wall model resembles the shape of a typical monotonic moment-curvature (moment-rotation) relation for a reinforced concrete cross section.

Figure 6.11 compares the analytical lateral load – top displacement response prediction obtained using a model with the constitutive relation by Chang and Mander (1994) implemented for concrete, with that obtained using the constitutive relation by Yassin (1994). The primary shortcoming of the constitutive model by Yassin is the inability of the model to simulate gradual gap closure due to progressive contact stresses within the cracks in concrete. Sudden crack closure (see Fig. 6.5) results in a pronounced and overestimated pinching behavior (i.e., characteristic variation in section stiffness from unloading to reloading in the opposite direction) for the wall. This is represented in Figure 6.11, where a sudden change in wall lateral stiffness is observed when the constitutive model by Yassin (1994) is used. In contrast, the constitutive model by Chang and Mander (1994) yields a progressive and gradual pinching behavior; that is, the model by Chang and Mander successfully simulates the gradual closure of cracks (see Fig. 6.4) due to progressive contact stresses occurring across cracks.

As discussed in Chapter 7, the analytical model accurately represents the stiffness degradation properties upon unloading and the wall pinching behavior (as well as other attributes of cyclic wall response) observed in test results when the constitutive model by Chang and Mander is used. Therefore, the constitutive model by Yassin was not used in any further studies. However, the constitutive model by Yassin is a simple and widely used (e.g., OpenSees) alternative, and can be efficiently used when accurate prediction of wall unloading and pinching properties is of secondary concern. The two responses depicted in Figure 6.11 are not notably different in the regions other than those associated with unloading and reloading in opposite direction, although the shape of the monotonic compression and tension envelopes of the stress-strain relations by Chang and Mander and Yassin are significantly different (compare Figs. 6.4 and 6.5). This highlights the fact that the analytical model response for the wall and loading regime used in this study is not very sensitive to the shape of the envelopes used for modeling the monotonic stress-strain behavior of concrete. The sensitivity of the model response to

constitutive material parameters, as well as model parameters, is investigated in the following section.

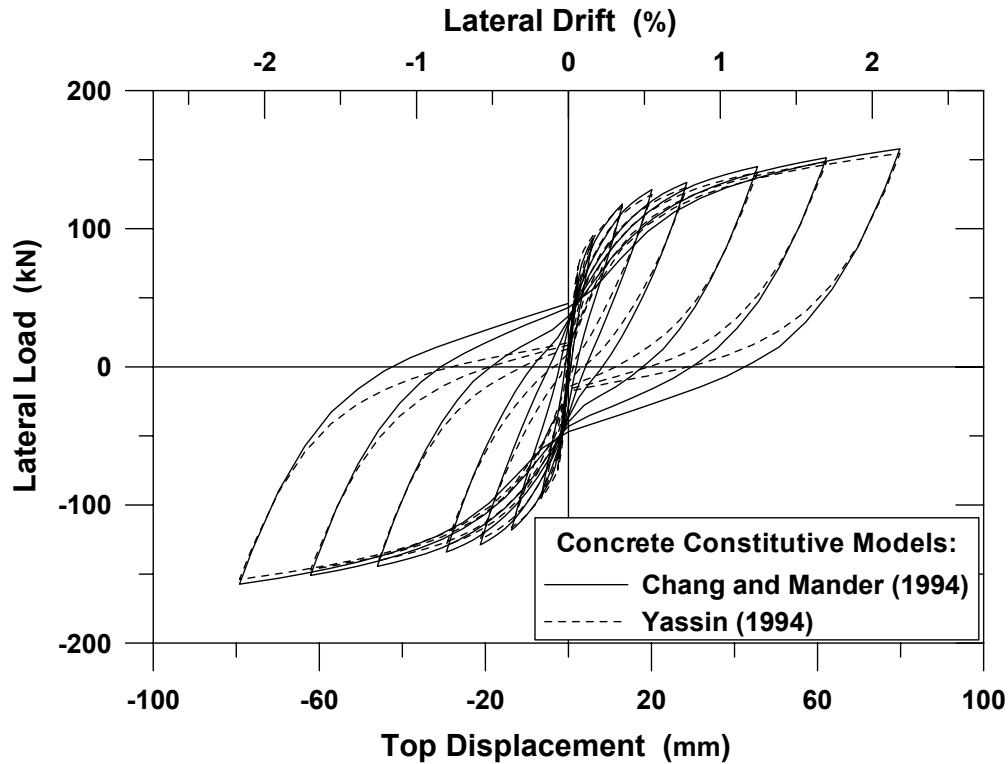


Fig. 6.11 Analytical load-displacement response predictions obtained using different constitutive relations for concrete

6.3 PARAMETRIC SENSITIVITY STUDIES

It has been observed that in addition to the model parameters (number of macro wall elements (m), number of uniaxial elements or macro-fibers within each element (n), and center of rotation parameter (c), properties of the uniaxial hysteretic constitutive models defined for the materials influence the analytical response predictions. The sensitivity of the results obtained with the model to both model and material constitutive parameters is addressed in the following subsections.

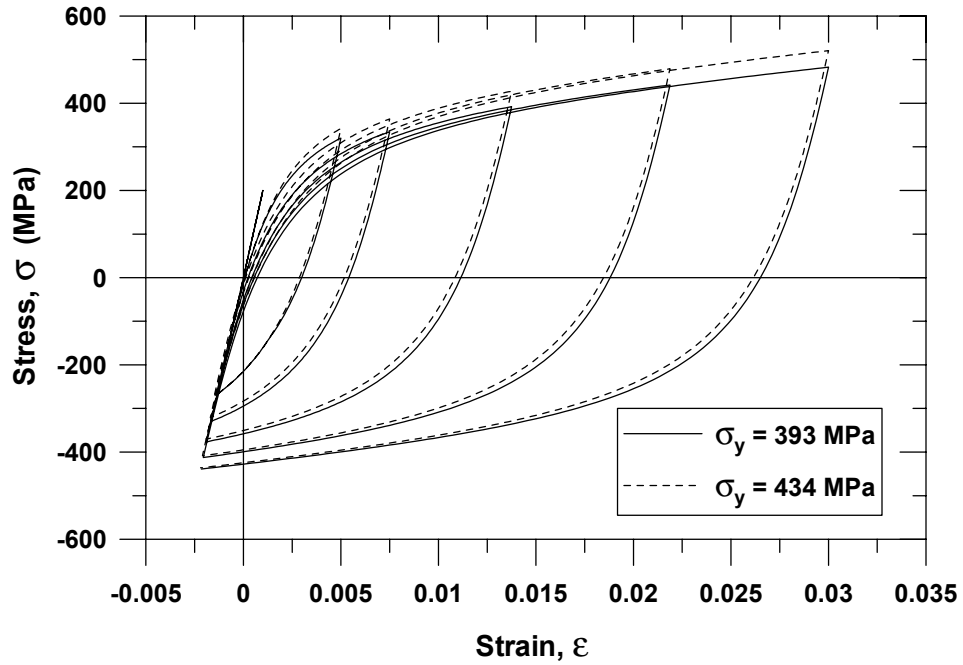
6.3.1 Material Constitutive Parameters

The MVLEM implemented in this study relates the predicted flexural response directly to material behavior without incorporating any additional empirical relations, as done in prior

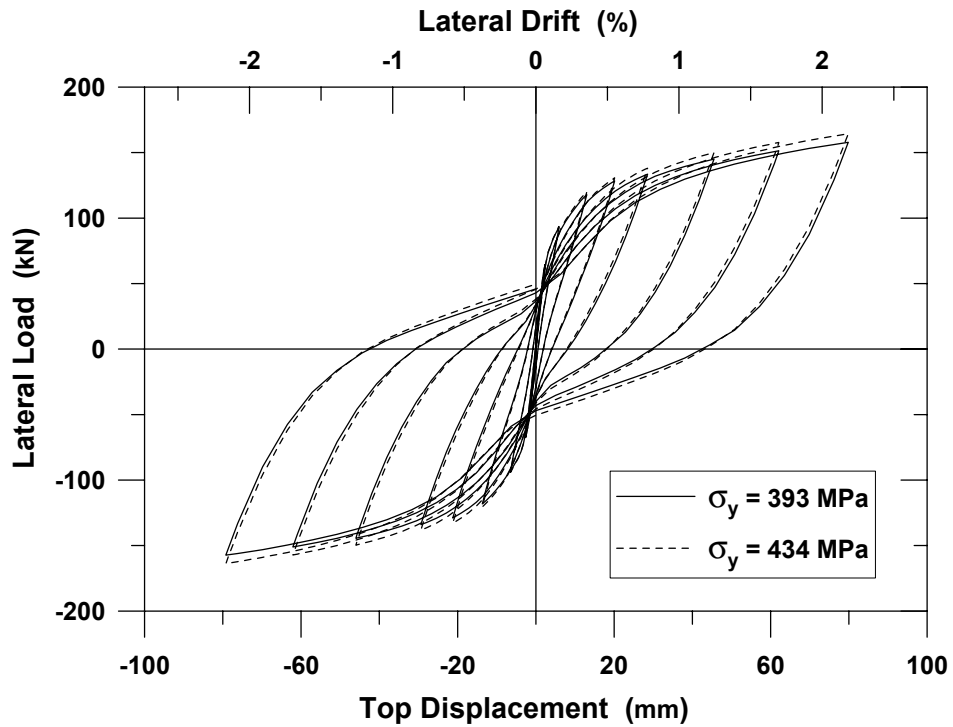
studies (Fischinger et al., 1990; Fajfar and Fischinger, 1990; Fischinger et al., 1991, 1992). It has been observed that the predicted load-displacement response is, as expected, influenced by the properties of the stress-strain relations implemented for the longitudinal reinforcement and the unconfined and confined concrete; therefore, it is necessary to understand how variations in the material constitutive laws influence the results obtained using the model, particularly in the context of performance-based seismic design.

The material constitutive parameters associated with the implemented steel stress-strain law are the modulus of elasticity (E_0), the yield stress (σ_y), the strain-hardening ratio (b) and the parameters (R_0 , a_1 and a_2) influencing the cyclic curvature of the transition curve between the elastic and yield asymptotes. Values for E_0 , σ_y , and b are obtained from monotonic stress-strain tests conducted on bare rebar specimens, allowing for a reliable calibration. However, the values for the yield stress (σ_y) and strain-hardening ratio (b) in tension should be modified to consider the tension-stiffening effect on the reinforcing bars, and can be calibrated for average values using relations such as those proposed by Belarbi and Hsu (1994). Figure 6.12 illustrates the sensitivity of the analytical lateral load – top displacement response to the value of the tensile yield stress (σ_y) selected for reinforcing steel. Figure 6.12(a) shows sample stress-strain histories generated by the steel constitutive model for two different values selected for the tensile steel yield stress, whereas the corresponding lateral load – top displacement responses of the wall specimen predicted by the analytical model are compared in Figure 6.12(b). As expected, selecting a higher level of yield stress for steel in tension results in a larger prediction of the wall lateral load capacity at all drift levels. Figure 6.13 shows the sensitivity of the model response to the strain-hardening ratio (b) of steel in tension. Selection of a larger strain-hardening ratio value yields a larger post-yield lateral stiffness of the wall, and thus larger lateral load capacities at post-yield drift levels (i.e., 0.5%–2% drift).

The calibration of parameters R_0 , a_1 and a_2 (accounting for the cyclic degradation of the curvature coefficient R) requires cyclic test results, which are not commonly available. Figure 6.14(a) shows sample stress-strain histories generated by the steel constitutive model for two different sets of values for parameters R_0 , a_1 , and a_2 , calibrated by prior researchers (Filippou et al., 1994; Elmorsi et al., 1998) based on cyclic test results on reinforcing steel bars.

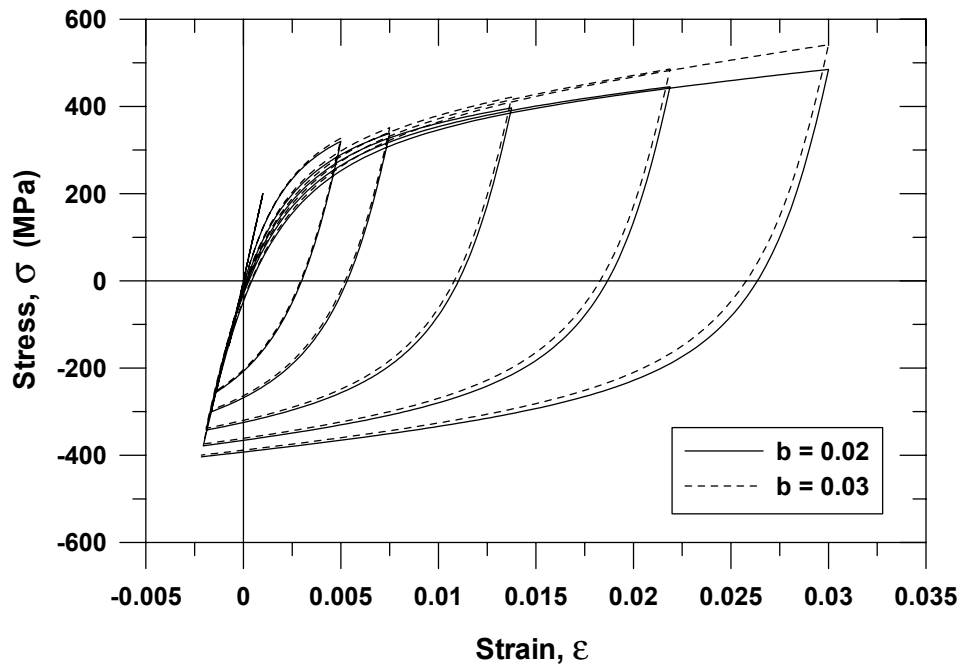


(a) Steel stress-strain response histories

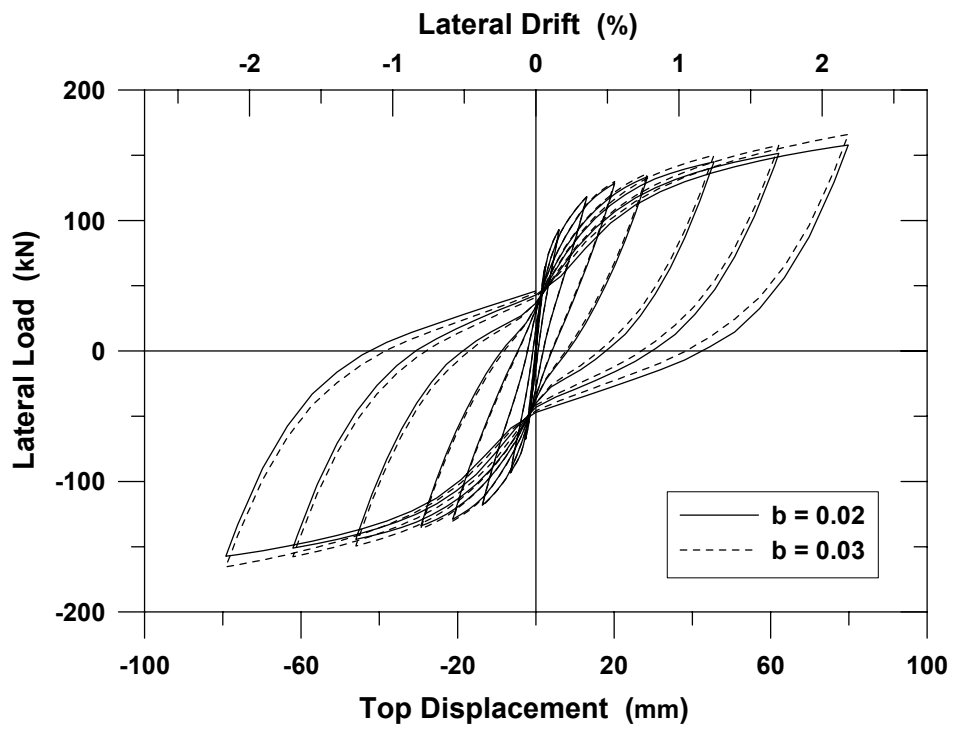


(b) Analytical load-displacement response predictions

Fig. 6.12 Sensitivity of analytical response to steel yield stress

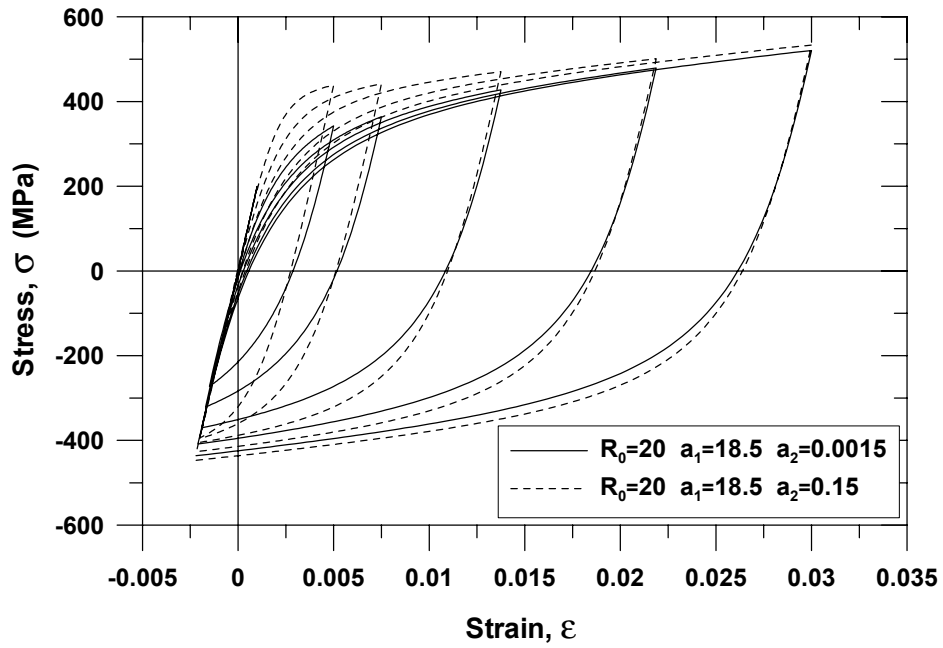


(a) Steel stress-strain response histories

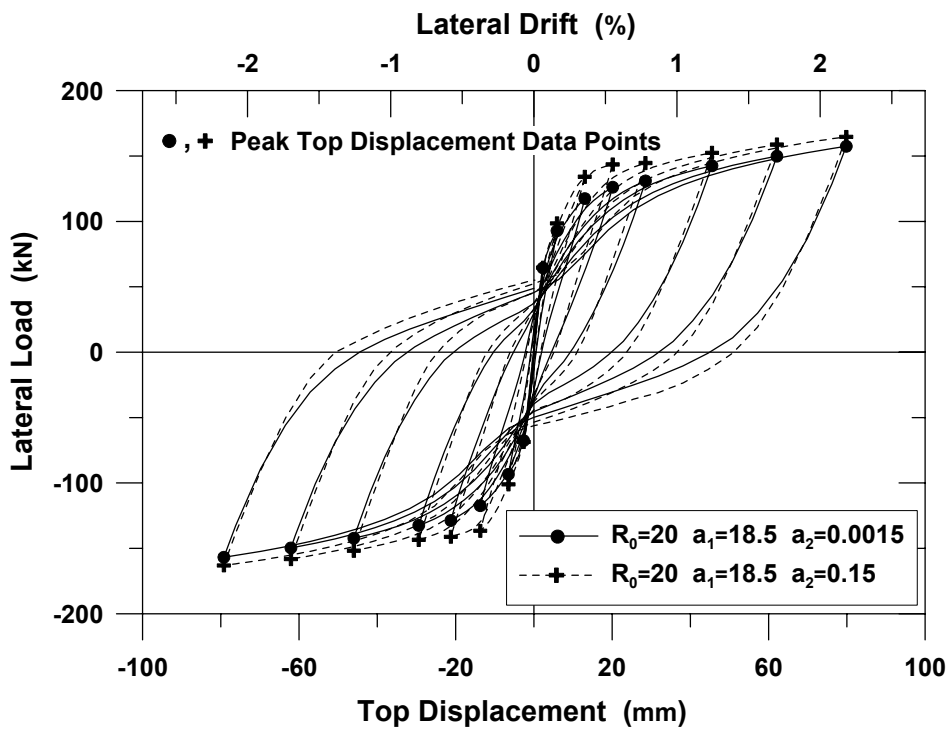


(b) Analytical load-displacement response predictions

Fig. 6.13 Sensitivity of analytical response to steel strain-hardening ratio



(a) Steel stress-strain response histories



(b) Analytical load-displacement response predictions

Fig. 6.14 Sensitivity of analytical response to hysteretic parameters for steel

The analytical lateral load – top displacement responses of the wall specimen predicted by the MVLEM using the specified values for the material parameters (R_0 , a_1 , and a_2 in Fig. 6.14(a)) are shown in Figure 6.14(b). The lateral load capacity of the wall is significantly influenced by these hysteretic parameters; primarily in the region where the steel is not subjected to high post-yield strains (e.g., 0.5%–0.75% drift). Cyclic degradation of the lateral stiffness during unloading and plastic (residual) displacements at zero lateral load also depend on the selection of these parameters, as shown in Figure 6.14(b).

The material parameters associated with the implemented concrete stress-strain relation are the monotonic (envelope) parameters (E_c , f'_c or f_t , ϵ'_c or ϵ_t , r) and the hysteretic parameters (Δf , $\Delta \epsilon$, E_{pl} , E_{sec}) defined for compression and tension (Fig. 4.13). The empirical relations used to define these parameters for monotonic and cyclic compression (for both confined and unconfined concrete) were validated by Chang and Mander (1994) using extensive experimental data from column tests. The relations defining the parameters for cyclic tension, however, were obtained using limited experimental data. Furthermore, the observed tensile strength and stress-strain properties of concrete depend strongly on the testing conditions (Chang and Mander, 1994) and considerable scatter is observed in the data scattering, making it difficult to assign values for the parameters that define the concrete tensile stress-strain relation. Therefore, the sensitivity of the predicted wall response to concrete stress-strain parameters investigated here focuses on concrete tensile strength and the hysteretic parameters related to cyclic tension, as well as because model results are less sensitive to variations in the parameters describing the behavior of concrete in compression.

Figure 6.15 illustrates how the predicted monotonic and cyclic lateral load – top displacement responses of the wall specimen (with applied axial load 7% of axial load capacity) are influenced by selection of the tensile strength (peak tensile stress) for concrete (f_t). The strain at peak tensile stress (ϵ_t) was varied proportionally with the peak tensile stress, while the shape parameter r was kept constant. Neglecting the contribution of concrete in tension results in a lower prediction of the wall lateral stiffness and a slightly lower prediction of the wall lateral strength compared with results that include the contribution of concrete in tension. Furthermore, variation in the assumed tensile strength for concrete influences the cyclic properties of the predicted response, as shown in Figure 6.15.

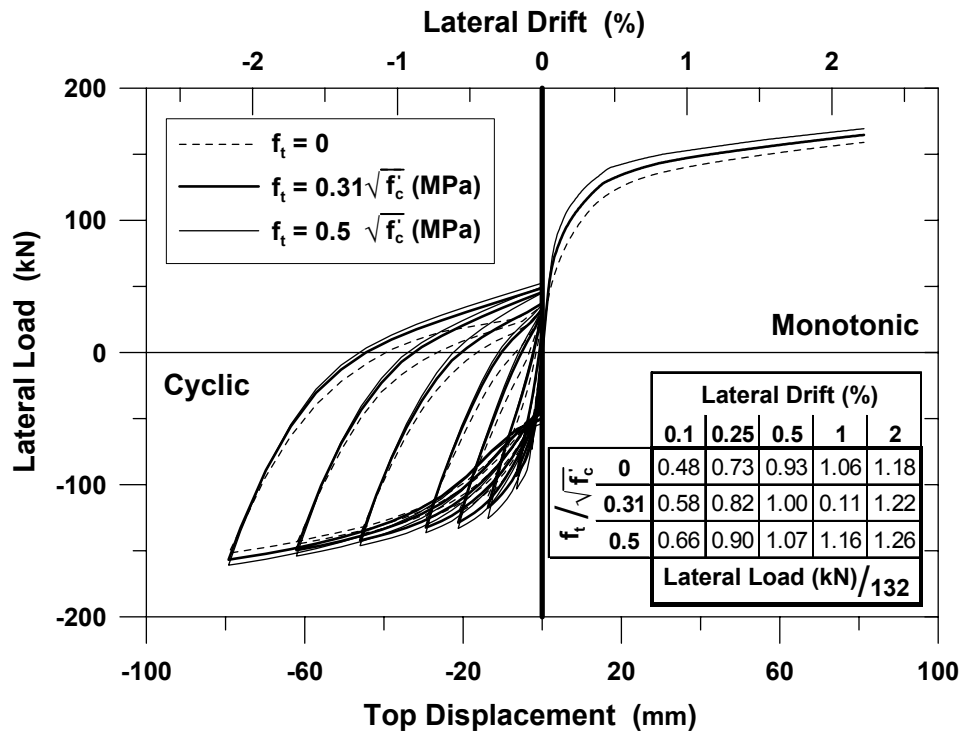


Fig. 6.15 Effect of concrete tensile strength on analytical response

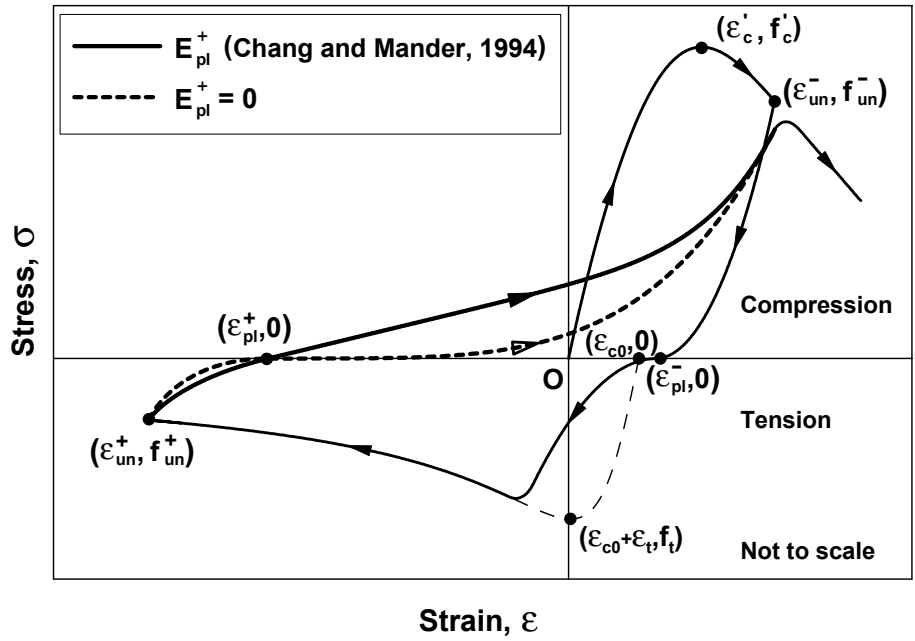
The hysteretic parameters associated with the cyclic concrete stress-strain law in tension are the plastic stiffness (E_{pl}^+) and secant stiffness (E_{sec}^+) upon unloading from, and stress and strain offsets (Δf^+ and $\Delta \epsilon^+$) upon return to the tension envelope (Fig. 4.13). The predicted wall response is not notably influenced by the stress and strain offsets, since the offsets influence the shape of the stress-strain curve within a very small range of tensile stresses. On the other hand, the predicted wall response is significantly influenced by values selected for the plastic and secant stiffnesses for unloading in tension because these parameters control the starting strain and initial slope for the gap closure region of the concrete stress-strain law. Figure 6.16(a) compares sample stress-strain histories generated by the constitutive relation for concrete with the original expression derived by Chang and Mander (1994) for the plastic stiffness in tension (E_{pl}^+) and an illustrative value of zero, and Figure 6.16(b) compares the corresponding predicted load-displacement responses of the wall obtained using 17 MVLEM elements along the wall height (8 of the MVLEM elements stacked along the bottom one fourth of the wall height and the rest distributed uniformly over the wall height) with 22 uniaxial elements along the wall length, and $c = 0.4$. The figures reveal that the shape of the unloading and reloading curves of the predicted load-displacement response is governed by the selection of the value for plastic

stiffness (E_{pl}^+), which together with the secant stiffness (E_{sec}^+), governs the progressive gap closure properties (i.e., pinching) of the concrete stress-strain relation. Using a value of zero for E_{pl}^+ results in an abrupt change in the lateral stiffness of the wall from unloading to reloading in the opposite direction, and thus a much more pronounced pinching behavior (similar to the cyclic response in Figure 6.15, when concrete tensile stresses are neglected, i.e., $f_t = 0$; and thus the plastic stiffness for unloading in tension is zero), whereas implementing the original relation imposes a more gradual change in the lateral stiffness of the wall. However, the variation in the pinching behavior does not change the lateral strength and stiffness of the wall at peak top displacement (displacement reversal) points, since the enforced peak displacements of the wall are increasing for successive loading cycles.

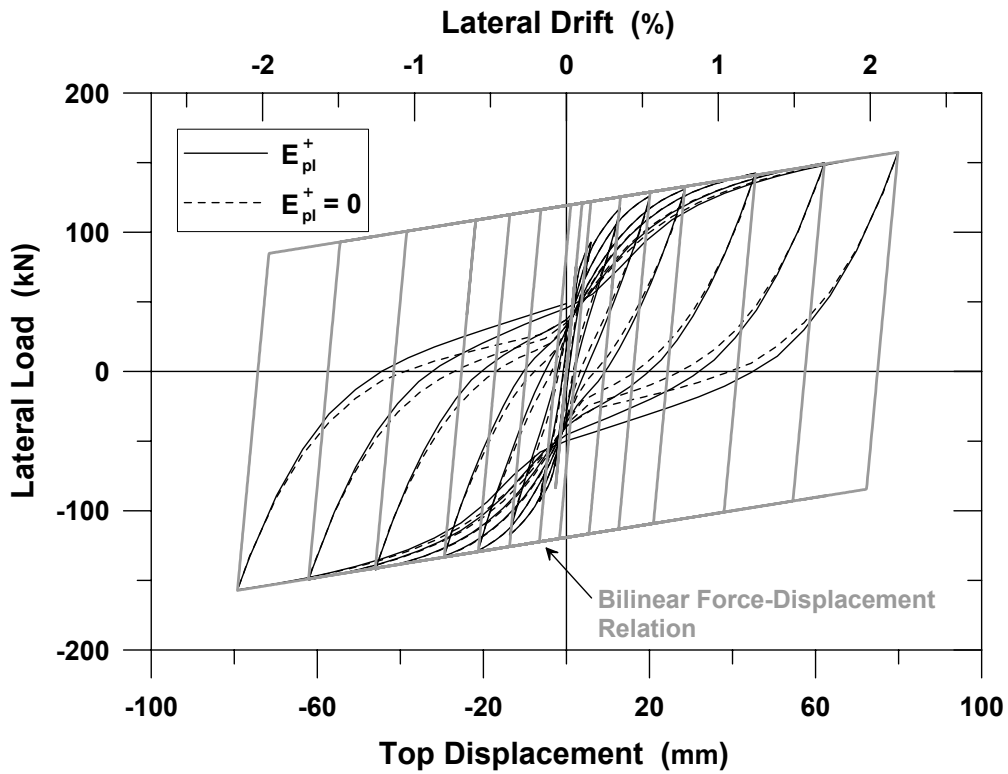
Similar behavior is observed in the analytically predicted position of the neutral axis and the predicted longitudinal strains. Figure 6.16(c) shows the position of the neutral axis predicted in the MVLE at the base of the wall obtained by using the two different expressions for the tensile plastic stiffness (E_{pl}^+). The neutral axis positions reach the same local limit values at peak displacement data points, and variation between the two cases is enhanced as the displacement (or rotation) of the wall approaches zero. Finally, Figure 6.16(d) illustrates the influence of the plastic stiffness on predicted longitudinal strain histories for the element at the base of the wall. For the two cases investigated, the strains at both the extreme fiber and centroid are identical at peak displacement data points; however, noticeable variation is observed in the strains (more distinctly at the centroid) as the wall displacement approaches zero.

The variation in the unloading and reloading regions of the predicted response (Fig. 6.16(b)) has only a marginal effect on the energy dissipation capacity of the wall model. Calculating the hysteretic energy dissipation capacity for the plots in Figure 6.16(b) normalized by that of a bilinear lateral load – top displacement relation yields values of 0.66 for the response obtained by using the relation for the tensile plastic stiffness defined by Chang and Mander (1994), and 0.64 using a zero value for the tensile plastic stiffness.

Variation in the secant stiffness defined for concrete in tension (E_{sec}^+), influences wall response in approximately the same way as changes in the plastic stiffness (E_{pl}^+).

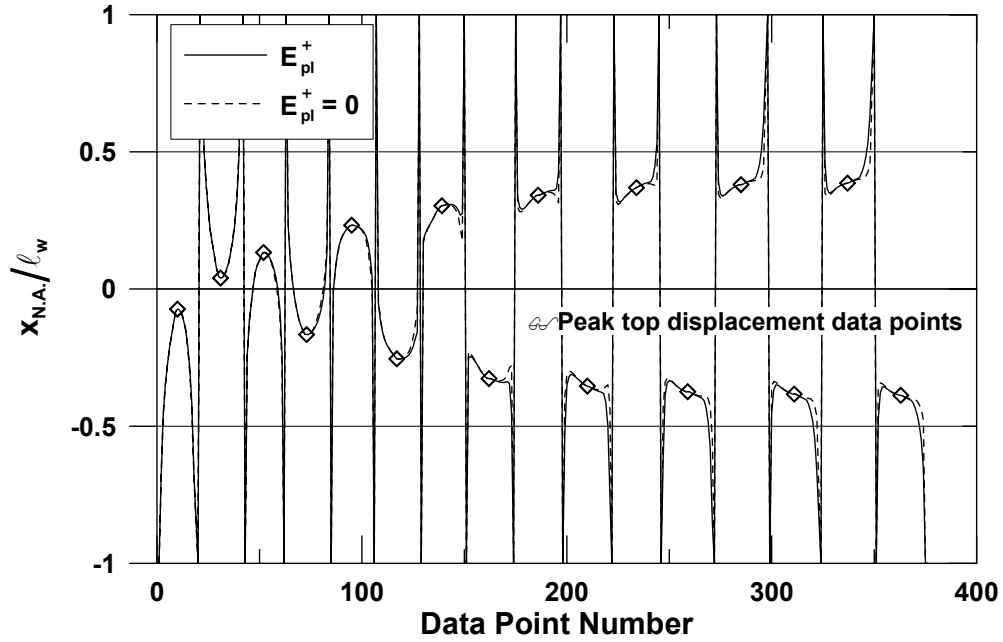


(a) Concrete stress-strain response histories

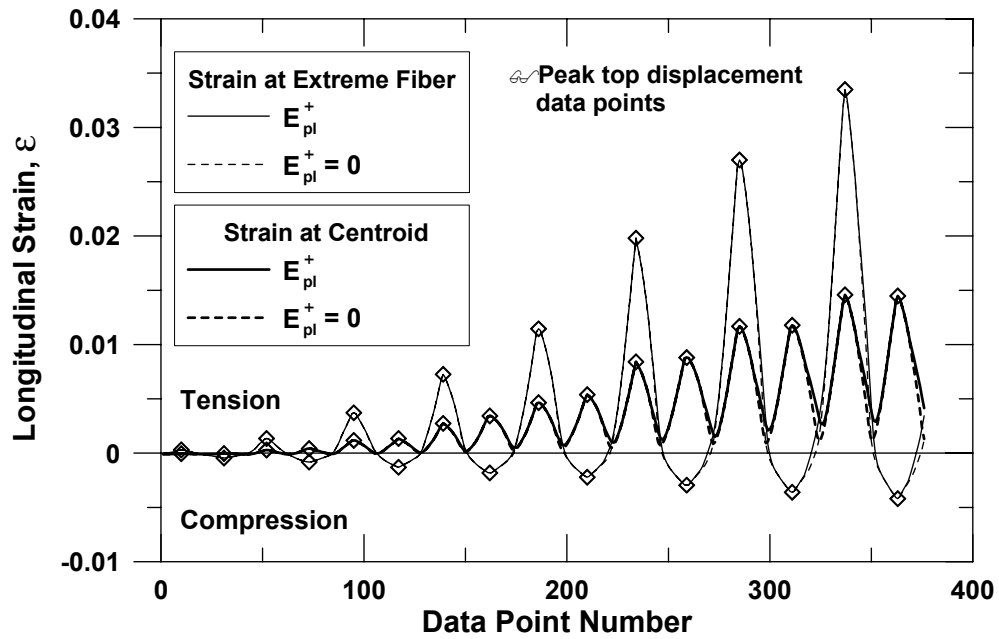


(b) Predicted load-displacement responses

Fig. 6.16 Effect of concrete tensile plastic stiffness on analytical response



(c) Predicted position of the neutral axis



(d) Predicted longitudinal strain histories

Fig. 6.16 (cont'd.)

The empirical relations defined by Chang and Mander for the plastic stiffness and secant stiffness in tension were obtained from limited experimental data (Yankelevsky and Reinhardt, 1987) with imposed tensile strains reaching a value of approximately 0.003. However, the tensile strains in walls are likely to reach much larger values (e.g., 0.035 in this example); thus, using the Chang and Mander empirical relations for such high levels of tensile strain may be inappropriate. Calibration of these two hysteretic parameters for a broader range of tensile strains, and also accounting for the tension-stiffening effect, would refine the modeling of the gap closure region of the concrete stress-strain behavior, and the prediction of the wall pinching behavior. Fortunately, the concrete model proposed by Chang and Mander (1994) provides a flexible approach that allows recalibration of such parameters to control gap closure properties of concrete for an improved overall representation of wall force-deformation relations.

It has been observed that the model results are less sensitive to variation in the parameters defining the monotonic and hysteretic stress-strain relation for concrete in compression, provided that the values used for the parameters are within reasonable range such as those obtained by using the empirical relations recommended by Chang and Mander. The empirical relations relate the parameters for compression (i.e., modulus of elasticity E_c , strain at peak compressive stress ϵ_c' , parameter r defining the shape of the compression envelope (Eqs. 4.49–4.51), and hysteretic parameters for compression including stress and strain offsets (Δf^- and $\Delta \epsilon^-$), and unloading plastic stiffness and secant stiffness (E_{pl}^- and E_{sec}^-) to the value selected for the unconfined compressive strength (peak unconfined compressive stress, f_c') of concrete (Eqs. 4.78–4.81). The governing parameter f_c' can be feasibly calibrated with monotonic stress-strain tests conducted on concrete specimens (e.g., 152.5 x 305 mm standard cylinders).

Figure 6.17 compares the lateral load – top displacement responses predicted by the wall model for a 25% variation in the unconfined compressive strength (f_c') of concrete. The responses are not noticeably different, although all of the parameters associated with the monotonic and hysteretic parameters of the constitutive stress-strain relation for concrete in compression (E_c , ϵ_c' , r , Δf^- , $\Delta \epsilon^-$, E_{pl}^- , E_{sec}^-) are varied based on the value selected for f_c' . The result indicates that, for the wall properties and loading protocol used in this study, the model response is insensitive to either the value of the compressive strength selected for concrete, or any of the parameters associated with the shape of the monotonic or hysteretic stress-strain branches for concrete in compression as long as there is no extreme variation in the assumed

compressive strength of concrete and the values selected for the monotonic and hysteretic constitutive parameters for concrete in compression are within the range of typically expected variation.

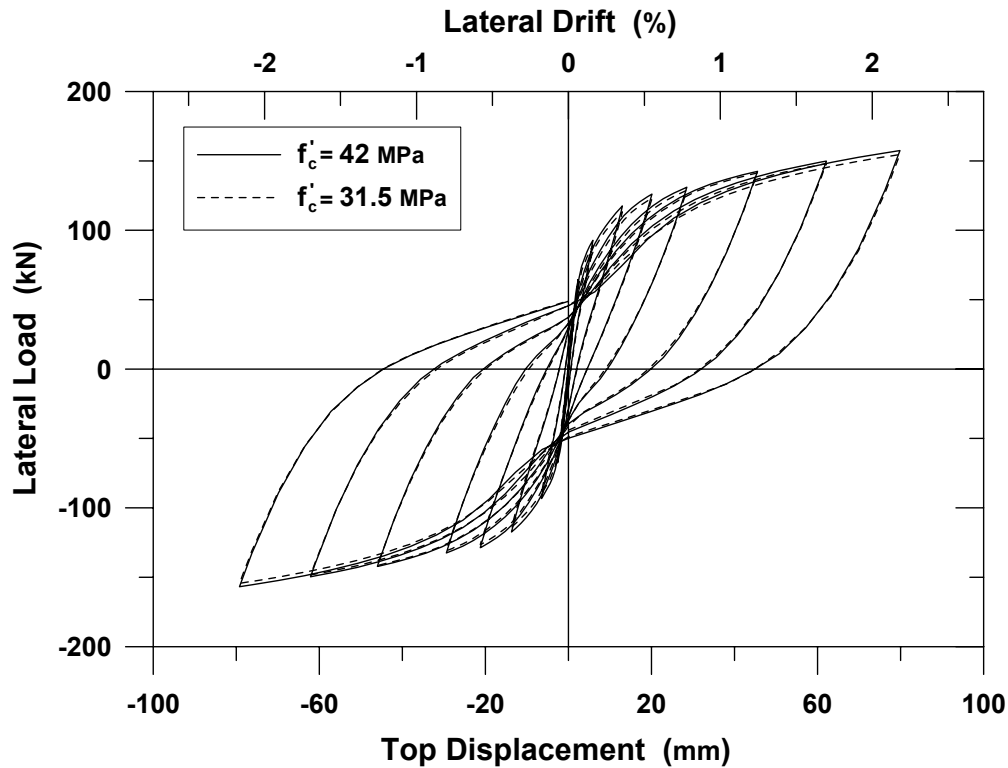


Fig. 6.17 Sensitivity of analytical response to concrete compressive strength and associated parameters

The wall model, together with the nonlinear solution strategy implemented in this study, can simulate the strength degradation associated with the descending (post-peak) branch of the concrete stress-strain constitutive model. This is shown in Figure 6.18, where the analytical lateral load – top displacement responses are compared for an extreme (50%) variation in the unconfined compressive strength of concrete. As observed in the figure, the concrete compressive strength does not significantly influence the lateral load capacity of the wall prior to strength degradation due to the post-peak branch of the concrete stress-strain relation (progressive concrete crushing). However, it influences the lateral drift level at which strength degradation is initiated.

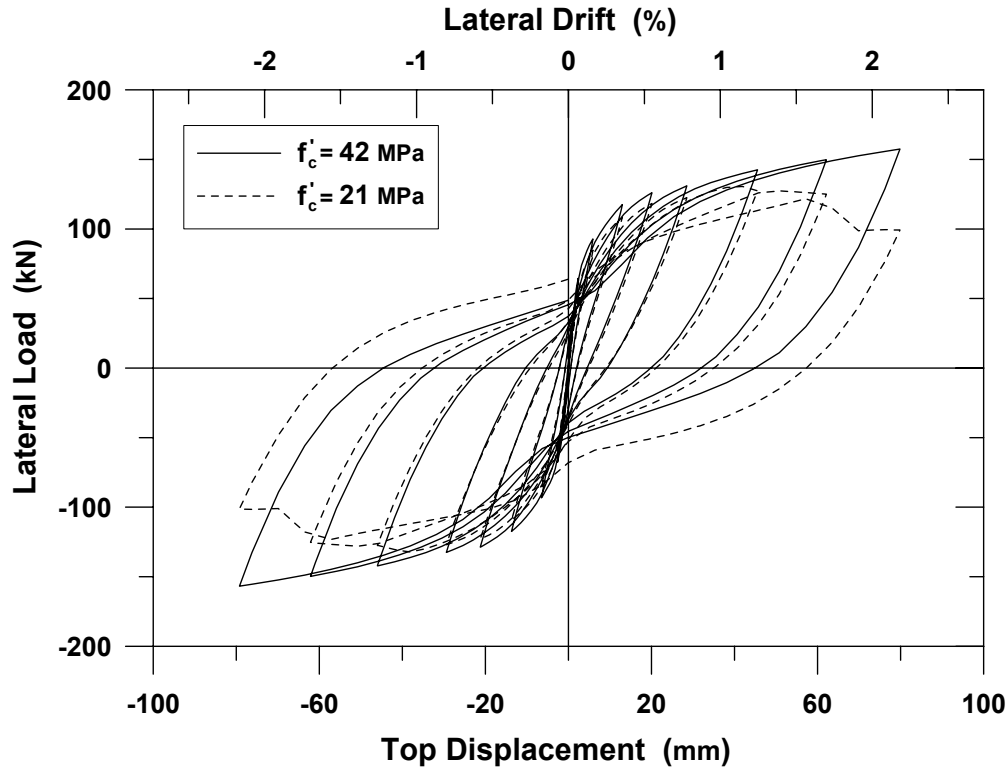


Fig. 6.18 Strength degradation in analytical response

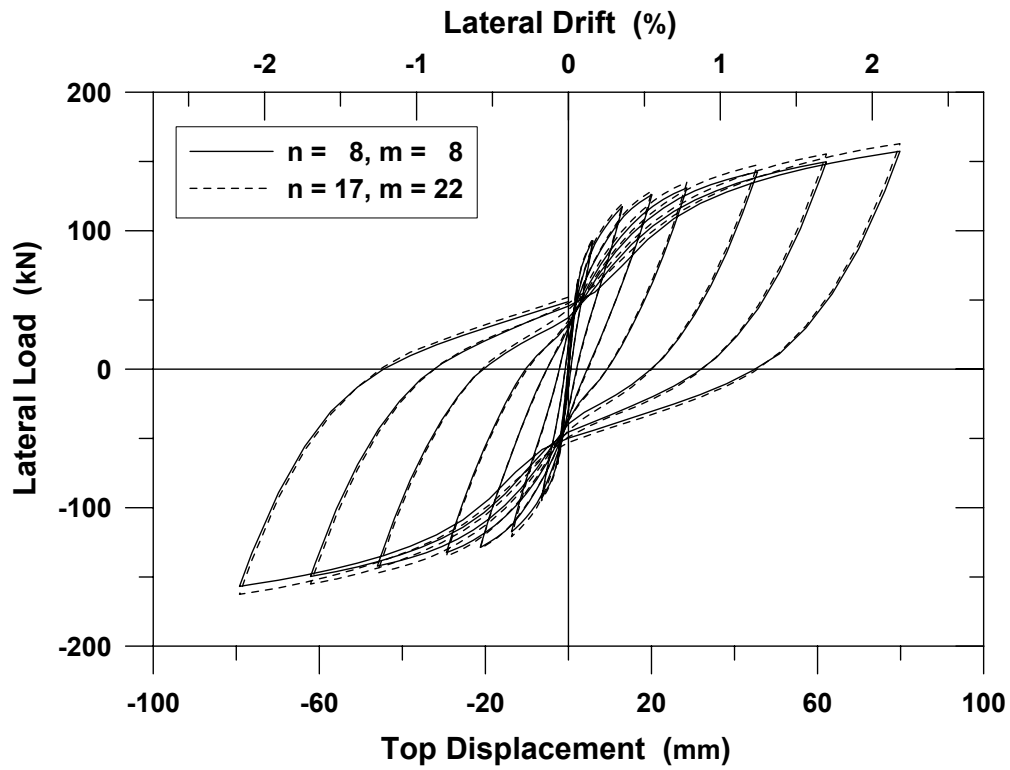
6.3.2 Model Parameters

Apart from material constitutive parameters, the only parameters associated with the analytical wall model are the number of uniaxial elements used along the length of the wall cross section (n), the number of MVLEM elements stacked on top of each other along the height of the wall (m), and the parameter defining the location of the center of rotation along the height of each MVLEM element (c) (Fig. 6.1). Sensitivity of the simulated wall response to variations of these parameters was investigated.

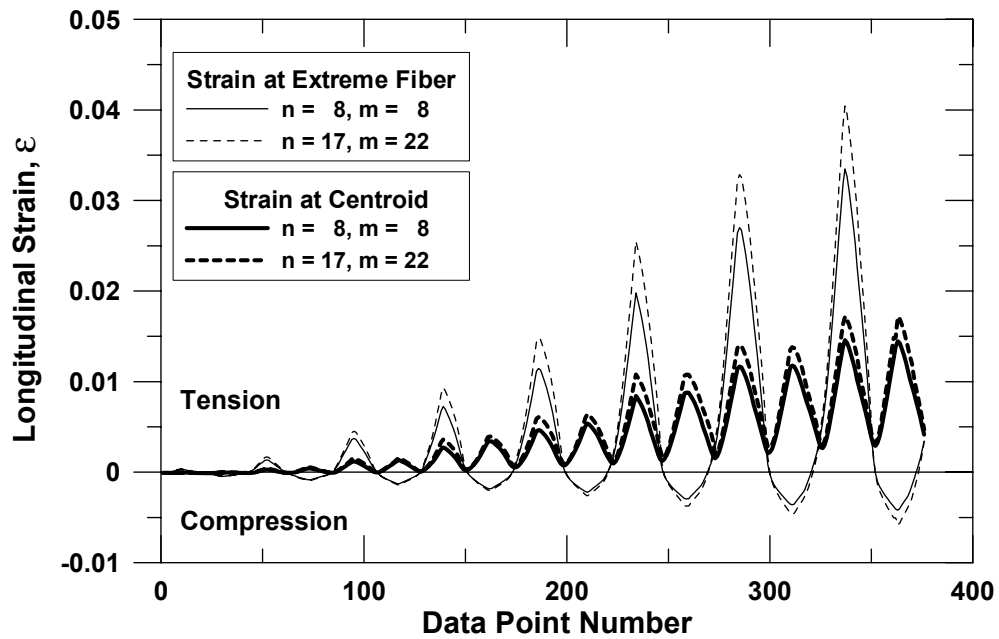
It has been observed that the calculated global response (i.e., lateral load versus top displacement) is not very sensitive to the selection of either the number of MVLEM elements along the height of the wall or the number of vertical elements along the wall length provided that reasonable values are selected in order to adequately represent the overall wall geometry. Figure 6.19(a) shows a comparison of the lateral load – top displacement response predicted by using either 8 MVLEM elements along the wall height with 8 uniaxial elements along the length

of the wall or by using 17 MVLEM elements along the wall height (8 of the MVLEM elements stacked along the bottom one fourth of the height where the inelastic deformations are expected, and the rest distributed uniformly over the wall height) with 22 uniaxial elements along the wall length. The comparison indicates that increasing the number of vertical line elements or the number of MVLEM elements does not significantly change the prediction of the global response (i.e., lateral load versus top displacement); however, use of more elements is valuable in terms of obtaining more detailed information on local behavior, such as the state of stress and strain or moment curvature response at a given location. For example, results shown in Figure 6.19(b) compare the average longitudinal strain histories predicted at the extreme concrete fiber and the centroid of the wall in the MVLE at the base of the two wall model configurations used for the plots in Figure 6.19(a) ($n = 8, m = 8$ and $n = 17, m = 22$). Using more MVLEs over the height of the wall allows for an improved local prediction of the strains, although the results obtained using the “rough” model ($n = 8, m = 8$) are quite good. As well, using more uniaxial elements along the wall length allows for a more refined description of the wall cross section. Therefore, the model incorporates the flexibility to choose how much detail is desired in the analytical results.

The sensitivity of analysis results to the parameter defining the location of the center of rotation along the height of each MVLEM element (c) is illustrated in Figure 6.20. Figure 6.20(a) compares the predicted lateral load – top displacement (global) response by using a wall model with 8 MVLEM elements (and 8 uniaxial elements) for a value of $c = 0.4$ (recommended by Vulcano et al., 1988) and an illustrative extreme value of $c = 0.0$ (center of rotation at the bottom of each MVLEM element). Decreasing the value of parameter c leads to a higher prediction of rotations and lateral displacements of the wall, resulting in a slightly lower prediction of the wall strength and lateral stiffness. However, this extreme variation in parameter c does not influence the characteristic shape of the load-displacement response significantly. As proposed by Fischinger et al. (1990), stacking more wall elements along wall height (especially in the region where inelastic deformations are expected) reduces the change in curvature within each element, thus diminishing the influence of the parameter c on the response. Figure 6.20(b) compares the predicted global wall response for $c = 0.4$ and $c = 0.0$ using a wall model with 17 MVLEM elements with 8 of the elements stacked along the bottom one fourth of the wall height. The two responses are very similar.

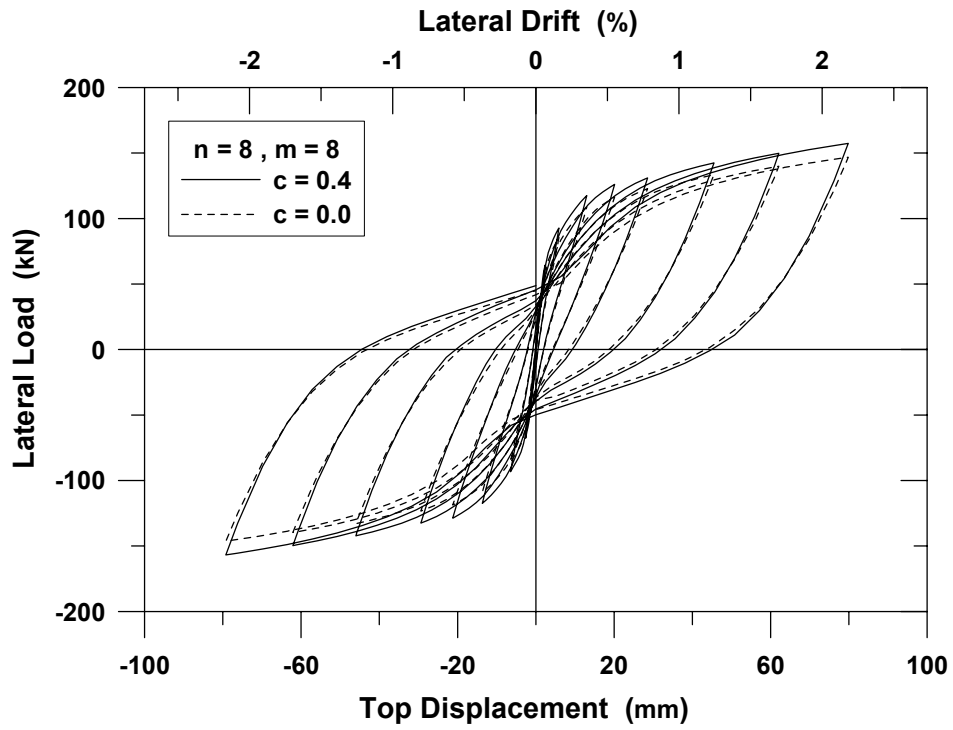


(a) Lateral load – top displacement responses

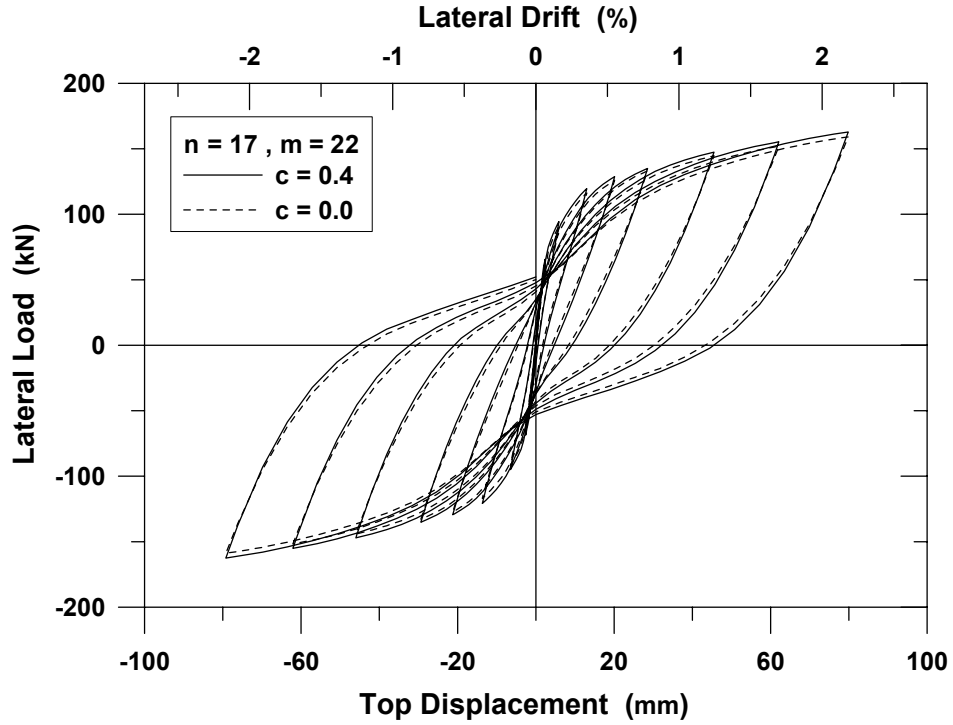


(b) Longitudinal strain histories in the MVLE at the base of the wall

Fig. 6.19 Sensitivity of response to number of MVLEM and uniaxial elements



(a) Analytical model with 8 MVLEM elements and 8 uniaxial elements



(b) Analytical model with 17 MVLEM elements and 22 uniaxial elements

Fig. 6.20 Sensitivity of response to center of rotation parameter c

6.4 SUMMARY

This chapter demonstrates the effectiveness of the present analytical model in simulating the behavioral features associated with the inelastic response of slender RC structural walls. The attributes of the responses obtained using the analytical model were studied. Variations of model and material parameters were investigated to identify the sensitivity of analytically predicted global and local wall responses to changes in these parameters as well as to identify which parameters require the greatest care with respect to calibration.

Based on analysis results, it was verified that the MVLEM captures important response characteristics associated with cyclic behavior of slender reinforced concrete structural walls governed by flexure. The analytical model is able to simulate important behavioral features including shifting of the neutral axis along the wall cross section, and the effect of fluctuating axial force, which are commonly ignored in simple models. Characteristics of the cyclic response, including stiffness degradation and strength deterioration, hysteretic shape, and pinching behavior are clearly captured in the analysis results.

The modeling approach adopted in this study involves implementing refined hysteretic uniaxial stress-strain laws instead of simplified (ad hoc) force-deformation rules to track nonlinear responses. This allows the designer to relate analytical responses directly to physical material behavior and provides a more robust modeling approach, where model improvements result from improvement in constitutive models and refinement in the spatial resolution of the discrete model. The constitutive relations implemented in the wall model provide a direct and flexible approach to incorporate important material behavioral features (e.g., Bauschinger's effect in reinforcing steel, hysteretic behavior of concrete in continuous compression and tension, progressive gap closure, tension-stiffening effect) into the analysis. It has been observed that the model responses are sensitive not only to material parameters associated with the monotonic stress-strain behavior, but also significantly by variation in the hysteretic parameters defined for the steel (R_0 , a_1 , a_2) and for concrete in tension (E_{pl}^+ , E_{sec}^+). Thus, careful calibration of these parameters is important for an improved prediction of the cyclic wall response.

Overall, the macroscopic wall model presented here provides a flexible platform to assess the influence of various material and behavioral features in the nonlinear responses of slender RC structural walls. Details on calibration of the model and correlation of predicted responses

with extensive test results, at both global and local response levels, are presented in the following chapter.

7 Flexural Modeling — Experimental Calibration and Verification

This chapter presents detailed information on the calibration of the analytical macro-model and comparison of model results with experimental results for slender reinforced concrete walls. Comprehensive correlation studies were conducted to compare the analytically predicted and experimentally observed behavior of slender RC walls with rectangular and T-shaped cross sections at various response levels by processing the test measurements to allow for a direct comparison of the predicted and measured flexural responses. Comparisons not only allow for a better understanding of the inelastic behavior of RC walls, but also identify model capabilities as well as ways to improve the model.

7.1 OVERVIEW OF EXPERIMENTAL STUDIES

The wall specimens tested by Thomsen and Wallace (1995, 2003) were used to calibrate and assess the analytical model. Experimental results were obtained for four, approximately quarter-scale wall specimens. The walls tested included two walls with rectangular cross sections (RW1, RW2), and two walls with T-shaped cross sections (TW1, TW2), with the primary variable in the test program being the level of detailing provided at the wall boundaries. A brief overview of these studies is provided in the following sections, with more detailed information concerning the wall tests presented by Thomsen and Wallace (1995, 2003).

7.1.1 Test Specimen Information

The walls were 3.66 m tall and 102 mm thick, with web and flange lengths of 1.22 m (Fig. 7.1). Floor slabs were provided at 0.915 m intervals over the height of the T-shaped walls (consisting of four stories).

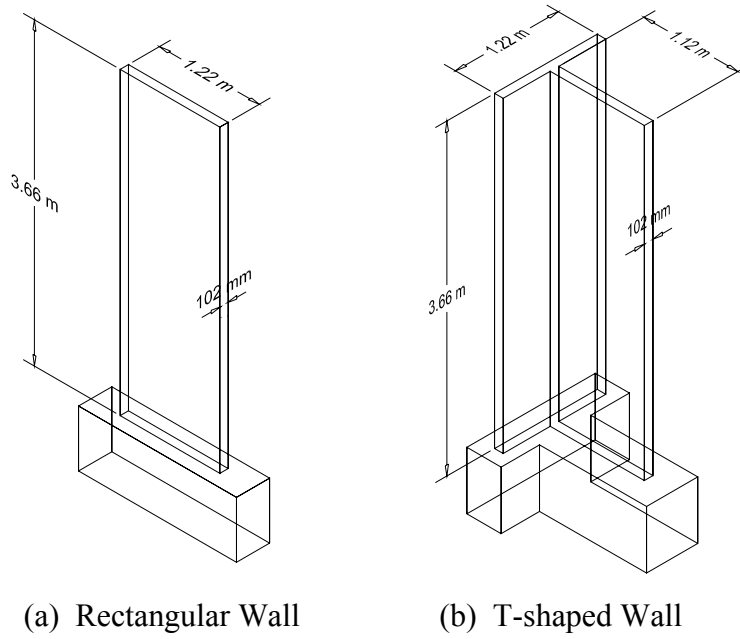


Fig. 7.1 RC wall specimens tested by Thomsen and Wallace (1995)

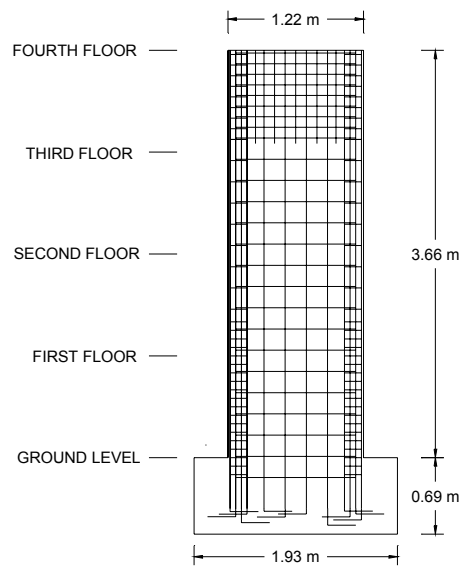


Fig. 7.2 Profile view of specimen RW2 showing placement of reinforcement

Typical material properties were selected for design, i.e., $f'_c = 27.6$ MPa and $\sigma_y = 414$ MPa. The wall specimens were proportioned based on a prototype building designed using the strength requirements of the Uniform Building Code (1994); however, detailing requirements at the boundaries of the wall specimens were evaluated using the displacement-based design approach presented by Wallace (1994, 1995). Longitudinal reinforcement at wall boundaries consisted of 8 - #3 ($d_b = 9.53$ mm) bars, whereas uniformly distributed web reinforcement consisted of two curtains of deformed #2 ($d_b = 6.35$ mm) bars.

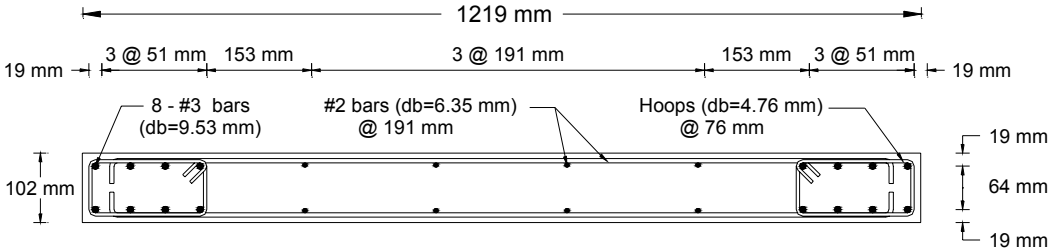
Transverse reinforcement at wall boundaries comprises 4.76 mm diameter smooth wire that was annealed to give material properties similar to those of Grade 60 (414 MPa) reinforcing steel. Well-detailed boundary elements were provided at the edges of the walls over the bottom 1.22 m (l_w) of each wall. A capacity design approach was used to avoid shear failure, and favorable anchorage conditions existed for the vertical reinforcement anchored with 90-degree hooks within the pedestal at the base of the walls (Fig. 7.2). Sample reinforcing details for a rectangular wall specimen RW2 and for a T-shaped wall specimen TW2 (at wall base levels) are shown in Figure 7.3.

7.1.2 Materials

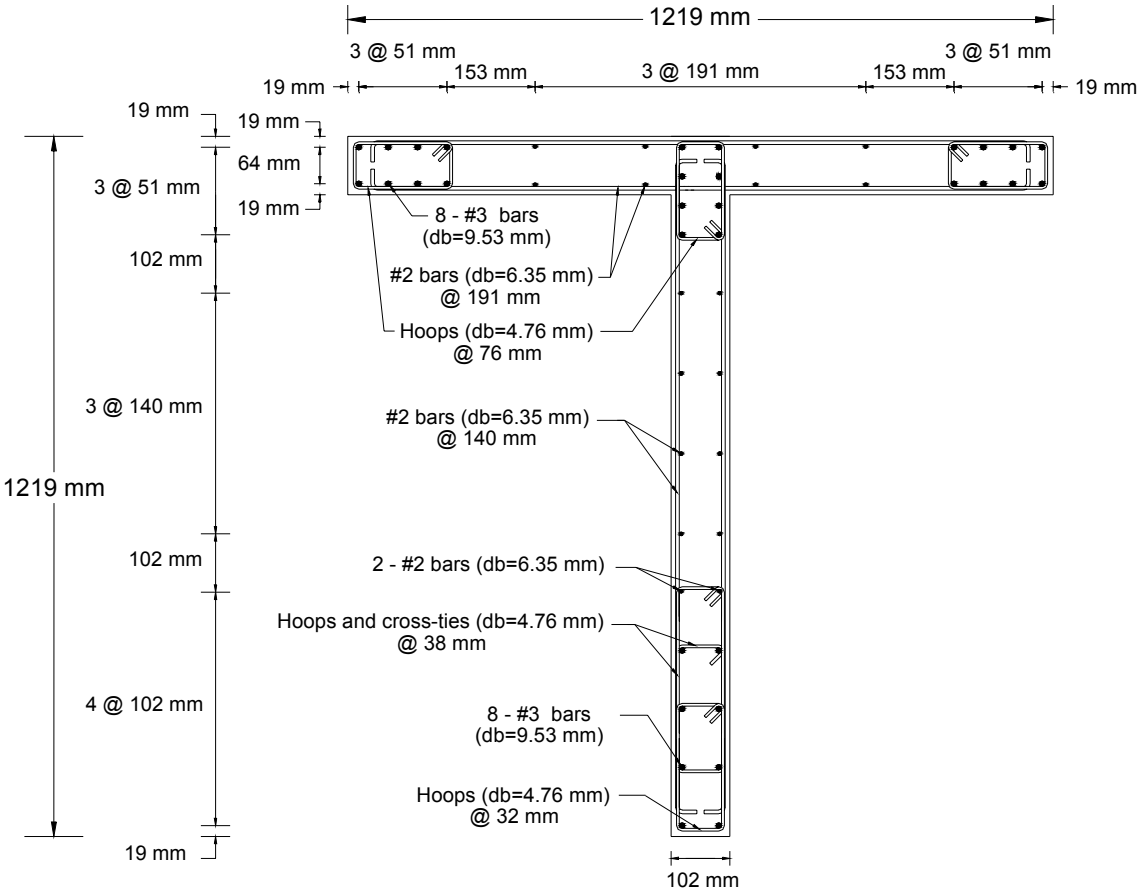
The compressive strength of concrete used for design of the wall specimens was 27.6 MPa; however, concrete compressive strengths at the time of testing ranged from 28.7 to 58.4 MPa, with mean compressive strengths at the base of the wall specimens (0–0.91 m) of approximately 32.8 MPa for the specimens RW1 and TW1, and 42.8 MPa for the specimens RW2 and TW2. Peak compressive stress was reached for a cylinder compressive strain of approximately 0.002 for all specimens. Figure 7.4 plots the stress-strain relations, measured at the time of testing using 152.4 mm x 304.8 mm standard cylinder specimens, of the concrete used in the construction of the walls.

Three different types of reinforcing steel were used in the tests: (1) typical Grade 60 (414 MPa), deformed #3 ($d_b = 9.53$ mm) bars as longitudinal reinforcement, (2) deformed #2 ($d_b = 6.35$ mm) bars uniformly distributed web steel, and (3) 4.76 mm diameter smooth wire as transverse reinforcement in the boundary regions. Figure 7.5 plots the measured longitudinal stress-strain relations for each type of reinforcement. The #3 ($d_b = 9.53$ mm) bars used as

longitudinal boundary reinforcement had typical Grade 60 properties; however, the other two types of steel exhibited some atypical behavior. The deformed #2 ($d_b = 6.35$ mm) bars used as uniformly distributed web reinforcement had a yield stress of approximately 448 MPa; however, they did not exhibit a well-defined yield plateau. The 4.76 mm diameter smooth wire was annealed to lower the yield stress from approximately 552 MPa to approximately 448 MPa; however, the strain-hardening region of the annealed wire was relatively flat (Fig. 7.5).

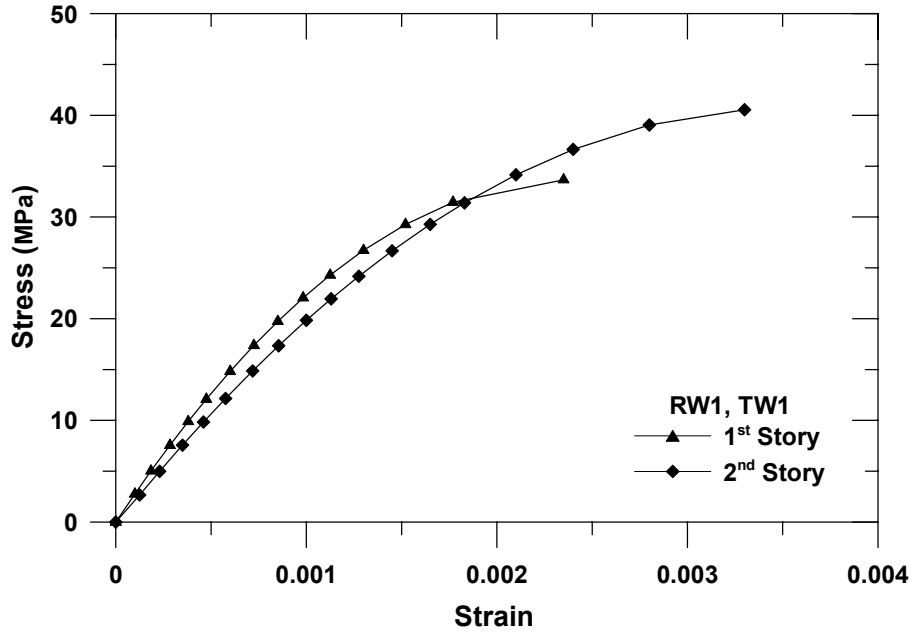


(a) Specimen RW2

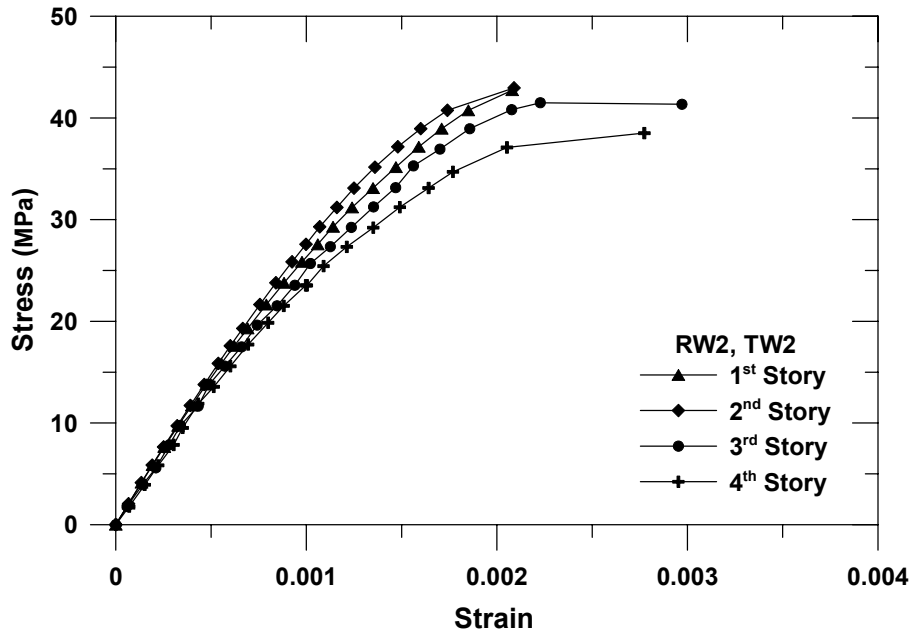


(b) Specimen TW2

Fig. 7.3 Wall cross-sectional views



(a) Specimens RW1 and TW1



(a) Specimens RW2 and TW2

Fig. 7.4 Measured concrete stress-strain relations

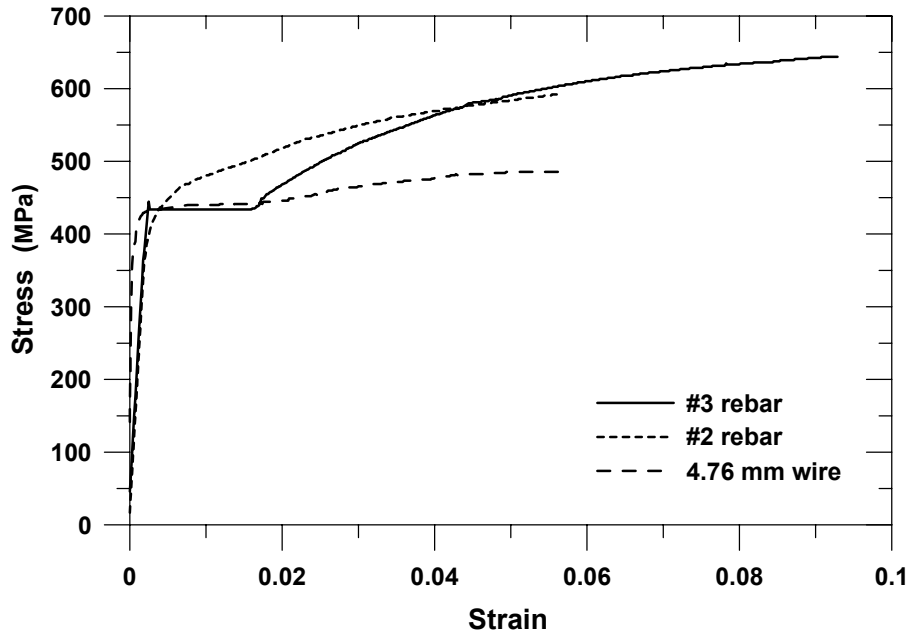


Fig. 7.5 Measured steel stress-strain relations

7.1.3 Testing Apparatus

The wall specimens were tested in an upright position in the Structural Engineering Research Laboratory (SERL) at Clarkson University. Figure 7.6 shows a schematic of the overall test setup. A photograph of the setup is shown in Figure 7.7. The walls were rigidly mounted to the strong floor through the use of eight 32 mm diameter high-strength steel tie-down rods, passing through the specimens' pedestals.

A specially fabricated load transfer assembly was used to transfer both axial and lateral loads to the wall specimen. The steel assembly was made of back-to-back channel sections (C-12x68's) welded together with a 19 mm gap between them to allow the post-tensioning strands to pass through. The load transfer assembly was attached to the wall specimen using 25 mm diameter threaded rods that were cast integrally with the fourth story of each specimen. Six threaded rods were used to attach the assembly to the rectangular walls, whereas nine rods were used on the T-shaped walls. Axial stress was applied by hydraulic jacks mounted on top of the load transfer assembly (Fig. 7.8). Post-tensioning strands were anchored in the specimen's pedestal and run up through the back-to-back channels and through the hollow jacks. An axial stress of approximately $0.10A_g f'_c$ was maintained throughout the duration of each test.

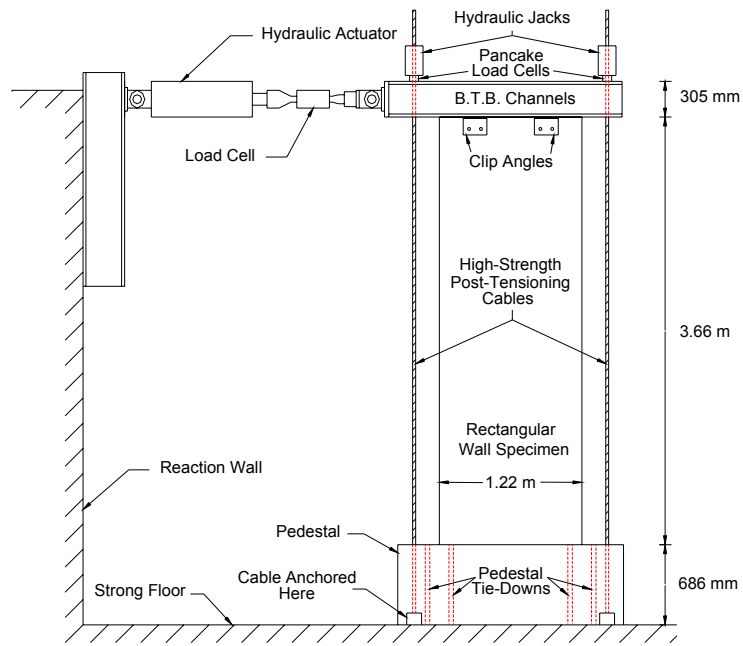


Fig. 7.6 Schematic of test setup (Thomsen and Wallace, 1995)



Fig. 7.7 Photograph of test setup (Thomsen and Wallace, 1995)



Fig. 7.8 Load transfer assembly

Cyclic lateral loads were applied to the walls by a 556 kN hydraulic actuator that was mounted horizontally to a reaction wall approximately 3.81 m above the base of the walls. Both ends of the actuator used a pin connection that allowed the actuator to rotate freely in the vertical plane throughout the tests (Fig. 7.9).



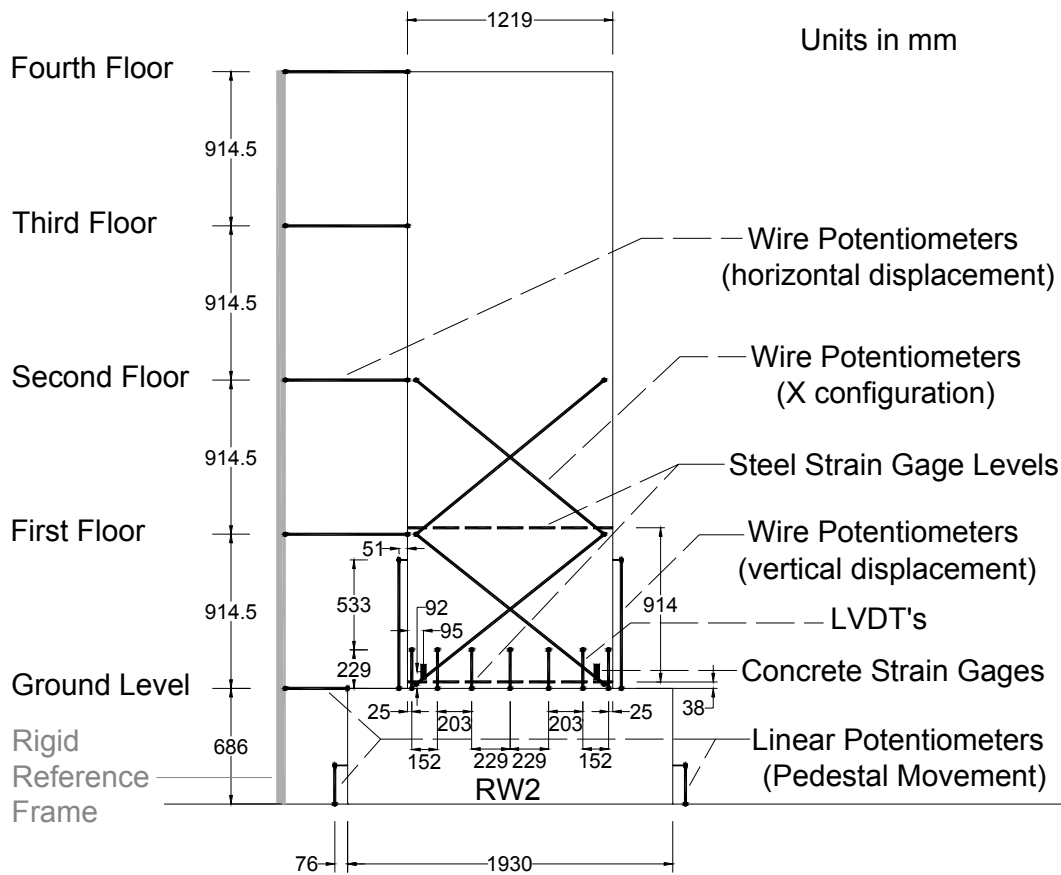
Fig. 7.9 Hydraulic actuator

Out-of-plane support was provided during each test to provide stability. A steel truss was placed between the top of the wall specimens and the reaction wall parallel to the specimen's web, allowing free movement parallel to the load direction but preventing perpendicular motion.

In this manner, twisting of the wall was eliminated and out-of-plane restraint was provided. The support system also did not inhibit vertical wall movement.

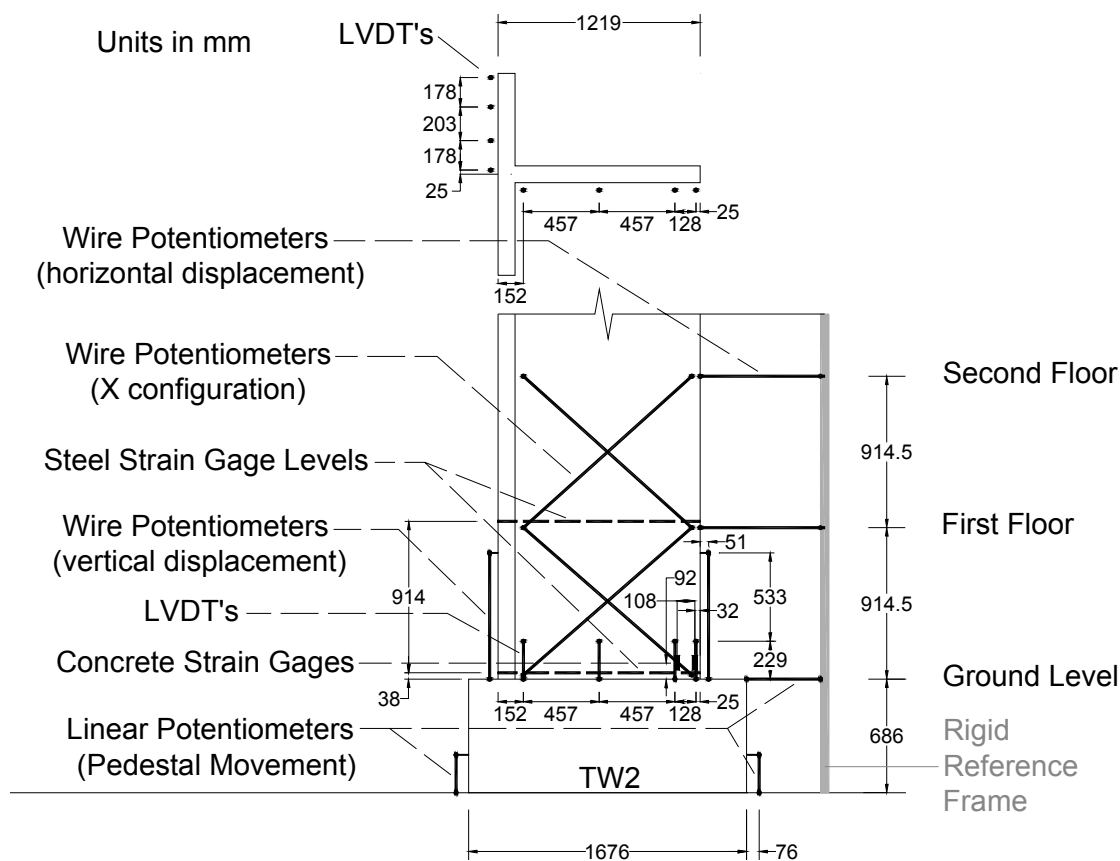
7.1.4 Instrumentation and Data Acquisition

Instrumentation was used to measure displacements, loads, and strains at critical locations for each wall specimen (Fig. 7.10). Wire potentiometers, linear potentiometers, and linear variable differential transducers (LVDTs) were used to measure displacement response. Load cells were used to measure axial and lateral loads, and strain gages were used to measure strains in the concrete and the reinforcing steel.



(a) Specimen RW2

Fig. 7.10 Instrumentation on wall specimens



(b) Specimen TW2

Fig. 7.10 (cont'd.) Instrumentation on wall specimens

A rigid steel reference frame was mounted to the strong floor at the end of the wall specimen to provide a location for instrumentation to be attached. Four wire potentiometers were mounted to the reference frame to measure lateral displacements at 0.91 m intervals (at floor levels) over the wall height. A linear potentiometer also was mounted horizontally on the pedestal to measure any horizontal slip of the pedestal along the strong floor. Two additional linear potentiometers were mounted vertically at each end of the pedestal to measure rotation caused by uplift of the pedestal from the strong floor (Figs. 7.10–7.11).

Axial loads were measured using hollow pancake load cells and lateral cyclic loads were measured using a 667 kN load cell mounted in series with the hydraulic actuator. The load cell used to measure lateral loads can be seen in Figure 7.8.

Shear deformations were measured through the use of wire potentiometers mounted on the bottom two stories (in an “X” configuration) of each specimen (Fig. 7.10). Figure 7.12 shows a photograph of the wire potentiometers used to measure shear deformations on specimen RW2.

Axial (vertical) displacements at the wall boundaries were measured using two wire potentiometers mounted between the base and first-story level at each end of the walls (Fig. 7.10). Wall base rotations were obtained by taking the difference in the axial displacements measured by the two wire potentiometers and dividing the difference in relative axial displacements by the distance between the potentiometers.

Linear variable differential transducers (LVDTs) were mounted vertically (Figs. 7.10, 7.13), over a gage length of 229 mm, at various locations along the web and flange of each wall so that axial strains and section curvatures could be calculated. The rectangular walls were instrumented with five (RW1) and seven (RW2) LVDTs spaced along the length of the wall, whereas the T-shaped walls had four LVDTs mounted along the web and four mounted along the outside face of the flange (Fig. 7.10).

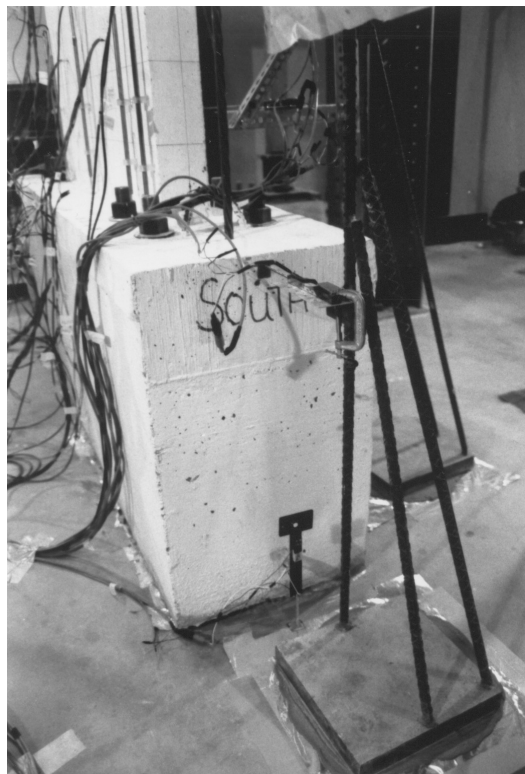


Fig. 7.11 Instrumentation used to measure pedestal movement

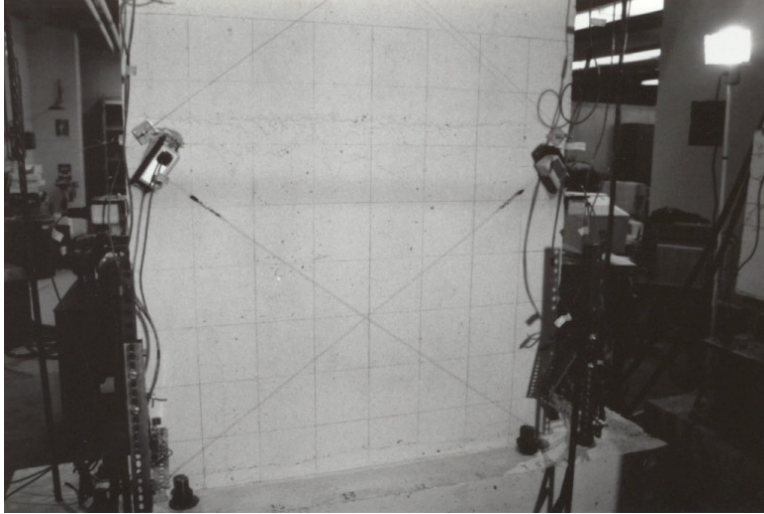


Fig. 7.12 Wire potentiometers used to measure shear deformations

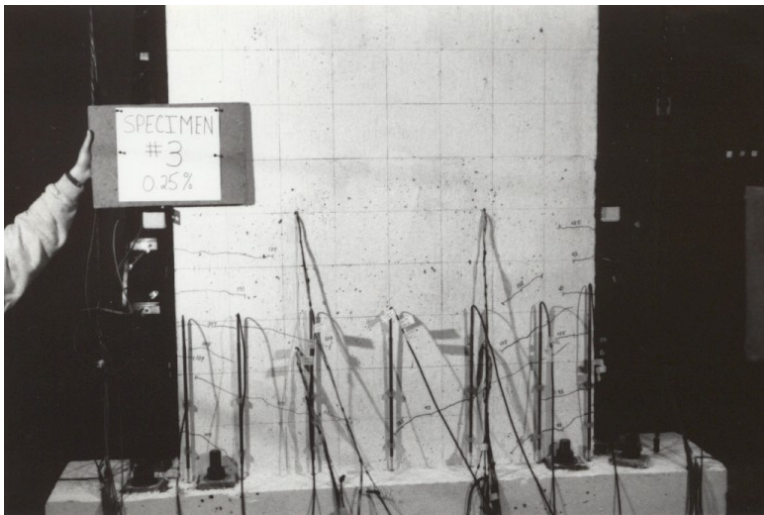


Fig. 7.13 Instrumentation located within first story

Axial concrete strains within the boundary regions of specimens RW2 and TW2 also were measured using embedded concrete strain gages (Fig. 7.10). The center of these gages were located approximately 92 mm above the pedestal interface, with one gage in each boundary element for RW2, whereas TW2 had two gages in the web boundary element. The gages were oriented vertically. Figure 7.14 shows a photograph of the embedded concrete strain gages located in the boundary regions of specimen RW2.

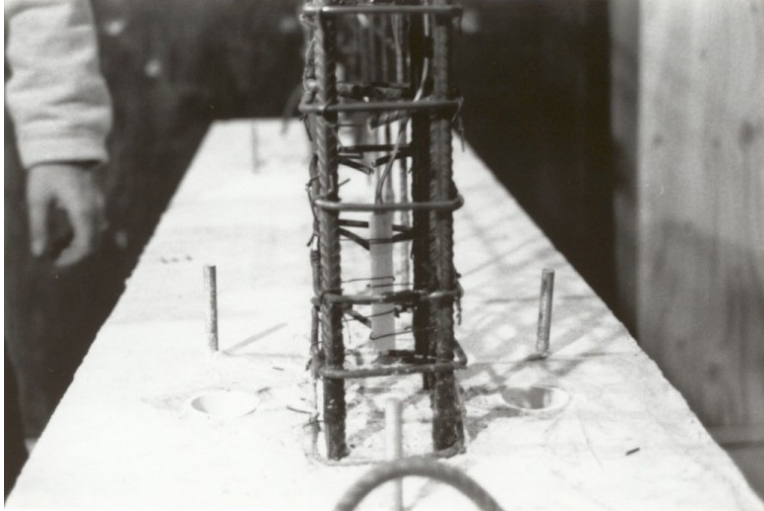


Fig. 7.14 Embedded concrete strain gage in boundary element

The strains in the reinforcing steel also were measured through the use of strain gages at wall base and first-story levels. All three types of reinforcement (longitudinal, uniformly distributed web, and transverse boundary) were monitored at various locations. The longitudinal reinforcing bars (#3, $d_b = 9.53$ mm) were instrumented at two distinct levels; just above the wall-pedestal interface (at approximately 25 mm above the pedestal), and close to the first floor level (at approximately 0.95 m above the pedestal) (Fig. 7.10). The vertical web reinforcement (#2 bars, $d_b = 6.35$ mm) was also instrumented at those levels. The horizontal web bars were instrumented at various heights of the walls as well as at various positions along the length of the walls (see Thomsen and Wallace, 1995). The transverse boundary reinforcement (4.76 mm diameter wire) was heavily instrumented at critical locations of the cross section. Gages were installed on the transverse boundary reinforcement located just above the pedestal, and approximately 229 and 457 mm above the pedestal.

7.1.5 Testing Procedure

Testing was initiated by taking a reading from all instruments prior to load application. The axial load was then applied through the use of hand pumps. Once the axial load reached its specified level (approximately $0.10A_g f'_c$), valves on the hand pumps were shut off to ensure that the load would remain constant throughout the test. The axial load was monitored continuously by either the load cells or by the pressure gages attached directly to the hand pumps.

The reversed cyclic loads were then applied under displacement control. The first drift level to be applied was approximately 0.1%, followed by 0.25%. The drift level was then increased in 0.25% increments up to 1.0%. For specimens RW2 and TW2, the next drift level applied was 1.5% and another drift level of 1.0% followed. The drift was then increased in 0.5% increments up to 2.5% for RW2 and 3% for TW2. At least two complete cycles were performed at each drift level. A total of 20 full cycles for RW2 and 22.5 cycles for TW2 were applied. Figure 7.15 plots the applied lateral drift routines that were followed for testing of specimens RW2 and TW2. Specimens RW1 and TW1 were subjected to a fewer number of cycles prior to reaching wall failure (see Thomsen and Wallace, 1995). All measurements were read by a computer data acquisition system at 32 points throughout each cycle.

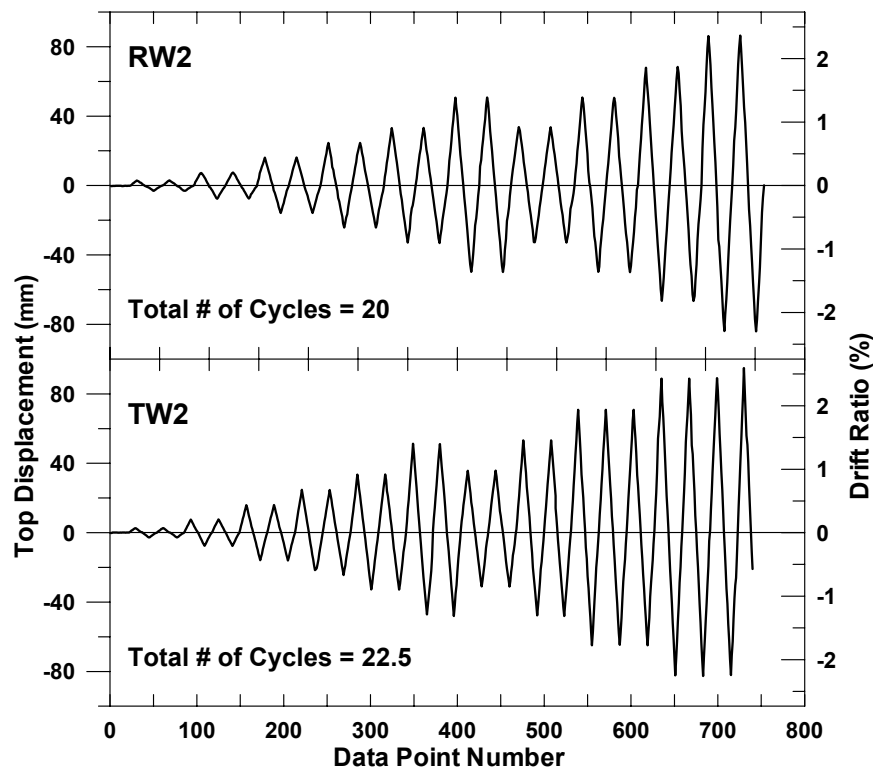


Fig. 7.15 Lateral drift routines for specimens RW2 and TW2

7.2 CALIBRATION OF ANALYTICAL MODEL

In this study, calibration of the analytical model and comparison of analytical and experimental results is limited to the rectangular wall specimen RW2 and the T-shaped wall specimen TW2 because specimens RW2 and TW2 were observed to withstand many cycles of inelastic

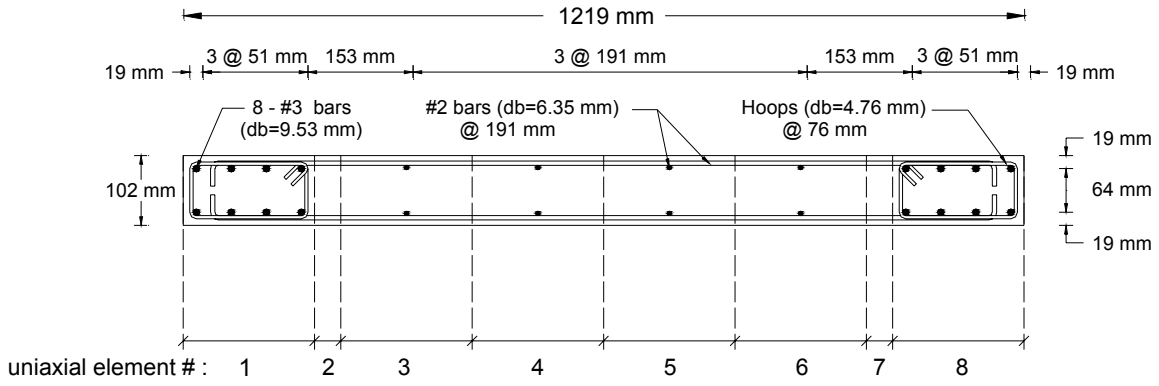
deformation until failure. In the following sections, calibration of model and material parameters are described.

7.2.1 Calibration for Model Geometry

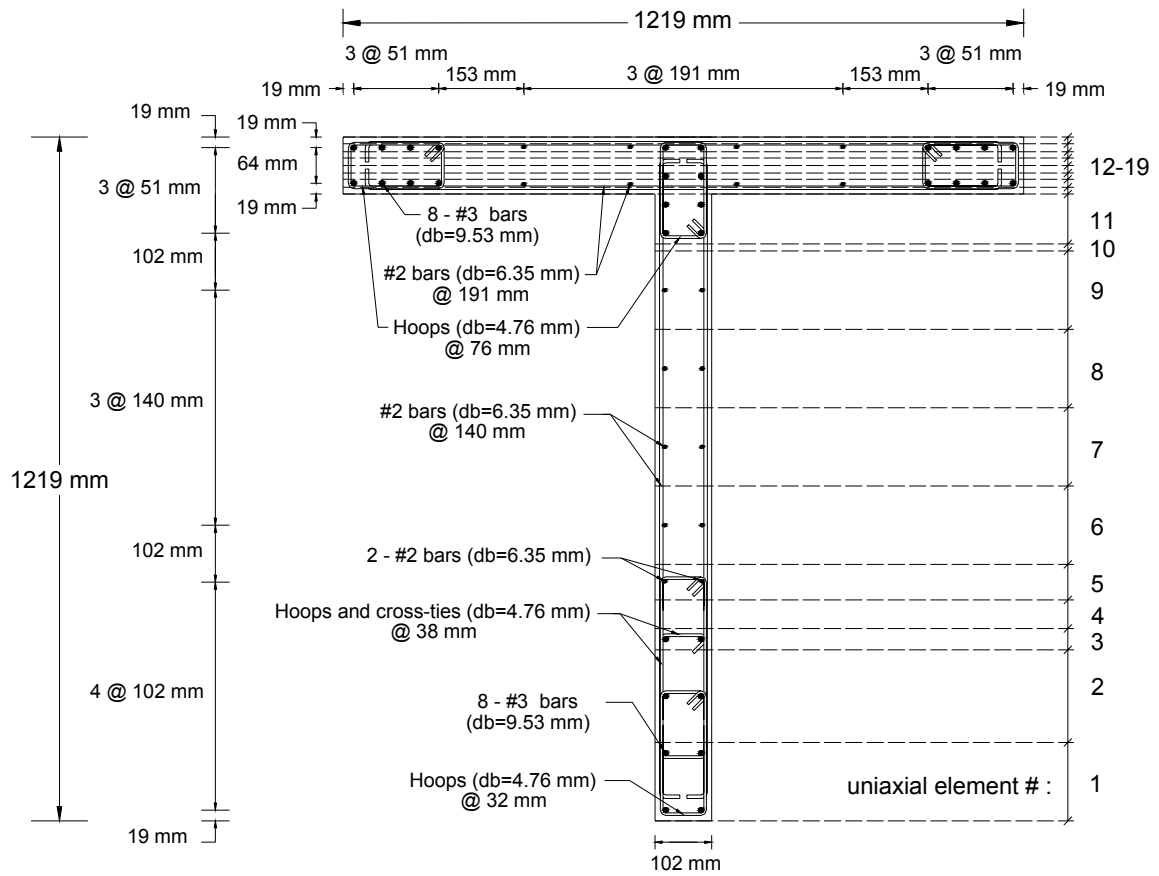
Figure 7.16 displays possible model configurations, with 8 elements stacked upon each other ($m = 8$), with 8 uniaxial elements defined along the length of the wall ($n = 8$) for specimen RW2, and 19 uniaxial elements ($n = 19$) for specimen TW2. A refined configuration with 8 uniaxial elements was assigned for the flange specimen TW2, since the neutral axis was expected to be within the flange during loading subjecting the flange to compression.

The tributary area on the cross section assigned to each uniaxial element is also indicated on Figure 7.16. As discussed in Chapter 6, increasing the number of uniaxial elements or the number of MVLEs along wall height does not change significantly the prediction of the global response (i.e., lateral load versus wall story displacements); however, use of more MVLEs along wall height is valuable in terms of obtaining more detailed information on responses at a given location. Thus, the analytical model is refined for subsequent comparisons and discussions for local responses by modifying the number of MVLEs along wall height, depending on the location where a local response comparison between the analytical and experimental results is desired (e.g., LVDT locations, steel strain gage locations, concrete strain gage locations, wire potentiometer locations).

For the refined analytical models, 16 MVLEM elements were used for the modeled walls ($m = 16$), with 8 elements along the first-story height, 4 elements along the second story, and 2 elements along the third and fourth stories. A value of 0.4 was selected for the parameter c defining the center of relative rotation for each wall element, based on prior studies (Vulcano et al., 1988). As also discussed in Chapter 6, using a large number of MVLEs along wall height, as has been done in this study, will diminish the influence of the parameter c on the predicted response.



(a) Specimen RW2



(b) Specimen TW2

Fig. 7.16 Model discretization and tributary area assignment

7.2.2 Calibration for Constitutive Material Parameters

7.2.2.1 Steel Stress-Strain Relations

The reinforcing steel stress-strain relation (Fig. 7.17) described by the Menegotto and Pinto (1977) model (as extended by Filippou et al., 1983) was calibrated to reasonably represent the experimentally observed properties of the longitudinal reinforcement used in the experimental study. An elastic modulus of $E_0 = 200$ GPa was assigned to the steel stress-strain model based on monotonic stress-strain tests conducted on the #3 ($d_b = 9.53$ mm) and #2 ($d_b = 6.35$ mm) deformed bars used at the wall boundaries and within the web, respectively. Tensile yield strengths of $\sigma_y = 434$ MPa and $\sigma_y = 448$ MPa, and a strain-hardening ratio of $b = 0.02$ were assigned for the bare #3 and #2 bars, respectively. These parameters also were used to calibrate the stress-strain relation for the reinforcing bars in compression. The yield strength and strain-hardening parameters for the bare bars in tension were modified according to the empirical relations proposed by Belarbi and Hsu (1994) to include the effect of tension stiffening on steel bars embedded in concrete.

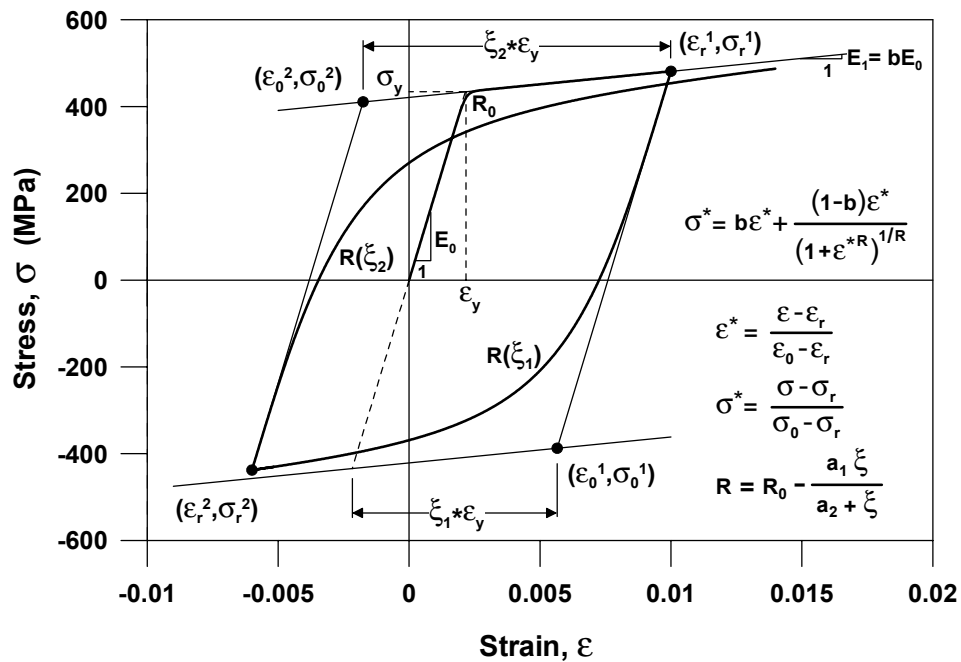


Fig. 7.17 Constitutive model for reinforcing steel and associated parameters

Figure 7.18 shows the calibrated analytical steel stress-strain relations in tension and compression, as well as stress-strain test results for the reinforcement used in the construction of the wall specimens.

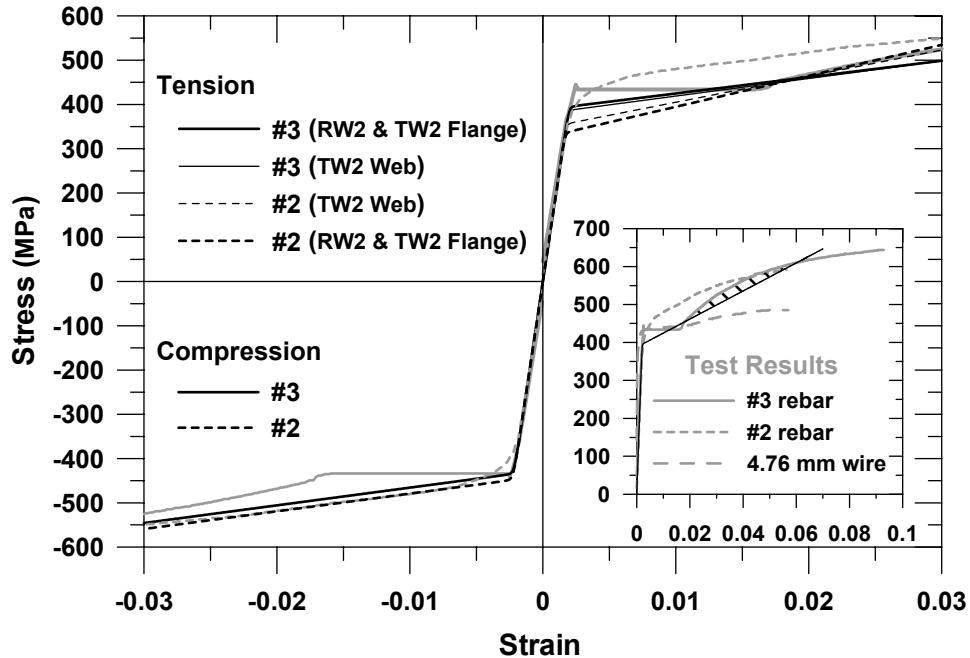


Fig. 7.18 Calibration of constitutive model for reinforcing steel

The parameters used for the calibration of the steel stress-strain relation for compression and tension are provided in Tables 7.1–7.2. The parameters σ_y and b for tension differ along the length of the walls due to the variation of the longitudinal steel area ratios based on the findings presented Belarbi and Hsu (1994).

The calibration of parameters R_0 , a_1 , and a_2 (accounting for the cyclic degradation of the curvature coefficient R and the Bauschinger effect) requires cyclic test results, which are generally not available. Elmorsi et al. (1998) used values of $R_0 = 20$, $a_1 = 18.5$, and $a_2 = 0.0015$ based on the experimental results carried out by Seckin (1981); the same values were used in this study. As discussed by Dodd and Restrepo-Posada (1995), the hysteretic properties of steel associated with the Bauschinger effect are sensitive to the carbon content of the steel, and thus, variations in the behavior are possible. The sensitivity of the model response with regard to these parameters is discussed in Chapter 6.

Table 7.1 Calibrated parameters for concrete in tension and steel in compression

Concrete in Tension					#3 Rebar in Compression			#2 Rebar in Compression		
f_t (MPa)	ε_t	E_c (GPa)	ε_{cr}	r	σ_y (Mpa)	E_0 (GPa)	b	σ_y (MPa)	E_0 (GPa)	b
2.03	0.00008	31.03	∞	1.2	434	200	0.02	448	200	0.02

Table 7.2 Calibrated parameters for concrete in compression and steel in tension

Material	Parameter	RW2		TW2				
		Boundary (Confined)	Web (Unconfined)	Flange (Confined)	Flange (Unconfined)	Flange-Web Intersection (Confined)	Web (Unconfined)	Web (Confined)
Concrete in Compression	f'_c (Mpa)	47.6	42.8	43.9	42.8	43.9	42.8	57.1
	ε'_c	0.0033	0.0021	0.0024	0.0021	0.0024	0.0021	0.0056
	E_c (GPa)	31.03	31.03	31.03	31.03	31.03	31.03	31.03
	ε_{cr}	0.0037	0.0022	0.0025	0.0022	0.0025	0.0022	0.0073
	r	1.90	7.00	3.80	7.00	3.80	7.00	1.45
#3 Rebar in Tension	σ_y (MPa)	395		395		395		387
	E_0 (GPa)	200		200		200		200
	b	0.0185		0.0185		0.0185		0.02
#2 Rebar in Tension	σ_y (MPa)		336		336		356	
	E_0 (GPa)		200		200		200	
	b		0.0350		0.0350		0.0295	

7.2.2.2 Concrete Stress-Strain Relations

The monotonic envelope curves of the implemented concrete hysteretic stress-strain relation for compression and tension allow control on the shape of both the ascending and descending (i.e., pre-peak and post-peak) branches of the stress-strain behavior. The curves can be calibrated for selected values of peak stress, strain at peak stress, elastic modulus, and also via the parameter r defining the shape of the envelope curve, allowing for model refinement. The envelope curve used in the analytical model for concrete in compression (Fig. 7.19) was calibrated for unconfined concrete using results of monotonic stress-strain tests conducted at time of testing on standard 152.4 mm x 304.8 mm cylinder specimens of the concrete used in the construction of the walls (Fig. 7.20). The compressive strength was assigned a value of $f'_c = 42.8$ MPa in accordance with the observed compressive strength at the first-story height (0 to 0.91 m) of the test specimens; whereas the strain at peak compressive stress, ε'_c , was set equal to 0.0021. The

initial tangent modulus (elastic modulus) of concrete was assigned a value of $E_c = 31$ GPa. The shape of the envelope curve was refined to simulate the measured stress-strain relation by calibrating the parameter r to a value of 7.0, where r defines the shape of the envelope curve (see Chapter 4).

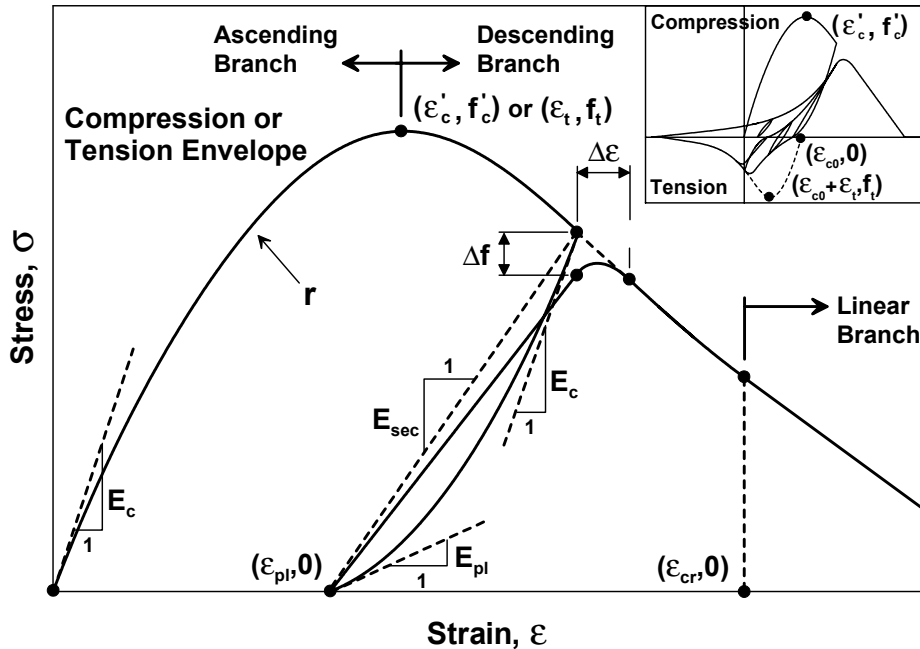


Fig. 7.19 Constitutive model for concrete and associated parameters

The concrete tensile strength was determined from the relation $f_t = 0.31\sqrt{f'_c}$ (MPa) as 2.03 MPa, and a value of 0.00008 was selected for the strain (ϵ_t) at peak monotonic tensile stress as suggested by Belarbi and Hsu (1994) based on a series of tests on RC panels with concrete cylinder compressive strengths (f'_c) ranging between 36.9 MPa and 47.7 MPa, which is consistent with the compressive strength of concrete used for the construction of the wall specimens ($f'_c = 42.8$ MPa). The elastic modulus in tension was assigned the same value used for compression ($E_c = 31$ GPa). An r -value of 1.2 was used to define the shape of the monotonic tension envelope so that it reasonably agreed with the average post-crack stress-strain relation proposed by Belarbi and Hsu (1994) based on the effects of tension stiffening on concrete (Fig. 7.21).

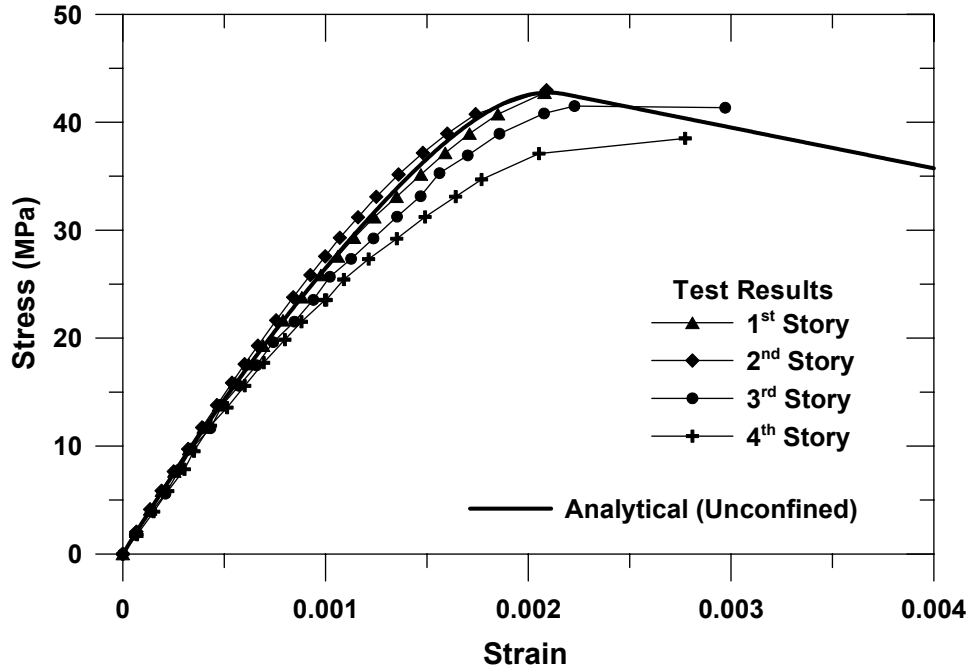


Fig. 7.20 Calibration of constitutive model for unconfined concrete in compression

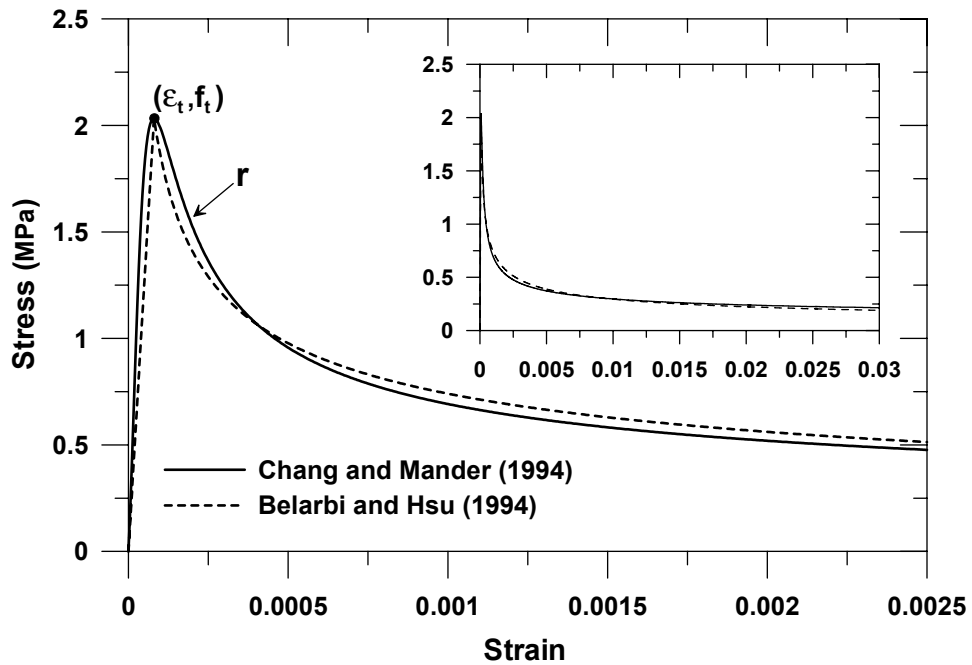


Fig. 7.21 Calibration of constitutive model for concrete in tension

The compression envelope used in the analytical model for confined concrete was calibrated using the empirical relations proposed by Mander et al. (1988a) for the peak compressive stress and the strain at peak compressive stress. The confined concrete stress-strain behavior was manipulated based on the area, configuration, spacing, and yield stress of the transverse reinforcement (Fig. 7.4; 435 MPa for the 4.76 mm wire) in the confined regions within the first-story height (0–0.91 m) of the test specimens. Accordingly, in the analytical model, the peak compressive stress (compressive strength of confined concrete) and the strain at peak compressive stress were modified within the confined concrete areas located at the wall boundaries. Figure 7.22 compares the monotonic stress-strain relations used in the wall models for confined and unconfined concrete with the relations proposed by Saatcioglu and Razvi (1992). The strain ϵ_{cr} , where the monotonic stress-strain relation enters a linear stress degrading range after reaching the peak value, was calibrated such that the post-peak slope of the present stress-strain model agrees with the post-peak slope of the Saatcioglu and Razvi model for both confined and unconfined concrete (Fig. 7.22). The parameters used for the calibration of the monotonic (envelope) stress-strain relations for concrete in tension and for confined and unconfined concrete in compression are presented in Tables 7.1–7.2. The parameters for unconfined concrete were also used for the cover concrete areas at the wall boundaries.

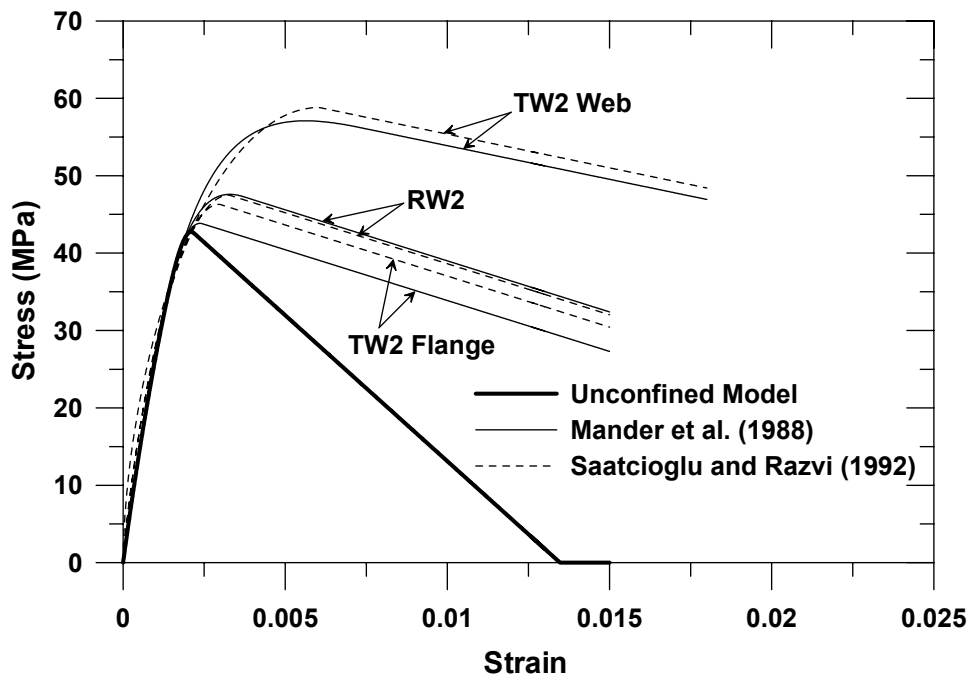


Fig. 7.22 Calibration of constitutive model for confined concrete

The hysteretic stress-strain rules defined by Chang and Mander (1994) were used to simulate the cyclic behavior of both confined and unconfined concrete relations implemented in the wall model. The cyclic properties of the stress-strain relation by Chang and Mander are controlled by key hysteretic parameters including secant stiffness (E_{sec}) and plastic stiffness (E_{pl}) upon unloading from, and stress and strain offsets (Δf and $\Delta \epsilon$) upon return to, the compression envelope (Fig. 7.19). An extensive column database was used by Chang and Mander (1994) to develop empirical relations for these parameters. The same empirical relations were used in the present model, as they were found to produce consistent results when used with the values specified for the remaining model and material parameters. Further details on the implemented concrete stress-strain relation can be found in Chapter 4 and in Chang and Mander (1994).

7.2.2.3 Shear force–Deformation Relation

The study presented in this Chapter focuses on modeling of the flexural responses; thus a linear elastic force-deformation behavior was adopted for the horizontal “shear” spring. The experimental results were separated into flexural and shear response components using the methodologies described in Massone and Wallace (2004). In order to compare model results directly with the measured flexural responses, the stiffness of the shear spring (k_H) was assigned a very large (~infinite) value.

7.3 MODEL RESULTS AND COMPARISON WITH EXPERIMENTAL RESULTS

The analytical model was implemented in Matlab (MathWorks, 2001) to allow comparison between experimental and analytical results. A displacement-controlled nonlinear analysis strategy was selected in order to correlate the model results with results of the drift-controlled cyclic tests subjected to prescribed lateral displacement histories at the top of the walls. Details of the solution strategy are provided in Chapter 5.

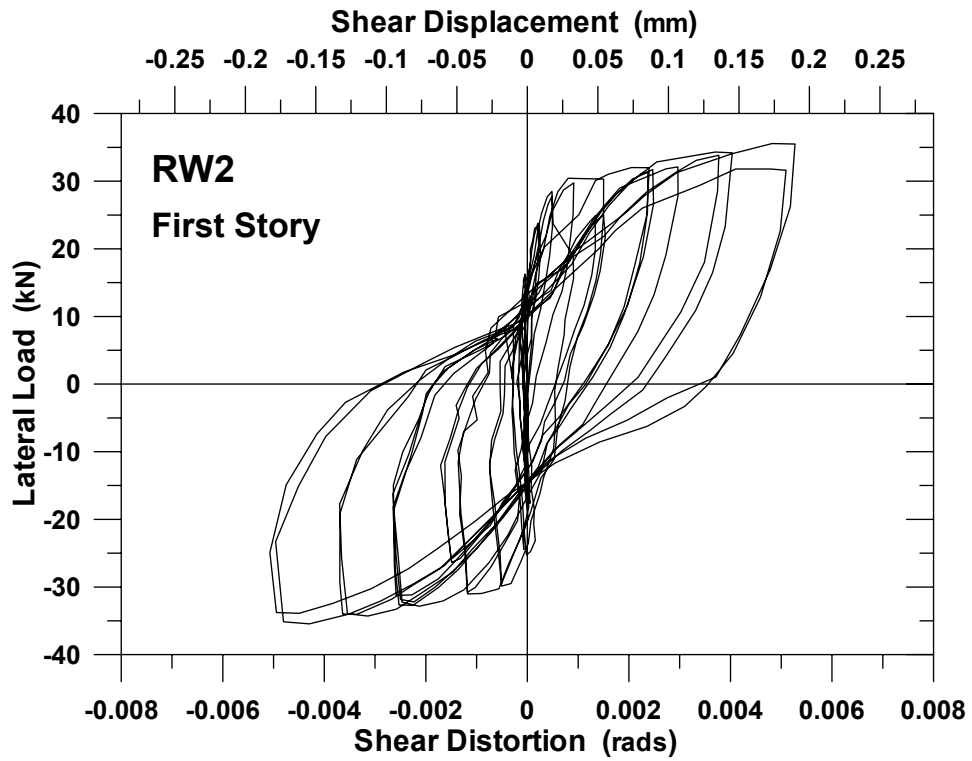
Prior to analysis, the lateral top displacement history applied during testing and the measured lateral story displacement histories for each specimen were corrected to remove

displacement contributions resulting from shear and pedestal movement to allow for a direct comparison of the measured and predicted flexural responses.

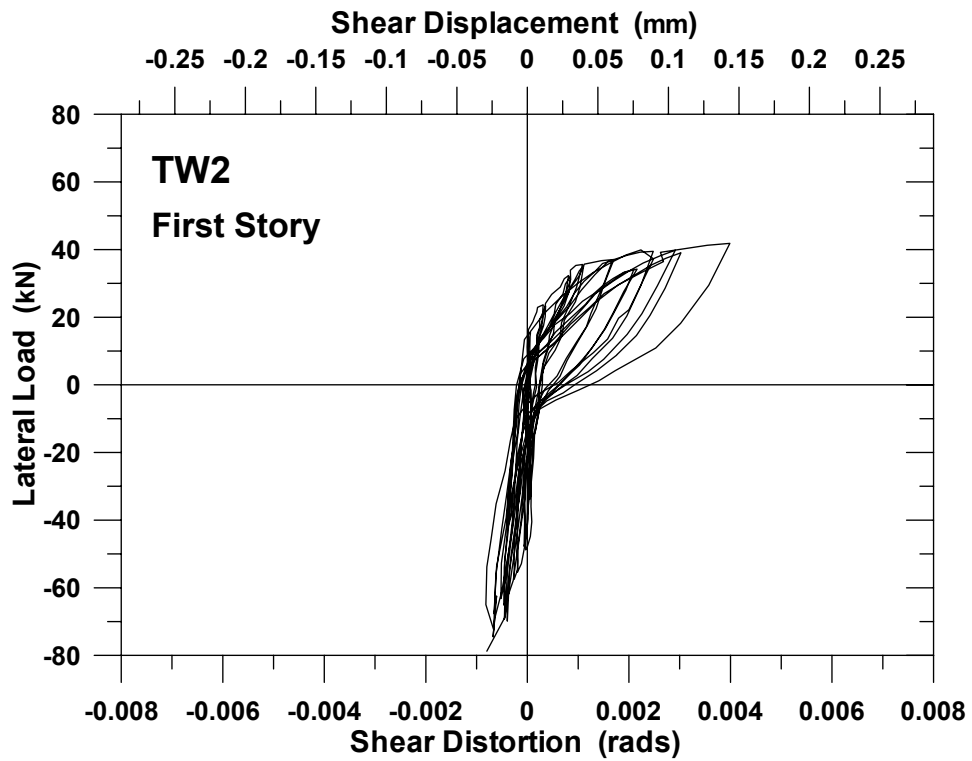
Measurements obtained in horizontal and vertical linear potentiometers mounted on the pedestals (Fig. 7.10) were used to remove displacements caused by pedestal rotation (caused by uplift) and pedestal sliding in the direction of the applied load. Wall shear deformations were calculated using data from wire potentiometers mounted on the bottom two stories of each specimen (Fig. 7.10) using the procedure recommended by Massone and Wallace (2004). The largest shear deformations were concentrated within the first-story height of the walls (Fig. 7.23), where shear yielding was observed together with flexural yielding. The measured lateral load – shear deformation response in the second story was observed to follow an approximately linear elastic relation (Fig. 7.24); thus, the shear deformations in the third and fourth stories of the wall specimens were estimated for the entire loading history using the linear elastic shear stiffness values derived for the second-story level (~ 100 MN/rad for RW2 and ~ 160 MN/rad for TW2).

It should be mentioned that one of the “X” configuration wire potentiometers mounted on the first story of specimen TW2 failed at data point (load step) number 558. The shear deformations in the first story for the remainder of the loading history were obtained by extrapolation assuming that the proportionality between the measured shear deformations and the measured first-story rotations (rotations were measured via the two vertical wire potentiometers mounted to wall ends in Figure 7.10) before the instrument failed, applies after the instrument failed.

Figure 7.25 compares the lateral top displacement history applied to specimens RW2 and TW2 during testing, with lateral top displacement histories obtained after subtracting the contributions due to pedestal movement and shear deformations. Table 7.3 lists the corresponding peak (reversal) lateral top displacement values for the first cycle of each applied drift level. A considerable reduction is observed in the top displacement values due to the contributions of both pedestal movement and shear deformations.

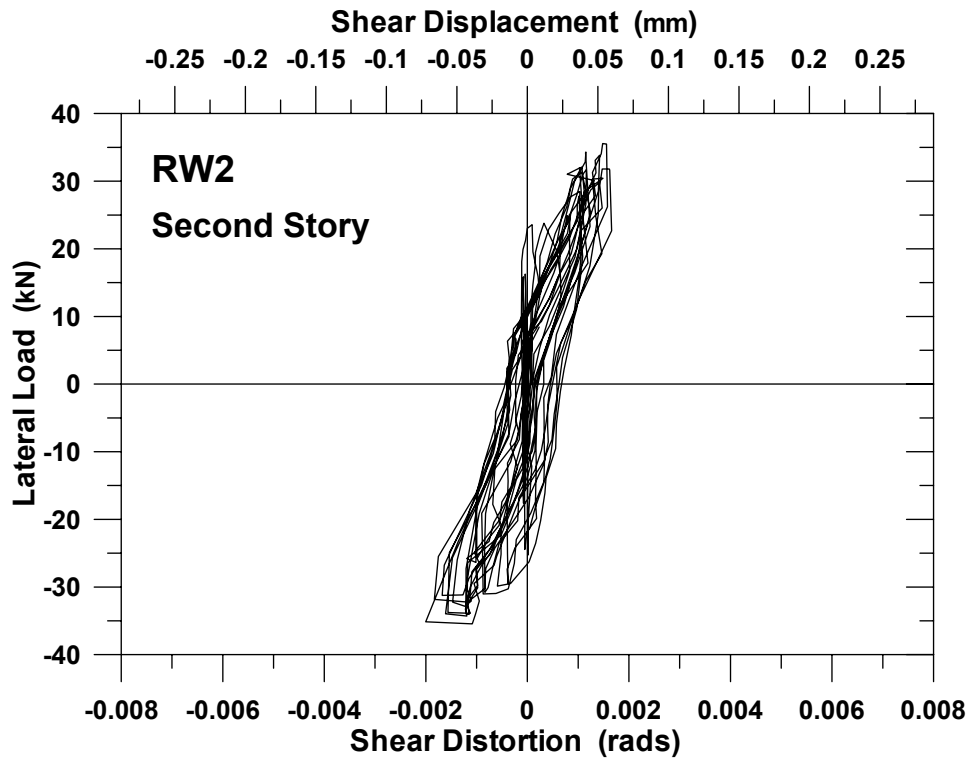


(a) Wall RW2

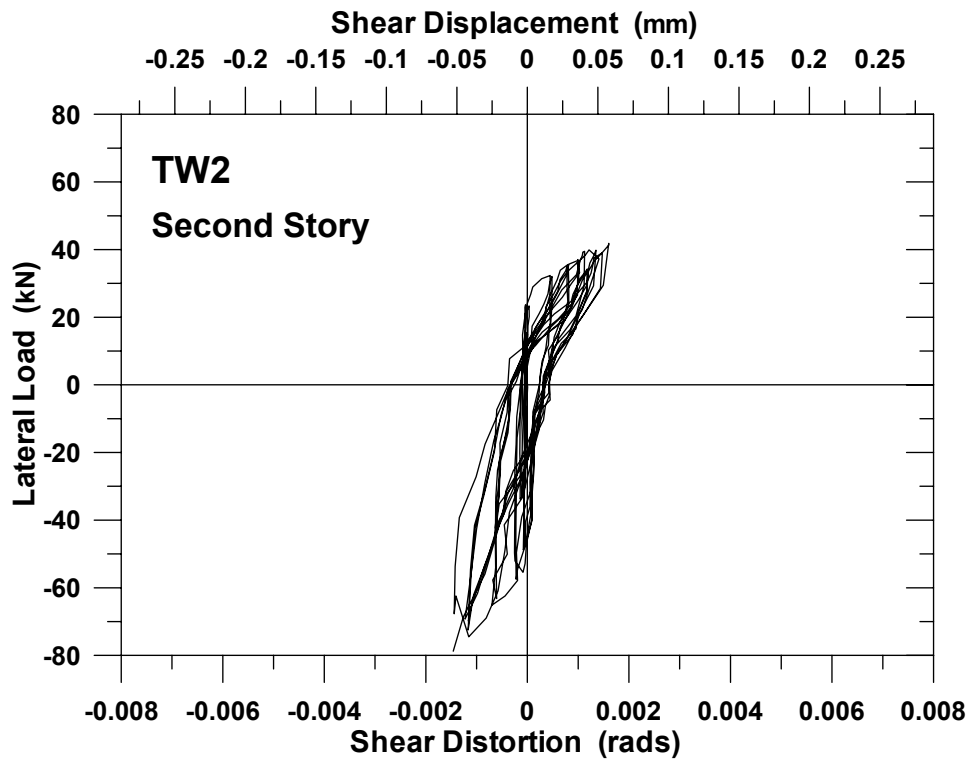


(b) Wall TW2

Fig. 7.23 Measured first-story shear deformations



(a) Wall RW2



(b) Wall TW2

Fig. 7.24 Measured second-story shear deformations

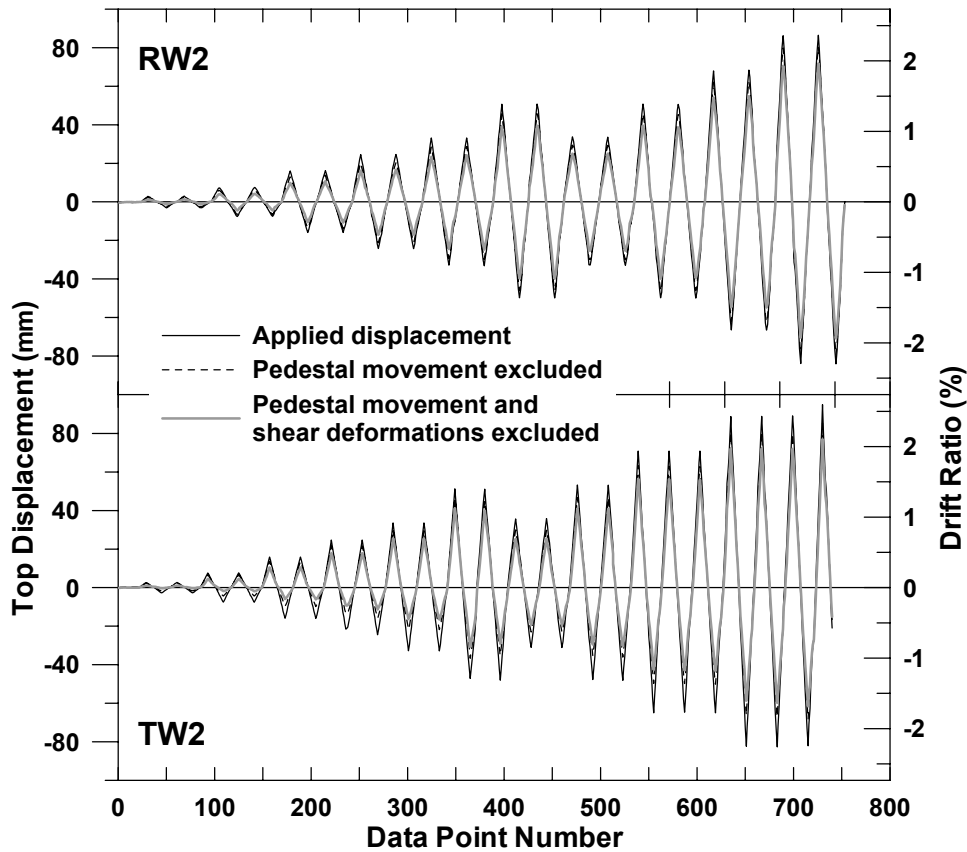


Fig. 7.25 Top lateral displacement history of wall specimens

Table 7.3 Peak lateral top displacements at applied drift levels

Wall	Load Direction	Top Displacement	Lateral Drift (%)							
			0.1%	0.25%	0.5%	0.75%	1.0%	1.5%	2.0%	2.5%
RW2	Positive	(a)	2.9	7.2	16.1	24.5	33.1	50.6	67.9	86.2
		(b)	2.3 [81] ¹	5.9 [82]	13.0 [81]	20.1 [82]	28.5 [86]	45.5 [90]	62.1 [91]	79.8 [93]
		(c)	1.2 [52] ²	4.0 [68]	9.9 [76]	16.2 [80]	23.4 [82]	39.4 [86]	54.2 [87]	70.6 [88]
	Negative	(a)	-3.2	-7.6	-15.9	-24.2	-32.8	-49.8	-66.5	-83.8
		(b)	-2.6 [83]	-6.5 [85]	-13.7 [86]	-21.2 [88]	-29.4 [90]	-46.0 [92]	-62.1 [93]	-79.2 [94]
		(c)	-1.3 [50]	-4.4 [67]	-10.6 [77]	-17.1 [80]	-24.5 [83]	-39.8 [86]	-54.6 [88]	-70.5 [89]
TW2	Positive	(a)	2.5	7.6	15.9	24.8	33.5	51.3	70.9	88.8
		(b)	2.1 [86]	6.6 [87]	13.7 [86]	21.7 [87]	29.9 [89]	46.5 [91]	63.3 [89]	80.2 [90]
		(c)	1.0 [47]	4.5 [68]	10.5 [77]	17.9 [83]	25.5 [85]	41.2 [89]	56.5 [89]	72.2 [90]
	Negative	(a)	-2.5	-7.6	-15.9	-21.2	-32.7	-47.1	-64.9	-82.2
		(b)	-1.6 [65]	-4.3 [57]	-9.7 [61]	-13.5 [64]	-21.7 [66]	-36.6 [78]	-49.6 [76]	-66.2 [80]
		(c)	-0.4 [26]	-1.8 [41]	-5.9 [61]	-9.4 [69]	-16.3 [75]	-30.9 [84]	-42.6 [86]	-58.7 [89]

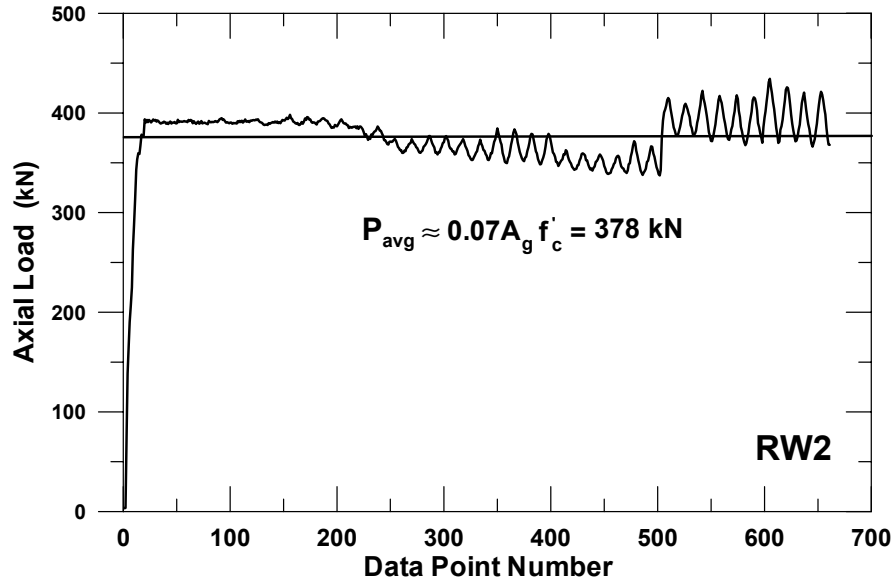
(a) Top displacement applied during testing (mm)

(b) Top displacement with pedestal movement contribution subtracted (mm)

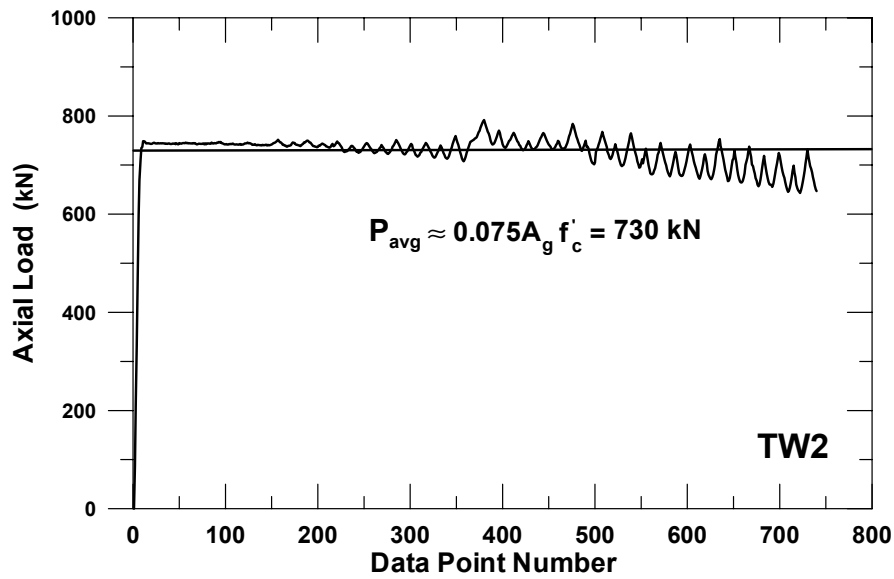
(c) Top displacement with pedestal movement and shear deformation contributions subtracted (mm)

¹[Value in brackets] = (b)/(a) (%)

²[Value in brackets] = (c)/(b) (%)



(a) Wall RW2



(b) Wall TW2

Fig. 7.26 Axial load history of wall specimens

The analytical models for specimens RW2 and TW2 were subjected to the modified top displacement histories determined using the procedures outlined in the prior paragraphs. The measured axial load histories applied on the wall specimens, as measured by load cells during testing (Fig. 7.26), were applied to the analytical models (on average, approximately $0.07A_g f'_c$ for RW2 and $0.075A_g f'_c$ for TW2, with variation of approximately $\pm 10\%$). Comparisons

between model predictions of the flexural responses and test results are summarized for RW2 and TW2 in the following sections.

7.3.1 Rectangular Wall, RW2

Figure 7.27 compares the measured and predicted lateral load – top flexural displacement responses for the rectangular wall specimen RW2. The analytical model captures reasonably well the measured response. Cyclic properties of the response, including stiffness degradation, hysteretic shape, plastic (residual) displacements, and pinching behavior are accurately represented in the analytical results; therefore, the cyclic properties of the implemented analytical stress-strain relations for steel and concrete produce good correlation for global response.

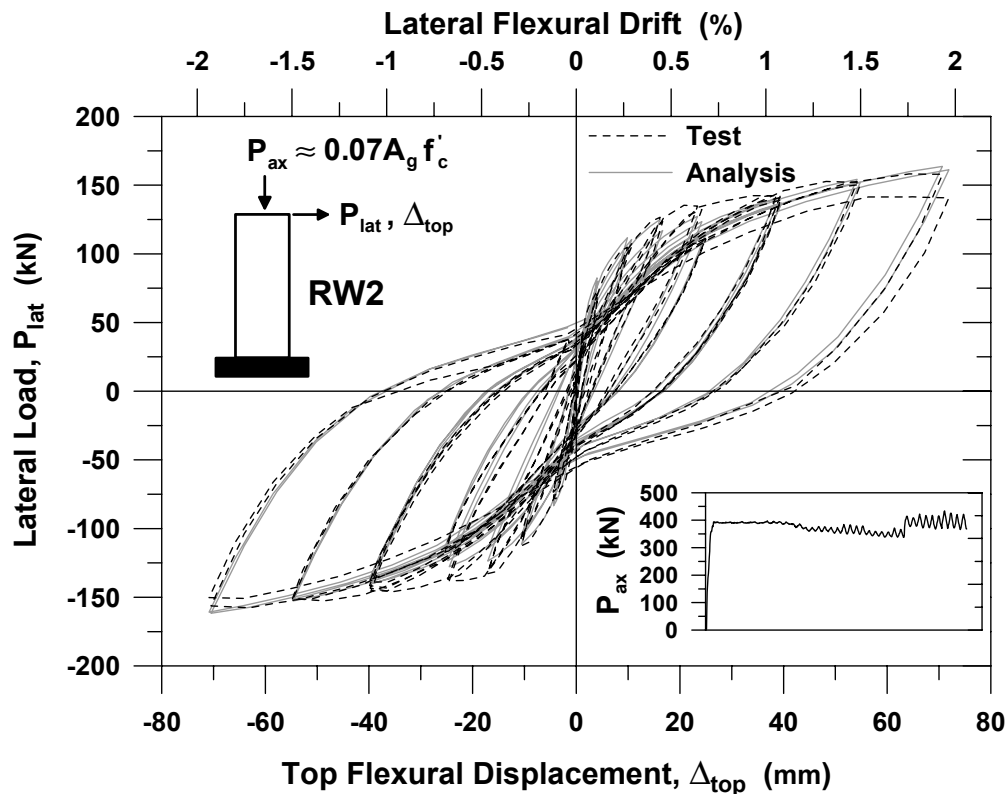


Fig. 7.27 Wall RW2, measured vs. predicted load-displacement responses

The lateral capacity of the wall is predicted very closely for most of the lateral drift levels. The underestimation of the wall capacity at intermediate drift levels (e.g., 0.5–1.5 % drift) can be attributed to the inability of the analytical stress-strain yield asymptote for steel in tension to model the curved strain-hardening region observed in the stress-strain tests for the #3 longitudinal reinforcing bars (see Fig. 7.18), as well as the uncertainty in the calibration of the cyclic parameters governing the implemented steel stress-strain relation (R_0 , a_1 , and a_2) and the parameters associated with concrete tensile strength (f_t and ε_t). Recalibration of the material parameters (e.g., $R_0 = 20$, $a_1 = 18.5$, $a_2 = 0.15$; and/or $f_t = 0.5\sqrt{f'_c}$ (MPa) and ε_t increased in proportion with f_t , with shape parameter r unchanged), would increase the predicted wall capacity for these intermediate drift levels and result in improved correlation. However, such recalibration would impair the correlation for the wall capacity at other drift levels, as well as the cyclic properties of the wall response including plastic (residual) displacements and pinching. The reader should refer to Chapter 6 for information on the sensitivity of model results to these material parameters.

Figure 7.28 shows a comparison of the lateral flexural displacements of the wall, at peak top displacement (top displacement reversal) data points for each drift level, measured by the horizontal wire potentiometers at the first-, second-, and third-story levels, (Fig. 7.10); with the results of the analysis. The analytical model provides a good prediction of the wall lateral displacement profile, and the distribution of deformations along wall height. The reader should note that the drift levels noted in the caption of Figure 7.28, and in all subsequent figures, correspond to “nominal” drift levels applied to the wall during testing, versus actual drift levels (i.e., measured top displacement modified to remove contributions from pedestal and shear deformations that are reported in this chapter).

Figure 7.29 plots the measured and predicted lateral flexural displacement histories at the first-story height (0.91 m) and the rotations accumulated over the bottom 0.76 m of the wall (rotations were measured via the two vertical wire potentiometers mounted to wall ends (Fig. 7.10)). Again, very good agreement between the experimental and analytical results is observed, indicating that the model successfully predicts the nonlinear flexural deformations experienced within the plastic hinge region of the wall.

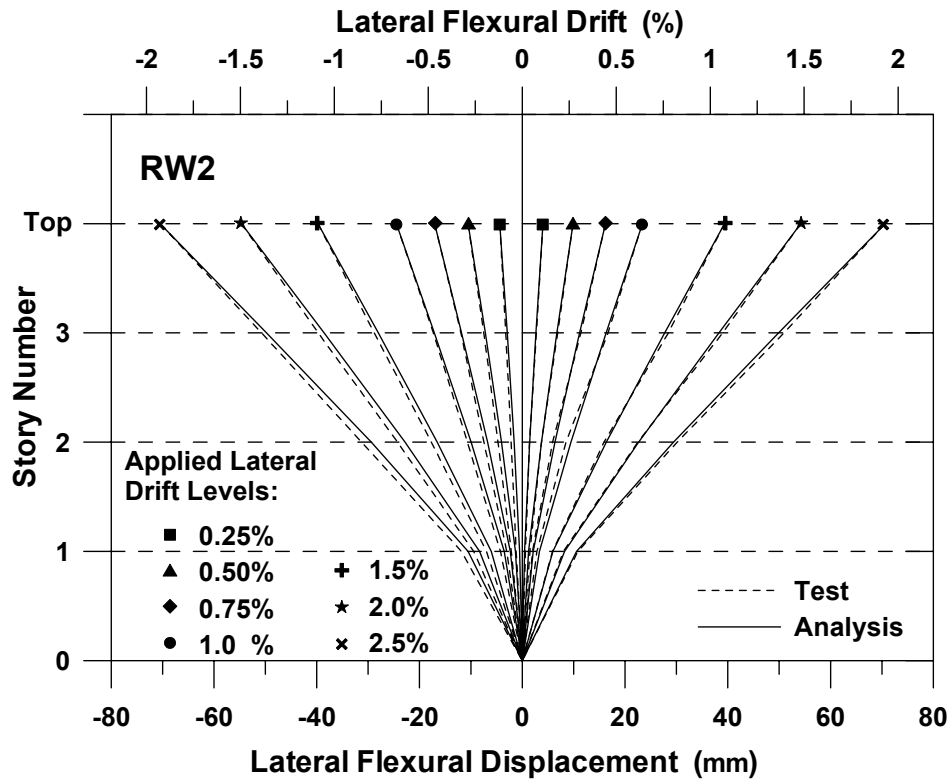
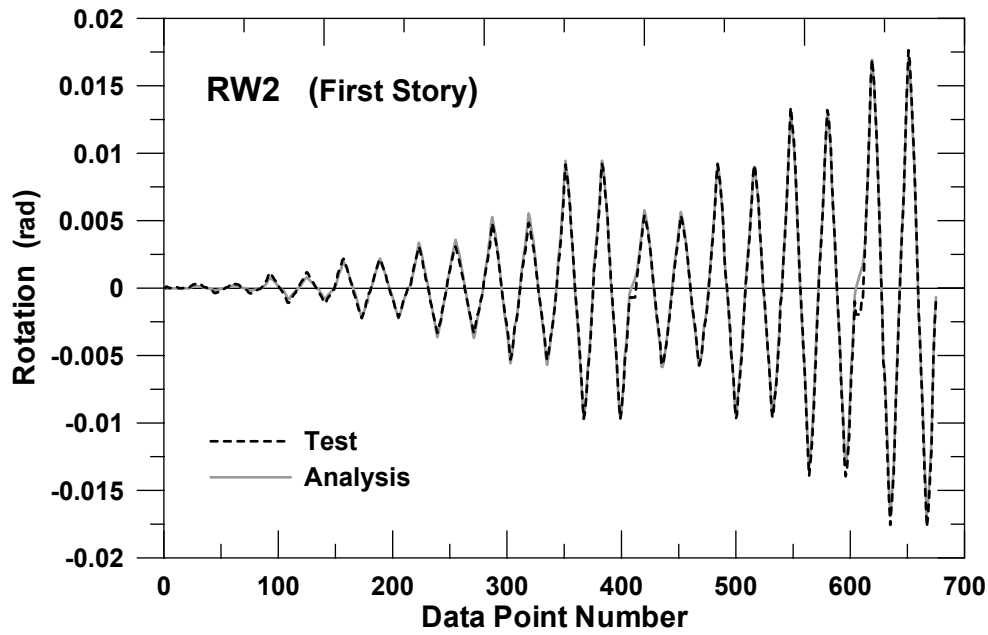


Fig. 7.28 Wall RW2, lateral displacement profiles

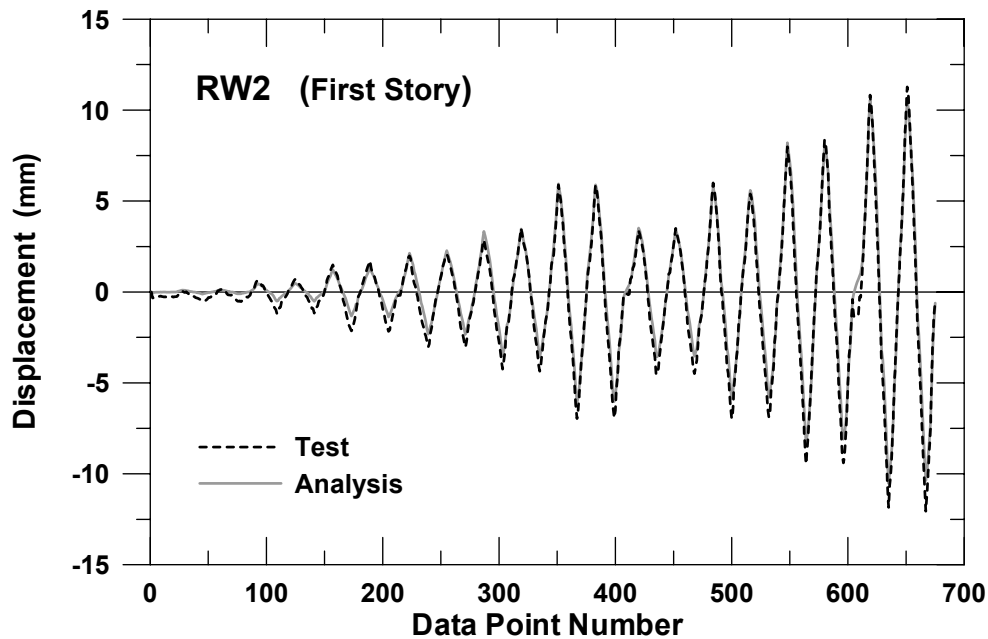
Measured and predicted responses at specific locations are compared in Figure 7.30, which plots the average concrete strains measured by the seven LVDTs over a 229 mm gage length at the base of the wall (Fig. 7.10), at applied peak positive top displacement (top displacement reversal) data points, for selected drift levels applied during testing. Similar trends were observed in the results for other drift levels and also for peak negative top displacement data points; therefore, only limited results are presented. Results shown in Figure 7.30 illustrate that the analytical model predicts reasonably well the tensile strain profile but significantly underestimates the compressive strains. A similar correlation is observed for the strains in longitudinal steel bars (measured by steel strain gages) at wall base level (Fig. 7.31), although the compressive strains in longitudinal reinforcement at the top of the first-story level are predicted reasonably well.

The larger measured compressive strains in concrete and longitudinal reinforcement located at the base of the wall may be due to stress concentrations induced at the wall-pedestal interface due to the abrupt change in geometry. As well, the larger compressive strains may be partially due to the nonlinear shear response that the wall specimen experienced within the first-story height. Finally, the measurements may have been influenced by the attachment of the

LVDTs to the wall specimen, as the LVDTs were affixed to blocks glued to the wall. Nevertheless, the underestimation of the compressive stresses does not apparently have a significant influence on the prediction of the global flexural response (Figs. 7.27–7.29) for the modeled wall and loading history used in this study.



(a) Rotations



(b) Lateral displacements

Fig. 7.29 Wall RW2, first-story flexural deformations

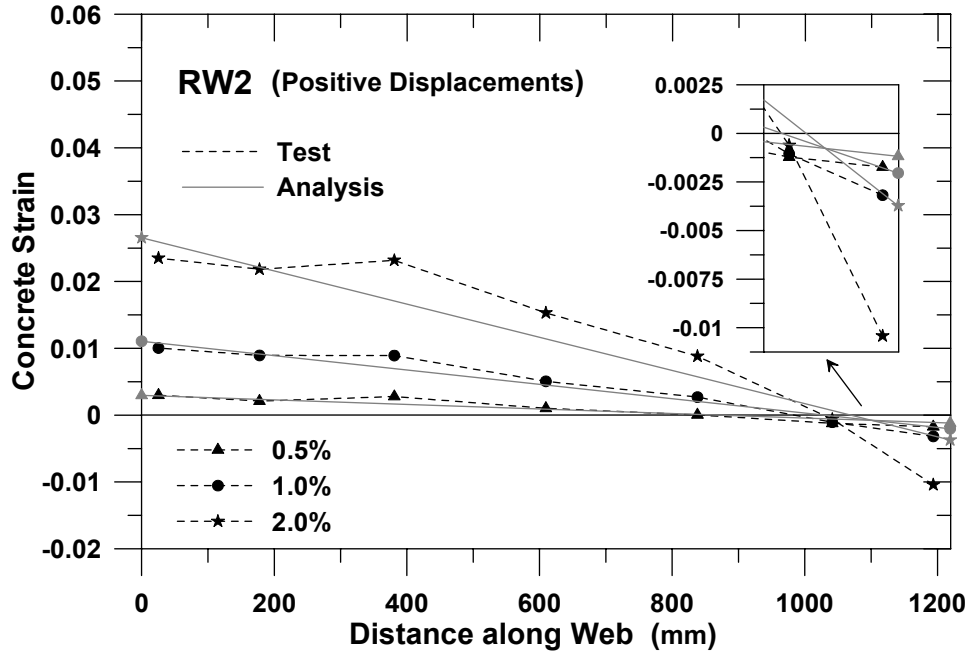


Fig. 7.30 Wall RW2, concrete strain measurements by LVDTs vs. predictions

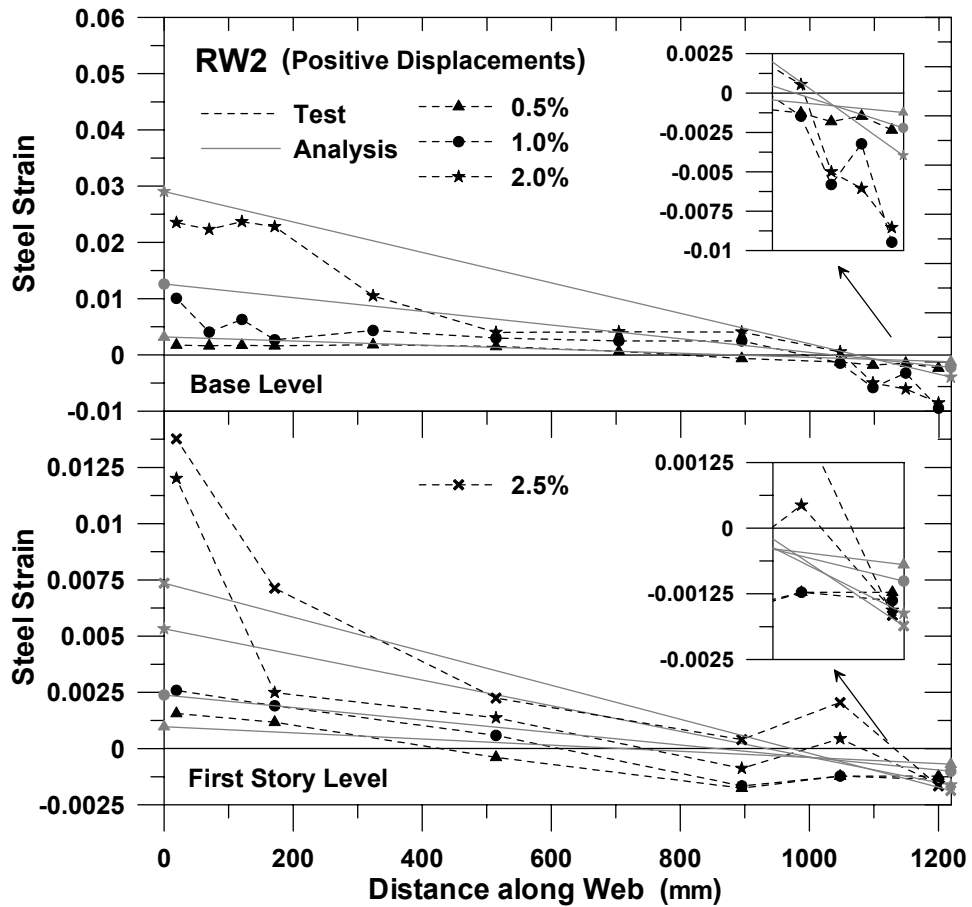


Fig. 7.31 Wall RW2, steel strain gage measurements vs. predictions

Figure 7.32 compares measured responses for a specific gage, an embedded concrete strain gage with gage length of 83 mm (Fig. 7.10), with results obtained with the model. The concrete strain gage data were available up to data point number 330 (0.75% drift level), at which time the gage failed. The analytical prediction again underestimates the measured compressive strains and overestimates the measured tensile strains (which are believed to be unreliable, as discussed below). Given the differences in the measured and predicted results, additional comparisons were made using strain histories measured by the LVDTs located on either side of the embedded concrete strain gage. Results obtained with the two LVDTs straddling the embedded concrete strain gage were used to estimate the strain at the location of the embedded concrete gage using linear interpolation. Results are presented up to data point number 515, at which time the readings in the LVDT closest to the wall edge become unreliable. It is observed that the analytical tensile strain predictions are in good agreement with the LVDT measurements in tension, as mentioned in the discussion of Figure 7.30. The readings for the embedded concrete strain gage are reasonably close to those obtained with the LVDTs for compressive strains, but the embedded gage fails to measure correctly the tensile strains (it appears that bond between the embedded concrete strain gage and the surrounding concrete is insufficient to measure accurately the large tensile strains that develop at wall boundaries).

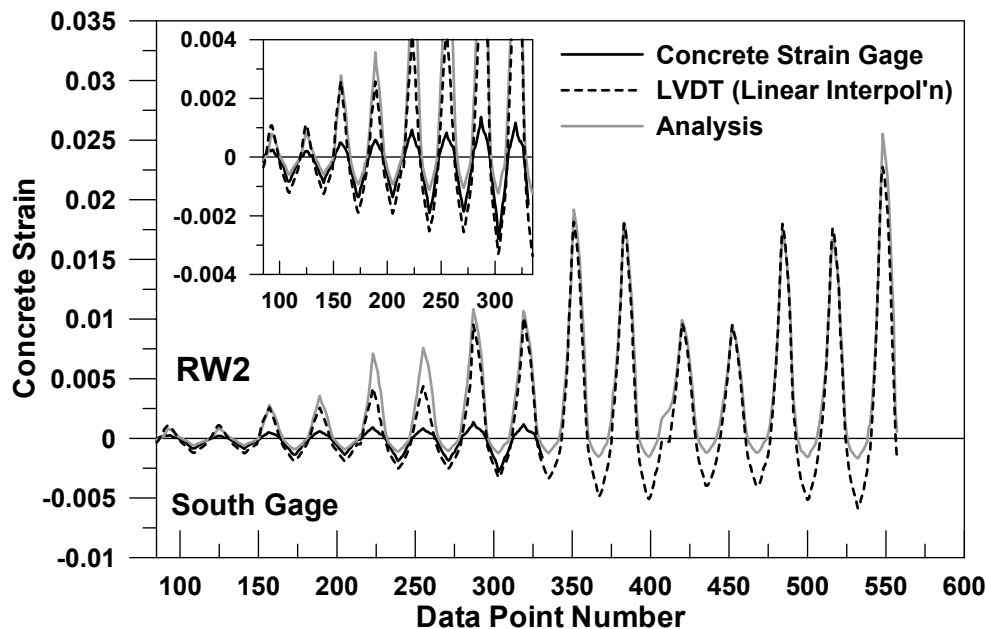


Fig. 7.32 Wall RW2, concrete strain gage measurements vs. predictions

Similar data trends were observed for the concrete strain gage located at the opposite wall boundary of specimen RW2. Overall, the results indicate that the analytical model underestimates the compressive strains but predicts reasonably well the magnitude and variation of the wall tensile strain histories, and that tensile strain measurements for the embedded concrete gage are not reliable.

7.3.2 T-Shaped Wall, TW2

Figures 7.33–7.40 compare the analytical model predictions with experimental results for the T-shaped wall specimen TW2. The correlation of the analytical and experimental results for the lateral load – top flexural displacement response (Fig. 7.33), story displacements (Fig. 7.34), and first-story displacement and rotations (Fig. 7.35) for TW2 resemble those for RW2, when the T-shaped specimen is subjected to displacements in the positive direction (when the wall flange is in compression). Therefore, the model provides a reasonably good prediction of the response for a T-shaped wall with the flange in compression, and the same conclusions noted for RW2 apply to TW2. This result implies that the plane section assumption, which assumes the entire flange is effective in compression for all drift levels, is appropriate and is consistent with the measured strain distributions along the flange.

The concrete strains (LVDT readings along the bottom 229 mm of the wall) and steel strains (steel strain gage readings mounted on longitudinal reinforcement at wall base level), measured along the wall flange at peak top displacement data points, are plotted and compared with analytical results in Figures 7.36–7.37 for selected drift levels. The measured compressive strains along the flange are approximately uniform for all applied drift levels, resulting in fairly good analytical prediction of the overall response for positive displacements. However, for negative displacements (when the wall flange is in tension), the analytical model overestimates the lateral load capacity of the wall (Fig. 7.33), underestimates the lateral displacements at the first-story level (Figs. 7.34–7.35), and overestimates the rotations over the bottom 0.76 m of the wall (Fig. 7.35). The reason for these discrepancies between the analytical and experimental results is the nonlinear tensile strain distribution experienced along the flange of the wall specimen during testing, when the wall is subjected to negative displacements. The measured tensile strains, both in steel and concrete, follow a nonlinear distribution along the width of the flange (Figs. 7.36 and 7.37), which cannot be captured with the analytical model, which is based

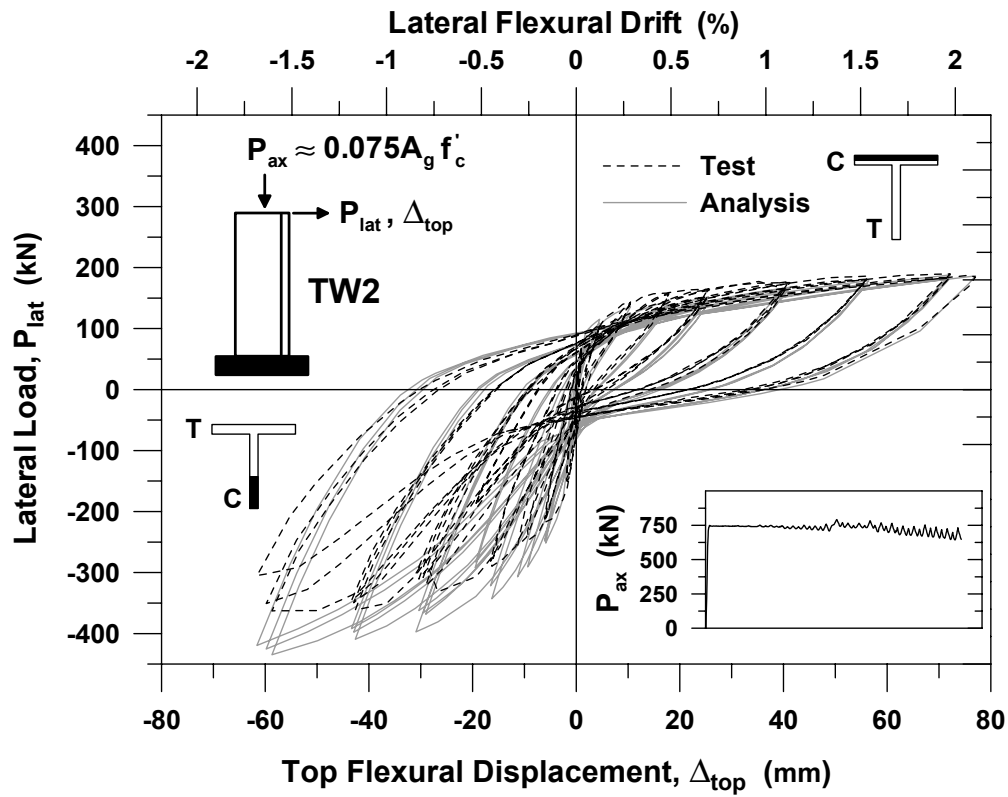


Fig. 7.33 Wall TW2, measured vs. predicted load-displacement responses

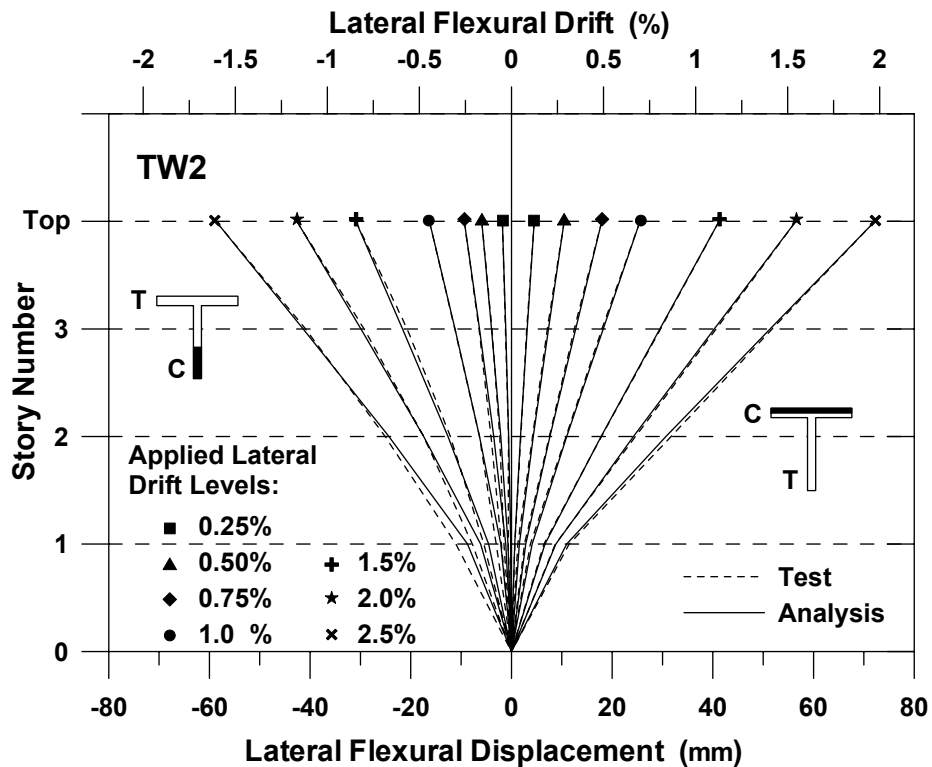
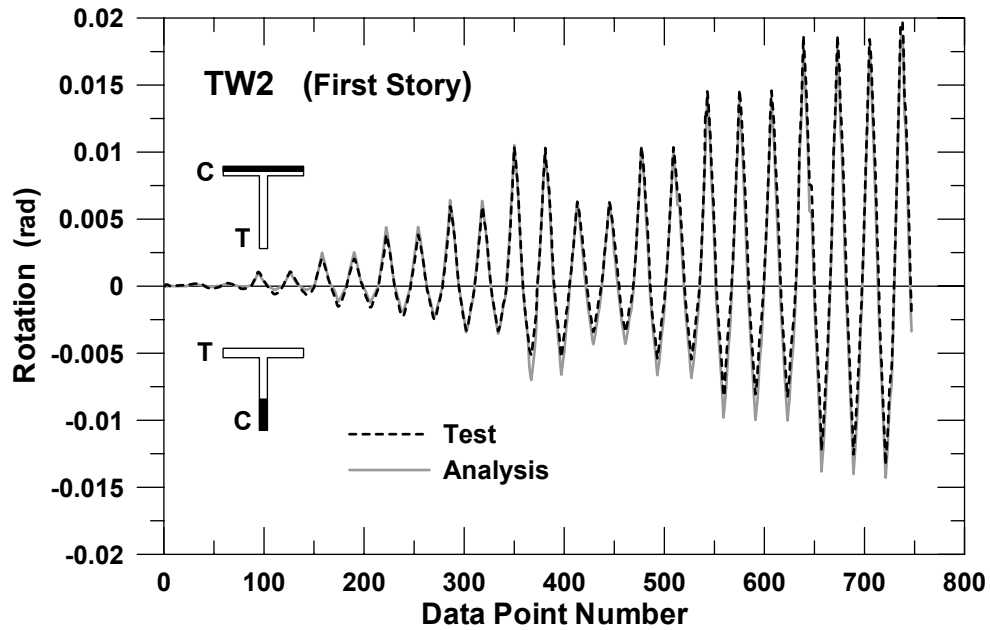
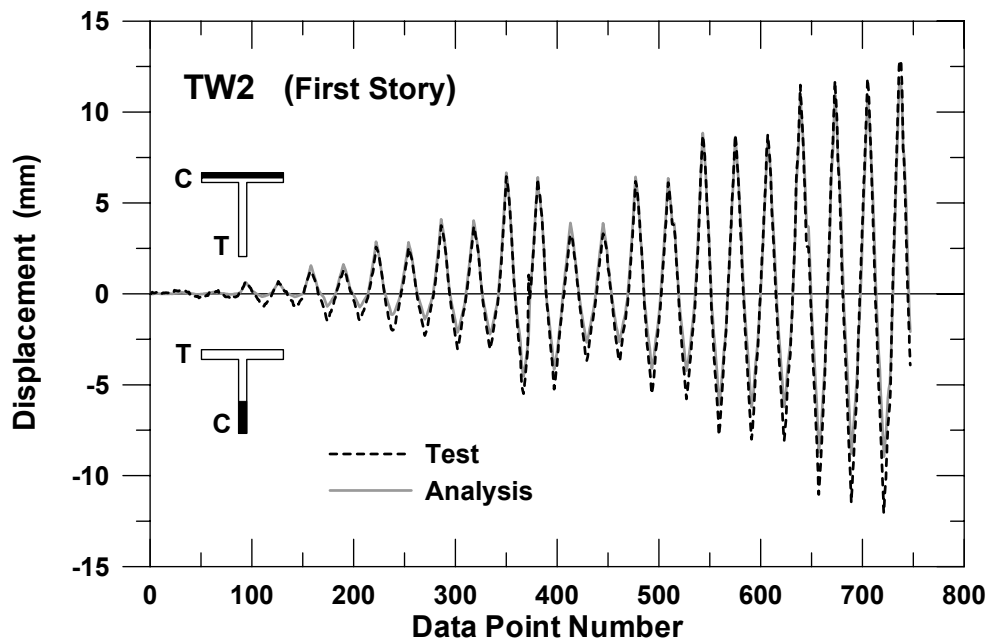


Fig. 7.34 Wall TW2, lateral displacement profiles

on a plane section assumption that produces a uniform tensile strain distribution along the flange. Because of this assumption, flange tensile strains are overestimated, leading to overestimation of the lateral load capacity of the wall when the flange is in tension.



(a) Rotations



(b) Lateral displacements

Fig. 7.35 Wall TW2, first-story flexural deformations

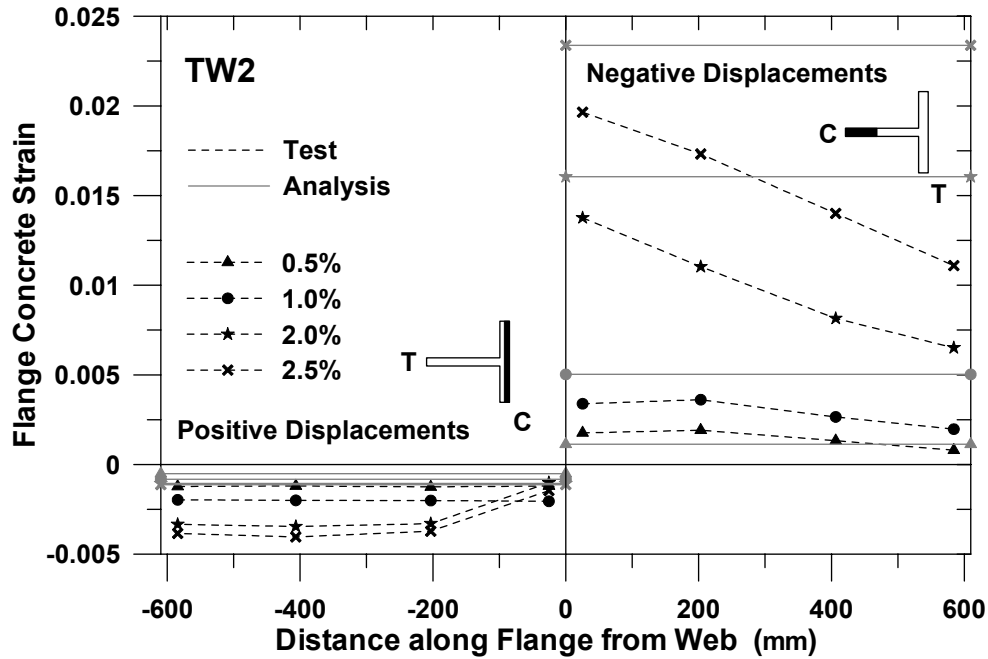


Fig. 7.36 Wall TW2, measured concrete strains along wall flange vs. predictions

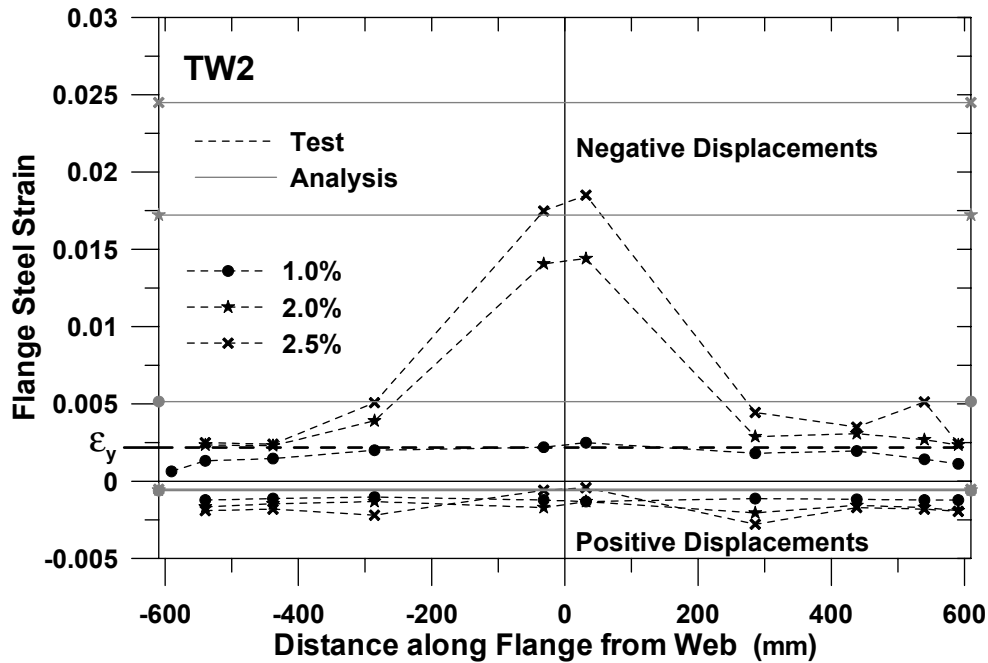


Fig. 7.37 Wall TW2, measured steel strains along wall flange vs. predictions

The experimentally observed nonlinear tensile strain distribution along the flange is also the reason for overestimation of the first-story rotations and the underestimation of the first-story displacements (Fig. 7.35) by the analytical model. The first-story displacements predicted by the

model are lower (despite overestimation of the inelastic rotations due to large tensile strains) because the length of the plastic hinge region (the height over which steel yielding is observed) is larger in the analytical model than that experienced by the wall specimen during testing.

The results presented in Figures 7.36–7.37 also reveal that the analytical model for the wall specimen TW2 significantly underestimates the compressive strains in steel and concrete (as was the case for RW2). Concrete and steel strains measured by the LVDTs and steel strain gages along the length of the specimen web (including the web-flange intersection) are plotted for peak top displacement points for selected lateral drift levels in Figures 7.38–7.39. The distribution of tensile strains along the web is predicted with reasonable accuracy. It is interesting to observe that the measured tensile strains in concrete (Fig. 7.38) tend to decrease suddenly at the web-flange intersection due to the change in cross-section geometry.

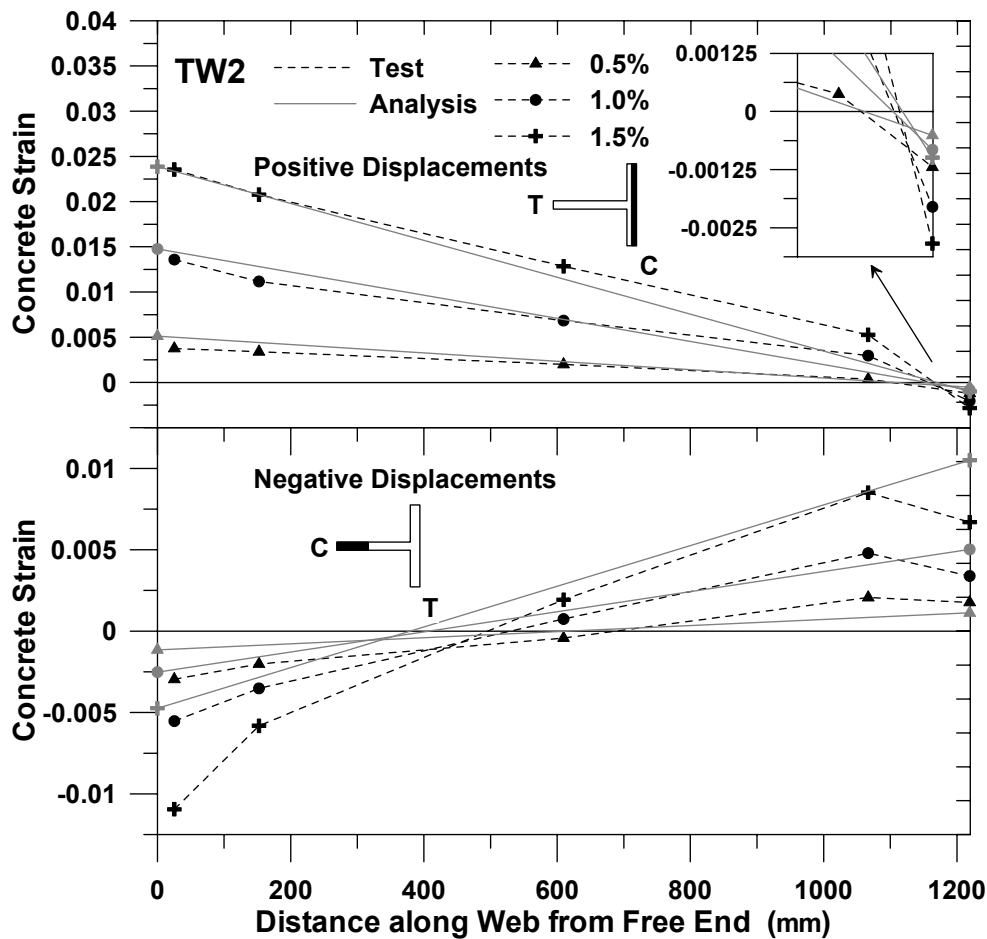


Fig. 7.38 Wall TW2, concrete strain measurements by LVDTs vs. predictions

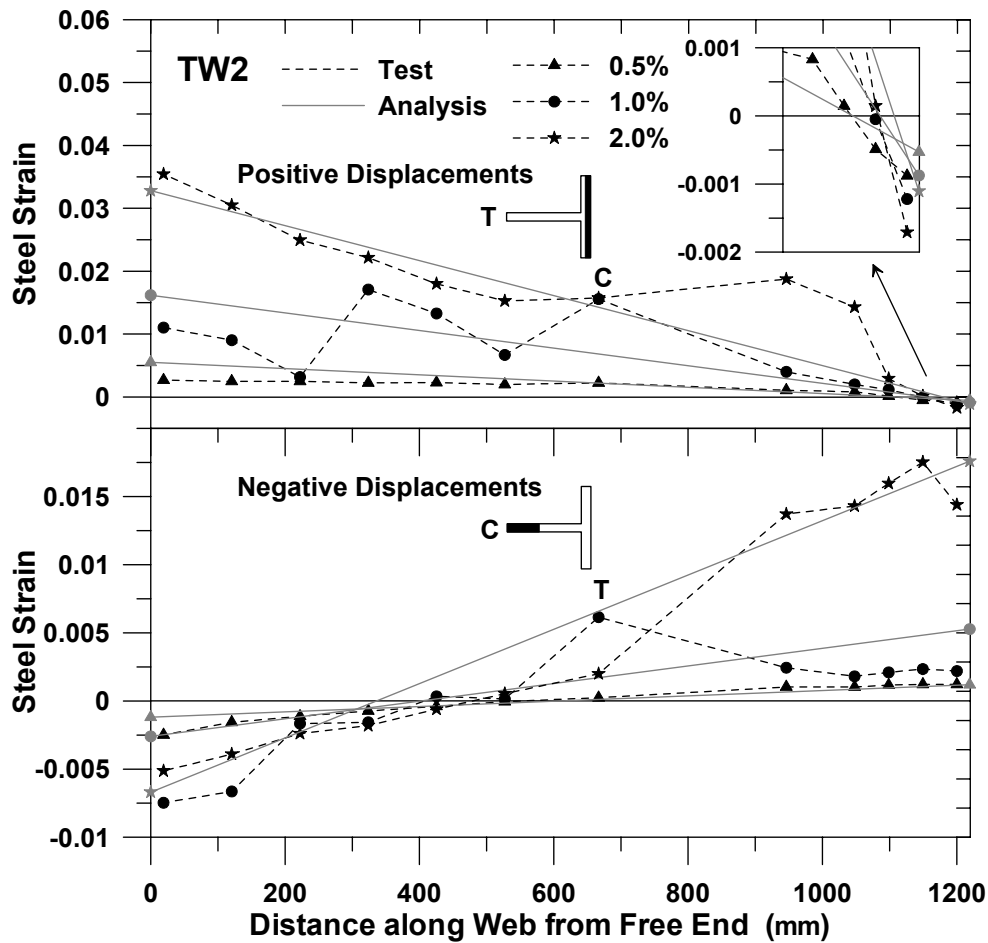


Fig. 7.39 Wall TW2, steel strain gage measurements at wall base level vs. predictions

The longitudinal strain history for concrete predicted by the analytical model is compared to results obtained with embedded concrete strain gages (Fig. 7.10), as well as results obtained by linear interpolation between LVDTs located at the wall boundary (Fig. 7.10), in Figure 7.40. It is again evident that the analytical model underestimates the compressive strains but predicts reasonably well the tensile strain history. The concrete strain gage measurements are in reasonable agreement with the LVDT readings for compressive strains, but the embedded gages do not accurately measure tensile strains.

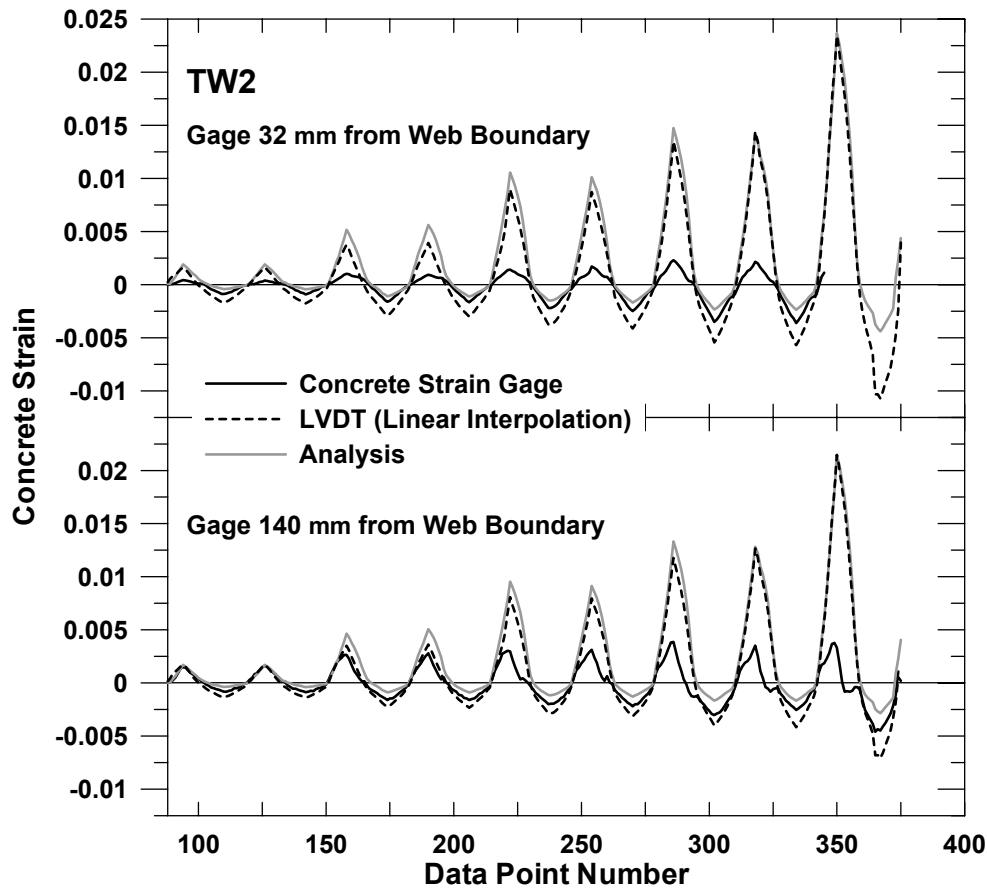


Fig. 7.40 Wall TW2, concrete strain gage measurements vs. predictions

7.4 SUMMARY

The intent of this chapter was to convey detailed information on the calibration of the multiple-vertical-line-element model (MVLEM) and present comprehensive correlation studies between the analytically predicted and experimentally observed behavior of slender RC walls with rectangular and T-shaped cross sections at various response levels. The constitutive relations implemented into the MVLEM for concrete and reinforcing steel were calibrated based on the mechanical properties of the materials used in the construction of the walls modeled, and via parameters previously verified by other researchers (e.g., for confinement, tension stiffening, cyclic stress-strain behavior of steel and concrete). Wall test results were processed to exclude the contributions of pedestal movement and shear deformation components to allow for a direct comparison of the experimental results with the flexural response prediction of the analytical

model. The analytical model was subjected to the same conditions experienced during testing (e.g., loading protocol, minor fluctuations in applied axial load). A refined configuration was used for the model in order to predict the responses at specific locations where instrumentation was provided for the tests. The correlation of the experimental and analytical results was investigated in detail, at various response levels and locations (e.g., story displacements, rotations over the first-story level, average strains in steel and concrete).

It was observed that the MVLE model, as implemented here, provides a good prediction of the experimentally observed responses (wall lateral load capacity at varying drift levels, wall displacement profile, average rotations and displacements over the region of inelastic deformations) of the wall with rectangular cross section. The wall stiffness is well represented both prior to, and after wall yielding, and the yield point is captured effectively. The model provides a reasonably accurate prediction of wall tensile strains and the position of the neutral axis, whereas the compressive strains tend to be underpredicted, possibly due to stress concentrations at wall-pedestal interface or nonlinear shear deformations experienced within the nonlinear flexural deformation region of the wall.

The same level of accuracy is observed in the prediction of the global response for T-shaped walls when the flange is in compression, where the wall effectively behaves like a wall with a rectangular cross section. When the flange is in tension, discrepancies between the results obtained with the analytical model and the experimental results are observed for the wall lateral load capacity and the displacements and rotations along the wall. Wall lateral load capacity and inelastic rotations tend to be overestimated whereas inelastic lateral displacements are underpredicted due to the observed nonlinear tensile strain distribution along the flange of the wall, which cannot be captured by the MVLE model as implemented in this study.

8 Modeling of Coupled Shear and Flexural Responses: Analytical Model Description

As described in the previous chapter, the multiple-vertical-line-element model, as implemented in this study, provides an accurate prediction of experimentally observed flexural wall response at various response levels (wall load-displacement response, wall lateral load capacity at varying drift levels, wall displacement profile, average rotations and displacements over the region of inelastic deformations) for walls with rectangular cross sections. However, the model considers uncoupled shear and flexural responses, and an improved modeling methodology is necessary for simulating realistically the nonlinear shear responses associated with the interaction between shear and flexural response components observed even in relatively slender RC walls (Massone and Wallace, 2004).

Analytical models have been proposed to consider the observed coupling between flexural and shear components of RC wall response. A recognized methodology involves implementing the finite element method together with a constitutive RC membrane model that follows a rotating-angle modeling approach (e.g., modified compression field theory, Vecchio and Collins, 1986; rotating-angle softened-truss model, Pang and Hsu, 1995). A methodology based on adopting this idea for a fiber model, was proposed by Petrangeli et al. (1999) to couple shear response with flexural and axial responses. The analytical model proposed in this study is based on applying the methodology developed by Petrangeli to the multiple-vertical-line-element model. A description of the proposed modeling approach to incorporate coupling of wall flexural and shear responses is presented in this chapter.

8.1 EXPERIMENTAL EVIDENCE OF FLEXURE-SHEAR INTERACTION

In order to demonstrate the observed coupling of flexural and shear responses in walls, deformations associated with flexure and shear were investigated for two, well-instrumented,

approximately quarter-scale slender wall specimens with rectangular cross sections (specimen RW2 tested by Thomsen and Wallace, 2004, and specimen SRCW1 tested by Sayre, 2003) to assess their relative contributions to wall displacements. A summary of this experimental investigation is provided in the following section; additional information is available in Massone and Wallace (2004).

8.1.1 OVERVIEW OF TESTS

The two slender wall specimens used to assess the relative deformations associated with shear and flexure were proportioned and detailed using capacity design and displacement-based design approaches, respectively. The wall specimens were tested in an upright position. An axial load of approximately $0.10Agf'c$ was applied to the wall specimens using hydraulic jacks mounted on top of the load transfer assembly. The axial stress was held constant throughout the duration of each test. Cyclic lateral displacements were applied to the walls by a hydraulic actuator mounted horizontally to a reaction wall at 3.81 m above the base of specimen RW2 and to a reaction frame at 4.88 m above the base of specimen SRCW1.

Specimen RW2 (also described in Chapter 7) was 3.66 m tall and 102 mm thick, with a web length of 1.22 m. The longitudinal reinforcement at wall boundaries consisted of 8 – #3 ($A_b = 71 \text{ mm}^2$) bars, whereas web reinforcement consisted of two curtains of deformed #2 ($A_b = 32 \text{ mm}^2$) bars placed horizontally and vertically, with a spacing of 189 mm on center. Specimen SRCW1 was a structural steel reinforced concrete wall 4.88 m tall, 152 mm thick, and 1.22 m long. Vertical reinforcement at wall boundaries consisted of a W6x9 section ($A_{b1} = 1729 \text{ mm}^2$) surrounded by 8 – #4 ($A_{b2} = 1032 \text{ mm}^2$) bars. The web reinforcement consisted of two curtains of horizontal and vertical #3 bars with a spacing of 152 mm on center. Design concrete compressive strengths were 27.6 MPa for specimen RW2 and 34.5 MPa for specimen SRCW1. Grade 60 (414 MPa) bars were used for longitudinal and web reinforcement of the specimens. For SRCW1, A572, Grade 50 (345 MPa) W6x9 sections were used.

Instrumentation was used to measure displacements, loads, and strains at critical locations for each wall specimen. Wire potentiometers (WPs) were mounted to a rigid steel reference frame to measure lateral displacements along the height of the wall (Fig. 8.1). Linear potentiometers (LPs) were mounted horizontally and vertically on the wall foundation to measure any horizontal slip of the pedestal along the strong floor as well as rotations caused by

uplift of the pedestal from the strong floor. Measurements from the WPs used to record lateral displacements were corrected to remove the contribution of pedestal slip and rotation to lateral displacements.

Axial (vertical) displacements at the wall boundaries were measured using two WPs mounted directly to the wall ends. These measurements were used to calculate wall story rotations by dividing the difference in relative axial displacements by the distance between the potentiometers. Shear deformations within the first two (RW2) and three (SRCW1) levels of the wall specimens were determined using measurements from WPs placed diagonally on the walls, in an “X” configuration (Fig. 8.1).

Linear variable differential transducers (LVDTs), oriented vertically over the wall length just above the wall - pedestal interface, were used to obtain average axial strain and allow for the determination of section curvature. The strains in the reinforcing steel also were measured through the use of strain gages near the wall base and at other locations (Thomsen and Wallace, 2004; Sayre, 2003).

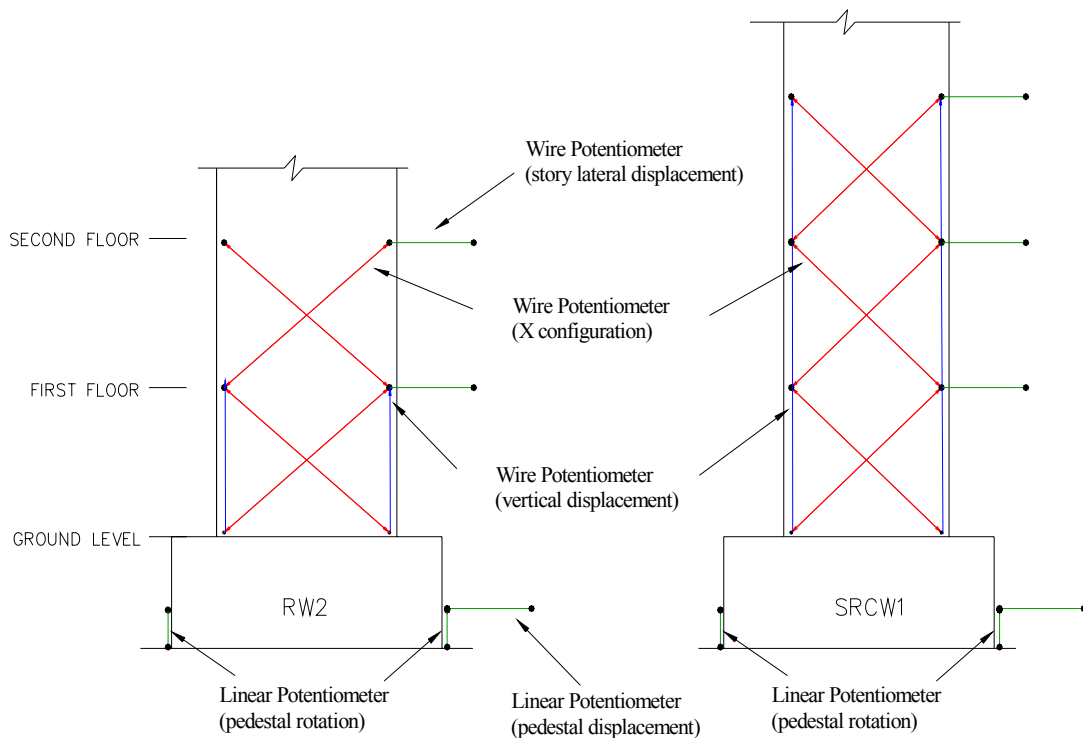


Fig. 8.1 General instrument configuration: RW2 and SRCW1

8.1.2 Instrumentation for Measuring Flexural and Shear Deformations

A common approach used to determine average (story) shear deformations for shear wall tests is to use measurements from displacement gages placed diagonally in an “X” configuration (e.g., Thomsen and Wallace, 2004; see Fig. 8.2). However, as shown by Massone and Wallace (2004), measurements obtained from the diagonal gages are influenced by flexural deformations if the center of rotation of the story does not coincide with the geometric center of the story height. The average shear deformations calculated using an “X” configuration may result in overestimation of the shear deformations if not corrected to account for flexural deformations.

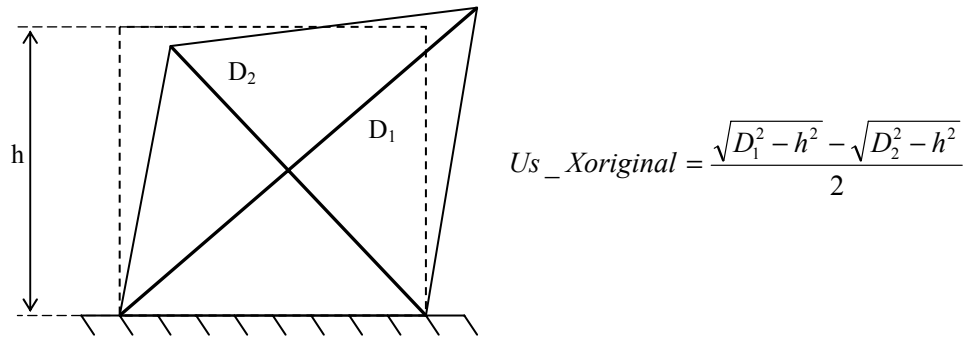


Fig. 8.2 Uncorrected shear deformation measured at wall base

8.1.3 Measurement of Flexural Deformations

To determine the contribution of the flexural deformations to the lateral displacement at the top of a story, the location of the centroid of curvature distribution (center of rotation) of the story must be estimated. The flexural displacement at the top of the first story for a given curvature distribution is calculated as:

$$U_f = \underline{\alpha} \underline{\theta} h \quad (8.1)$$

where $\underline{\theta}$ is rotation over story level, h is the story height, and $\underline{\alpha}$ is the relative distance from the top of the first story to the centroid of the curvature distribution. In this study, a value of $\underline{\alpha} = 0.67$ was used, which is consistent with prior research (Thomsen and Wallace, 2004).

8.1.4 Measurement of Shear Deformations: Corrected “X” Configuration

As proposed by Massone and Wallace (2004), the uncorrected story shear displacement measured through the use of the “X” configuration of WPs and the story flexural displacement measured using the vertical WPs at the wall boundaries can be used in combination to obtain a “corrected” average story shear displacement ($Us_Xcorrected$) as:

$$Us_Xcorrected = Us_Xoriginal + \left(\frac{1}{2} - \underline{\alpha} \right) \cdot \underline{\theta} \cdot h \quad (8.2)$$

where $Us_Xoriginal$ obtained using only the diagonal WP (X configuration) measurements would give a biased estimation of the story shear displacement, due to contribution of flexural deformations.

8.1.5 Experimental Force versus Displacement Relations for Shear and Flexure

Using the methodology described above to separate the contributions of shear and flexural deformations in measured wall displacements, lateral load versus top and story deformation relations can be determined. Figure 8.3 plots the applied story shear force versus measured flexural (Fig. 8.3a) and shear (Fig. 8.3b) displacements within the first and second stories of specimen RW2. Figure 8.4 plots the same relations for the first through third stories of specimen SRCW1. Relations derived from the experimental data are compared to analytical results for linear elastic analyses for a “fully cracked” section stiffness for flexure and an elastic shear stiffness. The cracked section stiffness is obtained from a sectional analysis, as a secant stiffness to the point of first yield of reinforcement. For simplicity, a linear elastic shear stiffness is assumed.

Results for specimen RW2 are presented in Figure 8.3. At the second-story level of specimen RW2, shear displacements were evaluated using only the diagonal potentiometer (X configuration) measurements without correction given in Equation 8.2 because vertical potentiometers were not provided during testing along the second-story height (Fig. 8.1). The story shear force versus flexural displacement relations for specimen RW2 (Fig. 8.3a) reveal that (1) the cracked stiffness obtained from a moment versus curvature analysis reasonably captures the measured lateral stiffness of the wall prior to yield, (2) yielding of flexural reinforcement

occurs at a lateral load close to that associated with the lateral load to reach the wall nominal moment (131 kN), and (3) yielding occurs primarily in the first two levels.

The story shear force versus shear displacement relations (Fig. 8.3b) reveal that (1) inelastic shear behavior occurred in the first story despite a nominal shear capacity ($V_n = 276$ kN) of approximately twice the applied story shear (133 kN), (2) inelastic deformations were limited to essentially the first story, and (3) the elastic shear stiffness approximately represents the measured shear stiffness in regions where flexural yielding was not observed (i.e., the second level). The observed results clearly demonstrate coupling of wall inelastic shear and flexural responses; inelastic shear deformations were observed simultaneously with inelastic flexural deformations.

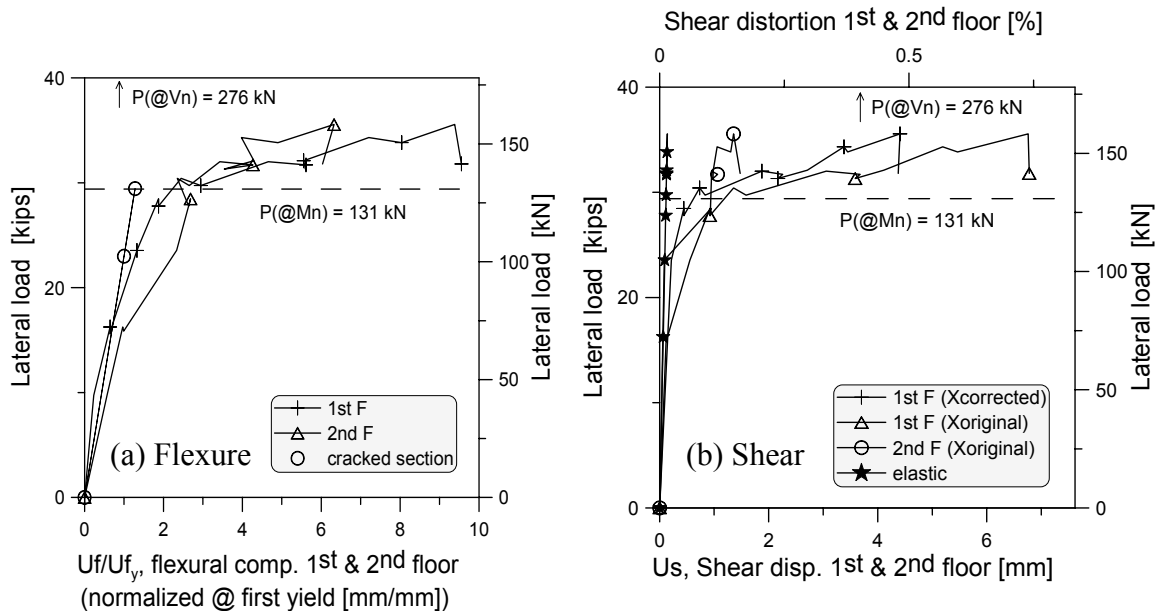


Fig. 8.3 First- and second-story deformations: RW2

Similar relations for the wall specimen SRCW1 are presented in Figure 8.4. Vertical and diagonal wire potentiometers were provided along the bottom three stories of specimen SRCW1 (Fig. 8.1); therefore, the shear displacement measurements at the first-, second-, and third-story levels of SRCW1 were corrected based on Equation 8.2. The story shear force versus flexural displacement relations in Figure 8.4(a) reveal findings similar to those for specimen RW2, except that slip between the structural steel section and the concrete appears to have contributed significantly to a loss of stiffness within the first story of specimen SRCW1. The story shear

force versus shear displacement relations (Fig. 8.4b) reveal that inelastic shear behavior was experienced within the first and second stories of the wall despite a nominal shear capacity ($V_n = 651$ kN) of approximately twice the applied story shear (310 kN). The observed inelastic shear deformations in the first-story level, and also to a lesser degree in the second-story level, clearly demonstrate the coupling of inelastic flexural and shear deformations. As well, the flexural and shear force–deformation relations reach yielding at approximately the same time. This behavior, which has also been observed in prior studies (e.g., Takayanagi et al., 1979), has been established for the tests evaluated using an unbiased methodology for evaluating shear deformations, and the results verified through the use of redundant measurements for multiple test specimens (Massone and Wallace, 2004).

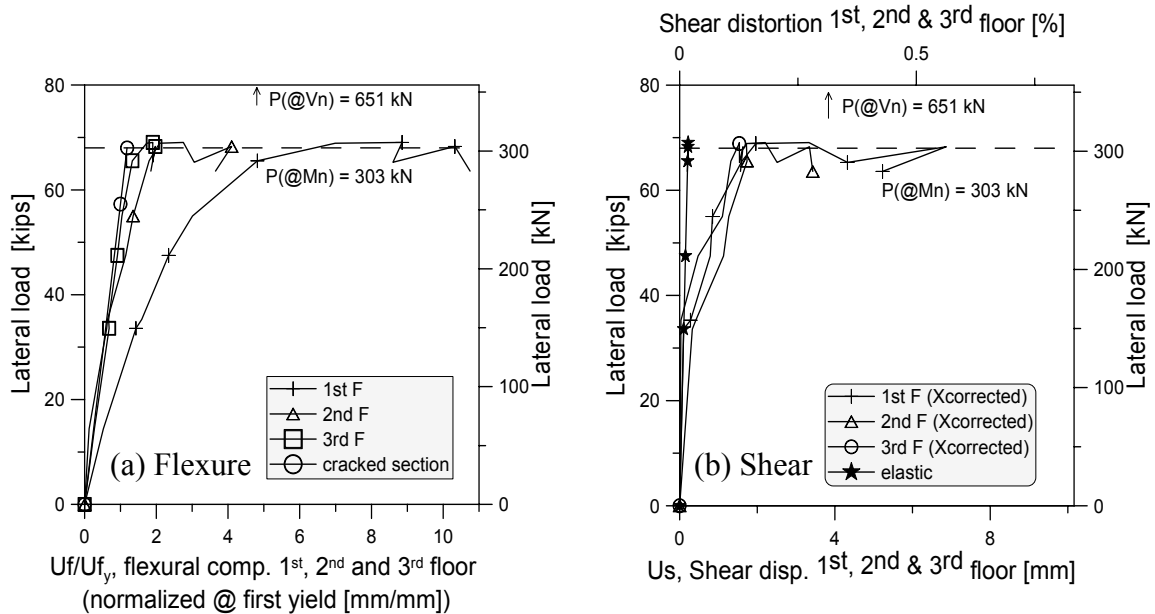


Fig. 8.4 Story deformations: SRCW1

8.2 BASE MODEL: MULTIPLE-VERTICAL-LINE-ELEMENT MODEL (MVLEM)

The formulation of the multiple-vertical-line-element model (MVLEM) was extended to simulate the observed coupling behavior between nonlinear flexural and shear responses in RC walls. The MVLEM, as described in Chapter 3, resembles a two-dimensional fiber model, simplified such that element rotations (curvatures) are concentrated at the center of rotation defined for each element. In the MVLEM, a single average value of curvature is assumed for

each model element, as opposed to a generic displacement-based fiber model implementation where a linear curvature distribution (displacement interpolation function) is used between element nodes and the curvature distribution is integrated at Gaussian points to obtain element rotations and displacements. A structural wall is modeled as a stack of MVLEs, which are placed one upon the other, and the coupled axial-flexural response of each MVLE is simulated by a series of uniaxial elements (or macro-fibers) connected to infinitely rigid beams at the top and bottom (e.g., floor) levels (Fig. 8.5(a)) that enforce a plane section assumption. A horizontal spring placed at the center of rotation (at relative height ch) of each MVLE, with a prescribed nonlinear force-deformation behavior, is commonly used to simulate the shear response of the element. Shear and flexural responses are considered uncoupled in the original formulation of the MVLEM. The constitution and kinematics of the MVLEM are explained in detail in Chapter 3.

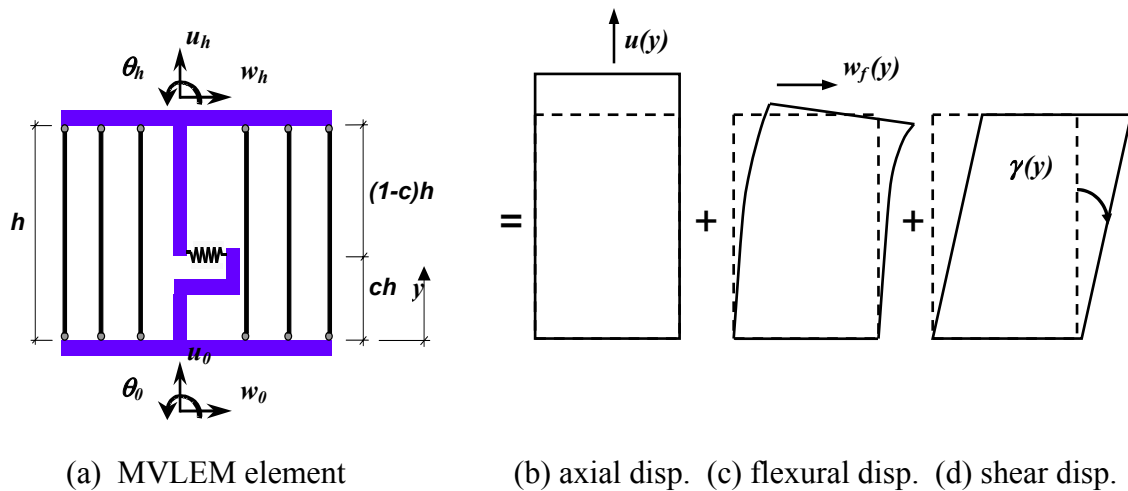


Fig. 8.5 MVLEM element and incorporated displacement field components

8.3 INCORPORATING DISPLACEMENT INTERPOLATION FUNCTIONS

The original formulation of the multiple-vertical-line-element model was modified to accommodate displacement interpolation functions and integration (Gaussian) points for practical implementation of the model into computational platforms (e.g., OpenSees) in which the displacement-based fiber model formulation is already built in. However, derivation of the displacement interpolation functions implemented in the model incorporate the definition of an element center of rotation in order to distinguish between model lateral displacements resulting from shear and flexural deformations. The element center of rotation is defined at a fraction of

the element height ch , as in the case of the original MVLEM. Geometrically, the center of rotation is defined as the point for which the transverse flexural displacement of the element (Δw_f , defined in Eq. 8.3), is equivalent to the displacement associated with the rigid body displacement of the element, resulting from the rotation ($\Delta\theta$, defined in Eq. 8.4) that the element undergoes at the center of rotation. Accordingly, the center of the curvature (ϕ) distribution (or the center of rotation) of the element is located at the relative element height ch , as shown in Figure 8.6.

$$\Delta w_f = \int_0^h \phi x' dx' = - \int_h^0 \phi (h-x) dx = h \int_0^h \phi dx - \int_0^h \phi x dx \quad (8.3)$$

$$\Delta\theta = \int_0^h \phi dx \quad (8.4)$$

$$ch = \frac{\int_0^h \phi x dx}{\int_0^h \phi dx} = \frac{h\Delta\theta - \Delta w_f}{\Delta\theta} = h - \frac{\Delta w_f}{\Delta\theta} \Rightarrow \Delta w_f = h(1-c)\Delta\theta \quad (8.5)$$

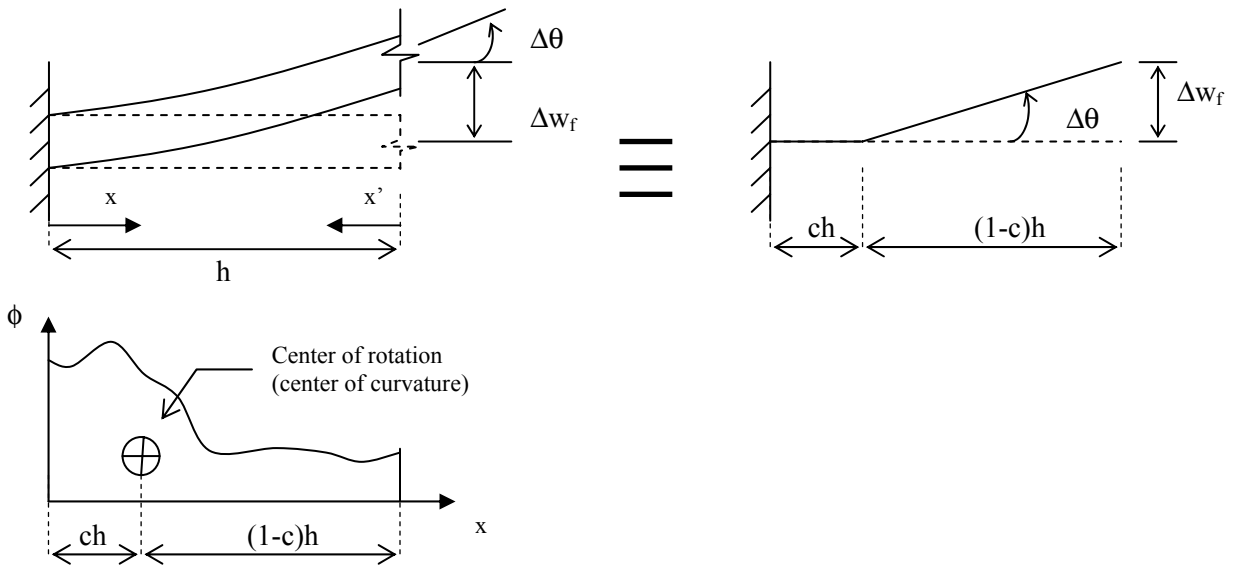


Fig. 8.6 Definition of center of rotation

In an attempt to locate the center of rotation for a slender cantilever wall, experimental results from Sayre (2003) were investigated by Massone and Wallace (2004). Curvature distributions measured by linear transducer (LVDT) pairs were used to evaluate the center of rotation along the first-story level of a slender steel-reinforced concrete wall specimen.

Experimental data points were found to give an average center of rotation coefficient of $c = 0.4$ (Fig. 8.7) for the entire loading range, without significant scatter of the data when the wall is subjected to nonlinear deformations. Therefore, a value of $c = 0.4$ is used in this study. Use of $c = 0.4$ is also consistent with the studies by Vulcano et al. (1988) and Orakcal et al. (2004), who recommended the same value for c , based on comparison of the analysis results using the MVLEM with results of wall tests.

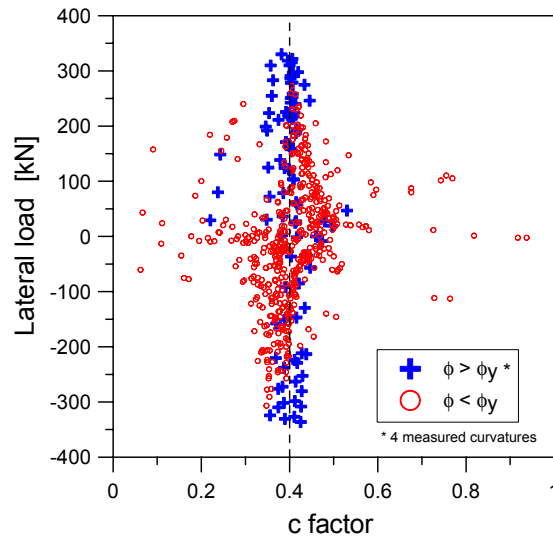


Fig. 8.7 Center of rotation for specimen SRCW3

The displacement interpolation functions implemented into the analytical model represent the three displacement field components shown in Figure 8.5, which are associated with the axial (u), flexural (w_f), and shear (γ) deformations (or strains) of the element. Other than implementing the idea of a center of rotation to segregate model transverse displacements into shear deformation (integration of shear strain) and flexural deformation (double integration of curvature distribution) components, the derivation of the displacement interpolation functions considers a linear variation of axial deformations and curvatures, and a uniform distribution of shear strain along the longitudinal axis (y) of the model element. Accordingly, the displacement field of the two-node model element, with respect to the six degrees of freedoms illustrated in Figure 8.5(a) is obtained as:

$$\begin{bmatrix} u(y) \\ w_f(y) \\ \gamma(y) \end{bmatrix} = \begin{bmatrix} 1-y/h & 0 & 0 & y/h & 0 & 0 \\ 0 & 1 & yc_1 & 0 & 0 & -yc_1+y \\ 0 & -1/h & -c & 0 & 1/h & c-1 \end{bmatrix} \cdot \begin{bmatrix} u_0 \\ w_0 \\ \theta_0 \\ u_h \\ w_h \\ \theta_h \end{bmatrix} \quad (8.6)$$

$$c_1 = 1 + (3c-2)y/h + (1-2c)(y/h)^2. \quad (8.7)$$

This derivation considers that the rotation of the element longitudinal axis is described as $w' = dw/dy = \theta + \gamma$ (Fig. 8.8), where w represents the total lateral element displacement (displacements due to flexure (w_f) and shear), θ is the relative rotation of the cross-section rotation, and γ is the uniform shear strain value (uniform along the element height and across element cross section). As shown in Figure 8.8, when only the flexural deformation is considered, the longitudinal axis of the element remains orthogonal to the element cross section, and therefore the flexural lateral displacement (w_f) is directly related to the rotation of the cross section (θ) as $dw_f/dy = \theta$.

The displacement field is then rearranged, to be consistent with the finite element formulation, in terms of axial displacement (u), total lateral displacement (w) and section rotation (θ), yielding to:

$$\begin{bmatrix} u(y) \\ w(y) \\ \theta(y) \end{bmatrix} = \begin{bmatrix} 1-y/h & 0 & 0 & y/h & 0 & 0 \\ 0 & 1-y/h & yc_3 & 0 & y/h & -yc_3 \\ 0 & 0 & c_4 & 0 & 0 & 1-c_4 \end{bmatrix} \cdot \begin{bmatrix} u_0 \\ w_0 \\ \theta_0 \\ u_h \\ w_h \\ \theta_h \end{bmatrix} = \underline{N}(y) \cdot U_N \quad (8.8)$$

$$c_3 = 1 - c + (3c-2)y/h + (1-2c)(y/h)^2 \quad (8.9)$$

$$c_4 = 1 + 2(3c-2)y/h + 3(1-2c)(y/h)^2 \quad (8.10)$$

where $\underline{N}(y)$ represents the element displacement interpolation functions for axial displacement, transverse displacement, and rotation, and U_N is the set of element nodal displacements.

From the displacement field, the strain field is derived as:

$$\begin{bmatrix} \varepsilon(y) \\ \phi(y) \\ \gamma(y) \end{bmatrix} = \begin{bmatrix} \frac{du}{dy} \\ \frac{d\theta}{dy} \\ \gamma \end{bmatrix} = \begin{bmatrix} -1/h & 0 & 0 & 1/h & 0 & 0 \\ 0 & 0 & 2c_2/h & 0 & 0 & -2c_2/h \\ 0 & -1/h & -c & 0 & 1/h & c-1 \end{bmatrix} \cdot \begin{bmatrix} u_0 \\ w_0 \\ \theta_0 \\ u_h \\ w_h \\ \theta_h \end{bmatrix} = \underline{B}(y) \cdot U_N \quad (8.11)$$

$$c_2 = -2 + 3c + 3(1-2c)y/h \quad (8.12)$$

where $\underline{B}(y)$ represents the element strain interpolation functions for axial strain (ε), curvature (ϕ), and shear strain (γ).

Incorporating these interpolation functions for displacement and strain converts the kinematic formulation of the MVLE to a displacement-based fiber element, with special interpolation functions adopted to incorporate shear deformations.

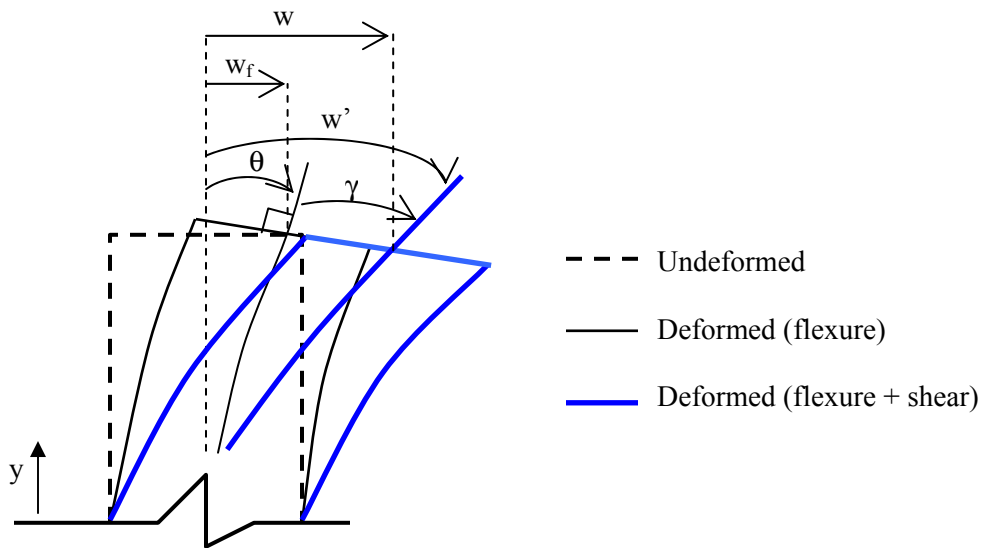


Fig. 8.8 Element section rotation

8.4 NONLINEAR ANALYSIS SOLUTION STRATEGY: FINITE ELEMENT FORMULATION

Similar to the original MVLE, the linearized equilibrium equation to conduct a quasi-static analysis using the present model can be expressed in the form of Equation 8.13. For simplicity, the following equations are expressed at the element level. A direct stiffness assembly, together

with an iterative nonlinear analysis solution strategy (as described in Chapter 5), would be required to perform a quasi-static analysis of an entire wall using the present element.

$$\underline{K} \cdot \Delta U_N + f^{int} - f^{dist} - f^{nodal} = 0 \quad (8.13)$$

The equilibrium equation represents the externally applied forces, in the form of distributed or nodal forces. The distributed load (per unit length) vector is defined as $P(y) = [p(y) \ q(y) \ m(y)]^t$, where $p(y)$ corresponds to the intensity of the distributed axial load, $q(y)$ represents the distributed transverse load, and $m(y)$ is the distributed moment. The distributed vector force (at the six element degrees of freedom shown in Figure 8.5(a)) can be expressed as:

$$f^{dist} = \int_0^h \underline{N}(y)^t \cdot [p(y) \ q(y) \ m(y)]^t dy \quad (8.14)$$

where $\underline{N}(y)$, as previously described, represents the displacement interpolation functions for axial displacement, transverse displacement, and rotation.

The nodal forces are defined based on the magnitude of the axial forces, bending moments and shear forces applied at the element degrees of freedom. The nodal-force vector is thus expressed as:

$$f^{nodal} = [N_0 \ M_0 \ V_0 \ N_h \ M_h \ V_h]^t \quad (8.15)$$

where axial forces (N), moments (M) and shear forces (V) are defined at both ends of the element (ends denoted by subscripts 0 and h).

To attain equilibrium, the internal resisting force increments at the nodal degrees of freedom of the model element must balance the externally applied force increments, for each increment of nodal displacements applied on the element. The internal resisting forces at the element degrees of freedom are determined by integrating the axial forces (N) and the shear forces (V) resisted by each vertical sub-elements of the model element, as:

$$\begin{aligned} f^{int} &= \int_0^h \underline{B}(y)^t \cdot [N(y) \ M(y) \ V(y)]^t dy \quad (8.16) \\ &= \int_0^h \underline{B}(y)^t \cdot \left[\sum_i f^i \quad \sum_i f^i x_i \quad \sum_i f_H^i \right]^t dy \end{aligned}$$

where $\underline{B}(y)$ represents the element strain interpolation functions for axial strain, curvature, and shear strain, and f_i is the axial force on each vertical sub-element, f_H^i is the shear

force on each vertical sub-element, and x^i is the horizontal position of each vertical sub-element relative to the longitudinal axis of the element.

The stiffness matrix \underline{K} of the element, with respect to the displacements at the six element degrees of freedom shown in Figure 8.5(a) is derived as:

$$\underline{K} = \int_0^h \underline{B}(y)^t \cdot \underline{D} \cdot \underline{B}(y) dy \quad (8.17)$$

where \underline{D} relates the internal forces on the element with element deformations (axial strain ε , curvature ϕ , and shear strain γ), and is expressed as:

$$\underline{D} = \begin{pmatrix} \frac{\partial N}{\partial \varepsilon} & \frac{\partial N}{\partial \phi} & \frac{\partial N}{\partial \gamma} \\ \frac{\partial M}{\partial \varepsilon} & \frac{\partial M}{\partial \phi} & \frac{\partial M}{\partial \gamma} \\ \frac{\partial V}{\partial \varepsilon} & \frac{\partial V}{\partial \phi} & \frac{\partial V}{\partial \gamma} \end{pmatrix} = \begin{pmatrix} \sum_i \frac{\partial f^i}{\partial \varepsilon_y^i} & \sum_i \frac{\partial f^i}{\partial \varepsilon_y^i} x_i & \sum_i \frac{\partial f^i}{\partial \gamma_{xy}} \\ \sum_i \frac{\partial f^i}{\partial \varepsilon_y^i} x_i & \sum_i \frac{\partial f^i}{\partial \varepsilon_y^i} x_i^2 & \sum_i \frac{\partial f^i}{\partial \gamma_{xy}} x_i \\ \sum_i \frac{\partial f_H^i}{\partial \varepsilon_y^i} & \sum_i \frac{\partial f_H^i}{\partial \varepsilon_y^i} x_i & \sum_i \frac{\partial f_H^i}{\partial \gamma_{xy}} \end{pmatrix} \quad (8.18)$$

where $\varepsilon_y^i = \varepsilon + \phi x_i$ is the axial strain on each vertical sub-element and x_i is the horizontal position (distance from element longitudinal axis) of each vertical sub-element.

Finally the term ΔU_N in Equation 8.15 is the incremental nodal-displacement vector and is expressed as:

$$\Delta U_N = [\Delta u_0 \quad \Delta w_0 \quad \Delta \theta_0 \quad \Delta u_h \quad \Delta w_h \quad \Delta \theta_h]^t \quad (8.19)$$

8.5 MODELING OF SHEAR-FLEXURE INTERACTION

The analytical model proposed in this study, incorporates RC panel behavior in the multiple-vertical-line-element-model (the original formulation of which considers uncoupled flexural and shear responses) in order to capture the experimentally observed shear-flexure interaction in RC walls (e.g., Massone and Wallace, 2004). The proposed wall model involves modifying the MVLEM by assigning a shear spring for each uniaxial element. Each uniaxial element is then treated as a RC panel element, with membrane actions, i.e., uniform normal and shear stresses applied in the in-plane direction. Therefore, the interaction between flexure and shear is incorporated at the uniaxial element (fiber) level. To represent constitutive panel behavior, a rotating-angle modeling approach, as applied in the derivation of the modified compression field

theory (MCFT, Vecchio and Collins, 1986) or the rotating-angle softened-truss model (RA-STM, Pang and Hsu, 1995), can be used. The constitutive rotating-angle modeling approach adopted in this study follows the RA-STM; however, a more refined constitutive stress-strain model for concrete in compression, which is calibrated with a large set of experimental results, is implemented. Constitutive stress-strain models for materials are applied along the principal directions of the strain field (i.e., principal strain directions 1 and 2), to obtain the stress field associated with the principal directions. It is assumed that the principal stress and strain directions coincide (as suggested by Vecchio and Collins, 1986; Pang and Hsu, 1995).

Accordingly, the axial and shear responses of each uniaxial (panel) element are coupled, which further allows coupling of flexural and shear responses of the MVLEM, since the axial response of the uniaxial elements constitute the overall flexural response of each MVLE. Details of the methodology are described in the following subsection.

8.6 NUMERICAL METHODOLOGY FOR PROPOSED MODEL

In the following description of the methodology, the uniaxial (panel) elements located within each model element (also called strips) are denoted by (*i*) and the model elements are denoted by (*j*):

1. The deformations or strains within the components of each element (*j*) are determined from the six prescribed degrees of freedom, (u_x , u_y , and θ at both ends of the model element) shown in Figure 8.9. Assuming that the shear strain is uniform along the section and that plane sections remain plane, the axial strain (ϵ_y), and shear distortion (γ_{xy}) components of the strain field are calculated for the entire section (for all the strips (*i*)) based on the prescribed degrees of freedom for the current analysis step. Accordingly, each strip (*i*) (Fig. 8.9) has two input variables, axial strain (ϵ_y) and shear distortion (γ_{xy}), based on element (*j*) deformations. The horizontal (or transverse) normal strain within each strip (ϵ_x) is initially estimated to complete the definition of the strain field, allowing stresses and forces to be determined from the constitutive material relations and geometric properties (dimensions and reinforcement and concrete areas) for each strip. For the initial estimate of the horizontal strain within each strip (ϵ_x), a zero value or the resulting value from the previous load step can be used. The output variables associated

with the input strains ε_y and γ_{xy} are the axial stress, σ_y , and the shear stress, τ_{xy} , for each strip (i).

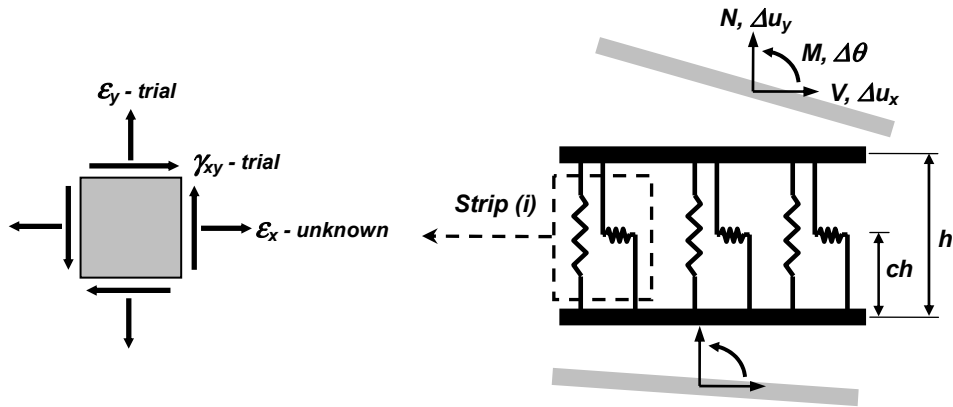


Fig. 8.9 Trial displacement state at section (j) of coupled model element

2. A numerical procedure (Newton's method) is employed to linearize the equilibrium equation and iterate on the unknown quantity ε_x (horizontal normal strain in each strip i) to achieve horizontal equilibrium for a given σ_x (resultant horizontal normal stress) within each strip. The horizontal stress σ_x is the resultant of stress components in concrete and steel that balances normal stress resulting from loads applied in the horizontal direction. Due to a lack of information and as an initial approximation, the horizontal stress σ_x within each strip was assumed to be equal to zero (no resultant stress), which is consistent with the boundary conditions at the sides of a wall with no transverse loads applied over its height. The horizontal strain, ε_x , is used as an iterative parameter for convenience.

(a) For a trial value of horizontal strain (ε_x , together with the prescribed values of axial strain (ε_y) and shear distortion (γ_{xy})), the strain field (principal orientation angle α , and the principal strains ε_1 and ε_2) is defined for each strip (i) (Fig. 8.10). It is assumed that the same orientation angle (α) applies for the principal directions of both the strain (ε_1 , ε_2) and the stress fields (σ_{c1} , σ_{c2}). Using the constitutive material relations implemented for concrete and steel (Fig. 8.11), and compatible strains for the two materials (assuming perfect bond), the stresses in concrete along the principal directions and stresses in reinforcement along the vertical and horizontal directions are

determined. As noted earlier, a uniaxial stress-strain model is used for the reinforcing steel; therefore stresses in reinforcement are calculated in horizontal and vertical directions (based on ϵ_x and ϵ_y , based on the assumption that reinforcement is provided in the vertical and horizontal directions, or transformed to equivalent reinforcement in the horizontal and vertical directions).

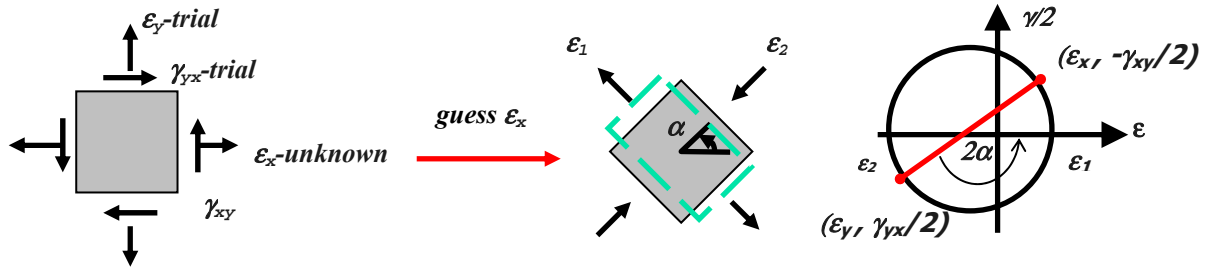


Fig. 8.10 Trial strain state at section (j) of coupled model element

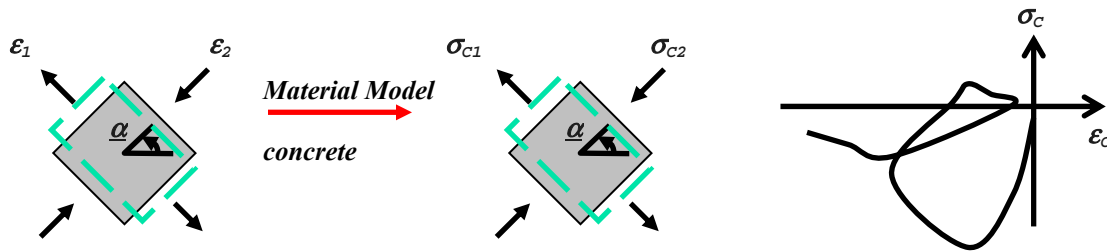


Fig. 8.11 Trial stress state at strip (i) in section (j) in principal directions

(b) Stresses in concrete are transformed (Fig. 8.12) from the principal directions to the reference coordinate directions (x - y) and the resulting concrete forces are superimposed with the forces in the reinforcement based on the concrete and steel areas within each strip (Fig. 8.13). The resultant gives average normal and shear stresses in each strip (i) as:

$$\tau_{xy} = -\frac{\sigma_{c1} - \sigma_{c2}}{2} \cdot \sin(2 \cdot \alpha) \quad (8.20)$$

$$\sigma_x = \sigma_{cx} + \rho_x \cdot \sigma_{sx} = \frac{\sigma_{c1} + \sigma_{c2}}{2} - \frac{\sigma_{c1} - \sigma_{c2}}{2} \cdot \cos(2 \cdot \alpha) + \rho_x \cdot \sigma_{sx} \quad (8.21)$$

$$\sigma_y = \sigma_{cy} + \rho_y \cdot \sigma_{sy} = \frac{(\sigma_{c1} + \sigma_{c2})}{2} + \frac{(\sigma_{c1} - \sigma_{c2})}{2} \cdot \cos(2 \cdot \alpha) + \rho_y \cdot \sigma_{sy} \quad (8.22)$$

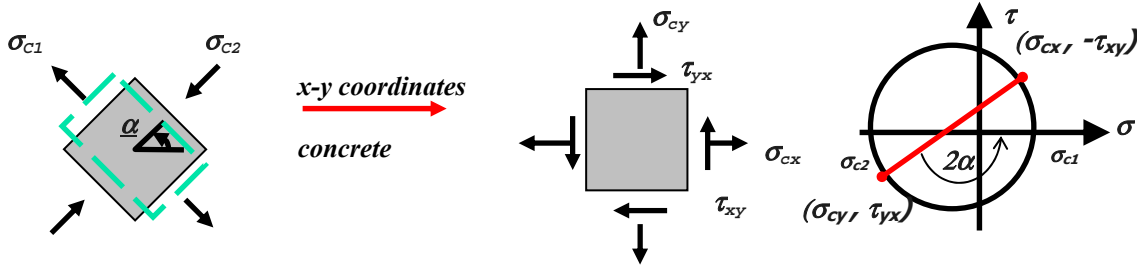


Fig. 8.12 Trial stress state for concrete at strip (*i*) in section (*j*) in x-y direction.

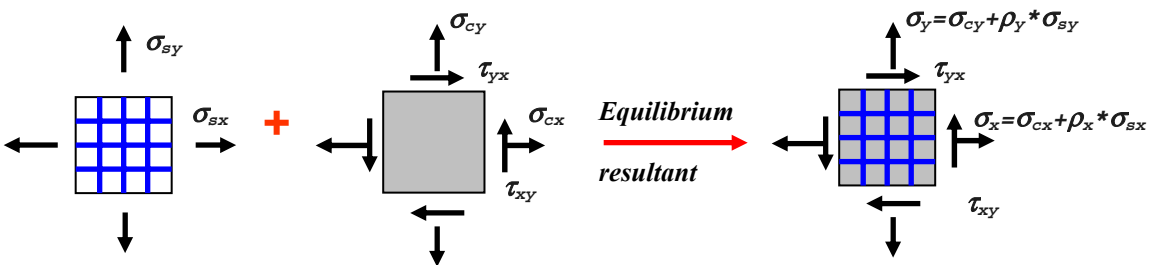


Fig. 8.13 Trial stress state for concrete and steel (combined) in x-y direction

(c) Equilibrium is checked in the horizontal direction (σ_x) for each strip (*i*), until equilibrium is achieved for the specified horizontal strain ϵ_x .

3. Once horizontal equilibrium is achieved for a specified tolerance within each strip, vertical stresses in the strips are assembled to determine the total resisting axial force and bending moment of each element, whereas the shear forces in the strips are assembled to determine the total resisting shear force of the element.
4. Consequently, global equilibrium is checked for the overall wall model by comparing the applied and resisting forces, and global iterations are performed on the model degrees of freedom until global equilibrium is satisfied. Figure 8.14 shows a flowchart with the internal numerical procedure.

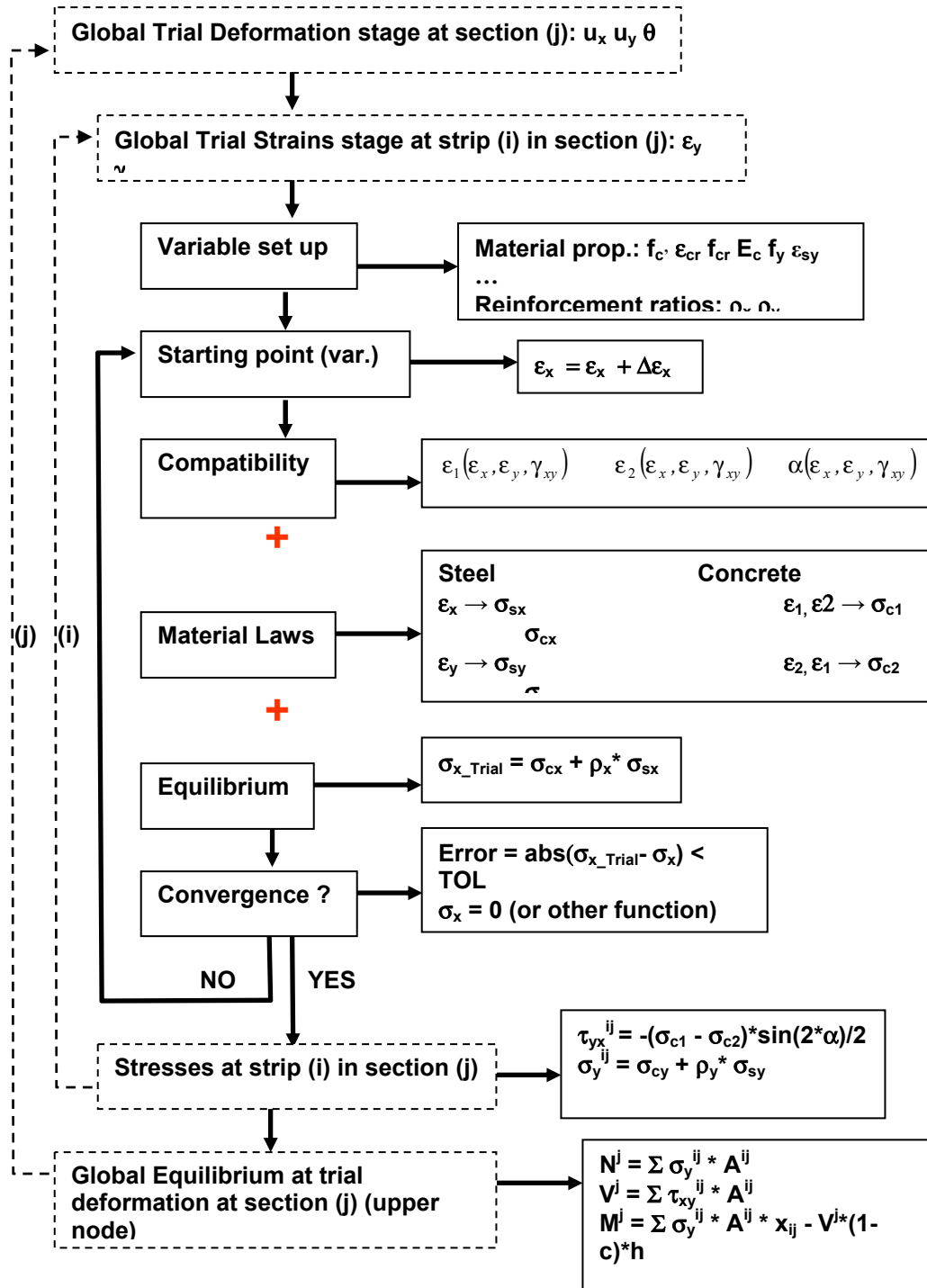


Fig. 8.14 Flowchart for biaxial behavior

8.7 MATERIAL CONSTITUTIVE MODELS

As described in the previous section, the proposed modeling approach involves using two-dimensional RC panel elements subjected to membrane actions, where the stiffness and force-

deformation properties of the panel elements are derived directly from material stress-strain relations. Therefore, details of the constitutive relations used for reinforcing steel and concrete are described in this section.

8.7.1 Constitutive Model for Reinforcing Steel

The stress-strain relation implemented in the wall model for reinforcing steel is the well-known uniaxial constitutive model of Menegotto and Pinto (1973), as described in Chapter 4. The relation is in the form of curved transitions (Fig. 8.21), each from a straight-line asymptote with slope E_0 (modulus of elasticity) to another asymptote with slope $E_I = bE_0$ where parameter b is the strain-hardening ratio. The curvature of the transition curve between the two asymptotes is governed by the parameter R (Fig. 8.21), the cyclic degradation of which permits the Bauschinger effect to be represented. Cyclic properties of constitutive relation are not incorporated in the present wall model; the model is yet to be extended for cyclic analysis. However, the cyclic stress-strain response generated by the model is also illustrated in Figure 8.21 for further discussions.

To consider the effects of tension stiffening on reinforcement, Belarbi and Hsu (1994) developed alternative average tensile stress-strain relations for steel bars embedded in concrete. Belarbi and Hsu (1994) identified how the average stress-strain relation of reinforcing steel bars surrounded by concrete is different than the stress-strain relation of bare steel bars. The most important difference was found to be the lowering of the yield stress, σ_y , as yielding of a reinforced concrete element occurs when the steel stress at the cracked section reaches the yield strength of the bare bar. At the same time, the average steel stress smeared along the length of the element reaches a level lower than that of the yield stress of the bare bar. The so-called single-curve model can be directly incorporated in the Menegotto and Pinto equation, and has been used for the calibration of the present wall model. As proposed by Belarbi and Hsu (1994), and based on experimental data from the RC panels and an analytical model, the effective stress and strain (intersection of the elastic and yield asymptotes) for bars embedded in concrete correspond to approximately 91% of the yield stresses and strains of bare bars ($\sigma_y^{eff} = 0.91 \sigma_y$, $\varepsilon_y^{eff} = 0.91 \varepsilon_y$) and the monotonic curvature parameter R_0 is described by the following empirical relation:

$$R_0 = \frac{1}{9B - 0.2} \leq 25 \quad (8.23)$$

$$B = \frac{1}{\rho} \left(\frac{f_{cr}}{\sigma_y} \right)^{1.5} \quad (8.24)$$

where f_{cr} is the concrete cracking stress and ρ is the cross-sectional area ratio of the longitudinal steel bars in the RC element (limited to a minimum of 0.25% in Mansour et al., 2001). The monotonic curvature parameter R_0 is limited to a value of 25, where the limiting value practically represents a sharp corner between the elastic and yield asymptotes.

The so called “kinking effect” (reduction of effective yield stress due to dowel action along the cracks) incorporated by Pang and Hsu (1995) in the original rotating-angle softened-truss model is disregarded in this study based on later experimental observations by Hsu and Zhu (2002), who stated that the kinking effect can be neglected.

For the case of cyclic loading, parameters σ_r and ε_r represent the stress and strain at each point of strain reversal, which together form the origin of elastic asymptote with slope E_0 , and parameters σ_0 and ε_0 are the stress and strain at the point of intersection of the elastic and yield. For monotonic loading, the cyclic stress and strain parameters retain the values $\sigma_r = 0$, $\varepsilon_r = 0$, $\sigma_0 = \sigma_y^{eff}$, and $\varepsilon_0 = \varepsilon_y^{eff}$. Furthermore, for loading the curvature parameter R held constant ($R=R_0$), since there is no cyclic reduction (Bauschinger effect) in the curvature of the stress-strain relation.

8.7.2 Constitutive Model for Concrete

To obtain a reliable model for panel (membrane) behavior, the constitutive relation implemented in the analytical model for concrete should consider the effects of membrane (panel) compression softening (reduction in principal compressive stresses in concrete due to cracking under tensile strains in the orthogonal direction), and tension stiffening (average post-peak tensile stresses in concrete due to the bonding of concrete and reinforcing steel between cracks). Properties of the constitutive model adopted in this study for concrete are described in the following subsections. For clarity, tensile and compressive stresses and strains are represented in terms of absolute values.

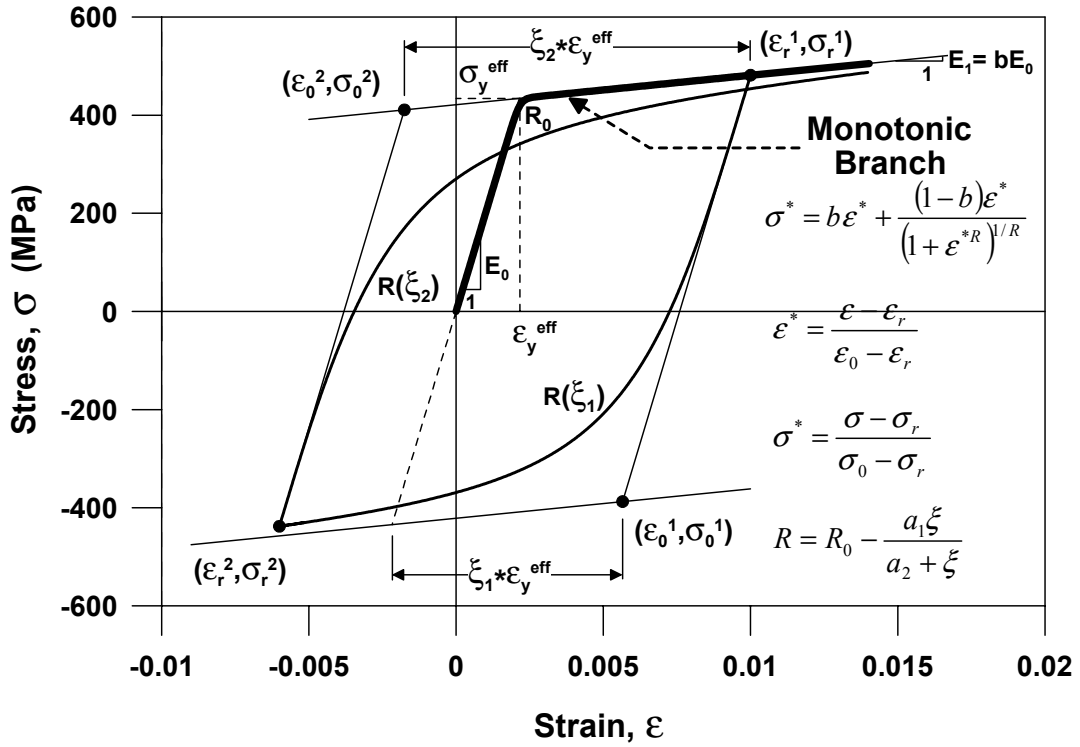


Fig. 8.15 Constitutive model for reinforcing steel

To incorporate the tension-stiffening effect in the stress-strain behavior of concrete in tension, the average (smeared) stress-strain relation proposed by Belarbi and Hsu (1994) (Fig. 8.22) is implemented, which is consistent with the selected constitutive material law for steel based on average stresses and strains. To describe the stress-strain behavior of concrete in compression, the Thorenfeldt base curve, calibrated by Collins and Porasz (1989), Wee et al. (1996) and Carreira and Kuang-Han (1985), and updated via the introduction of the compression softening parameter proposed by Vecchio and Collins (1993), is used. The envelope curve selected allows for higher strain in low-strength concrete and a better correlation in the degrading branch for high-strength concrete, where the envelope tends to be linear. The Thorenfeldt base curve, which is based on the Popovics (1973) equation, takes the form (Fig. 8.23):

$$\sigma_c = f'_c \frac{n \left(\frac{\epsilon_c}{\epsilon_0} \right)}{n-1 + \left(\frac{\epsilon_c}{\epsilon_0} \right)^{nk}} \quad (8.25)$$

where f'_c is the peak compressive stress (e.g., concrete compressive cylinder strength) and ϵ_0 is the strain at peak compressive stress for unconfined concrete in compression. For defining of the strain at peak compressive stress (ϵ_0), the expression proposed by Wee et al. (1996) is used (Fig. 8.23). The following expressions proposed by Collins and Porasz (1989) are used for the equation parameters n and k , for calibration of the model for relatively high-strength concrete:

$$n = 0.8 + \frac{f'_c (MPa)}{17} \quad (8.26)$$

$$k = \begin{cases} 1 & , 0 \leq \epsilon \leq \epsilon_0 \\ 0.67 + \frac{f'_c (MPa)}{62} & , \epsilon_0 \leq \epsilon \end{cases} \quad (8.27)$$

For concrete with lower compressive strengths (e.g., $f'_c < 20$ MPa), the following expressions proposed by Carreira and Kuang-Han (1985) are considered for the same parameters:

$$n = 1.55 + \left(\frac{f'_c (MPa)}{32.4} \right)^3 \quad (8.28)$$

$$k = 1 \quad (8.29)$$

An important consideration in modeling the behavior of a RC panel element under membrane actions is incorporating the compression softening effect. The softening effect has been experimentally observed by many authors (e.g., Belarbi and Hsu, 1995; Vecchio and Collins, 1986) mainly as a reduction in the compressive capacity of concrete panels along the principal compressive direction undergoing tensile strains in the other principal direction. Some models have also included softening in the compressive strain (e.g., Belarbi and Hsu, 1995; Vecchio and Collins, 1993), reducing the strain at the peak compressive stress for concrete. Vecchio and Collins (1993) used a large experimental database from tests on RC panels to propose different models representing compression softening. In the tests, concrete strength (f'_c) for all specimens varied from 10 MPa to 90 MPa, where the main concentration of tests was in the range 20–30 MPa. The concrete constitutive model was based on two main curves: the Hognestad parabola and the Thorenfeldt curve. Both models were modified to include softening in stress and strain. The so-called Model B, based on the Thorenfeldt curve, which considers only a reduction in peak compressive stress ($\sigma_c^{Model B} = \beta \sigma_c$), is implemented in this study, since

Vecchio and Collins (1993) observed that more complicated models (including also reduction in the strain at peak stress, ϵ_0) are only marginally better for incorporating the compression softening effect. Accordingly, the reduction factor to be applied to the peak compressive stress for concrete in compression (Fig. 8.23) is given by the expression:

$$\beta = \frac{1}{0.9 + 0.27 \frac{\epsilon_1}{\epsilon_0}} \quad (8.30)$$

where ϵ_1 is the principal tensile strain (Eq. 8.64 applies only when ϵ_1 is a tensile strain) and the ratio ϵ_1/ϵ_0 is considered positive.

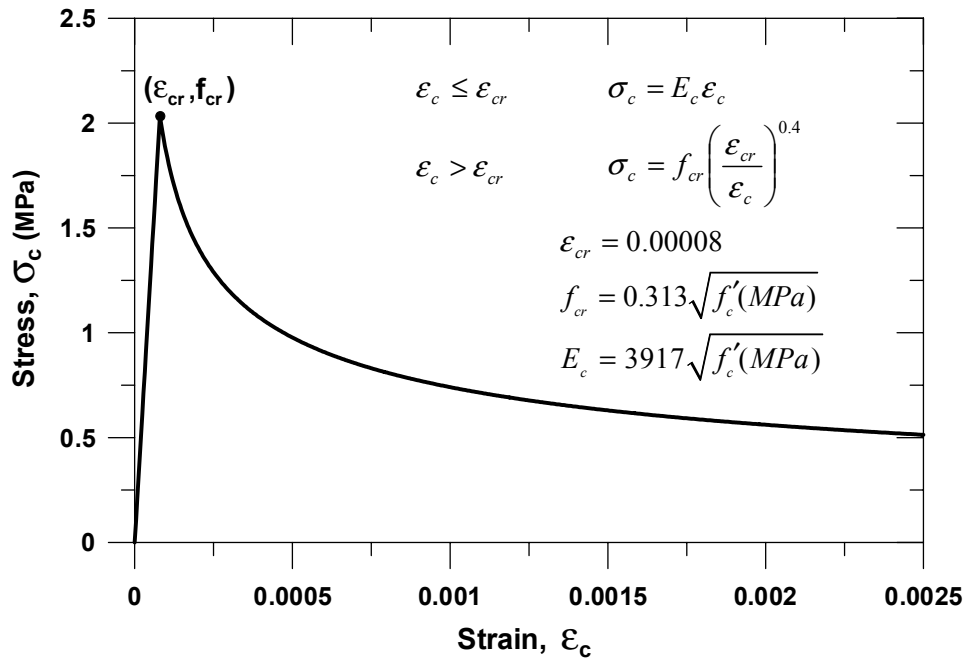


Fig. 8.16 Constitutive model for concrete in tension

The formulation of the analytical model presented in this chapter, together with the material constitutive models used and the numerical solution methodologies described, has been implemented into OpenSees (“OpenSees”) to conduct nonlinear analyses for evaluating the validity and accuracy of the analytical model in simulating coupled shear and flexural responses in RC walls. Experimental calibration of the model and comparison of model results with results of tests conducted on both slender and squat wall specimens are presented in the following chapter.

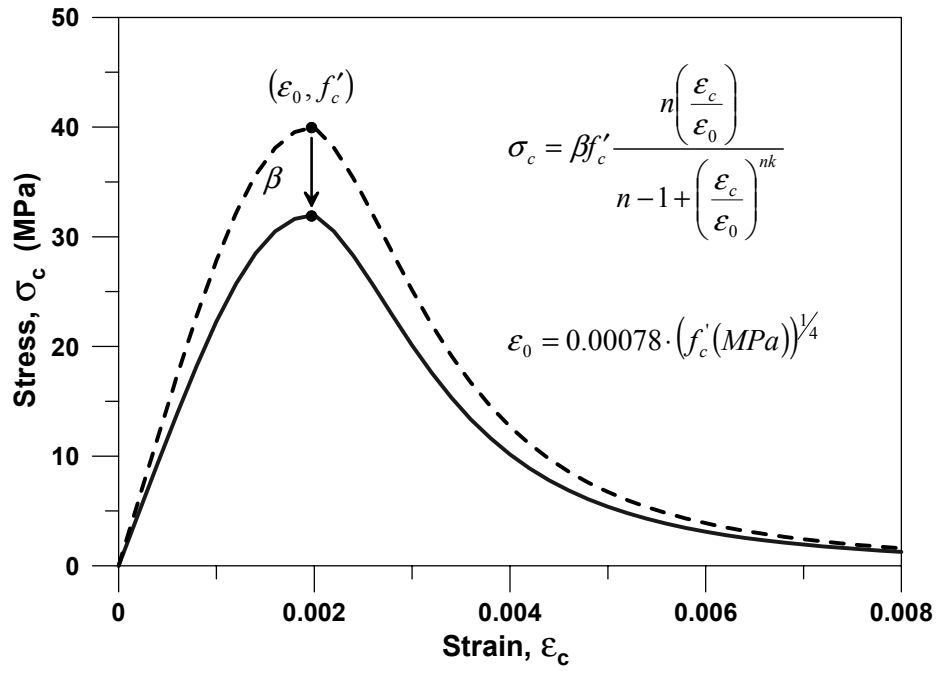


Fig. 8.17 Constitutive model for concrete in compression

9 Modeling of Coupled Shear and Flexural Responses — Experimental Verification

The analytical model described in the previous chapter integrates material constitutive models with a rotating-angle modeling approach to assemble a constitutive RC panel model. In modeling of wall response, the analytical model incorporates further assumptions: the plane sections remain plane kinematic, there is a uniform distribution of shear strains along the wall length, and there is an assumed zero value for the resultant horizontal stress (σ_x) within each strip of the model element. Due to the simplifications associated with the implemented membrane (panel) material model (e.g., compression softening effect on stress only), idealizations of the rotating-angle approach (e.g., principal strain and stress fields coincide assumption), and the assumptions involved in the formulation of the present wall model (plane sections, uniform shear strains, zero horizontal stresses), the validity of the model needs to be investigated for different wall configurations. Therefore, this section presents information on the correlation of preliminary model results with experimental results in order to evaluate the modeling approach. First, results of the constitutive panel model are compared to experimental results from RC panel tests to validate the response of model sub-elements. Then, the responses simulated by the wall model are compared to test results on slender and short wall specimens. A discussion based on experimental observations regarding the model assumptions (i.e., uniform shear strain distribution along wall length and zero horizontal resultant stress across the wall) is also provided.

9.1 PANEL BEHAVIOR

To verify the constitutive material models selected and the constitutive panel behavior incorporated in the present wall model, results from tests conducted by prior researchers on RC panel specimens subjected to pure shear loading conditions are compared to analytical responses

obtained using the constitutive panel model adopted. Two different sets of test series are used for the comparisons (series A and B and series PV). Series A and B were tested by Pang and Hsu (1995). The tested RC panel specimens were 1.4 m x 1.4 m x 178 mm thick, and were uniformly reinforced with reinforcement area ratios varying between 0.6% and 3%. In-plane loads were applied such that an equivalent pure shear loading condition (shear forces orthogonal/parallel to the reinforcement) was achieved. Series PV was tested by Vecchio and Collins (1982). The specimens had dimensions of 0.89 m x 0.89 m x 70 mm thick, and were uniformly reinforced with reinforcing ratios varying between 0.7 and 1.8%. Pure shear loads were applied along the sides of the specimens.

The constitutive panel element used in the present study was calibrated based on the material properties and specimen geometry of selected test specimens, and subjected to a pure shear loading condition to simulate the test conditions. Accordingly, comparisons of analytical results with experimental results for the shear stress – shear strain response of the selected panels are shown in Figure 9.1. As observed in the figure, a good correlation is obtained between the element responses and test results, validating the selection of the constitutive material models and the formulation of the panel elements incorporated in the present wall model. However, it must be noted that the correlations presented are not for generalized loading conditions; responses under only pure shear loading conditions are considered.

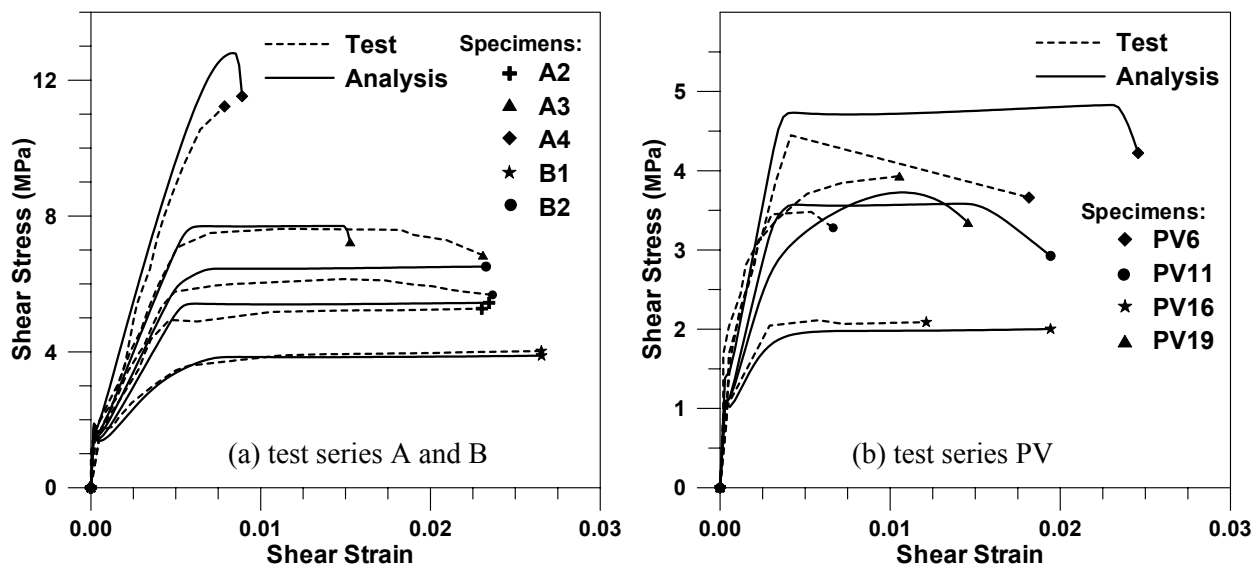


Fig. 9.1 Test results vs. model element predictions for panel responses

9.2 SLENDER WALL RESPONSE

Experimental observations indicate coupling between shear and flexural responses, even for relatively slender walls (e.g., Massone and Wallace, 2004). Thus, correlation of preliminary model results with results from a slender wall test is presented.

9.2.1 Test Overview

The rectangular wall specimen (specimen RW2 described in Chapter 8) tested by Thomsen and Wallace (2004) was proportioned using a capacity design approach, and boundary element details were based on using a displacement-based design methodology. Sufficient shear capacity was provided for the wall specimen to resist the shear that developed for the probable wall moment, using ACI 318-02 (Eq. 21.7). The wall specimen was 3.66 m tall and 102 mm thick, with a web length of 1.22 m. The wall specimen was tested in an upright position, undergoing top lateral cyclic displacements, while an axial load of approximately $0.07A_gf'_c$ was held constant throughout the duration of the test. More detailed information concerning the wall tests is presented in Thomsen and Wallace (2004).

9.2.2 Model Calibration

To discretize the wall cross section for the analytical model, 16 strips (panel elements) were defined along the length of the wall specimen, with corresponding tributary areas for concrete and vertical reinforcement assigned to each strip. The horizontal reinforcement area was set constant for all of the strips, which was consistent with the horizontal reinforcement used for the specimen. A total of 8 model elements (each consisting of 16 strips) were stacked along the height of the wall. The constitutive relations implemented in the model for reinforcing steel and concrete were calibrated to represent the experimentally observed properties of the materials used in the experimental study (using results of monotonic stress-strain tests conducted on concrete and rebar specimens). Confinement and tension-stiffening effects were incorporated in modeling (e.g., Orakcal and Wallace, 2004).

9.2.3 Model Correlation with Test Results

Prior to analysis, the experimental results for wall lateral displacements at story levels were separated into flexural and shear response components using the methodologies described by Massone and Wallace (2004) (see also Chapter 8) to allow comparison of model results to local (e.g., story) shear and flexural response measurements. Results of monotonic analysis with the proposed model were compared with the cyclic test results for the slender wall specimen.

Figure 9.2 compares the analytical and experimental lateral load – top displacement responses for the wall specimen. As observed in Figure 9.2, the lateral load capacity and the lateral stiffness of the wall are significantly overestimated for lower lateral drift levels (i.e., up to 0.75% drift) and overestimated to a lesser extent for higher lateral drift levels. The overestimation of the wall capacity and stiffness, especially at lower drifts, can be attributed to the fact that analysis results for monotonic loading are compared to cyclic test results. The cyclic degradation of the curvature parameter R (Fig. 8.21) associated with the implemented constitutive model for reinforcing steel influences significantly the wall lateral load capacity and stiffness prediction, especially within the pre-yield and relatively low post-yield drift levels (Orakcal et al., 2004). The present monotonic constitutive model for reinforcement does not consider the cyclic degradation of the parameter R , impairing the response prediction. It must be noted that results presented are preliminary, and additional studies to incorporate cyclic behavior and to improve the material relations for a more refined calibration are under way.

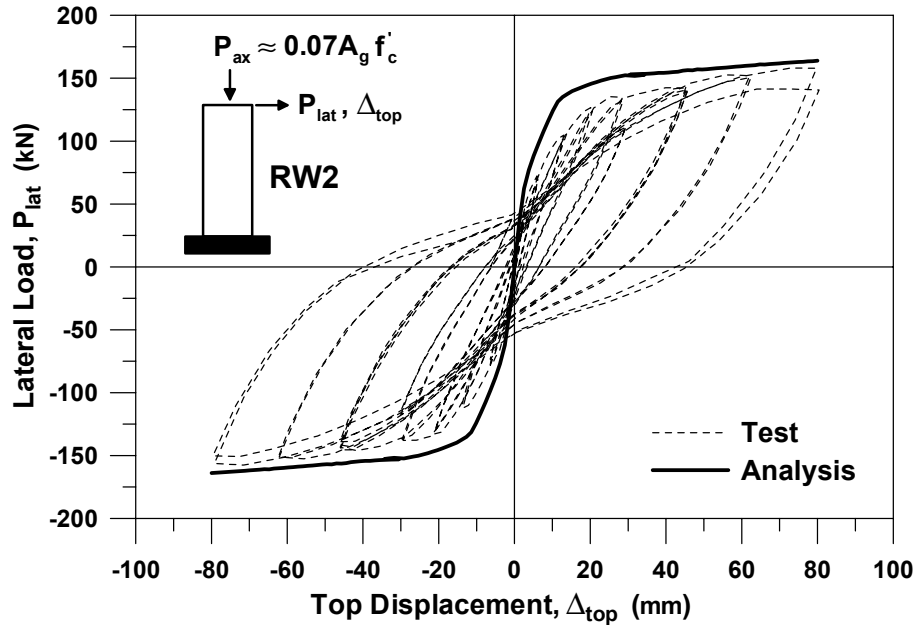


Fig. 9.2 Lateral load – top displacement response of specimen RW2

Figure 9.3 presents the correlation of analytical and experimental results for the lateral load – flexural displacement and lateral load – shear displacement responses at the first-story level of specimen RW2. The figure reveals that the model overestimates the flexural deformations and underestimates the shear deformations measured within the first story of the wall specimen. Again, the correlations would be significantly improved upon incorporating cyclic analysis. However, as observed in the figures, the model is capable of capturing the nonlinear shear deformations experienced simultaneously with the nonlinear flexural deformations within the first story of the wall specimen, and thus successfully incorporates coupling of nonlinear shear and flexural responses that were observed experimentally even for a relatively slender wall.

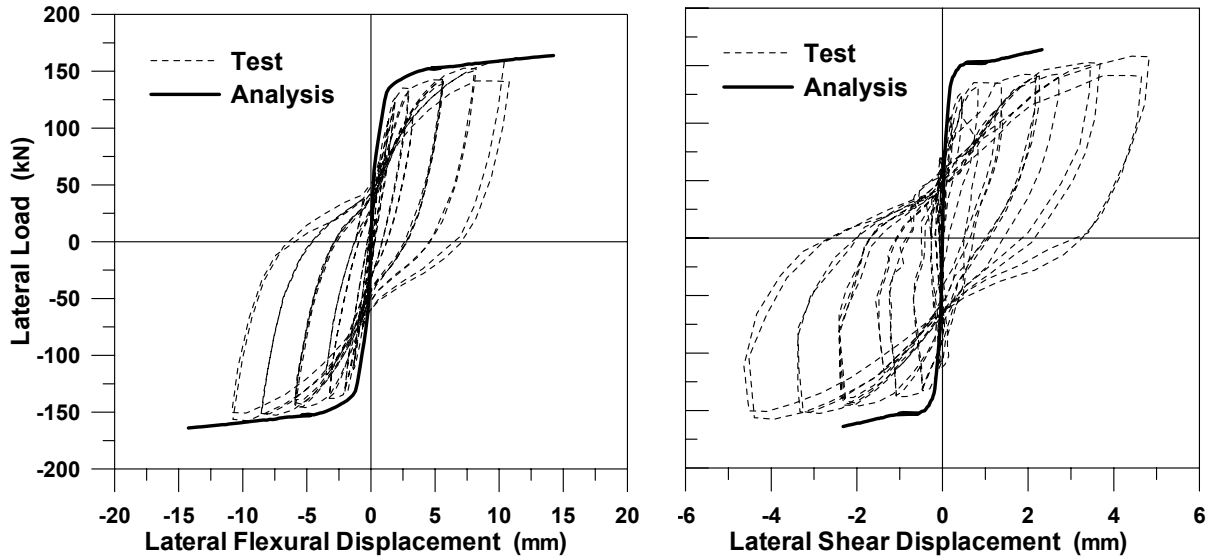


Fig. 9.3 Lateral load–displacement responses at first-story level (RW2)

9.3 SHORT WALL RESPONSE

As mentioned earlier, the proposed methodology to couple shear and flexural responses involves three main assumptions: shear strains are uniformly distributed across the wall cross section, the resultant horizontal stresses along the length of the wall are zero, and plane sections remain plane. In the case of tall walls, the first assumption (i.e., uniform distribution of shear strain) may not influence significantly the overall wall response, since the governing response component is flexure. However, for short walls, using the same assumption may not be reasonable due to possible presence of different modes of deformation (e.g., warping) or different load transfer mechanisms (e.g., strut action), or other possible reasons such as the so-called Saint-Venant’s effect, where the relatively small height of the wall may not be adequate to allow redistribution of stresses concentrated within the proximity of the points of load application or where support reactions are present. Such effects introduce nonuniformity in stresses and strains that may change considerably the observed wall response. A similar condition applies to the zero horizontal stress and plane section assumptions.

Thus, correlation of model results with test results on short wall specimens is presented to assess the validity of the modeling approach for short walls. A more detailed calibration and correlation study is under way; only general comparisons with limited experimental data are

included here. Test results available in the literature for four specimens with low shear-span ratios are used for the comparisons.

9.3.1 Overview of Tests

Two wall specimens tested by Hidalgo et al. (2002) (specimens 10 and 16), and two specimens reported by Hirosawa (1975) (specimens 74 and 152) are investigated here. These four wall tests were selected because they represent a variety of wall configurations, specimen sizes, and loading conditions. For each of the four selected test specimens, the amount of shear reinforcement provided was no less than the minimum specified in the ACI 318-02 (2002), i.e., $\rho_{min}=0.0025$. General specimen information for the four wall tests is shown in Table 9.1. As shown in the table, all specimens had shear-span ratios ($M/(Vl)$) between 0.35–1.0. Specimens 10, 16, and 152 were designed to fail in shear. In those cases, the shear capacity was about half the capacity to reach flexural failure. Specimen 74, in the other hand, was reported to fail in flexure, but primarily deformed in shear. However, according to ACI 318-02, flexural and shear capacities are similar (Fig. 9.4(a)).

Specimens 10 and 16 had similar reinforcement configurations; the shear-span ratio was the main varying parameter between the two specimens (0.69 and 0.35 for specimens 10 and 16, respectively). Relatively low shear-span ratios were achieved in the testing of these specimens via fixing the base of the walls and avoiding rotations at the top of the walls by applying the lateral load at specimen midheight, which produces a linear bending moment distribution with moments equal in magnitude and opposite in direction applied at the wall ends. Both specimens were designed to fail in shear by providing a relatively large amount of longitudinal reinforcement at wall boundaries. Specimen 74 is the only specimen subjected to axial load and is also the specimen with the largest shear-span ratio ($M/(Vl)=1.0$). It was tested under a cantilever loading condition, with lateral load applied at the top of the wall. Another distinct property of the specimen is that the shear and flexural capacities (according to ACI 318-02) of the specimen are close, the shear capacity being slightly lower. Finally, specimen 152, having a barbell-shaped cross section, was tested as a short beam with a concentrated transverse load applied at midspan. From symmetry, half of the specimen represents a short wall where half of the applied transverse load corresponds to an equivalent lateral load applied to the wall, yielding a shear-span ratio of 0.56.

Table 9.1 Properties of selected short wall specimens

Reported by			Hidalgo et al. (2002)		Hirosawa (1975)	
Test no			10	16	74	152
<i>lw</i>	clear length	(cm)	130	170	170	208
<i>hw</i>	total height	(cm)	180	120	170	152
<i>tw</i>	web thickness	(cm)	8	8	16	16
<i>lb</i>	boundary length	(cm)	-	-	-	32
<i>tb</i>	boundary thickness	(cm)	-	-	-	32
<i>M/(Vl)</i>	shear-span ratio	-	0.69	0.35	1.00	0.56
<i>ρ_h</i>	web horizontal steel ratio	(%)	0.25	0.25	0.57	0.62
<i>ρ_v</i>	web vertical steel ratio	(%)	0.25	0.25	0.61	0.58
<i>Ab</i>	boundary vertical steel	(cm ²)	7.6	6	15.5	66.4
<i>N</i>	axial load	(kN)	0	0	533	0

9.3.2 Model Calibration

The analytical model was calibrated to represent the geometric properties of the wall specimens, using 8 model elements stacked along the height of each wall, where each element model consisted of 8 strips (panel elements) defined along the length of the wall. Two strips were defined for each boundary element of the specimens, whereas the remaining 4 were used to discretize the web. Similar to the case for the slender wall, a more refined discretization of the model did not change considerably the analytical responses obtained for the short walls; this issue is addressed in a subsequent section. Corresponding tributary areas for concrete and vertical reinforcement were assigned to each strip, whereas a constant horizontal reinforcement area was used for each strip. Similar to the case for the slender wall test, the constitutive material parameters were calibrated based on available experimental data reported on the mechanical properties of the materials used in the construction of the wall specimens.

9.3.3 Model Correlation with Test Results

Figure 9.4 shows the correlation of experimental and analytical results for the lateral load – displacement response of each of the four wall specimens. Analytical results were not obtained for large lateral displacement values within the post-peak (degrading) branch of analytical response, since the results in that range are subject to the so-called damage localization problem (i.e., analysis results for the degrading response are sensitive to the discretization of the model elements). Thus, degrading responses are not considered in the present study.

As observed in Figure 9.4(a), a very good correlation is obtained between test results and results of the proposed coupled shear-flexure model for specimen 74 ($M/(Vl)=1.0$). Since the design flexural and shear capacities of the specimen are close, to consider the possibility that the response of the specimen is governed by nonlinear flexural deformations (i.e., the specimen does not experience significant nonlinear shear deformations), Figure 9.4(a) also includes an analytical flexural response prediction (with shear deformations not considered) obtained using a fiber model. The same geometric discretization and material constitutive models used in the coupled model were adopted for the fiber model, with the distinction that the panel elements (strips) of the coupled model were replaced with uniaxial (fiber) elements, and the constitutive model used for concrete in compression did not incorporate the biaxial compression softening factor coefficient (β). Figure 9.4(a) illustrates that although the flexural (fiber) model provides a ballpark estimation of the wall lateral load capacity, (predicted lateral load capacities approximately 750 kN and 980 kN, respectively for the coupled and flexural models), the load-displacement response obtained by the flexural model is significantly different than the measured response and the coupled model response. After a lateral load of 450 kN, significant lateral stiffness degradation is observed in both the test results and results of the coupled model but not in the flexural model. This result demonstrates how the proposed model, which couples shear and flexural responses, is able to simulate observed responses with substantially greater accuracy than a flexural model, particularly for wall specimens where the nominal shear and flexural capacities are nearly equal.

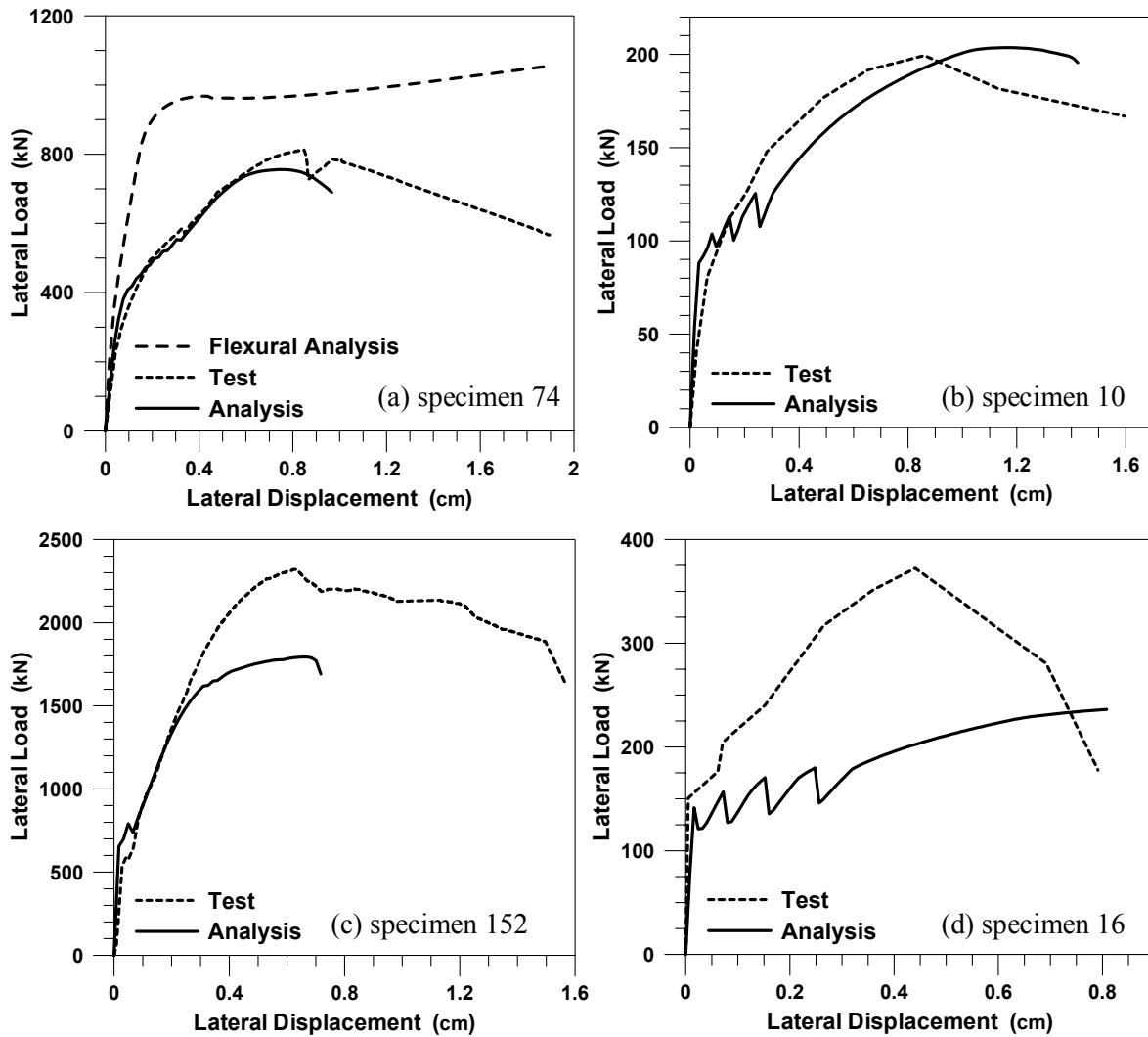


Fig. 9.4 Lateral load–displacement responses for short wall specimens

The correlation between results of the coupled model and test results for specimen 10 ($M/(VI)=0.69$) is similar to that of specimen 74 (Fig. 9.4b). The model provides a good prediction of the lateral load capacity and lateral stiffness of the wall specimen for most of the top displacement history, although the wall specimen reaches its peak lateral load capacity at a smaller top displacement than that predicted by the model. The sudden lateral load reductions observed in the model response are due to sequential cracking of concrete, whereas such behavior is not observed in test results. Refining the model discretization (increasing the number of strips used along the length of the wall) would invoke a more gradual and continuous shape for the analytical load-displacement response.

A relatively poor correlation is obtained between model and test results for the peak lateral load capacity of specimen 152 ($M/(Vl)=0.56$), for which the model underestimates the peak lateral load capacity of the specimen by approximately 25% of the measured value (Fig. 9.4c). However, the analytical model provides a good prediction of the wall lateral stiffness at lower lateral load levels, and the general shape of the nonlinear response simulated by the model is reasonable.

However, the correlation for specimen 16 ($M/(Vl)=0.35$) is far from being reasonable, where the analytical model underpredicts the measured lateral load capacity of the wall by up to 50% for the entire loading history (Fig. 9.4d). Specimen 16 was subjected to the same loading conditions as specimen 10 ($M/(Vl)=0.69$) and also had a similar reinforcement configuration; the shear-span ratio was the main differentiating parameter between the two specimens. Thus the difference between the accuracy in the predictions presented in Figures 9.4(b) and (d) is associated directly with variation in shear-span ratios of the two specimens.

Overall, the correlations indicate that the accuracy of the proposed model in predicting wall response is progressively impaired as the shear-span ratio of the wall modeled is reduced. The best correlation is obtained for specimen 74 ($M/(Vl)=1.0$), whereas results for specimen 16 ($M/(Vl)=0.69$) were generally good. Results for specimen 152 ($M/(Vl)=0.56$) showed a relatively poor but reasonable correlation, and the model was not successful in predicting the response of specimen 16 ($M/(Vl)=0.35$). Therefore, it is apparent that the validity of the modeling approach and the model assumptions are violated as wall shear-span ratios decrease. In a wall with a small shear-span ratio, stresses and strains can follow significantly nonlinear distributions as opposed to the assumptions incorporated in the present model (uniform shear strain distribution and zero horizontal stress along wall length).

9.4 SENSITIVITY OF SHORT WALL ANALYTICAL RESULTS TO MODEL DISCRETIZATION

A parametric study was conducted to investigate the sensitivity of the analytical results to the number of model elements stacked along wall height and the number of strips defined along wall length. The pre-peak region of the analytical load-displacement response was found to be insensitive to the selection of either the number of elements or the number of strips provided that reasonable values are selected in order to adequately represent the overall wall geometry. Figure

9.5(a) shows a comparison of the lateral load-displacement responses predicted by stacking 8 model elements with a varying number of strips defined along the length of the wall specimen 74 (shear-span ratio of 1.0). Figure 9.5(b) compares the results obtained using 8 strips along wall length, and varying the number of model elements stacked along wall height. The correlations presented in Figure 9.5 for specimen 74 is typical for all of the walls (including the slender wall specimen RW2) investigated herein.

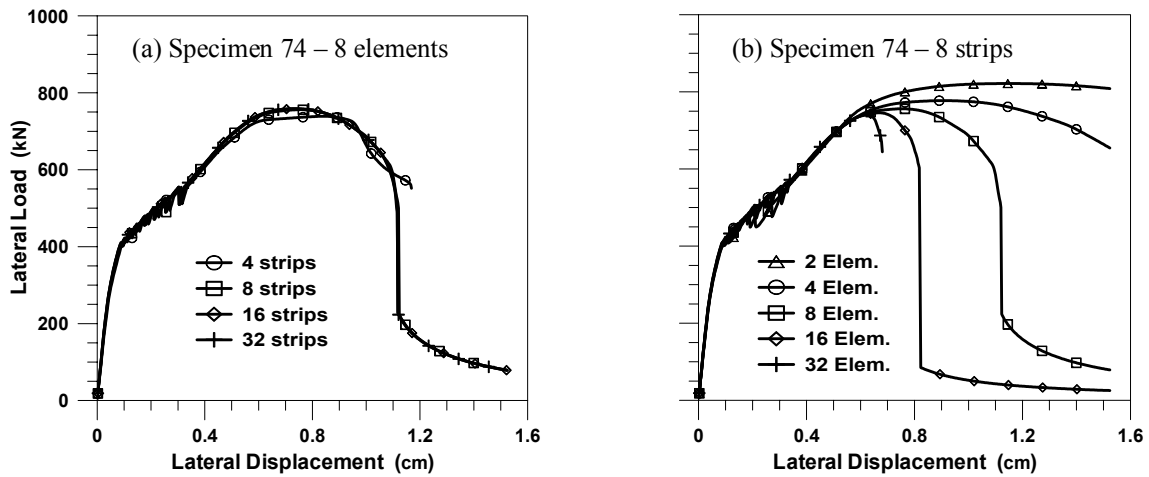


Fig. 9.5 Sensitivity of model results to number of strips and model elements

Results shown in Figure 9.5(a) indicate that increasing the number of strips does not change significantly the predicted load-displacement response. However, increasing the number of strips invokes a more gradual and continuous shape for the response, with smaller magnitudes of sudden lateral load reductions due to sequential cracking of concrete (incursion into the post-peak region of the tensile stress-strain relation) within each strip. Figure 9.5(b) shows that the predicted lateral load capacity of the wall and the pre-peak region of the predicted load-displacement response are marginally sensitive to the number of elements stacked along the wall height. However, as shown in Figure 9.5(b), the variation in the wall capacity is not substantial for the walls investigated in this study.

Figure 9.5(b) also shows that the degrading region (and initiation of the degrading region) of the predicted load-displacement response is highly sensitive to the selection of the number of elements. This behavior is due to damage localization effects associated with the crushing of concrete in compression (incursion into the post-peak region of the compressive stress-strain

relation). For the walls investigated, wall lateral load capacity is governed by the compressive strength of concrete (i.e., the failure mode is concrete crushing). Thus, the post-peak region of the stress-strain behavior of concrete in compression controls the degrading region of the analytical load-displacement response. The present model cannot reliably predict this strength degradation, without implementation of a proper damage localization parameter to calibrate the post-peak (descending) region of the compressive stress-strain behavior of concrete based on the size (height) of the elements used. This study focuses on predicting the pre-peak load-displacement response and the lateral load capacity of walls; modeling of damage localization and predicting degrading responses is not addressed.

9.5 EXPERIMENTAL SHEAR STRAIN AND HORIZONTAL NORMAL STRAIN DISTRIBUTIONS IN SHORT WALLS

As a supporting discussion on the potential of improving the model assumptions for a better representation of short wall response, measured shear and horizontal strain distributions as part of an experimental program are presented. Results of two wall tests conducted by Maier and Thurlimann (1985) were investigated.

Two identical wall specimens (specimens S1 and S2), with shear-span ratios of 1.0 and barbell-shaped cross sections with large boundary zones were loaded monotonically under a cantilever loading condition with lateral loads applied at the top of the walls. The specimens were 1.2 m height, 1.18 m long (boundary elements included) and 0.1 m thick. The boundary elements were 0.4 m long and 0.1 m thick. Uniform steel web reinforcement was included in vertical and horizontal directions. The steel reinforcement ratio in both directions was 1%. The boundaries were reinforced with longitudinal rebars in a ratio of 1.26% of the boundary area. The compressive concrete capacity was 36.9 MPa and the yield stress of the reinforcement 574 MPa. Both specimens were loaded with a constant axial load. Specimen S1 had an axial load of about $0.07f_cA_g$, whereas specimen S2 had a higher axial load of about $0.25A_gf_c$ (where A_g corresponds to the total cross-section area).

9.5.1 Shear Strain Distributions

Vertical and horizontal displacements were measured at 63 points that constitute a mesh on the web of the specimen (Fig. 9.6a), and shear strains were calculated from the displacement measurements at each point on the mesh. Results obtained for the two specimens were similar in terms of shear strain distributions; thus, results for only specimen S2 are presented here.

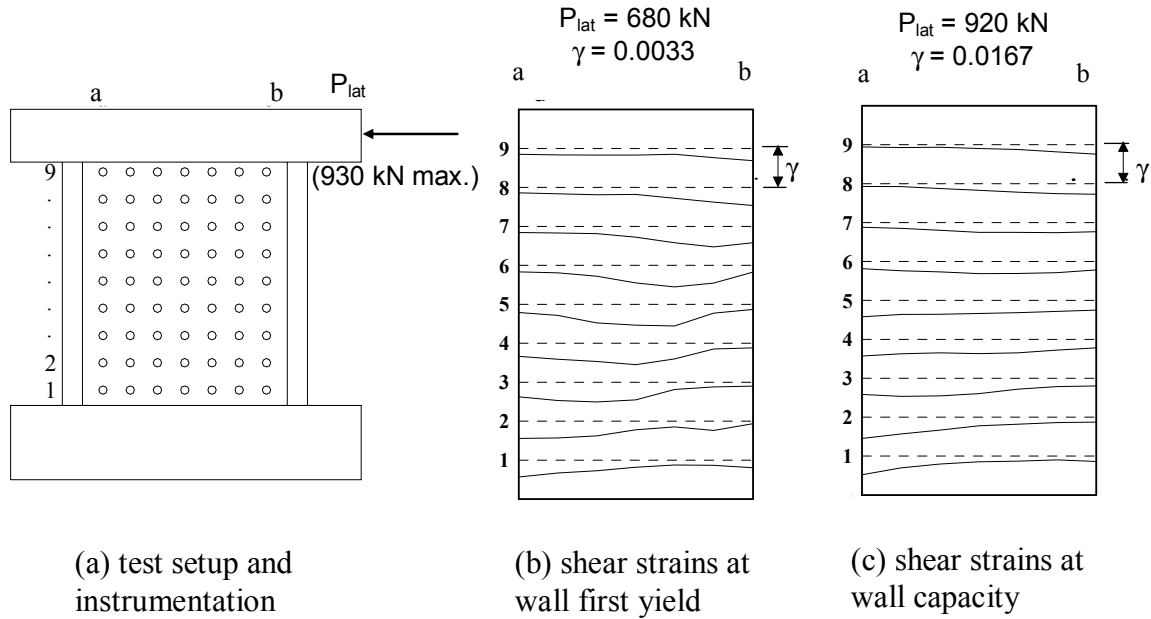


Fig. 9.6 Shear strain measurements for specimen S2

For two different lateral load levels (corresponding to yielding of the wall and at maximum wall capacity), the distribution of shear strains along the horizontal direction at different vertical levels of the wall specimen are plotted in Figure 9.6(b)–(c). The shear strains at each vertical level are plotted using a continuous line along the horizontal direction, and the horizontal dotted lines represent a zero shear strain line for reference. The figure reveals a systematic nonlinear shear strain distribution, at both lateral load levels. The shear strains are distributed in the horizontal direction at different vertical wall levels such that the position of the maximum shear strain experienced at each vertical level approximately follows a diagonal line traced between the point of the applied load and the lower opposite corner (compression strut). This contradicts the model assumption that shear strains are distributed uniformly along the length of the wall, as observed here for a wall with a shear-span ratio of 1.0. Comparison of

experimental and model results for specimen 74 (see previous section), which also has a shear-span ratio of 1.0, is very good; therefore, the model assumption works well in this case. However, the nonlinear distribution of shear strains may be more pronounced for shorter walls, which may modify the responses of wall specimens with smaller shear-span ratios (e.g., specimen 16).

9.5.2 Horizontal Normal Strain Distributions

As complementary to the previous discussion related to experimental versus assumed shear strain distribution, another discrepancy and potential improvement of the model assumptions of short wall response is presented. In this case, measured horizontal strain distributions as part of the experimental program by Maier and Thurlimann (1985) are presented. The results only for specimen S2 are included here.

The same two different lateral load levels (corresponding to yielding of the wall and at maximum wall capacity) used for the shear strain distributions in the previous discussion were used in this analysis. The distribution of horizontal strains along the horizontal direction at different vertical levels of the wall specimen is plotted in Figure 9.7(b)–(c). As was the case for shear strains, the peak values of the horizontal normal strain measurements follow compression strut. Furthermore, on average, the horizontal strain measurements decrease. In both load cases (Fig. 9.7(b)–(c)), the horizontal strain at levels 1 (bottom) and 9 (top) are relatively small compared to all other levels, and the strains tend to increase closer to wall midheight. Although this affect is also apparent in the measured shear strain distributions, it is much more pronounced for horizontal strains. The effect is clearly observed in Figure 9.8, which plots average horizontal strain (average over the cross section) measurements along wall height.

Figure 9.8 shows the average horizontal normal strains measured at different levels along the height of the wall for three different applied load levels ($P = 920\text{kN}$ at wall capacity, $P = 680\text{kN}$ at wall first yield and $P = 810\text{kN}$ as an intermediate case). Analytical (model) results are also included in the figure; however, analysis results are only available for the first two load levels, as the analytical model predicted the wall to fail before it reaches a load of 810 kN. As observed in the experimental results, the horizontal strain measurements have maximum values at wall midheight, and progressively decrease to zero values at the top and the bottom of the wall. In contrast, the analytical model, which assumes zero-resultant horizontal stress at every

location on the wall, predicts the horizontal strains to be increasing from the top (where lateral load is applied) to the bottom of the wall. This implies that the analytical model overestimates the horizontal strains in the vicinity of the top and bottom ends of the wall.

The experimental distribution of the horizontal normal strains along the height of the wall is partially due to the so-called constraining effect of beam and pedestal located at the top and bottom of the wall, and has been observed also by other researchers (e.g., Hsu, 1988; Cheng et al., 1993). The significance of considering this effect in the modeling methodology is described in the following section.

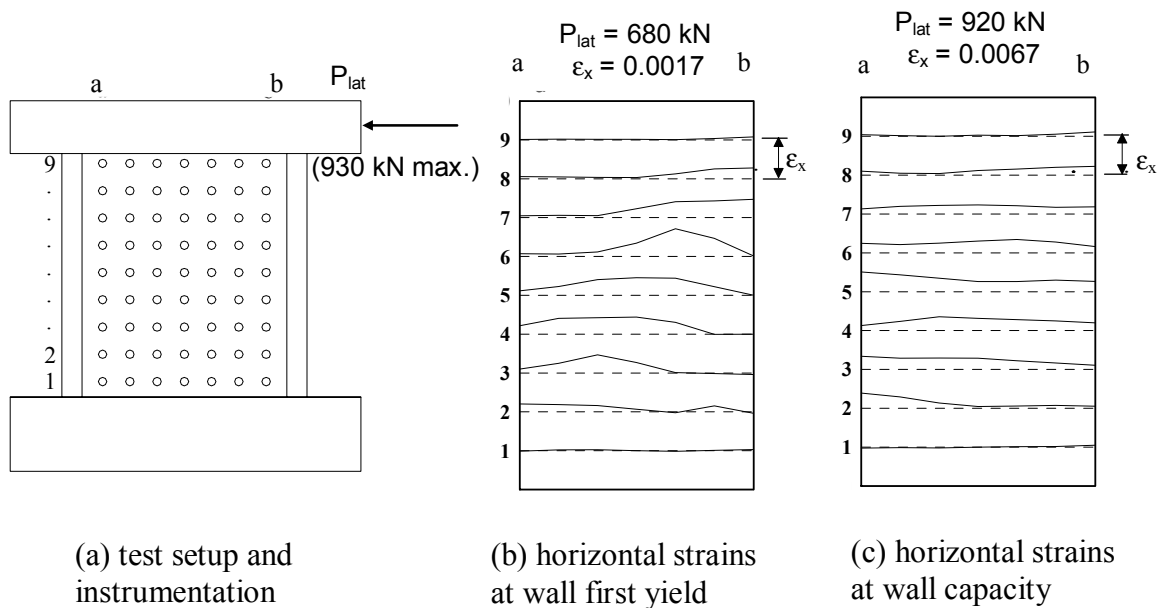


Fig. 9.7 Horizontal strain (ϵ_x) measurements for specimen S2

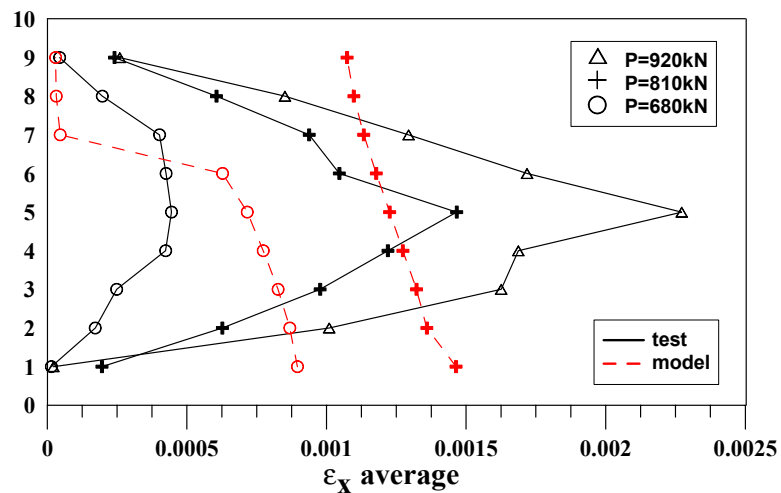


Fig. 9.8 Average horizontal strain (ϵ_x) measurements for specimen S2

9.6 SENSITIVITY OF SHORT WALL ANALYTICAL RESULTS TO THE ZERO-RESULTANT-HORIZONTAL-STRESS ASSUMPTION

As discussed in a previous section, the validity of the modeling approach and the model assumptions are violated as wall shear-span ratios decrease. In walls with relatively small shear-span ratios (e.g., specimens 152 and 16), the distribution of stresses and strains can be significantly different than the assumptions incorporated in the present model (uniform shear strain distribution along wall length and zero-resultant horizontal stress along wall length and height), impairing the correlation between model predictions and test results.

As part of ongoing studies to improve the formulation of the model for a better prediction of the response of walls with low shear-span ratios, the sensitivity of the model results to variations in the zero-resultant-horizontal-stress assumption was investigated. Prior studies by Cheng et al. (1993) revealed that, for walls with low aspect ratios (e.g., $h/l = 0.5$), the horizontal strains developed along the length of the wall are significantly reduced, especially in regions close to the top and bottom of the wall, partially due to the constraining effect of the pedestal (or beam) at the bottom and the beam at the top of the wall. Thus, for modeling, using an assumption of zero horizontal normal strain ($\epsilon_x = 0$), especially in regions close to the top and bottom of the wall, may be more appropriate than assuming zero-resultant horizontal stress ($\sigma_x = 0$) along the entire height of a wall with a low shear-span ratio.

To investigate this idea, the formulation of the present model was modified to represent an extreme case of assuming zero horizontal strains ($\epsilon_x = 0$) along the entire height and length of a wall, and the analysis was repeated for the wall specimens 152 ($M/(Vl)=0.56$) and 16 ($M/(Vl)=0.35$). The numerical methodology used to conduct the new analyses was simpler, since defining a zero value for the horizontal strain in each strip completes the definition of the strain field for each strip. Thus, the internal iteration scheme described in step 2 of the numerical methodology became redundant.

Figure 9.9 compares the results of the new analyses ($\epsilon_x = 0$) with test results, as well as with analytical results obtained previously using a zero horizontal stress ($\sigma_x = 0$) assumption. As shown in the figure, the analytical load-displacement responses obtained using the zero horizontal strain assumption yield much higher lateral stiffness and lateral load capacity for the walls compared to the results of the prior analyses obtained using the zero horizontal stress assumption. The experimentally obtained load-displacement responses fall in between these two

analytical responses, which represent extreme cases associated with wall boundary conditions ($\sigma_x = 0$ is the static boundary condition at the sides of a wall, and $\varepsilon_x = 0$ is the kinematic boundary condition at the top and bottom of a wall with rigid beams, or pedestals at the top and bottom). Therefore, it is obvious that a more detailed description of the distribution of the horizontal normal strains and stresses is necessary for an accurate prediction of the response of these walls.

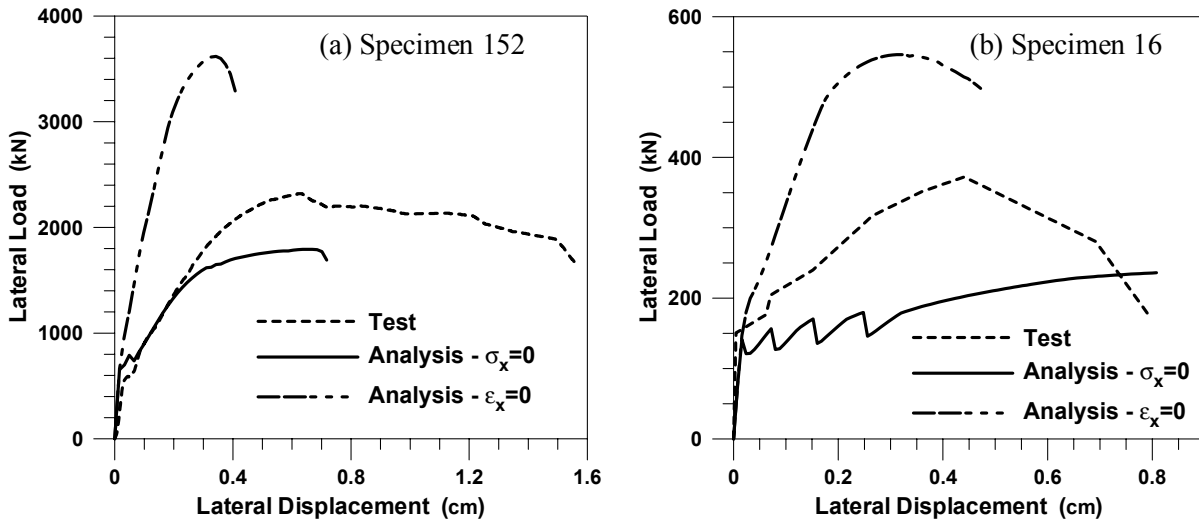


Fig. 9.9 Lateral load-displacement responses for short wall specimens 152 and 16 — zero horizontal stress and zero horizontal strain cases

In this study, reasonable response predictions were obtained using the extreme zero horizontal stress assumption for a slender wall and for two short walls with shear-span ratios of 1.0 and 0.69. Neither the zero horizontal stress nor the zero horizontal strain assumption worked well for walls with shear-span ratios of 0.56 and 0.35. It must be noted that although specimen 16 ($M/(VI) = 0.35$) had a relatively low shear-span ratio, the aspect (height-to-length) ratio of this wall is twice its shear-span ratio, since this wall was tested under loading conditions resulting in double curvature (with moments at wall ends equal in magnitude and opposite in direction). Furthermore, the transverse beams (pedestals) at the top and bottom of specimen 152 ($M/(VI) = 0.56$) were relatively small (i.e., only twice as thick as the wall), possibly falling short of producing a pronounced “constraining effect” in the horizontal direction. Thus, the zero horizontal strain condition, as suggested by Cheng et al. (1993) for walls with low aspect ratios (i.e., $h/l = 0.5$) and with pedestals at top and bottom, may not have been a reasonable assumption in modeling the responses of these particular walls. The zero horizontal stress assumption also is

inaccurate; however, better predictions were obtained and the results generally did not overestimate the strength, stiffness, or ductility capacity. Further experimental and analytical studies are under way to characterize short RC wall behavior as well as to improve the modeling assumptions for better prediction of short wall response.

10 Summary and Conclusions

The objective of this study was to investigate an effective modeling approach that integrates important material characteristics and behavioral response features (e.g., neutral axis migration, tension stiffening, progressive gap closure, nonlinear shear behavior) for a reliable prediction of the inelastic response of reinforced concrete structural walls. For this purpose, the multiple-vertical-line-element model (MVLEM) was improved via implementing refined constitutive relations for materials, and incorporating shear-flexure coupling behavior. Attributes of the model response were investigated to assess the capability of the model to incorporate critical material and behavioral features in wall response predictions. Variation of model and material parameters were studied to identify the sensitivity of analytically predicted global and local wall responses to changes in these parameters as well as to identify which parameters require the greatest care with respect to calibration. Detailed calibration of the model and comprehensive correlation studies were conducted to compare the analytically predicted and experimentally observed behavior for slender RC walls with rectangular and T-shaped cross sections at various response levels, as well as for short walls with various shear-span-to-depth ratios.

Conclusions regarding the efficiency of the modeling approach adopted here, related observations on critical modeling issues, as well as recommendations on how the modeling approach could be improved, are presented in the following sections.

10.1 FLEXURAL MODELING

The analytical model adopted here for simulating wall flexural responses resembles a macroscopic fiber model, which is the current state-of-the-art tool for modeling slender reinforced concrete structural elements. Based on analysis results, it was verified that the MVLEM captures important response characteristics associated with cyclic behavior of slender

reinforced concrete structural walls governed by flexure. The analytical model is able to simulate important behavioral features including shifting of the neutral axis along the wall cross section, and the effect of fluctuating axial force, which are commonly ignored in simple models. Characteristics of the cyclic wall response, including stiffness degradation and strength deterioration, hysteretic shape, and pinching behavior are clearly captured in the analysis results.

Apart from material constitutive parameters, the only parameters associated with the flexural model are the number of uniaxial elements used along the length of the wall cross section, the number of MVLEM elements stacked on top of each other along the height of the wall, and the parameter defining the location of the center of rotation along the height of each MVLEM element. It has been observed that model results are not very sensitive to the selection of either the number of MVLEM elements along the height of the wall or the number of uniaxial elements along the wall length, provided that reasonable values are selected in order to adequately represent the overall wall geometry. However, use of more elements is valuable in terms of obtaining more detailed information on local behavior, such as the state of stress and strain or moment curvature response at a given location. Furthermore, as also investigated by Fischinger et al. (1990), stacking more MVLEM elements along the wall height, especially in the regions where inelastic deformations are expected, results in smaller variations in the moment and curvature along the height of each element, diminishing the influence of the parameter c on the response. Therefore, the model efficiently integrates the simplicity of a macroscopic model with the flexibility to choose how much detail is desired in the analytical results.

The MVLEM implemented in this study relates the predicted flexural response directly to uniaxial material behavior without incorporating any additional empirical relations. The approach adopted here involves implementing state-of-the-art cyclic constitutive relations for concrete and reinforcing steel to track the nonlinear response of the model sub-elements, versus the use of simplified (ad hoc) force-deformation rules as applied to more recent modifications of the MVLEM. This allows the designer to relate analytical responses directly to physical material behavior and provides a more robust modeling approach, where model improvements result from improvement in constitutive models. The constitutive relations implemented in this study provide a direct and flexible approach to incorporate important material behavioral features (e.g., Bauschinger's effect in reinforcing steel, hysteretic behavior of concrete in continuous compression and tension, progressive gap closure, tension-stiffening effect) into the analysis.

The stiffness and force-deformation properties of the model sub-elements are derived from uniaxial stress-strain behavior of materials; therefore, responses obtained using the present wall model are governed by the properties and parameters of the adopted material constitutive relations. For a reliable prediction of wall responses, it is critical that the stress-strain relations adopted in the wall model are flexible and allow calibration of their constitutive parameters based on the mechanical properties of the materials used in the construction of the walls modeled, or based on parameters previously verified by other researchers (e.g., for confinement, tension stiffening, cyclic stress-strain behavior of steel and concrete). It has been observed that the model responses are not only sensitive to material parameters associated with the monotonic stress-strain behavior, but are also influenced significantly by variation in the hysteretic parameters defined for steel and for concrete in tension, which cannot easily be calibrated, since tests to assess cyclic material behavior are not commonly conducted. Thus, careful calibration of these parameters is important for an improved prediction of the cyclic wall response. The constitutive relations and the calibration methodology used in this study are recommended for a reliable response prediction.

The MVLE model, as implemented in this study, provides an accurate prediction of flexural wall behavior observed during tests at various response levels (wall load-displacement response, wall lateral load capacity at varying drift levels, wall displacement profile, average rotations and displacements over the region of inelastic deformations) for a wall with rectangular cross section. The model can predict with reasonable accuracy the measured tensile strains and the position of the neutral axis throughout the test, whereas the compressive strains tend to be underpredicted. The reason for the underestimation of compressive strains may be stress concentrations induced at wall-pedestal interface or nonlinear shear deformations experienced within the nonlinear flexural deformation region of the wall.

The same level of accuracy persists in the response prediction for a T-shaped wall when the flange is in compression. When the flange is in tension, discrepancies between the results obtained with the analytical model and the experimental results are observed for the wall lateral load capacity and the displacements and rotations along the wall. Wall lateral load capacity and inelastic rotations are overestimated, whereas inelastic lateral displacements are underestimated due to the observed nonlinear tensile strain distribution along the flange of the wall, which can not be captured with the analytical model, since it is based on a plane section assumption that produces a uniform tensile strain distribution along the flange.

10.2 SHEAR-FLEXURE INTERACTION MODEL

The analytical model adopted in this study to simulate coupled shear and flexural wall responses provides a reasonably accurate response prediction for a slender wall, considering that results of monotonic analysis were compared with cyclic test results. The model overestimates the flexural deformations and underestimates the shear deformations experienced by the wall; however, the coupling of nonlinear shear and flexural responses was clearly and realistically represented.

Comparisons between analytical model responses and test results for short walls show that the accuracy of the proposed model in predicting wall responses is better for walls with relatively higher shear-span-to-depth ratios. Comparing limited test results with preliminary model responses, the model was found to provide good response predictions for walls with relatively large shear-span ratios (1.0 and 0.69). The analytical load-displacement responses were found to be insensitive to model discretization (i.e., number of model sub-elements used), provided that reasonable values are selected in order to adequately represent the overall wall geometry. Based on the correlations presented, it is recommended to use the material models implemented and the level of discretization used in this study to model the shear-flexural response of walls with relatively large shear-span ratios.

Increasingly significant discrepancies are observed between the analytical and experimental results for walls with lower shear-span ratios (0.56 and 0.35). Therefore, the modeling approach and assumptions need to be improved in order to obtain reliable response predictions for shorter walls. It has been observed that the model has the potential to provide improved response predictions for such short walls, upon modifying the model assumptions to represent a reasonable distribution of horizontal stresses and strains in a wall, and especially upon incorporation of horizontal normal strain distribution function along the height of a wall, representing the constraining effect of beams or pedestals located at the top and bottom. The model results are promising; ongoing work focuses on refinement of the analytical model and the adopted material constitutive relations, incorporating cyclic response analyses, and conducting extensive experimental calibration and correlation studies.

10.3 SUGGESTED IMPROVEMENTS TO ANALYTICAL MODELS

1. For a reliable prediction of T-shaped wall response, modifications to the flexural model to account for the variation of longitudinal strain along the wall flange are needed (e.g., implementation of a nonlinear strain distribution relation such as proposed by Pantazopoulou and Moehle, 1988).
2. The flexural model can be extended to incorporate nonlinear dynamic responses, via adaptation of an incremental dynamic analysis algorithm that involves step-by-step numerical integration using Newmark's method (1959) and the force-controlled Newton-Raphson iteration scheme described in Chapter 5, to obtain the nonlinear dynamic response of the model.
3. The flexural model can also be extended to allow direct modeling of three-dimensional responses, by revising the formulation to consider biaxial bending.
4. Available axial models for bond-slip and reinforcing bar buckling can be feasibly incorporated within the uniaxial sub-elements of the analytical models.
5. The shear-flexure interaction model can be extended to simulate coupled shear and flexural responses of walls under cyclic loading.
6. The accuracy of the shear-flexure interaction model in capturing responses of short walls (especially for walls with shear-span-to-depth ratios smaller than 0.7) can be significantly improved upon implementing realistic horizontal normal strain distributions, representing the constraining effect of the pedestals or beams at the boundaries of the walls.

Overall, the multiple-vertical-line-element-model, as adopted in this study, provides an effective means to model cyclic flexural responses, at both the global and local levels, of slender reinforced concrete structural walls, subject to limitations that also apply for a two-dimensional fiber model. The model provides a flexible platform to assess the influence of various material and wall attributes on the nonlinear response of slender RC structural walls, as well as a practical platform for implementing further improvements. The improvement of the model to incorporate coupling of shear and flexural responses not only allows capturing of nonlinear shear deformations in even relatively slender walls but also provides reasonably accurate monotonic response predictions for short walls with shear-span-to-depth ratios of larger than 0.7.

Implementation of the model into the computational platform OpenSees will provide design engineers improved analytical capabilities to model the behavior of structural walls and their interaction with other structural elements, which is essential for application of performance-based design.

REFERENCES

- Aristizabal-Ochoa, J. D. 1983. Cracking and shear effects of structural walls. *ASCE Journal of Structural Engineering* 109(5): 1267–1275.
- Belarbi, H., and T. C. C. Hsu. 1995. Constitutive laws of softened concrete in biaxial tension-compression. *ACI Structural Journal* 92(5): 562–573.
- Belarbi, H., and T. C. C. Hsu. 1994. Constitutive laws of concrete in tension and reinforcing bars stiffened by concrete. *ACI Structural Journal* 91(4): 465–474.
- Bolong, Z. W., W. Mingshun, and Z. Kunlian. 1980. A study of hysteretic curve of reinforced concrete members under cyclic loading. *Proceedings, 7th World Conference on Earthquake Engineering* (6). Istanbul, Turkey. 509–516.
- Carreira, D. J., and C. Kuang-Han. 1985. Stress-strain relationship for plain concrete in compression. *ACI Structural Journal* 82(6): 797–804.
- Chang, G. A., and J. B. Mander. 1994. Seismic energy based fatigue damage analysis of bridge columns: Part I — evaluation of seismic capacity. *NCEER Technical Report No. NCEER-94-0006*. State University of New York. Buffalo, New York.
- Cheng, F. Y., G. E. Mertz, M. S. Sheu, and J. F. Ger. 1993. Computed versus observed inelastic seismic low-rise RC shear walls. *ASCE Journal of Structural Engineering* 119(11): 3255–3275.
- Clarke, M. J., and G. J. Hancock. 1990. A study of incremental-iterative strategies for non-linear analyses. *International Journal for Numerical Methods in Engineering* (29): 1365–1391.
- Collins, M. P., and A. Porasz. 1989. Shear strength for high strength concrete. In: *Design Aspects of High Strength Concrete* (Bull. No. 193). Comité Euro-International du Béton (CEB). 75–83.
- Collins, P. M., and D. Mitchell. 1991. *Prestressed concrete structures*. Prentice Hall. Upper Saddle River, New Jersey.
- Colotti, V. 1993. Shear behavior of RC structural walls. *ASCE Journal of Structural Engineering* 119(3): 728–746.
- Colotti, V., and A. Vulcano. A. 1987. Behavior of reinforced concrete structural walls subjected to severe cyclic loadings (in Italian). *Proceedings, Italian Association of Reinforced and Prestressed Concrete Conference*. Stresa, Italy. 87–102.

- Dodd, L. L., and J. I. Restrepo-Posada. 1995. Model for predicting cyclic behavior of reinforcing steel. *ASCE Journal of Structural Engineering* 121(3): 433–445.
- Elmorsi, M., M. R. Kianush, and W. K. Tso. 1998. Nonlinear analysis of cyclically loaded reinforced concrete structures. *ACI Structural Journal* 95(6): 725–739.
- Fajfar, P., and M. Fischinger. 1990. Mathematical modeling of RC structural walls for nonlinear seismic analysis. *Proceedings, European Conference on Structural Dynamics* (2). Bochum, Germany. 471–478.
- FEMA. 2000. *Prestandard and Commentary for the Seismic Rehabilitation of Buildings*. 2000. Report No. FEMA–356. Federal Emergency Management Agency.
- Filippou, F. C., E. G. Popov, and V. V. Bertero. 1983. Effects of bond deterioration on hysteretic behavior of reinforced concrete joints. *EERC Report No. UCB/EERC–83/19*. Earthquake Engineering Research Center. University of California. Berkeley, California.
- Fischinger, M., T. Vidic, J. Selih, P. Fajfar, H. Y. Zhang, and F. B. Damjanic. 1990. Validation of a macroscopic model for cyclic response prediction of RC walls. In N. B. Bicanic, and H. Mang (eds.): *Computer Aided Analysis and Design of Concrete Structures* (2). Pineridge Press. Swansea, United Kingdom. 1131–1142.
- Fischinger, M., T. Vidic, and P. Fajfar. 1991. Evaluation of the inelastic response of a RC building with a structural wall designed according to Eurocode 8. *Proceedings, International Conference on Buildings with Load Bearing Concrete Walls in Seismic Zones*. Paris. France. 487–498.
- Fischinger, M. T. Vidic, and P. Fajfar. 1992. Nonlinear seismic analysis of structural walls using the multiple-vertical-line-element model. In H. Krawinkler, and P. Fajfar (eds.): *Nonlinear Seismic Analysis of RC Buildings*. Elsevier Science Publishers Ltd. London and New York. 191–202.
- Gopalaratnman, V. S., and S. P. Shah. 1985. Softening response of plain concrete under direct tension. *Journal of the American Concrete Institute* 82(3): 310–323.
- Hidalgo, P. A., C. A. Ledezma, and R. M. Jordan. 2002. Seismic behavior of squat reinforced concrete shear walls. *Earthquake Spectra* 18(2): 287–308.
- Hirosawa, M. 1975. Past experimental results on reinforced concrete shear walls and analysis on them. *Kenchiku Kenkyu Shiryo* (6), Building Research Institute, Ministry of Construction, Japan.

- Hsu, T. T. C., and R. R. H. Zhu. 2002. Softened membrane model for reinforced concrete elements in shear. *ACI Structural Journal* 99(4): 460–469.
- Hsu, T. T. C., and Zhang. 1996. Tension stiffening in reinforced concrete membrane elements. *ACI Structural Journal* 93(1): 108–115.
- Hsu, T. T. C. 1988. Softened truss model theory for shear and torsion. *ACI Structural Journal* 85(6): 624–635.
- International Conference of Building Officials. 1994. *Uniform Building Code* (1994). Whittier, California.
- Kabeyasawa, T., H. Shiohara, S. Otani, and H. Aoyama. 1983. Analysis of the full-scale seven-story reinforced concrete test structure. *Journal of the Faculty of Engineering, The University of Tokyo* 37(2): 431–478.
- Kabeyasawa, T. 1997. Design of RC shear walls in hybrid wall system. *Proceedings, Fourth Joint Technical Coordinating Committee, U.S.-Japan Cooperative Seismic Research on Composite and Hybrid Structures*. Monterey, California.
- Karsan, I. D., and J. O. Jirsa. 1969. Behavior of concrete under compressive loadings. *ASCE Journal of the Structural Division*. 95(12): 2543–2563.
- Kent, D.C. and R. Park. 1971. Flexural members with confined concrete. *ASCE Journal of the Structural Division* 97(7): 1969–1990.
- Keshavarzian, M., and W. C. Schnobrich. 1984. Computed nonlinear response of reinforced concrete wall-frame structures. *Report No. SRS 515*. University of Illinois. Urbana, Champaign.
- Maier, J., and B. Thurlimann. 1985. Bruchversuche an stahlbetonscheiben (in German). *Report*. Institut für Baustatik und Konstruktion, Eidgenössische Technische Hochschule. Zurich, Germany.
- Mander, J. B., M. J. N. Priestley, and R. Park. 1984. Seismic design of bridge piers. *Report No: 84-2*. Department of Civil Engineering. University of Canterbury. Christchurch, New Zealand.
- Mander, J. B., M. J. N. Priestley, and R. Park. 1988a. Theoretical stress-strain model for confined concrete. *ASCE Journal of Structural Engineering* 114(8): 1804–1826.
- Mander, J. B., M. J. N. Priestley, and R. Park. 1988b. Observed stress-strain model of confined concrete. *ASCE Journal of Structural Engineering* 114(8): 1827–1849.

- Mansour, M., J. Lee, and T. T. C. Hsu. 2001. Cyclic stress-strain curves of concrete and steel bars in membrane elements. *ASCE Journal of Structural Engineering* 127(12): 1402–1411.
- Massone, L.M., and J. W. Wallace. 2004. Load-deformation responses of slender reinforced concrete walls. *ACI Structural Journal* 101(1): 103–113.
- Matlab. 2001. The MathWorks. Inc. Natick, Massachusetts.
- Menegotto, M., and E. Pinto. 1973. Method of analysis for cyclically loaded reinforced concrete plane frames including changes in geometry and non-elastic behavior of elements under combined normal force and bending, *Proceedings, IABSE Symposium*. Lisbon, Portugal.
- Okamoto, S., S. Shiomi, and K. Yamabe. 1976. Earthquake resistance of prestressed concrete structures. *Proceedings, AIJ Annual Convention*. 1251–1252.
- OpenSees. Open System for Earthquake Engineering Simulation. Pacific Earthquake Engineering Research Center, University of California. Berkeley, California.
- Orakcal, K., J. W. Wallace, and J. P. Conte. 2004. Nonlinear modeling and analysis of slender reinforced concrete walls. *ACI Structural Journal* 101(5): 688–699.
- Orakcal, K., and J. W. Wallace. 2004. Modeling of slender reinforced concrete walls. *Proceedings, 13th World Conference on Earthquake Engineering*. Vancouver, Canada.
- Palermo, D., and F. J. Vecchio. 2003. Compression field modeling of reinforced concrete subjected to reversed loading: formulation. *ACI Structural Journal* 100(5): 616–625.
- Pang, X.D., and T. T. C. Hsu. 1995. Behavior of reinforced concrete membrane elements in shear. *ACI Structural Journal* 92(6): 665–679.
- Pantazopoulou, S. J., and J. P. Moehle. Simple analytical models for t-beams in flexure. *ASCE Journal of Structural Engineering*. 114(7): 1507–1523.
- Petrangeli, M., P. E. Pinto, and V. Ciampi. 1999a. Fiber element for cyclic bending and shear of RC structures I: theory. *ASCE Journal of Engineering Mechanics* 125(9): 994–1001.
- Petrangeli, M. 1999b. Fiber element for cyclic bending and shear of RC structures II: verification. *ASCE Journal of Engineering Mechanics* 125(9): 1002–1009.
- Popovics, S. 1973. A numerical approach to the complete stress-strain curve of concrete. *Cement and Concrete Research* 3(4): 583–599.
- Pang, X. D., and T. T. C. Hsu. 1995. Behavior of reinforced concrete membrane elements in shear. *ACI Structural Journal* 92(6): 665–679.
- Powell, G., and J. Simons. 1981. Improved iteration strategy for nonlinear structures. *International Journal for Numerical Methods in Engineering* (17): 1455–1467.

- RAM Perform. 2003. *RAM International*. Carlsbad, California.
- Riks, E. 1979. An incremental approach to the solution of snapping and buckling problems. *International Journal of Solids and Structures* (15): 529–551.
- Rizkalla, S. H., and L. S. Hwang. 1984. Crack prediction for members in uniaxial tension. *Journal of the American Concrete Institute* 81(6): 572–579.
- Saatcioglu, M., and S. R. Razvi. 1992. Strength and ductility of confined concrete. *ASCE Journal of Structural Engineering* 118(6): 1590–1607.
- Sayre, B. 2003. Performance evaluation of steel reinforced shear walls. *MS Thesis*. University of California. Los Angeles, California.
- Scott, B. D., R. Park, and M. J. N. Priestley. 1982. Stress-strain behavior of concrete confined by overlapping hoops at low and high strain rates. *Journal of the American Concrete Institute* 79(1): 13–27.
- Seckin, M. 1981. Hysteretic behavior of cast-in-place exterior beam-column sub-assemblies. *Dissertation*. University of Toronto. Toronto, Canada.
- Sinha, B. P., K. H. Gerstle, and L. G. Tulin. 1964. Stress-strain relations for concrete under cyclic loading. *Journal of the American Concrete Institute* 61(2): 195–211.
- Spooner, D. C., and J. W. Dougill. 1975. A quantitative assessment of damage sustained in concrete during compression loading. *Magazine of Concrete Research* 27(92): 151–160.
- Stanton, J. F., and H. D. Mc Niven. 1979. The development of a mathematical model to predict the flexural response of reinforced concrete beams subjected to cyclic loads, using system identification. EERC Report No. UCB/EERC–79/2. Earthquake Engineering Research Center. University of California. Berkeley, California.
- Takayanagi, T., A. T. Derecho, and W.G. Corley. 1979. Analysis of inelastic shear deformation effects in reinforced concrete structural wall systems. *Proceedings, CSCE–ASCE–ACI–CEB International Symposium*. Ontario, Canada. 545–579.
- Takayanagi, T., and W. C. Schnobrich. 1976. Computed behavior of reinforced concrete coupled shear walls. *Report No. SRS 434*. University of Illinois. Urbana, Champaign.
- Tanigawa, Y., and Y. Uchida. 1979. Hysteretic characteristics of concrete in the domain of high compressive strain. *Proceedings, AIJ Annual Convention*. 449–450.
- Thomsen, J. H., and J. W. Wallace. 2004. Experimental verification of displacement-based design procedures for slender reinforced concrete structural walls. *ASCE Journal of Structural Engineering* 130(4): 618–630.

- Thomsen, J. H., and J. W. Wallace. 1995. Displacement-based design of reinforced concrete structural walls: an experimental investigation of walls with rectangular and t-shaped cross-sections. *Report No. CU/CEE-95/06*. Department of Civil Engineering. Clarkson University. Postdam. New York.
- Tsai, W. T. 1988. Uniaxial compressional stress-strain relation of concrete. *ASCE Journal of Structural Engineering* 114(9): 2133–2136.
- Vecchio, F. J. 2000. Disturbed stress field model for reinforced concrete: formulation. *ASCE Journal of Structural Engineering* 126(9): 1070–1077.
- Vecchio, F. J., and M. P. Collins. 1993. Compression response of cracked reinforced concrete. *ASCE Journal of Structural Engineering* 119(12): 3590–3610.
- Vecchio, F. J., and M. P. Collins. 1986. The modified compressional-field theory for reinforced concrete elements subjected to shear. *Journal of the American Concrete Institute* 83(22): 219–231.
- Vecchio, F. J., and M. P. Collins. 1982. The response of reinforced concrete to in-plane shear and normal stresses. *Publication No. 82-03*, Department of Civil Engineering, University of Toronto. Toronto, Canada.
- Vulcano, A., and V. V. Bertero. 1987. Analytical models for predicting the lateral response of RC shear walls: evaluation of their reliability. *EERC Report No. UCB/EERC-87/19*, Earthquake Engineering Research Center, University of California. Berkeley, California.
- Vulcano, A., and V. V. Bertero. 1986. Nonlinear analysis of RC structural walls. *Proceedings, 8th European Conference on EQ Engineering* (3). Lisbon. Portugal. 6.5/1–6.5/8.
- Vulcano, A., V. V. Bertero, and V. Colotti. 1988. Analytical modeling of RC structural walls. *Proceedings, 9th World Conference on Earthquake Engineering* (6). Tokyo-Kyoto, Japan. 41–46.
- Vulcano, A. 1992. Macroscopic modeling for nonlinear analysis of reinforced concrete structural walls. In H. Krawinkler, and P. Fajfar (eds.): *Nonlinear Seismic Analysis of RC Buildings*. Elsevier Science Publishers Ltd. London and New York. 181–190.
- Wallace, J. W. 1994. A new methodology for seismic design of reinforced concrete shear walls. *ASCE Journal of Structural Engineering*. 120(3): 863–884.
- Wallace, J. W. 1995. Seismic design of reinforced concrete shear walls, part 1: new code format. *ASCE Journal of Structural Engineering*. 121(1): 75–87.

- Wee, T.H., M. S. Chin, and M. A. Mansur. 1996. Stress-strain relationship of high-strength concrete in compression. *ASCE Journal of Materials in Civil Engineering* 8(2): 70–76.
- Wempner, G. A. 1971. Discrete approximations related to nonlinear theories of solids. *International Journal of Solids and Structures* (7): 1581–1599.
- Yankelevsky, D. Z., and H. W. Reinhardt. 1987. Response of plain concrete to cyclic tension. *ACI Materials Journal* 84(5): 365–373.
- Yassin, M. H. M. 1994. Nonlinear analysis of prestressed concrete structures under monotonic and cyclic loads. *Dissertation*. University of California. Berkeley, California.
- Yan, W., and J. W. Wallace. 1993. Analytical studies of four shear wall buildings using data from recent California earthquakes. *MS Thesis*. Department of Civil Engineering. Clarkson University. Postdam, New York.

PEER REPORTS

PEER reports are available from the National Information Service for Earthquake Engineering (NISEE). To order PEER reports, please contact the Pacific Earthquake Engineering Research Center, 1301 South 46th Street, Richmond, California 94804-4698. Tel.: (510) 665-3405; Fax: (510) 665-3420.

- PEER 2006/07** *Analytical Modeling of Reinforced Concrete Walls for Predicting Flexural and Coupled Shear-Flexural Responses.* Kutay Orakcal, Leonardo M. Massone, and John W. Wallace. October 2006.
- PEER 2006/04** *Probabilistic Seismic Evaluation of Reinforced Concrete Structural Components and Systems.* Tae Hyung Lee and Khalid M. Mosalam. August 2006.
- PEER 2006/02** *Pacific Earthquake Engineering Research Center Highway Demonstration Project.* Anne Kiremidjian, James Moore, Yue Yue Fan, Nesrin Basoz, Ozgur Yazali, and Meredith Williams. April 2006.
- PEER 2006/01** *Bracing Berkeley. A Guide to Seismic Safety on the UC Berkeley Campus.* Mary C. Comerio, Stephen Tobriner, and Ariane Fehrenkamp. January 2006.
- PEER 2005/16** *Seismic Response and Reliability of Electrical Substation Equipment and Systems.* Junho Song, Armen Der Kiureghian, and Jerome L. Sackman. April 2006.
- PEER 2005/15** *CPT-Based Probabilistic Assessment of Seismic Soil Liquefaction Initiation.* R. E. S. Moss, R. B. Seed, R. E. Kayen, J. P. Stewart, and A. Der Kiureghian. April 2006.
- PEER 2005/14** *Workshop on Modeling of Nonlinear Cyclic Load-Deformation Behavior of Shallow Foundations.* Bruce L. Kutter, Geoffrey Martin, Tara Hutchinson, Chad Harden, Sivapalan Gajan, and Justin Phalen. March 2006.
- PEER 2005/13** *Stochastic Characterization and Decision Bases under Time-Dependent Aftershock Risk in Performance-Based Earthquake Engineering.* Gee Liek Yeo and C. Allin Cornell. July 2005.
- PEER 2005/12** *PEER Testbed Study on a Laboratory Building: Exercising Seismic Performance Assessment.* Mary C. Comerio, editor. November 2005.
- PEER 2005/11** *Van Nuys Hotel Building Testbed Report: Exercising Seismic Performance Assessment.* Helmut Krawinkler, editor. October 2005.
- PEER 2005/10** *First NEES/E-Defense Workshop on Collapse Simulation of Reinforced Concrete Building Structures.* September 2005.
- PEER 2005/09** *Test Applications of Advanced Seismic Assessment Guidelines.* Joe Maffei, Karl Telleen, Danya Mohr, William Holmes, and Yuki Nakayama. August 2006.
- PEER 2005/08** *Damage Accumulation in Lightly Confined Reinforced Concrete Bridge Columns.* R. Tyler Ranf, Jared M. Nelson, Zach Price, Marc O. Eberhard, and John F. Stanton. April 2006.
- PEER 2005/07** *Experimental and Analytical Studies on the Seismic Response of Freestanding and Anchored Laboratory Equipment.* Dimitrios Konstantinidis and Nicos Makris. January 2005.
- PEER 2005/06** *Global Collapse of Frame Structures under Seismic Excitations.* Luis F. Ibarra and Helmut Krawinkler. September 2005.
- PEER 2005/05** *Performance Characterization of Bench- and Shelf-Mounted Equipment.* Samit Ray Chaudhuri and Tara C. Hutchinson. May 2006.
- PEER 2005/04** *Numerical Modeling of the Nonlinear Cyclic Response of Shallow Foundations.* Chad Harden, Tara Hutchinson, Geoffrey R. Martin, and Bruce L. Kutter. August 2005.
- PEER 2005/03** *A Taxonomy of Building Components for Performance-Based Earthquake Engineering.* Keith A. Porter. September 2005.
- PEER 2005/02** *Fragility Basis for California Highway Overpass Bridge Seismic Decision Making.* Kevin R. Mackie and Bozidar Stojadinovic. June 2005.
- PEER 2005/01** *Empirical Characterization of Site Conditions on Strong Ground Motion.* Jonathan P. Stewart, Yoojoong Choi, and Robert W. Graves. June 2005.
- PEER 2004/09** *Electrical Substation Equipment Interaction: Experimental Rigid Conductor Studies.* Christopher Stearns and André Filiatrault. February 2005.

- PEER 2004/08** *Seismic Qualification and Fragility Testing of Line Break 550-kV Disconnect Switches.* Shakhzod M. Takhirov, Gregory L. Fenves, and Eric Fujisaki. January 2005.
- PEER 2004/07** *Ground Motions for Earthquake Simulator Qualification of Electrical Substation Equipment.* Shakhzod M. Takhirov, Gregory L. Fenves, Eric Fujisaki, and Don Clyde. January 2005.
- PEER 2004/06** *Performance-Based Regulation and Regulatory Regimes.* Peter J. May and Chris Koski. September 2004.
- PEER 2004/05** *Performance-Based Seismic Design Concepts and Implementation: Proceedings of an International Workshop.* Peter Fajfar and Helmut Krawinkler, editors. September 2004.
- PEER 2004/04** *Seismic Performance of an Instrumented Tilt-up Wall Building.* James C. Anderson and Vitelmo V. Bertero. July 2004.
- PEER 2004/03** *Evaluation and Application of Concrete Tilt-up Assessment Methodologies.* Timothy Graf and James O. Malley. October 2004.
- PEER 2004/02** *Analytical Investigations of New Methods for Reducing Residual Displacements of Reinforced Concrete Bridge Columns.* Junichi Sakai and Stephen A. Mahin. August 2004.
- PEER 2004/01** *Seismic Performance of Masonry Buildings and Design Implications.* Kerri Anne Taeko Tokoro, James C. Anderson, and Vitelmo V. Bertero. February 2004.
- PEER 2003/18** *Performance Models for Flexural Damage in Reinforced Concrete Columns.* Michael Berry and Marc Eberhard. August 2003.
- PEER 2003/17** *Predicting Earthquake Damage in Older Reinforced Concrete Beam-Column Joints.* Catherine Pagni and Laura Lowes. October 2004.
- PEER 2003/16** *Seismic Demands for Performance-Based Design of Bridges.* Kevin Mackie and Božidar Stojadinovic. August 2003.
- PEER 2003/15** *Seismic Demands for Nondeteriorating Frame Structures and Their Dependence on Ground Motions.* Ricardo Antonio Medina and Helmut Krawinkler. May 2004.
- PEER 2003/14** *Finite Element Reliability and Sensitivity Methods for Performance-Based Earthquake Engineering.* Terje Haukaas and Armen Der Kiureghian. April 2004.
- PEER 2003/13** *Effects of Connection Hysteretic Degradation on the Seismic Behavior of Steel Moment-Resisting Frames.* Janise E. Rodgers and Stephen A. Mahin. March 2004.
- PEER 2003/12** *Implementation Manual for the Seismic Protection of Laboratory Contents: Format and Case Studies.* William T. Holmes and Mary C. Comerio. October 2003.
- PEER 2003/11** *Fifth U.S.-Japan Workshop on Performance-Based Earthquake Engineering Methodology for Reinforced Concrete Building Structures.* February 2004.
- PEER 2003/10** *A Beam-Column Joint Model for Simulating the Earthquake Response of Reinforced Concrete Frames.* Laura N. Lowes, Nilanjan Mitra, and Arash Altoontash. February 2004.
- PEER 2003/09** *Sequencing Repairs after an Earthquake: An Economic Approach.* Marco Casari and Simon J. Wilkie. April 2004.
- PEER 2003/08** *A Technical Framework for Probability-Based Demand and Capacity Factor Design (DCFD) Seismic Formats.* Fatemeh Jalayer and C. Allin Cornell. November 2003.
- PEER 2003/07** *Uncertainty Specification and Propagation for Loss Estimation Using FOSM Methods.* Jack W. Baker and C. Allin Cornell. September 2003.
- PEER 2003/06** *Performance of Circular Reinforced Concrete Bridge Columns under Bidirectional Earthquake Loading.* Mahmoud M. Hachem, Stephen A. Mahin, and Jack P. Moehle. February 2003.
- PEER 2003/05** *Response Assessment for Building-Specific Loss Estimation.* Eduardo Miranda and Shahram Taghavi. September 2003.
- PEER 2003/04** *Experimental Assessment of Columns with Short Lap Splices Subjected to Cyclic Loads.* Murat Melek, John W. Wallace, and Joel Conte. April 2003.
- PEER 2003/03** *Probabilistic Response Assessment for Building-Specific Loss Estimation.* Eduardo Miranda and Hesameddin Aslani. September 2003.

- PEER 2003/02** *Software Framework for Collaborative Development of Nonlinear Dynamic Analysis Program.* Jun Peng and Kincho H. Law. September 2003.
- PEER 2003/01** *Shake Table Tests and Analytical Studies on the Gravity Load Collapse of Reinforced Concrete Frames.* Kenneth John Elwood and Jack P. Moehle. November 2003.
- PEER 2002/24** *Performance of Beam to Column Bridge Joints Subjected to a Large Velocity Pulse.* Natalie Gibson, André Filiatrault, and Scott A. Ashford. April 2002.
- PEER 2002/23** *Effects of Large Velocity Pulses on Reinforced Concrete Bridge Columns.* Greg L. Orozco and Scott A. Ashford. April 2002.
- PEER 2002/22** *Characterization of Large Velocity Pulses for Laboratory Testing.* Kenneth E. Cox and Scott A. Ashford. April 2002.
- PEER 2002/21** *Fourth U.S.-Japan Workshop on Performance-Based Earthquake Engineering Methodology for Reinforced Concrete Building Structures.* December 2002.
- PEER 2002/20** *Barriers to Adoption and Implementation of PBEE Innovations.* Peter J. May. August 2002.
- PEER 2002/19** *Economic-Engineered Integrated Models for Earthquakes: Socioeconomic Impacts.* Peter Gordon, James E. Moore II, and Harry W. Richardson. July 2002.
- PEER 2002/18** *Assessment of Reinforced Concrete Building Exterior Joints with Substandard Details.* Chris P. Pantelides, Jon Hansen, Justin Nadauld, and Lawrence D. Reaveley. May 2002.
- PEER 2002/17** *Structural Characterization and Seismic Response Analysis of a Highway Overcrossing Equipped with Elastomeric Bearings and Fluid Dampers: A Case Study.* Nicos Makris and Jian Zhang. November 2002.
- PEER 2002/16** *Estimation of Uncertainty in Geotechnical Properties for Performance-Based Earthquake Engineering.* Allen L. Jones, Steven L. Kramer, and Pedro Arduino. December 2002.
- PEER 2002/15** *Seismic Behavior of Bridge Columns Subjected to Various Loading Patterns.* Asadollah Esmaeily-Gh. and Yan Xiao. December 2002.
- PEER 2002/14** *Inelastic Seismic Response of Extended Pile Shaft Supported Bridge Structures.* T.C. Hutchinson, R.W. Boulanger, Y.H. Chai, and I.M. Idriss. December 2002.
- PEER 2002/13** *Probabilistic Models and Fragility Estimates for Bridge Components and Systems.* Paolo Gardoni, Armen Der Kiureghian, and Khalid M. Mosalam. June 2002.
- PEER 2002/12** *Effects of Fault Dip and Slip Rake on Near-Source Ground Motions: Why Chi-Chi Was a Relatively Mild M7.6 Earthquake.* Brad T. Aagaard, John F. Hall, and Thomas H. Heaton. December 2002.
- PEER 2002/11** *Analytical and Experimental Study of Fiber-Reinforced Strip Isolators.* James M. Kelly and Shakhzod M. Takhirov. September 2002.
- PEER 2002/10** *Centrifuge Modeling of Settlement and Lateral Spreading with Comparisons to Numerical Analyses.* Sivapalan Gajan and Bruce L. Kutter. January 2003.
- PEER 2002/09** *Documentation and Analysis of Field Case Histories of Seismic Compression during the 1994 Northridge, California, Earthquake.* Jonathan P. Stewart, Patrick M. Smith, Daniel H. Whang, and Jonathan D. Bray. October 2002.
- PEER 2002/08** *Component Testing, Stability Analysis and Characterization of Buckling-Restrained Unbonded Braces™.* Cameron Black, Nicos Makris, and Ian Aiken. September 2002.
- PEER 2002/07** *Seismic Performance of Pile-Wharf Connections.* Charles W. Roeder, Robert Graff, Jennifer Soderstrom, and Jun Han Yoo. December 2001.
- PEER 2002/06** *The Use of Benefit-Cost Analysis for Evaluation of Performance-Based Earthquake Engineering Decisions.* Richard O. Zerbe and Anthony Falit-Baiamonte. September 2001.
- PEER 2002/05** *Guidelines, Specifications, and Seismic Performance Characterization of Nonstructural Building Components and Equipment.* André Filiatrault, Constantin Christopoulos, and Christopher Stearns. September 2001.
- PEER 2002/04** *Consortium of Organizations for Strong-Motion Observation Systems and the Pacific Earthquake Engineering Research Center Lifelines Program: Invited Workshop on Archiving and Web Dissemination of Geotechnical Data, 4–5 October 2001.* September 2002.

- PEER 2002/03** *Investigation of Sensitivity of Building Loss Estimates to Major Uncertain Variables for the Van Nuys Testbed.* Keith A. Porter, James L. Beck, and Rustem V. Shaikhutdinov. August 2002.
- PEER 2002/02** *The Third U.S.-Japan Workshop on Performance-Based Earthquake Engineering Methodology for Reinforced Concrete Building Structures.* July 2002.
- PEER 2002/01** *Nonstructural Loss Estimation: The UC Berkeley Case Study.* Mary C. Comerio and John C. Stallmeyer. December 2001.
- PEER 2001/16** *Statistics of SDF-System Estimate of Roof Displacement for Pushover Analysis of Buildings.* Anil K. Chopra, Rakesh K. Goel, and Chatpan Chintanapakdee. December 2001.
- PEER 2001/15** *Damage to Bridges during the 2001 Nisqually Earthquake.* R. Tyler Ranf, Marc O. Eberhard, and Michael P. Berry. November 2001.
- PEER 2001/14** *Rocking Response of Equipment Anchored to a Base Foundation.* Nicos Makris and Cameron J. Black. September 2001.
- PEER 2001/13** *Modeling Soil Liquefaction Hazards for Performance-Based Earthquake Engineering.* Steven L. Kramer and Ahmed-W. Elgamal. February 2001.
- PEER 2001/12** *Development of Geotechnical Capabilities in OpenSees.* Boris Jeremi . September 2001.
- PEER 2001/11** *Analytical and Experimental Study of Fiber-Reinforced Elastomeric Isolators.* James M. Kelly and Shakhzod M. Takhirov. September 2001.
- PEER 2001/10** *Amplification Factors for Spectral Acceleration in Active Regions.* Jonathan P. Stewart, Andrew H. Liu, Yoojoong Choi, and Mehmet B. Baturay. December 2001.
- PEER 2001/09** *Ground Motion Evaluation Procedures for Performance-Based Design.* Jonathan P. Stewart, Shyh-Jeng Chiou, Jonathan D. Bray, Robert W. Graves, Paul G. Somerville, and Norman A. Abrahamson. September 2001.
- PEER 2001/08** *Experimental and Computational Evaluation of Reinforced Concrete Bridge Beam-Column Connections for Seismic Performance.* Clay J. Naito, Jack P. Moehle, and Khalid M. Mosalam. November 2001.
- PEER 2001/07** *The Rocking Spectrum and the Shortcomings of Design Guidelines.* Nicos Makris and Dimitrios Konstantinidis. August 2001.
- PEER 2001/06** *Development of an Electrical Substation Equipment Performance Database for Evaluation of Equipment Fragilities.* Thalia Agnanos. April 1999.
- PEER 2001/05** *Stiffness Analysis of Fiber-Reinforced Elastomeric Isolators.* Hsiang-Chuan Tsai and James M. Kelly. May 2001.
- PEER 2001/04** *Organizational and Societal Considerations for Performance-Based Earthquake Engineering.* Peter J. May. April 2001.
- PEER 2001/03** *A Modal Pushover Analysis Procedure to Estimate Seismic Demands for Buildings: Theory and Preliminary Evaluation.* Anil K. Chopra and Rakesh K. Goel. January 2001.
- PEER 2001/02** *Seismic Response Analysis of Highway Overcrossings Including Soil-Structure Interaction.* Jian Zhang and Nicos Makris. March 2001.
- PEER 2001/01** *Experimental Study of Large Seismic Steel Beam-to-Column Connections.* Egor P. Popov and Shakhzod M. Takhirov. November 2000.
- PEER 2000/10** *The Second U.S.-Japan Workshop on Performance-Based Earthquake Engineering Methodology for Reinforced Concrete Building Structures.* March 2000.
- PEER 2000/09** *Structural Engineering Reconnaissance of the August 17, 1999 Earthquake: Kocaeli (Izmit), Turkey.* Halil Sezen, Kenneth J. Elwood, Andrew S. Whittaker, Khalid Mosalam, John J. Wallace, and John F. Stanton. December 2000.
- PEER 2000/08** *Behavior of Reinforced Concrete Bridge Columns Having Varying Aspect Ratios and Varying Lengths of Confinement.* Anthony J. Calderone, Dawn E. Lehman, and Jack P. Moehle. January 2001.
- PEER 2000/07** *Cover-Plate and Flange-Plate Reinforced Steel Moment-Resisting Connections.* Taejin Kim, Andrew S. Whittaker, Amir S. Gilani, Vitelmo V. Bertero, and Shakhzod M. Takhirov. September 2000.
- PEER 2000/06** *Seismic Evaluation and Analysis of 230-kV Disconnect Switches.* Amir S. J. Gilani, Andrew S. Whittaker, Gregory L. Fenves, Chun-Hao Chen, Henry Ho, and Eric Fujisaki. July 2000.

- PEER 2000/05** *Performance-Based Evaluation of Exterior Reinforced Concrete Building Joints for Seismic Excitation.* Chandra Clyde, Chris P. Pantelides, and Lawrence D. Reaveley. July 2000.
- PEER 2000/04** *An Evaluation of Seismic Energy Demand: An Attenuation Approach.* Chung-Che Chou and Chia-Ming Uang. July 1999.
- PEER 2000/03** *Framing Earthquake Retrofitting Decisions: The Case of Hillside Homes in Los Angeles.* Detlof von Winterfeldt, Nels Roselund, and Alicia Kitsuse. March 2000.
- PEER 2000/02** *U.S.-Japan Workshop on the Effects of Near-Field Earthquake Shaking.* Andrew Whittaker, ed. July 2000.
- PEER 2000/01** *Further Studies on Seismic Interaction in Interconnected Electrical Substation Equipment.* Armen Der Kiureghian, Kee-Jeung Hong, and Jerome L. Sackman. November 1999.
- PEER 1999/14** *Seismic Evaluation and Retrofit of 230-kV Porcelain Transformer Bushings.* Amir S. Gilani, Andrew S. Whittaker, Gregory L. Fenves, and Eric Fujisaki. December 1999.
- PEER 1999/13** *Building Vulnerability Studies: Modeling and Evaluation of Tilt-up and Steel Reinforced Concrete Buildings.* John W. Wallace, Jonathan P. Stewart, and Andrew S. Whittaker, editors. December 1999.
- PEER 1999/12** *Rehabilitation of Nonductile RC Frame Building Using Encasement Plates and Energy-Dissipating Devices.* Mehrdad Sasani, Vitelmo V. Bertero, James C. Anderson. December 1999.
- PEER 1999/11** *Performance Evaluation Database for Concrete Bridge Components and Systems under Simulated Seismic Loads.* Yael D. Hose and Frieder Seible. November 1999.
- PEER 1999/10** *U.S.-Japan Workshop on Performance-Based Earthquake Engineering Methodology for Reinforced Concrete Building Structures.* December 1999.
- PEER 1999/09** *Performance Improvement of Long Period Building Structures Subjected to Severe Pulse-Type Ground Motions.* James C. Anderson, Vitelmo V. Bertero, and Raul Bertero. October 1999.
- PEER 1999/08** *Envelopes for Seismic Response Vectors.* Charles Menun and Armen Der Kiureghian. July 1999.
- PEER 1999/07** *Documentation of Strengths and Weaknesses of Current Computer Analysis Methods for Seismic Performance of Reinforced Concrete Members.* William F. Cofer. November 1999.
- PEER 1999/06** *Rocking Response and Overturning of Anchored Equipment under Seismic Excitations.* Nicos Makris and Jian Zhang. November 1999.
- PEER 1999/05** *Seismic Evaluation of 550 kV Porcelain Transformer Bushings.* Amir S. Gilani, Andrew S. Whittaker, Gregory L. Fenves, and Eric Fujisaki. October 1999.
- PEER 1999/04** *Adoption and Enforcement of Earthquake Risk-Reduction Measures.* Peter J. May, Raymond J. Burby, T. Jens Feeley, and Robert Wood.
- PEER 1999/03** *Task 3 Characterization of Site Response General Site Categories.* Adrian Rodriguez-Marek, Jonathan D. Bray, and Norman Abrahamson. February 1999.
- PEER 1999/02** *Capacity-Demand-Diagram Methods for Estimating Seismic Deformation of Inelastic Structures: SDF Systems.* Anil K. Chopra and Rakesh Goel. April 1999.
- PEER 1999/01** *Interaction in Interconnected Electrical Substation Equipment Subjected to Earthquake Ground Motions.* Armen Der Kiureghian, Jerome L. Sackman, and Kee-Jeung Hong. February 1999.
- PEER 1998/08** *Behavior and Failure Analysis of a Multiple-Frame Highway Bridge in the 1994 Northridge Earthquake.* Gregory L. Fenves and Michael Ellery. December 1998.
- PEER 1998/07** *Empirical Evaluation of Inertial Soil-Structure Interaction Effects.* Jonathan P. Stewart, Raymond B. Seed, and Gregory L. Fenves. November 1998.
- PEER 1998/06** *Effect of Damping Mechanisms on the Response of Seismic Isolated Structures.* Nicos Makris and Shih-Po Chang. November 1998.
- PEER 1998/05** *Rocking Response and Overturning of Equipment under Horizontal Pulse-Type Motions.* Nicos Makris and Yiannis Roussos. October 1998.
- PEER 1998/04** *Pacific Earthquake Engineering Research Invitational Workshop Proceedings, May 14-15, 1998: Defining the Links between Planning, Policy Analysis, Economics and Earthquake Engineering.* Mary Comerio and Peter Gordon. September 1998.

- PEER 1998/03** *Repair/Upgrade Procedures for Welded Beam to Column Connections.* James C. Anderson and Xiaojing Duan. May 1998.
- PEER 1998/02** *Seismic Evaluation of 196 kV Porcelain Transformer Bushings.* Amir S. Gilani, Juan W. Chavez, Gregory L. Fenves, and Andrew S. Whittaker. May 1998.
- PEER 1998/01** *Seismic Performance of Well-Confined Concrete Bridge Columns.* Dawn E. Lehman and Jack P. Moehle. December 2000.